Summer 2015

# Accuracy of theory for calculating electron impact ionization of molecules

Hari Chaluvadi



Department: Physics

# ACCURACY OF THEORY FOR CALCULATING ELECTRON IMPACT IONIZATION OF MOLECULES

by

HARI HARA KUMAR CHALUVADI

A DISSERTATION

Presented to the Faculty of the Graduate School of the

MISSOURI UNIVERSITY OF SCIENCE AND TECHNOLOGY

In Partial Fulfillment of the Requirements for the Degree

DOCTOR OF PHILOSOPHY
in
PHYSICS

2015

Approved
Don H. Madison, Advisor
Jerry L. Peacher
Michael Schulz
Ulrich Jentschura
V.Samaranayake

## PUBLICATION DISSERTATION OPTION

This dissertation has been prepared as a collection of publications in the style utilized by the Journal of Chemical Physics, the Physical Review A, the Chemical Physics Letters, and the Jounrnal of Physics B. Twelve out of eleven articles have been published and the last publication is accepted for the publication. The Introduction in Section 1 and the Conclusions in Section 2 have been added for purposes normal to dissertation writing.

## ABSTRACT

The study of electron impact single ionization of atoms and molecules has provided valuable information about fundamental collisions. The most detailed information is obtained from triple differential cross sections (TDCS) in which the energy and momentum of all three final state particles are determined. These cross sections are much more difficult for theory since the detailed kinematics of the experiment become important. There are many theoretical approximations for ionization of molecules. One of the successful methods is the molecular 3-body distorted wave (M3DW) approximation. One of the strengths of the DW approximation is that it can be applied for any energy and any size molecule.

One of the approximations that has been made to significantly reduce the required computer time is the OAMO (orientation averaged molecular orbital) approximation. In this dissertation, the accuracy of the M3DW-OAMO is tested for different molecules. Surprisingly, the M3DW-OAMO approximation yields reasonably good agreement with experiment for ionization of $H_2$ and $N_2$. On the other hand, the M3DW-OAMO results for ionization of $CH_4$, $NH_3$ and DNA derivative molecules did not agree very well with experiment. Consequently, we proposed the M3DW with a proper average (PA) calculation.

In this dissertation, it is shown that the M3DW-PA calculations for $CH_4$ and $SF_6$ are in much better agreement with experimental data than the M3DW-OAMO results.

# ACKNOWLEDGEMENTS

First and foremost, I would like to thank my family for their unconditional love and support. They provided me with the confidence I needed to finish my degree.

I would like to thank my advisor, Dr. Madison, for his patience and guidance for my work. His expertise helped me conduct my research smoothly. I would also like to thank my committee: Dr. Jerry Peacher, Dr. M. Schulz, Dr. U. Jentschura, and Dr. V. Samaranayake.

I would like to thank the physics department for offering me a teaching assistant position. This position allowed me to focus on my academic studies.

I would like to thank all of my friends in both India and the United States, for their fruitful discussions and their friendship. I couldn’t imagine my life without you.

# TABLE OF CONTENTS

Page

SECTION

# LIST OF ILLUSTRATIONS

SECTION 1



PAPER I



PAPER II

PAPER III



PAPER IV



PAPER V

PAPER X



PAPER XI

PAPER XII

# LIST OF TABLES

# SECTION

## 1. INTRODUCTION

In fundamental physics, one of the most important unsolved problems is the few-body problem where we have to deal with more than two particles. Since we cannot solve the Schrodinger equation analytically for more than two particles, we have to use approximations for the theoretical models whose validity can only be checked by comparing with the experiments. One of the ways to study the few-body problem is through electron impact ionization of atoms or molecules.

Electron impact ionization is referred as (e,2e), In the initial channel we have one incident projectile electron and a target molecule, whereas in the final channel we have scattered projectile electron, ejected electron and ion, i.e., we have one electron in initial channel and two electrons in the final channel.

The most detailed information about ionizing collisions between an electron and molecule is obtained from the triple-differential cross sections (TDCS) in which the energy and momentum of all three final -state particles are determined. The molecular three-body distorted-wave (M3DW) approximation has been one of the most successful theories for calculating TDCS for molecules.

The study of electron-impact single ionization of atoms has provided valuable information about fundamental collisions for decades. More recently, molecules have

started to receive significant attention, at least partially due to the fact that there are potentially significant applications. For example, studies of the electron-impact ionization of biomolecules provide important information on the role of electrons in causing damage to DNA in biological systems. It is now well established that low-energy secondary electrons produced by high-energy primary radiation are responsible for much of the damage to DNA in living tissues.

In this dissertation, the validity of M3DW-OAMO (molecular 3-body distorted wave- orientation averaged molecular orbital) approximation for different molecules from small molecules to big molecules will be studied (you do not define OAMO in the theory section – you need to add this definition along with the proper average definition and description). In particular, we will examine the dependence on emission angles, energies and experimental geometry. Finally, for some cases where the OAMO approximation clearly does not work very well, we will look at results results obtained using the Proper Average method.

The experimental apparatuses used to measure (e,2e) collisions, use different geometries for the collisions. Here we will describe two common geometries - the scattering plane and the perpendicular plane. The scattering plane is the plane containing the incident and scattered projectile electron. In the perpendicular plane, the scattered projectile electron is in a plane perpendicular to the incident electron direction. In each of these planes, there are symmetric and asymmetric collisions determined by the energies and angles of the outgoing electrons. Symmetric means that both outgoing electrons have the same energy and make the same angle relative to the incident beam direction. For asymmetric scattering, the energies and angles are different.

The experimental apparatuses used to measure (e,2e) collisions, use different geometries for the collisions. Here we will describe two common geometries - the scattering plane and the perpendicular plane. The scattering plane is the plane containing the incident and scattered projectile electron. In the perpendicular plane, the scattered projectile electron is in a plane perpendicular to the incident electron direction. In each of these planes, there are symmetric and asymmetric collisions determined by the energies and angles of the outgoing electrons. Symmetric means that both outgoing electrons have the same energy and make the same angle relative to the incident beam direction. For asymmetric scattering, the energies and angles are different.

The symmetric scattering plane is defined when the incident, scattered and ejected electrons are lie in the detection plane as in Fig 1.1. The symmetric perpendicular plane is defined when the incident electron is incident perpendicular to the scattered and ejected electrons plane (detection plane) as in Fig 1.2.

The energy ($E_1$) and scattering angle of the scattered electron ($\theta_1$) and the energy of the ejected electron ($E_2$) are fixed for asymmetric geometries. For the asymmetric scattering plane as in Fig 1.3, the scattered and ejected electron are detected in the coplanar plane. For the asymmetric scattering plane as in Fig 1.4 the scattered electron is detected in the scattering plane and the ejected electron is detected in the perpendicular plane.

All geometries angles are summarized in the Table 1.1.

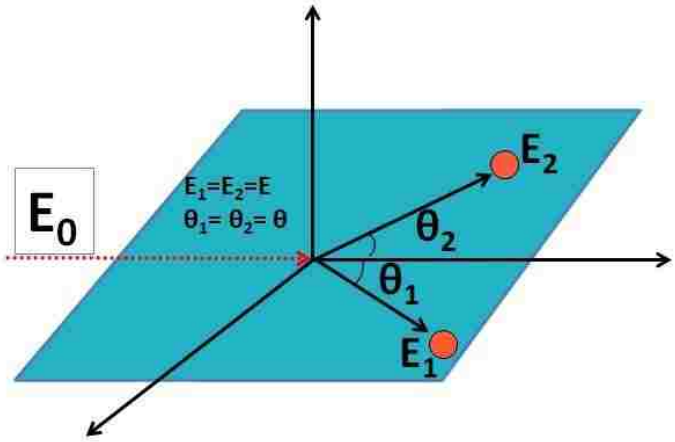


Figure 1.1 Symmetric Scattering Plane

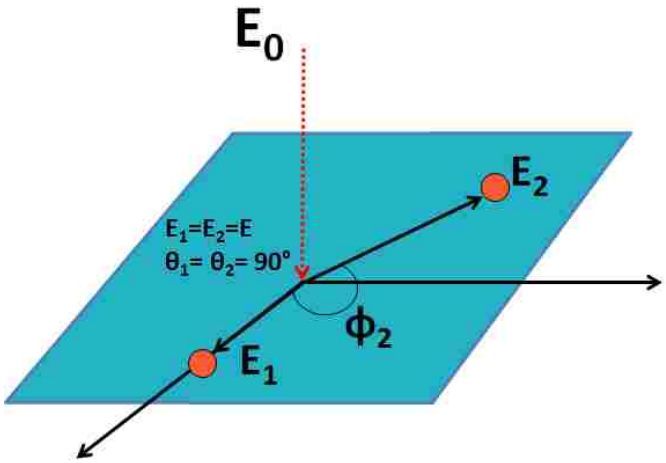


Figure 1.2 Symmetric Perpendicular plane

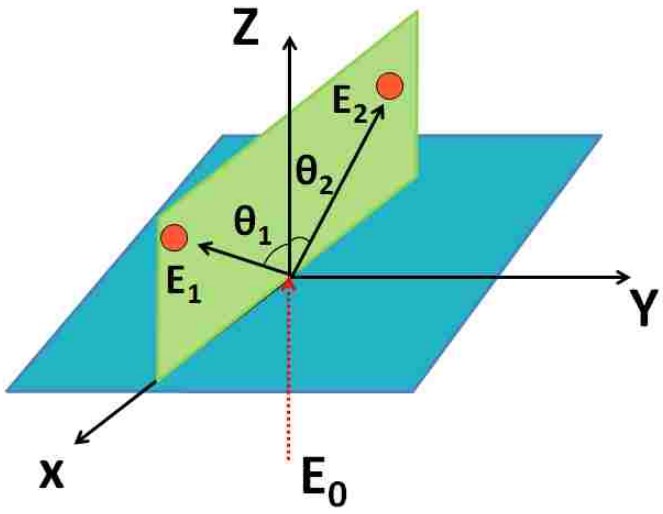


Figure 1.3 Asymmetric Scattering Plane

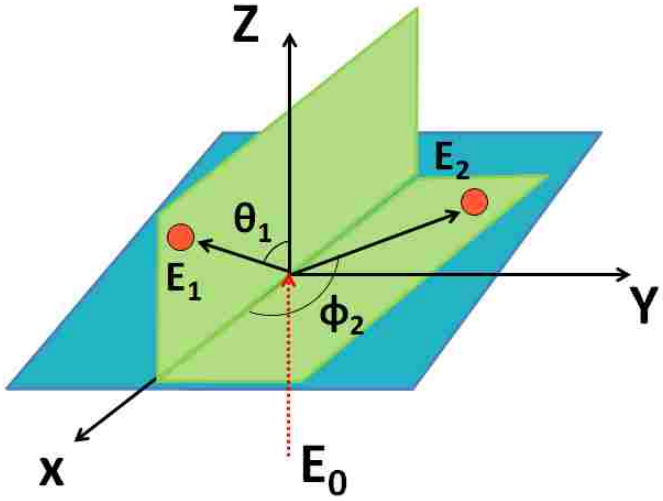


Figure 1.4 Asymmetric Perpendicular plane

Table 1.1 Angles for Geometries

| **Symmetric** | | **Asymmetric** | |
|---|---|---|---|
| Scattering plane | Perpendicular plane | Scattering plane | Perpendicular plane |
| $\Theta_1$ is variable | $\Theta_1 = 90°$ | $\Theta_1$ is fixed | $\Theta_1$ is fixed |
| $\varphi_1 = 0°$ | $\varphi_1 = 0°$ | $\varphi_1 = 0°$ | $\varphi_1 = 0°$ |
| $\Theta_2$ is variable | $\Theta_2 = 90°$ | $\Theta_2$ is variable | $\Theta_2 = 90°$ |
| $\varphi_2 = 180°$ | $\varphi_2$ is varibale | $\varphi_2 = 0°$ or 180° | $\varphi_2$ is varibale |

There are two types of collisions could happen between an electron and molecule, either elastic or inelastic scattering. Elastic collision can be described as no change in the internal structure of the molecule after the collision, where as there is a change in the internal structure for the molecule in inelastic collisions. In inelastic collisions. the molecule is either excited or ionized. In this thesis, we will be dealing with only ionization process.

For the (e,2e) ionization process We have

$$e_{in}^{-}(E_{in},\vec{k}_{in}) + X \rightarrow X^{+} + e_1^{-}(E_1,\vec{k}_1) + e_2^{-}(E_2,\vec{k}_2)$$

Where $e_{in}^{-}$ is incident electron, $e_1^{-}$ is scattered electron and $e_2^{-}$ is ejected electron. The energies $E_{in}$, $E_1$, $E_2$ and momenta $\vec{k}_{in}$, $\vec{k}_1$, $\vec{k}_2$ are the kinetic energies and the momenta of the incident, scattered, and ejected electrons respectively. Here energy is conserved $E_{in} = E_1+E_2+$Binding Energy and momentum is conserved too $\vec{k}_{in} = \vec{k}_1 + \vec{k}_2 + \vec{p}$ where $\vec{p}$ is the momentum of the ion. The momentum transferred by the scattered electron is represented as $\vec{q} = \vec{k}_{in} - \vec{k}_1$.

The physical quantity that completely describes the outcome of these collisions are called cross sections. The most detailed information is contained in the triple differential cross section which determines the probability for all possible processes and it gives information about all the possible kinematics of the electrons involved in the process of ionization. The triple differential cross section determines the probability that two outgoing electrons having energies of $E_1$ and $E_2$ will be found in solid angle $d\Omega_1$ and $d\Omega_2$ after the ionization.

$$TDCS = \frac{d\sigma}{d\Omega_1 d\Omega_2 dE_2}$$

The molecular 3-body distorted wave (M3DW) approximation is one of the successful theoretical approaches for calculating the TDCS.

**1.1 MOLECULAR 3-BODY THEORY**

We start with the prior form of the T-matrix [1]

$$T_{fi} = \left\langle \Phi_f^- \left| H - H_i \right| \Psi_i(\mathbf{r}_2, \xi)\, \chi_i^+(\mathbf{k}_i, \mathbf{r}_1) \right\rangle \qquad (1)$$

Where the incident projectile has momentum $\mathbf{k}_i$ and coordinate $\mathbf{r}_1$, a target electron with coordinate $\mathbf{r}_2$ is removed, the coordinates of all the passive target electrons are $(\xi)$, $H$ is the full exact Hamiltonian for the system, $H_i$ is an approximate Hamiltonian for the initial state of the system, and $\Phi_f^-$ is an exact final state wavefunction for the system satisfying incoming wave boundary conditions. The full Hamiltonian is given by

$$H = T_p + V_i + H_{\text{target}} \qquad (2)$$

Where $T_p$ is the kinetic energy operator for the projectile, $V_i$ is the initial state interaction between the projectile and the target, and $H_{\text{target}}$ is the Hamiltonian for the target. The approximate Hamiltonian for the initial state of the system is given by

$$H_i = T_p + U_i + H_{\text{target}} \tag{3}$$

Where $U_i$ is a spherically symmetric approximation for $V_i$. The initial state wavefunction satisfying outgoing wave boundary conditions $\left|\Psi_i(\mathbf{r}_2,\xi)\ \chi_i^+(\mathbf{k}_i,\mathbf{r}_1)\right\rangle$ is an eigenfunction of $H_i$

Where

$$H_{\text{target}}\left|\Psi_i(\mathbf{r}_2,\xi)\right\rangle = \varepsilon_i\left|\Psi_i(\mathbf{r}_2,\xi)\right\rangle \tag{4}$$

And

$$(T_p + U_i)\chi_i^+(\mathbf{k}_i,\mathbf{r}_1) = k_i^2\ \chi_i^+(\mathbf{k}_i,\mathbf{r}_1) \tag{5}$$

And the total energy is given by $E = \varepsilon_i + k_i^2$. In the M3DW approximation, the exact final state wavefunction is approximated as

$$\left\langle\Phi_f^-\right| = \left\langle\chi_f^-(\mathbf{k}_f,\mathbf{r}_1)\ \chi_e^-(\mathbf{k}_e,\mathbf{r}_2)\ C_{e-e}(\mathbf{k}_{12},\mathbf{r}_{12})\ \Psi_{ion}(\xi)\right| \tag{6}$$

Where $\Psi_{ion}(\xi)$ is the wavefunction of the residual ion, $\chi_e^-(\mathbf{k}_e,\mathbf{r}_2)$ is the wavefunction for the ejected electron which satisfies incoming wave boundary conditions, $\chi_f^-(\mathbf{k}_f,\mathbf{r}_1)$ is the wavefunction for the scattered projectile which also satisfies incoming wave boundary conditions, and $C_{e-e}(\mathbf{k}_{12},\mathbf{r}_{12})$ is the final state Coulomb interaction between the projectile electron and ejected electron. Within this approximation, the direct scattering amplitude is given by

$$T_{fi} = \left\langle\chi_f^-(\mathbf{k}_f,\mathbf{r}_1)\ \chi_e^-(\mathbf{k}_e,\mathbf{r}_2)\ C_{e-e}(\mathbf{k}_{12},\mathbf{r}_{12})\ \Psi_{ion}(\xi)\right|V_i - U_i\left|\Psi_i(\mathbf{r}_2,\xi)\ \chi_i^+(\mathbf{k}_i,\mathbf{r}_1)\right\rangle \tag{7}$$

Since $H - H_i = V_i - U_i$. The post-collision-interaction (PCI) between the two final state electrons is the Coulomb interaction

$$C_{e-e}(\mathbf{k}_{12}, \mathbf{r}_{12}) = e^{\frac{-\pi\gamma}{2}}\ \Gamma(1-i\gamma)\ {}_1F_1(i\gamma, 1, -i(k_{12}r_{12} + \mathbf{k}_{12} \bullet \mathbf{r}_{12})) \tag{8}$$

Here ${}_1F_1$ is a confluent Hypergeometric function, $\Gamma(1-i\gamma)$ is the gamma function, $\mathbf{k}_{12} = \mu\, \mathbf{v}_{12}$, $\mu = \frac{1}{2}$ is the reduced mass for two electrons, $\mathbf{v}_{12}$ is the relative velocity between the two electrons, and $\gamma$ is the Somerfield parameter $\gamma = \dfrac{1}{\mathbf{v}_{12}}$ which is a measure of the strength of the coulomb interaction between the two electrons.

For the lower energies and smaller molecules, it sometime seems that using the full Coulomb interaction of Eq. (8) tends to overestimate the effect of the PCI. We have found that the low energy approximation of Ward and Macek often yields better agreement with experimental data. In the Ward-Macek approximation, one replaces the actual final state electron-electron separation $\mathbf{r}_{12}$ by an average value directed parallel to $\mathbf{k}_{12}$. The average separation is given by

$$r_{12}^{ave} = \frac{\pi^2}{16\,\mathrm{E}_t}\left(1 + \frac{0.627}{\pi}\sqrt{\mathrm{E}_t}\,\ln \mathrm{E}_t\right)^2 \tag{9}$$

Where $\mathrm{E}_t$ is the total energy of the scattered and ejected electrons. With this approximation, the $C_{e-e}$ factor can be removed from the T-matrix integral which means that the computational difficulty reduces to that of the standard distorted-wave approximation. Since the cross section is proportional to the square of the T-matrix, in the Ward-Macek approximation the standard distorted wave cross sections are multiplied by

$$\left|C_{e-e}\right|^2 = N_{ee}\left|{}_1F_1(i\gamma, 1, -2ik_{12}r_{12}^{ave})\right|^2 \tag{10}$$

where $N_{ee}$ , called the Gamow factor, is defined as:

$$N_{ee} = \left| e^{\frac{-\pi\gamma}{2}} \Gamma(1 - i\gamma) \right|^2 = \frac{\frac{\pi}{k_{12}}}{(e^{\frac{\pi}{k_{12}}} - 1)} \tag{11}$$

Botero and Macek and Whelan *et al*. proposed neglecting the Hypergeometric function and just using the Gamow factor to approximate $C_{e-e}$.

Now let's look at the perturbation. The full potential is given by

$$V_i = \sum_{j=1}^{N} \frac{z_p(-1)}{r_{1j}} + V_{nuc} \tag{12}$$

Where $z_p$ is the projectile charge, N is the number of electrons in the target, and $V_{nuc}$ is the interaction with all the nuclei. If we have only one active electron, we approximate $V_i$ as follows

$$V_i = \frac{-z_p}{r_{12}} + u(\xi) + V_{nuc} \tag{13}$$

Where $u(\xi)$ is a spherically symmetric approximation for the interaction of the projectile electron with the passive target electrons $(\xi)$. The spherically symmetric approximation for $V_i$ is

$$U_i = u(2) + u(\xi) + V_{nuc} \tag{14}$$

Where $u(2)$ is the spherically symmetric potential for the interaction between the projectile and electron 2 and this potential will only depend on $r_1$, i.e.

$$u(2) = u(r_1) \tag{15}$$

Consequently,

$$V_i - U_i = \frac{-z_p}{r_{12}} - u(r_1) \tag{16}$$

This potential does not depend on $\xi$ so we can write the direct T-matrix (7) as

$$T_{fi} = \left\langle \chi_f^-(\mathbf{k}_f, \mathbf{r}_1)\, \chi_e^-(\mathbf{k}_e, \mathbf{r}_2)\, C_{e-e}(r_{12}) \left| \frac{-z_p}{r_{12}} - u(r_1) \right| \left\langle \Psi_{ion}(\xi) \middle| \Psi_i(\mathbf{r}_2, \xi) \right\rangle \chi_i^+(\mathbf{k}_i, \mathbf{r}_1) \right\rangle \tag{17}$$

The integral over the passive electron coordinates $(\xi)$ depends on $\mathbf{r}_2$ only so we define a single particle wavefunction (called the Dyson orbital for molecules or a single particle orbital for atoms). For molecules, the Dyson orbital also depends on the orientation of the molecule.

$$\psi_i(\mathbf{r}_2) = \left\langle \Psi_{ion}(\xi) \middle| \Psi_i(\mathbf{r}_2, \xi) \right\rangle \tag{18}$$

so that the standard M3DW T-matrix becomes

$$T_{fi} = \left\langle \chi_f^-(\mathbf{k}_f, \mathbf{r}_1)\, \chi_e^-(\mathbf{k}_e, \mathbf{r}_2)\, C_{e-e}(r_{12}) \left| \frac{-z_p}{r_{12}} - u(r_1) \right| \psi_i(\mathbf{r}_2)\, \chi_i^+(\mathbf{k}_i, \mathbf{r}_1) \right\rangle \tag{19}$$

The 3 continuum wavefunctions are called distorted waves and we calculate them numerically as described below. We have formed a collaboration with Chuangang Ning from Tsinghua University in Beijing, China who is an expert for calculating molecular orbitals using density functional theory along with the standard hybrid B3LYP functional by means of the ADF 2007 (Amsterdam Density Functional) program with the TZ2P (triple-zeta with two polarization functions) Slater type basis sets [2]

Finally, the cross section is calculated

$$\frac{d\sigma}{d\Omega_f d\Omega_e dE_e} = \frac{1}{(2\pi)^5} \frac{k_f k_e}{k_i} \left( |T_{dir}|^2 + |T_{exc}|^2 + |T_{dir} - T_{exc}|^2 \right) \tag{20}$$

Where $T_{dir}$ is the direct scattering amplitude of Eq. (19), and $T_{exc}$ is the exchange amplitude where $\mathbf{r}_1$ and $\mathbf{r}_2$ are exchanged in the final state wavefunction in Eq. (19).

## 1.2 CALCULATION OF THE CONTINUUM WAVEFUNCTIONS

The Hamiltonian for the initial state continuum wavefunctions can be expressed as

$$h_i = T + U_i(r) = -\nabla^2 + U_i(r) \tag{21}$$

Where $U_i(r)$ is the spherically symmetric distorting potential for the full interaction $V_i$ that is asymptotically zero, and we have used Rydberg energy units (i.e. $T = \nabla^2$ instead of $T = \frac{1}{2}\nabla^2$). Continuum wavefunctions for the Hamiltonian of Eq. (21) can be expanded in terms of partial waves as follows (asymptotic plane wave $e^{i\mathbf{k}\bullet\mathbf{r}}$ normalization, outgoing wave boundary conditions)

$$\begin{aligned}\chi_i^+(\mathbf{k}_i,\mathbf{r}_1) &= \frac{4\pi}{k_i r_1}\ \sum_{\ell m} i^\ell\ e^{i\sigma_\ell}\ \chi_\ell(k_i,r_1)\ Y_\ell^m(\hat{\mathbf{k}}_i)\ Y_\ell^{m*}(\hat{\mathbf{r}}_1) \\ &= \frac{1}{k_i r_1}\sum_{\ell} i^\ell\ e^{i\sigma_\ell}\ (2\ell+1)\ \chi_\ell(k_i,r_1)\ P_\ell(\cos\alpha)\end{aligned} \tag{22}$$

where $\alpha$ is the angle between $\mathbf{k}_i$ and $\mathbf{r}_1$, and $\sigma_\ell$ is the Coulomb phase shift (for asymptotic non-zero Coulomb potentials, this factor is unity for asymptotically zero potentials. Note that the distorted wave does not depend on the orientation of the coordinate system – only upon the relative angle between $\mathbf{k}_i$ and $\mathbf{r}_1$**.** If Eq. (22) is used in the Schrödinger equation

$$h_i\ \chi_i^+(\mathbf{k}_i,\mathbf{r}_1) = k^2\ \chi_i^+(\mathbf{k}_i,\mathbf{r}_1) \tag{23}$$

it can be seen that the radial function $\chi_\ell(k_i,r_1)$ satisfies the following differential equation

$$\left(\frac{d^2}{dr_1^2} - \frac{\ell(\ell+1)}{r_1^2} - U_i(r_1) + k_i^2\right)\ \chi_\ell(k_i,r_1) = 0 \tag{24}$$

The final state distorted waves are calculated in a similar manner except that the final state distorting potential $U_1$, which is asymptotically a Coulomb potential for charge +1, is used. If there is a large difference in final state energies, one would normally use the asymptotically neutral potential $U_i$ for the faster electron and the asymptotically Coulombic $U_1$ for the slower electron. The final state distorted wave Hamiltonian for $U_1$ is given by

$$h_1 = T + U_1(r) = -\nabla^2 + U_1(r) \tag{25}$$

And the final state radial function $\chi_\ell(k,r)$ $(k = k_1 \text{ or } k_2)$ satisfies the following differential equation

$$\left(\frac{d^2}{dr^2} - \frac{\ell(\ell+1)}{r^2} - U_1(r) + k^2\right) \chi_\ell(k,r) = 0 \tag{26}$$

If the distorting potential $U(r)$ is zero everywhere, $\chi_\ell(k,r)$ becomes a regular spherical function and the sum of Eq. (22) becomes a plane wave $e^{i\mathbf{k}\bullet\mathbf{r}}$. If the distorting potential is Columbic $U(r) = \frac{2 z_p z_t}{r}$, $\chi_\ell(k,r)$ becomes a regular Coulomb wavefunction. The Schrödinger Eq. (26) for Coulomb waves is very similar to the Kepler problem in classical mechanics. In classical mechanics, we define an effective potential

$$\begin{aligned} V_{eff} &= \frac{\ell^2}{r_1^2} + U_i(r_1) \\ &= \frac{\ell^2}{r_1^2} - \frac{z_t}{r_1} \end{aligned} \tag{27}$$

Where the negative means an attractive potential.

## 1.3 NUMERICAL CALCULATION OF DISTORTED WAVES

The results of calculating the T-matrix should not depend on the orientation of the coordinate system so you can chose any orientation you wish. Most people chose the z-axis parallel to the incident projectile-beam direction. However, for the 6D (6-dimensional) that we do, Steve Jones found that the numerical accuracy is significantly better if the z-axis is chosen parallel to the momentum transfer direction $\mathbf{q} = \mathbf{k}_i - \mathbf{k}_f$ where $\mathbf{k}_i$ and $\mathbf{k}_f$ are the incident and scattered momentum vectors for the projectile. Consequently the projectile is never parallel to the z-axis and the ejected electron has a high probability for leaving in this direction. The xz plane is the scattering plane, the +y axis is in the direction of $\mathbf{k}_i \; x \, \mathbf{k}_f$ and the scattered projectile is in the first quadrant (i.e. in the plane +x and $\phi = 0$).

Notice that the partial wave expansion of Eq. (22) depends on k and $\alpha$ where $\alpha$ is the angle between **k** and **r.**

We are using 2 different coordinate systems in the evaluation of the T-matrix – spherical for the target electron and cylindrical for the projectile.

However, the subroutine that calculates the distorted waves is written for spherical coordinates. Consequently, cylindrical coordinates $(\rho, \phi, z)$ are sent to this subroutine and the cylindrical coordinates are converted into spherical $(r, \theta, \phi)$ coordinates as follows. The $\phi-$coordinate is OK, since it is the same as the corresponding coordinate in spherical coordinates. For each $(\rho, z)$ coordinate, we find the corresponding $(r, \theta)$ value as follows

$$r = \sqrt{\rho^2 + z^2}$$
$$\theta = \arctan(\frac{\rho}{z}) \quad (28)$$

We have an array of $(r, \theta, \phi)$ values corresponding to the cylindrical coordinates for the particle of interest. The angle between **k** and **r** ( $\cos\alpha$ ) is calculated as follows:

$$\begin{aligned} x &= r \sin(\theta) \cos(\phi) \\ y &= r \sin(\theta) \sin(\phi) \\ z &= r \cos(\theta) \\ \mathbf{k} \bullet \mathbf{r} &= k_x x + k_y y + k_z z \\ \cos(\alpha) &= \mathbf{k} \bullet \mathbf{r}/(kr) \end{aligned} \quad (29)$$

The radial Schrödinger equation (24) is solved numerically using the Numerov method. Even though we only want the solution for something like 50 r-values, around 3000 r-values are required to get an accurate answer using the Numerov method. The Numerov method is designed for the generic second order differential equation of the form

$$\frac{d^2 S(x)}{dx^2} = f(x)\, S(x) \quad (30)$$

Comparing with the Schrödinger Eq. (24), We have

$$\frac{d^2 \chi_\ell(k,r)}{dr^2} = [\frac{\ell(\ell+1)}{r^2} + U_i(r) - k^2]\, \chi_\ell(k,r) \quad (31)$$

$$S = \chi_\ell(k,r)$$
$$f = \frac{\ell(\ell+1)}{r^2} + U_i(r) - k^2 \quad (32)$$

In the Numerov method, the second order Eq. (30) is converted to a 3 point difference equation

$$[1-\frac{h^2}{12}\ f(x+h)]\ S(x+h)\ = 2\,[\,1-\frac{h^2}{12}\ f(x)]\ S(x) - [1-\frac{h^2}{12}\ f(x-h)]\ S(x-h) + h^2\ f(x)\ S(x) \tag{33}$$

In the subroutine dw which we use, a new variable $T(x) = [\,1-\frac{h^2}{12}\ f(x)]\ S(x)$ is defined and the 3 points used for the difference equation are called

$$\begin{aligned} T(5) &= [\,1-\frac{h^2}{12}\ f(x+h)]\ S(x+h) \\ T(4) &= [\,1-\frac{h^2}{12}\ f(x)]\ S(x) \\ T(3) &= [\,1-\frac{h^2}{12}\ f(x-h)]\ S(x-h) \end{aligned} \tag{34}$$

so that the difference equation (33) becomes

$$T(5)\ = 2\,T(4) - T(3) + h^2\ f(4)\ S(4) \tag{35}$$

Where, a second order differential equation requires 2 boundary conditions for a solution. The first boundary condition comes from the expansion of eq. (22). Looking only at the radial part, we have

$$\frac{\chi_\ell(k,r)}{kr} \tag{36}$$

Which will become infinite at $r=0$ unless $\chi_\ell(k,0)=0$ so the first point is 0. The second point could be picked randomly, but there is a way of picking it semi-intelligently and there is a subroutine to do that (but it really does not matter what the 2nd point is). So the Numerov method starts with 2 points and then uses eq. (35) to get the 3rd point. Then it uses the 2nd and 3rd points plus (35) to get the 4th point and so forth until the end of the mesh is reached.

If the 2nd point is picked too large, then it can happen that the amplitude of the radial distorted wave can get bigger than the largest possible number for the computer. The original code was written for single precision numbers, and the largest single precision number is about $10^{30}$, so the magnitude of the wave is constantly monitored and, if it gets bigger than $10^{10}$, all points up to that point are divided by $10^{5}$.

The radial Schrödinger equation for $\chi_\ell(k,r)$ is calculated on a mesh of 3000 (or more) points. When you get to the end of the mesh, the wave you have is one of the infinite number of possible solutions of the differential equation (24). We have to normalize this wave so that it satisfies the proper scattering theory boundary condition. For outgoing wave boundary condition (+), we must have a plane wave plus outgoing spherical wave. In terms of a partial wave expansion, this boundary condition translates into

$$\chi_\ell(k,r) \to j_\ell(k,r) + T_\ell \; [\, g_\ell(k,r) + i j_\ell(k,r)] \tag{37}$$

Where $\frac{j_\ell(k,r)}{kr}$ and $-\frac{g_\ell(k,r)}{kr}$ are regular and irregular spherical Bessel functions or spherical Coulomb waves depending on the asymptotic charge [for asymptotic neutral charges, $j_0(k,r) = \sin(kr)$, $g_0(k,r) = \cos(kr)$ ]. In terms of the boundary condition, $j_\ell(k,r)$ corresponds to the plane wave, $[\, g_\ell(k,r) + i j_\ell(k,r)]$ corresponds to the outgoing spherical wave. This is easy to see for $\ell = 0$

$$\begin{aligned} &\chi_\ell(k,r) \to \sin(kr) + T_0 \; [\, \cos(kr) + i \sin(kr)] \\ &= \sin(kr) + T_0 \, e^{ikr} \end{aligned} \tag{38}$$

A distorted wave is actually a wavefunction for a particle that has elastically scattered from the spherically symmetric potential $U_i(r)$. From potential scattering, it can be shown that $T_\ell = e^{i\Delta\ell}\sin(\Delta\ell)$ where $\Delta\ell$ is the elastic scattering phase shift [3] .

To find $T_\ell$, the numerical wf and its first derivative are matched to eq. (37) and its first derivative i.e.

$$j_\ell(k,r) + T_\ell\ [\, g_\ell(k,r) + ij_\ell(k,r)] = \alpha_\ell = N\ \beta_\ell \tag{39}$$

where $\chi_\ell$ is the desired numerical solution, $\beta_\ell$ is the un-normalized numerical solution obtained froheorym the Numerov method, and N is the required normalizing factor. The first derivative is

$$\frac{d}{d(kr)}\{j_\ell(k,r) + T_\ell\ [\, g_\ell(k,r) + ij_\ell(k,r)]\} = \frac{d\ (N\beta_\ell)}{d(kr)} \tag{40}$$

or using primes to indicate $d(kr)$ derivatives

$$\{j_\ell'(k,r) + T_\ell\ [\, g_\ell'(k,r) + ij_\ell'(k,r)]\} = N\ \beta_\ell' \tag{41}$$

Divide Eq. (40) by Eq. (41)

$$\frac{j_\ell(k,r) + T_\ell\ [\, g_\ell(k,r) + ij_\ell(k,r)]}{j_\ell'(k,r) + T_\ell\ [\, g_\ell'(k,r) + ij_\ell'(k,r)]} = \frac{\beta_\ell}{\beta_\ell'} \tag{42}$$

Solve for $T_\ell$

$$T_\ell = \frac{j_\ell'(k,r)\ \beta_\ell - j_\ell(k,r)\ \beta_\ell'}{\left[\, g_\ell(k,r)\ \beta_\ell' - g_\ell'(k,r)\ \beta_\ell \right] - i\left[\, j_\ell'(k,r)\ \beta_\ell - j_\ell(k,r)\ \beta_\ell' \right]} \tag{43}$$

Once we know $T_\ell$, we can use Eq. (39) to find $\chi_\ell$ and then N

$$N = \frac{j_\ell(k,r) + T_\ell\ [\, g_\ell(k,r) + ij_\ell(k,r)]}{\beta_\ell} \tag{44}$$

A 5-point numerical derivative is used to find $\beta_\ell'$. The last 5 points of the mesh are used and the derivative is found for the middle of the 5 points which is the 3rd point back. Consequently, the matching is done 3 points from the end of the mesh. The regular and irregular spherical Bessel functions (or Coulomb wave functions) and their derivatives are evaluated 3 points from the end of the mesh using analytic expressions using a subroutine pubically available called coul90.

In the code, the distorted wave subroutine called dw returns a real array and a complex number called phasdw. Below we show that phasdw is $e^{i\Delta_\ell}$. The regular and irregular spherical Bessel (Coulomb) wavefunctions follow the same algebra as the sin's and cos's of Eq. (38).

$$\begin{aligned}
&\sin(kr) + T_0\ [\cos(kr) + i\sin(kr)] \\
&= \sin(kr) + e^{i\Delta\ell}\sin(\Delta\ell)\ [\cos(kr) + i\sin(kr)] \\
&= e^{i\Delta\ell}\{e^{-i\Delta\ell}\sin(kr) + \sin(\Delta\ell)\ [\cos(kr) + i\sin(kr)]\} \\
&= e^{i\Delta\ell}\{[\cos(\Delta\ell) - i\sin(\Delta\ell)]\sin(kr) + \sin(\Delta\ell)\ [\cos(kr) + i\sin(kr)]\} \\
&= e^{i\Delta\ell}\{\cos(\Delta\ell)\sin(kr) + \sin(\Delta\ell)\cos(kr)\}
\end{aligned} \tag{45}$$

Consequently, distorted wave can be written as a complex phase times a real function and subroutine dw returns this complex phase and a real function.

Once we have $\chi_\ell(k,r)$ on 3000 points, we interpolate onto the much smaller r-array which is used for the numerical integration. The sum of Eq. (22) is then done for all the quadrature $(r_i, \theta_j, \phi_k)$ points. The sum over $\ell$ is terminated when the current term to be added divided by the current sum is less than $10^{-7}$. To avoid the possibility that the current term might accidentally be small due to crossing zero or something, the sum is

not terminated until the current term divided by current sum has been less than $10^{-7}$ more than 5 times.

For the 2 final state distorted waves with complex conjugated incoming wave boundary conditions, we use the relation

$$\chi^{-}(\mathbf{k},\mathbf{r})^{*} = \chi^{+}(-\mathbf{k},\mathbf{r}) \tag{46}$$

along with

$$i^{\ell}\ Y_{\ell}^{m}(-\hat{\mathbf{k}}) = i^{-\ell}\ Y_{\ell}^{m}(\hat{\mathbf{k}}) \tag{47}$$

so that

$$\chi^{-}(\mathbf{k},\mathbf{r})^{*} = \sum_{\ell} i^{-\ell}\ e^{i\sigma_{\ell}}\ (2\ell+1)\ \chi_{\ell}(k,r)\ P_{\ell}(\cos\alpha) \tag{48}$$

where $\chi_{\ell}(k,r)$ satisfies the same boundary conditions of Eq. (37).

**PAPER**

# I. Low energy (e,2e) studies from $CH_4$: Results from symmetric coplanar experiments and molecular three-body distorted wave theory

K.L. Nixon[1], Andrew J. Murray[1], Hari Chaluvadi[2], Chuangang Ning[3] and D. H. Madison[2]

[1]Photon Science Institute, School of Physics and Astronomy, University of Manchester, Oxford Road, Manchester M13 9PL, United Kingdom

[2]Department of Physics, Missouri University of Science and Technology, Rolla, Missouri 65409, USA

[3]Department of Physics and Key Laboratory of Atomic and Molecular NanoSciences of MOE, Tsinghua University, Beijing 100084, People's Republic of China

## Abstract

Low energy experimental and theoretical triply differential cross sections are presented for electron impact ionization of methane ($CH_4$) for both the highest occupied molecular orbital (HOMO) and next highest occupied molecular orbital (NHOMO). The HOMO is a predominantly p-type orbital which is labeled 1t2 and the NHOMO is predominantly s-type labeled $2a_1$. Coplanar symmetric (symmetric both in final state electron energies and observation angles) are presented for final state electron energies

ranging from 2.5 eV to 20 eV. The theoretical M3DW (molecular three-body distorted wave) results are in surprisingly good agreement with experiment for the HOMO state and less satisfactory agreement for the NHOMO state. The molecular NHOMO results are also compared with the ionization of the 2s shell of neon which is the isoelectronic atom.

## Introduction

Electron scattering from molecules is a rich field with many important applications [Ref. 1 and references therein]. As an example, electron-molecule collisions are widely used in the technology industry for plasma devices and etching; they have an important role in developing more accurate medical imaging techniques and radiotherapies and natural phenomena such as auroras, planetary nebula and lighting also critically dependent on electron-molecule collisions. Understanding each of these processes requires accurate and detailed information of the collision dynamics between the electron and the target molecule. (e,2e) experiments which measure electron impact ionization, provide the most rigorous experimental data in the form of a triple differential cross section (TDCS). At low impact energies the probability of ionization is highest. As such, collisions in this energy region occur most abundantly and so it is important to characterize the interactions fully to describe the physical phenomena that are seen. Despite this, detailed experimental and theoretical examinations of electron-molecule collisions in this regime have been relatively few. This is due to the challenges presented to both theory and experiment when working in this energy regime and is also due to the nature of molecules, which are used as the targets. At low energies the collision dynamics are far from impulsive, and so effects such as post collision interactions, multiple collisions, target polarization and distortion of the associated wavefunctions of the target

and electrons involved in the interaction all must be considered and evaluated. These challenges have been largely overcome for atomic targets, and sophisticated theoretical models have been developed which provide good agreement with experimental data for many atoms [2-4].

Adopting molecules as the target in these studies is significantly more complicated. Generating experimental and theoretical data that can be directly compared is considerably more involved. One problem that arises is that molecules tend to have more closely spaced energy levels compared to atoms and these states are often unresolvable by experiment [5-8]. In this case, the measured TDCS arises from multiple orbitals making comparison with theory less conclusive. A further consideration that arises in most experiments is that the target molecules are randomly oriented in space, due to being produced from either an effusive gas beam or oven. This random orientation needs to be included in the theory before a direct comparison with experimental data can be attempted. Finally, molecules have multiple distributed nuclei that may each act as independent scattering centres. This non-central distribution considerably complicates the model due to a reduction of symmetry and makes the calculations computationally intensive. Notwithstanding these challenges, theoretical models are being developed for application to polyatomic molecules in the low energy regime and new experimental measurements are emerging [see Refs. 5-14 for examples of recent work]. A review of recent experimental and theoretical work for electron-impact ionization of molecules was given by Madison and Al Hagan [15].

Methane ($CH_4$) is the smallest hydrocarbon and so is a relatively simple polyatomic molecule. It has a highly symmetric tetrahedral structure with four equivalent

C-H bonds. There are five molecular orbitals in the $X^1A_1$ ground state. Molecular symmetry leads to triple degeneracy of the $1t_2$ highest occupied molecular orbital (HOMO), the lower orbitals being the $2a_1$ and $1a_1$ orbitals. This simple electronic structure has made methane an ideal prototype to model organic systems and so it has often been employed when developing models of biological matter or planetary atmospheres. Furthermore, methane is a potent greenhouse gas with a high global warming potential. This simple molecule also has significant technological uses such as in the development of plasma devices and in the fabrication of carbon nanotubes, nanowires and graphene [see Refs. 16-19 for examples]. In terms of the investigation instigated here, methane is an ideal target to help in understanding the discrepancies observed between experimental and theoretical data for molecules. The $2a_1$ next highest occupied molecular orbital (NHOMO) of methane has a very similar electron density to that of a carbon 2s atomic orbital [20]. As such, it is expected that this molecular orbital can be described by a much simpler atomic theory. More importantly, the $2a_1$ molecular orbital has s-electron characteristics and so has predominantly spherical symmetry. Any effects of the spherical averaging procedure utilized in a theoretical model should hence be minimized for such an orbital. A comparison between the experimental and theoretical data for this orbital should therefore reveal if the observed differences are due to this spherical averaging process. A further investigation of this premise, as carried out here, is to compare results from methane to the isoelectronic atom, neon. The atomic target clearly does not require spherical averaging within the theoretical model. Furthermore, this comparison should isolate key features seen in the TDCS due to the molecular nature of the target.

A number of (e,2e) studies of methane have been previously undertaken, mostly utilizing the high energy electron momentum spectroscopy (EMS) regime [21-24]. These studies demonstrate that accurate theoretical molecular wavefunctions are readily achievable. New studies of the collision dynamics from methane at intermediate energies were also carried out recently [10, 14].

The remainder of this paper is structured as follows: Section experimental apparatus outlines the pertinent feature of the (e,2e) spectrometer used to measure the triple differential cross sections, whereas Section theoretical framework describes the theoretical model used to predict the cross section. The results for both experiment and theory are presented and compared in Section results and discussion. Conclusions from this study are summarized in section 1.5.

## Experimental Apparatus

The coincidence data taken throughout this experimental study utilized the fully computer controlled and optimized (e,2e) spectrometer at the University of Manchester. This spectrometer has been described in detail elsewhere [25-27] and so only the features pertinent to this study are reproduced here. The spectrometer was operated in a ‘standard’ coplanar geometry where the momenta of the ingoing and outgoing electrons are within the same plane. Figure 1 depicts the coplanar scattering geometry used. The two outgoing electron momentum analyzers were independently rotated around the detection plane to map the probability of a collision event. This probability map is termed the triple differential cross section. In this study, a symmetric configuration was used, so that $\xi_1 = \xi_2 = \xi$ and $E_1 = E_2 = E$.

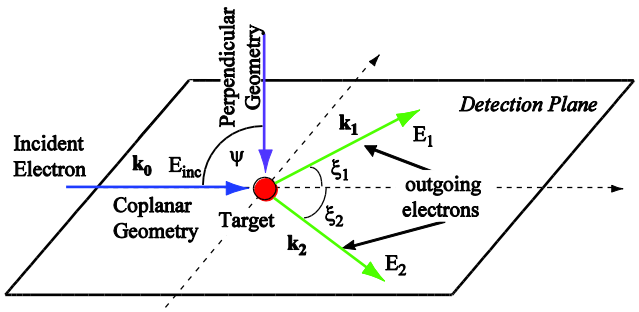


Figure 1: Schematic of the scattering geometry depicting the various angles employed. A coplanar geometry ($\psi$= 0°) is defined when the momenta of all three electrons lie in the detection plane. The analyzer angles ($\xi_1$ and $\xi_2$) are measured with respect to the incident electron beam $k_0$ in this plane. Non-coplanar geometries can also be accessed in this apparatus by lifting the electron gun out of the detection plane, although this feature was not utilized here.

High purity methane was admitted into the interaction region, controlled by a needle valve. Typical operating pressures of $9x10^{-6}$ Torr were used in the chamber, in conjunction with very low incident electron beam currents of ~70nA, in order to achieve good signal to background ratios.

Computer control and optimization of the electrostatic lenses within the electron analyzers allowed the automated tuning of the spectrometer at each new analyzer angle throughout data collection. The energy of the spectrometer was calibrated at the start of each new measurement so as to ensure data were taken at the peak of the coincidence binding energy spectrum. This study focused on the two outermost molecular orbitals within methane: the highest occupied $1t_2$ orbital with a binding energy ~ 14eV and the next highest occupied $2a_1$ orbital at ~ 23eV binding energy. A typical coincidence binding energy spectrum for these two orbitals is shown in Fig. 2. The data in Fig. 2 were taken under the same conditions, however, in two separate measurements since the power supply used to vary, the incident electron energy could only scan 10V. Figure 2 clearly demonstrates that the orbitals are fully resolved so that the coincidence data from each

orbital is uncontaminated by its neighbor. These well resolved structures eliminate one of the difficulties often encountered when studying molecules, since the data from each orbital can be measured separately for comparison with theory. It is also seen that the coincidence signal from the $2a_1$ orbital is significantly smaller than from the $1t_2$ orbital.

The experimental data presented here have not been measured on an absolute scale. Hence each data set has been normalized to unity at the peak. Each data set is derived from several sweeps of the electron analyzers around the detection plane, which were then averaged. The vertical error bars represent the standard error on this average, whereas the horizontal error bars represent the angular uncertainty due to the acceptance angles of the electron analyzers and the pencil angle of the electron gun.

## Theoretical Framework

The details of the molecular three-body distorted wave (M3DW) approximation have been presented elsewhere [28-30] so only a brief overview will be presented here. The M3DW TDCS is given by

$$\frac{d^5\sigma}{d\Omega_a d\Omega_b dE_b} = \frac{1}{(2\pi)^5}\frac{k_a k_b}{k_i}\left(\left|T_{dir}\right|^2 + \left|T_{exc}\right|^2 + \left|T_{dir} - T_{exc}\right|^2\right) \qquad (1)$$

where $\vec{k}_i$ is the initial state wave vector, $\vec{k}_a(\vec{k}_b)$ is the wave vector for the scattered (ejected) electron, and the direct and exchange amplitudes are $T_{dir}$ and $T_{exc}$, respectively:

$$T_{dir} = \left\langle \chi_a^-(\vec{k}_a, \mathbf{r}_1)\chi_b^-(\vec{k}_b, \mathbf{r}_2)C_{scat-eject}(r_{12})\,|\,V - U_i\,|\,\phi_{Dy}^{OAMO}(\mathbf{r}_2)\chi_i^+(\vec{k}_i, \mathbf{r}_1)\right\rangle \qquad (2)$$

$$T_{exc} = \left\langle \chi_a^-(\vec{k}_a, \mathbf{r}_2)\chi_b^-(\vec{k}_b, \mathbf{r}_1)C_{scat-eject}(r_{12})\,|\,V - U_i\,|\,\phi_{Dy}^{OAMO}(\mathbf{r}_2)\chi_i^+(\vec{k}_i, \mathbf{r}_1)\right\rangle \qquad (3)$$

In equations (2) and (3), $\mathbf{r}_1$ $(\mathbf{r}_2)$ is the co-ordinate of the incident (bound) electron, $\chi_i, \chi_a$, and $\chi_b$ are the distorted waves for the incident, scattered, and ejected electrons,

respectively, $C_{scat-eject}$ is the Coulomb interaction between the scattered projectile and ejected electron, and $\phi_{Dy}^{OAMO}$ is the Dyson orbital averaged over all orientations (OAMO – orientation averaged molecular orbital) [28] for the initial bound state wavefunction of the active electron. The molecular wavefunction was calculated using density functional theory along with the standard hybrid B3LYP [31] functional by means of the ADF 2007 (Amsterdam Density Functional) program [32] with the TZ2P (triple-zeta with two polarization functions) Slater type basis sets. For low energy electron-impact ionization, we have found that the full Coulomb interaction $C_{scat-eject}$ typically over estimates the strength of the electron-electron repulsion while the Ward-Macek approximation [33] yields better agreement with experiment so we have used the Ward-Macek approximation in this work.

The potential $V$ in equations (2) and (3) is the initial state interaction between the projectile and the neutral molecule, and $U_i$ is the initial-state spherically symmetric distorting potential which is used to calculate the initial-state distorted wave $\chi_i$. The Schrödinger equation for the incoming electron wavefunction is given by:

$$(T + U_i - \frac{k_i^2}{2})\chi_i^+(\vec{k}_i, \mathbf{r}) = 0 \qquad (4)$$

where $T$ is the kinetic energy operator, and the '+' superscript on $\chi_i^+(\vec{k}_i, \mathbf{r})$ indicates outgoing wave boundary conditions. The initial state distorting potential contains three components $U_i = U_S + U_E + U_{CP}$, where $U_S$ is the initial state spherically symmetric static potential which is calculated from the molecular charge density averaged over all angular orientations, $U_E$ is the exchange-distortion potential of Furness and McCarthy

[34], and $U_{CP}$ is the correlation-polarization potential of Perdew and Zunger [35] (see also Padial and Norcross [36]).

The two final channel distorted waves are obtained from a Schrödinger equation similar to equation (4)

$$(T + U_f - \frac{k_{a(b)}^2}{2})\chi_{a(b)}^{-}(\vec{k}_{a(b)}, \mathbf{r}) = 0 \qquad (5)$$

Here $U_f = U_I + U_E + U_{CP}$ where $U_I$ is the final state spherically symmetric static distorting potential for the molecular ion which is calculated using the same procedure as $U_S$ except that the active electron is removed from the charge distribution.

For the $1t_2$ state, the Dyson orbital averaged over all orientations $\phi_{Dy}^{OAMO}$ is zero due to the symmetry of the state (*i.e.*, there are exactly cancelling positive and negative contributions). To avoid this cancelation, we averaged the absolute value of the Dyson orbital instead of the actual orbital.

## Results and Discussion

### A. Accuracy of the OAMO wavefunctions

A reliable, accurate OAMO wavefunction for use as the $\phi_{Dy}^{OAMO}$ can be obtained by noting that the high energy (e,2e) EMS experiment provides a measurement of the Dyson orbital [37]. EMS results represent the square modulus of the momentum space wavefunction, which is the Fourier transform of a radial wavefunction averaged over all orientations. Consequently, one way to generate an accurate wavefunction would be to take the inverse Fourier transform of experimental EMS data. However, since the measurement is directly related to the square of the wavefunction, a unique solution for the inverse problem cannot be obtained due to cross terms. Alternatively, the accuracy of

the OAMO wavefunctions used in the M3DW theory can be evaluated by taking its Fourier transform and then comparing it with EMS data. Figure 3 compares the square modulus of the Fourier transform of the $\phi_{Dy}^{OAMO}$ for the $1t_2$ and $2a_1$ states with the momentum wavefunctions measured by Clark *et al.* [21]. It may be seen that there is reasonably good agreement with experiment for both states, which would indicate that the two averaging methods yield reasonable results. It is interesting and surprising to note that $1t_2$ state is in better agreement with the EMS measurements than the $2a_1$ state.

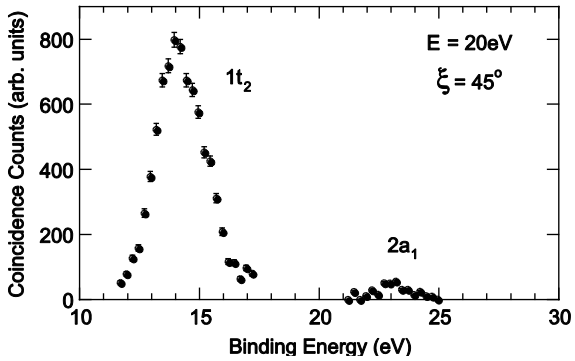


Figure 2: A typical coincidence binding energy spectrum obtained for CH4. These data were measured in a coplanar geometry with outgoing electron energies of 20eV at ξ= 45°. The two peaks correspond to the two highest orbitals, i.e., the $1t_2$ and $2a_1$ orbitals as labeled. The orbitals are easily resolved, so that the TDCS from each orbital is uncontaminated by its neighbor. The width of the HOMO is significantly increased from that due solely to the experimental resolution due to Jan-Teller distortion [21].

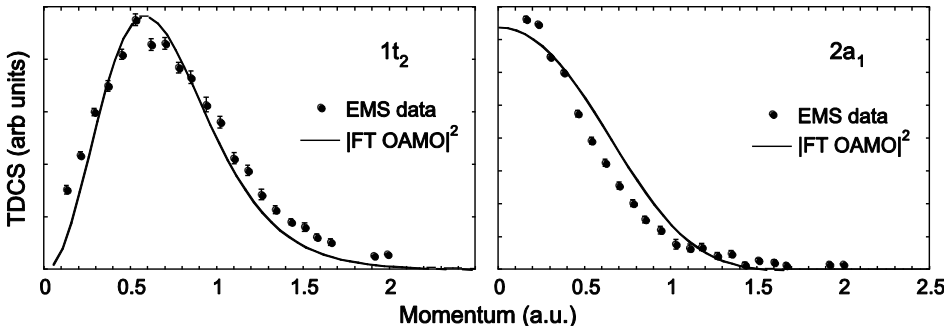


Figure 3: Comparison between experimental EMS data (dots) [21] and the square modulus of the Fourier transform of the orientational averaged molecular wavefunctions, $\phi_{Dy}^{OAMO}$, (lines) which were used to calculate the TDCS used in this study.

**B. Triple differential cross sections for methane**

**B.1. $1t_2$ state**

The experimental and calculated TDCS for the outermost, $1t_2$, orbital of methane are shown in Fig. 4. There is reasonably good qualitative agreement between experiment and theory. Both sets of data show the typical trends seen for atomic targets, despite the molecular nature of methane. At the highest energy, with outgoing electron energies of 20eV as shown in figure 4(a), a larger cross section is seen in the forward scattering direction ($\xi < 90°$), compared to scattering in the backward direction ($\xi > 90°$). This inverts as the energies are lowered, both in the theory and experiment. At the lowest energy of 2.5eV [Fig. 4(f)], the largest relative amplitude is predicted in the backward direction; however the apparatus cannot reach the scattering angles where this peaks. The theoretical prediction for the large angle peak position differs from that obtained experimentally.

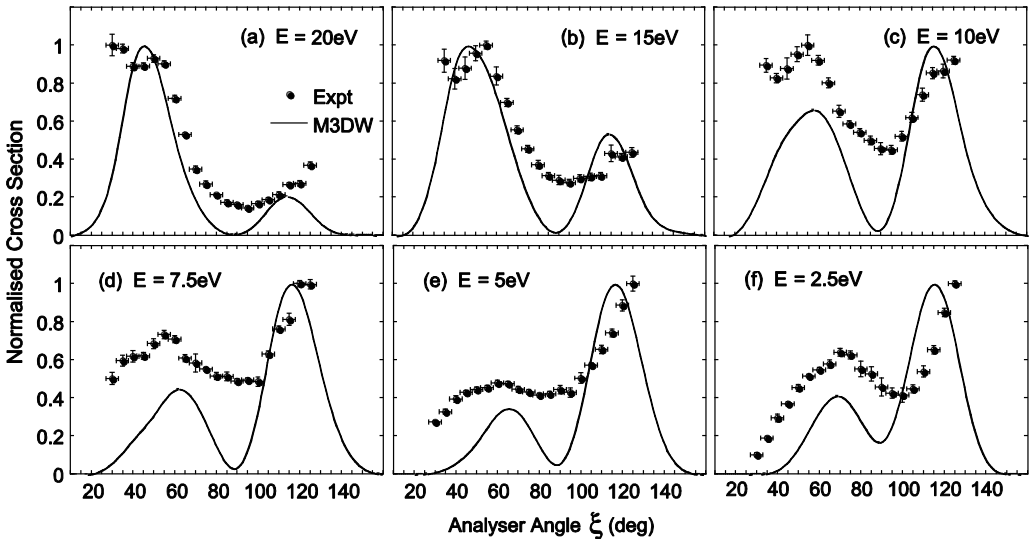


Figure 4: TDCS from the $1t_2$ HOMO state of $CH_4$ for coplanar symmetric kinematics. The energies of the outgoing electrons are shown on the respective plots. The experimental data (dots) and results from the Molecular 3-body Distorted Wave Approximation (M3DW) (lines) are depicted. The experimental and theoretical data have been independently normalised to unity at the peak for each energy.

As the energy of the outgoing electrons is lowered, it is expected that the Coulomb repulsion between outgoing electrons will play an increasingly important role, driving the electrons apart. This repulsion is called a post-collision-interaction (PCI). PCI would cause the forward scattering peak to shift toward $\xi = 90°$ in symmetric kinematics as the outgoing electron energy lowers, and the data presented here demonstrates this effect. PCI will also shift the backward scattering peak towards $\xi = 90°$, however this cannot be confirmed in this data since the backwards peak is beyond the angular range accessible to the experiment in all cases.

Overall, agreement between the experimental data and theoretical calculations is reasonable given the complexity of the interactions at these energies, and given the approximations that have been made as described in Sec. experimental apparatus. The peak positions for the forward scattering peak are in general well represented in the model. The movement of the forward peak toward $\xi = 90°$, as the energy is lowered is also reproduced. However, the backward scattering peak is predicted to be at lower scattering angles than is observed for all energies. Theory also predicts a deep minimum between the forward and backward peaks, whereas the data do not exhibit this. Further, the relative heights of the peaks for each incident energy are not in good agreement with the data. The relatively good agreement is, overall, surprising given the p-like symmetry of the $1t_2$ orbital, which has parity inversion through the molecular centre. This inversion symmetry has been lost in the averaging process so this approximation might be expected to cause significant differences between theory and experiment. It seems that the angular details of the bound state wavefunction must not be very important for low energies, although they may be the cause of some of the discrepancies that are seen.

**B.2. $2a_1$ state**

One of the key motivations for carrying out this study is that the $2a_1$ state of $CH_4$ is highly symmetric, and has no parity inversion through the molecular centre. As such, it is expected that the approximations used in the spherical averaging process should be far less severe than for the $1t_2$ state. Figure 5 shows the results for the $2a_1$ state. Again, the data show behavior similar to atomic targets, with a forward and backward peak being observed. However, a major difference in the data for this state is in the evolution of the peak at angles ~ $\xi$ = 90°, a feature that is not usually seen in atomic targets. This feature is small at higher outgoing energies, but becomes increasingly clear and more pronounced as the energy is decreased. Peaks in this region (where the outgoing electrons emerge back to back, *i.e.*, at $\xi$= 90°), are often attributed to PCI between the two outgoing electrons; however at the energies used here it is unlikely that PCI is the dominant cause. Further, the peak at $\xi$= 90° becomes more pronounced as the energy is lowered, rather than being due to a merger between the forward and recoil peaks. This new feature must therefore be considered as being due to an additional scattering phenomena that arises for this state.

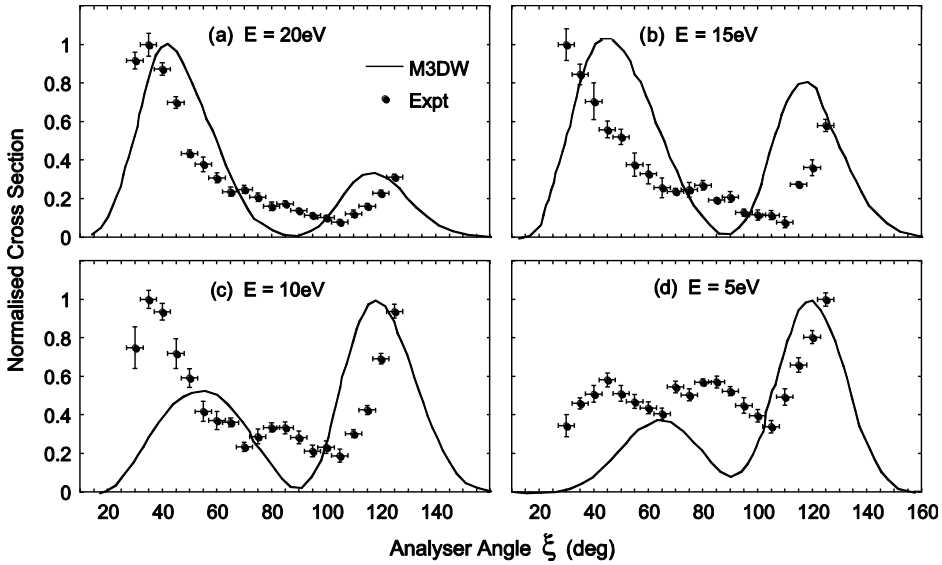


Figure 5: As for Figure 4, for the $2a_1$ NHOMO state of $CH_4$.

By contrast, the M3DW only predicts atomic-like structures, with a TDCS that differs little compared to that predicted for the $1t_2$ state. The model again produces two peaks, with a deep minimum between forward and backward scattering peaks. Although there is qualitative agreement between theory and experiment for the highest energies, theory does not predict the correct peak positions, relative heights or structure for the lower energies. In the spherical averaging process for the nuclei, the point charges from the hydrogen nuclei are spread out to a uniform distribution on a sphere which would make them much less effective as a scattering center [14]. Consequently, the fact that the theory predicts two lobes while experiment has three lobes, suggests that the three lobe might originate from scattering from the H nuclei, but experimental data from neon presented in Sec. TDCS for isoelectronic atom and molecule indicate that other processes may also be playing a role in producing the peak at $\xi = 90°$.

The limited agreement between experiment and theory for this state is surprising, given that this orbital was specifically selected for it's almost spherical structure and lack

of parity inversion. A contributing factor to this, given the relatively good agreement between theory and experiment for the $1t_2$ state, may be that the $2a_1$ state is deeper within the molecule (*i.e.* it is not the outermost orbital), so that scattering from the H nuclei may become more important, whereas the nuclei are more effectively screened for the outer $1t_2$ state.

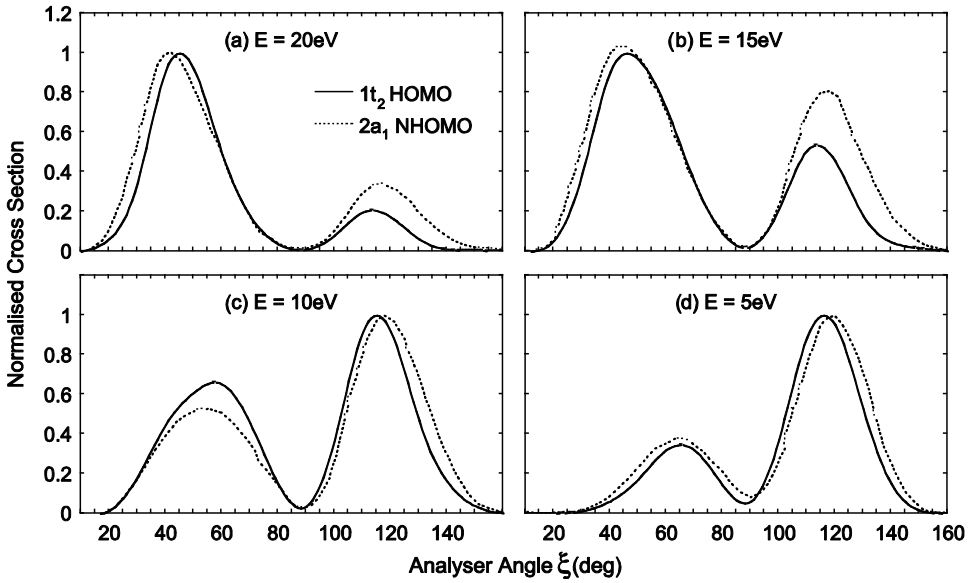


Figure 6: A comparison of the TDCS from the M3DW calculation for the $1t_2$ (solid line) and $2a_1$ (dashed line) normalized to unity at the peak. The theory predicts very similar structure for both states, although the absolute magnitudes are different.

Figure 6 shows the $1t_2$ and $2a_1$ theoretical results normalized to unity at the largest cross section. It is interesting to note that the results for the two states are very similar in structure (although they are different in their predicted magnitude, which is not seen in the comparison with the experimental data here due to normalization). This observation suggests that the main contributing factor to the calculated cross section for low energies is either the dynamics of the collision or the role of nuclear scattering which is the same for both molecular states–and that the nature of the orbital does not have a significant influence on the theoretical predictions.

**C. TDCS for isoelectronic atom and molecule**

By comparing the TDCS for the $2a_1$ state in $CH_4$ (IP = 23.05 eV) with the isoelectronic atom neon (IP = 48.5 eV), it may be possible to identify sources of the discrepancy between experiment and theory shown above. Given that the $2a_1$ MO in methane is considered to be equivalent to a relatively unaltered 2s carbon atomic orbital [20], it is anticipated that the TDCS from the $2a_1$ state may be similar to that of the analogous 2s atomic state in neon, since in each case there are six electrons outside the 2s shell. A comparison of the TDCS of the molecule with that of neon could then indicate if the lack of agreement between experiment and theory is primarily due to the molecular nature of the target. Since the theoretical model does not need to apply spherical averaging for atoms, the effect of this approximation is eliminated. Further, differences in the data for the atom and molecule may also arise from to the additional scattering centres of the hydrogen nuclei present in $CH_4$.

Figure 7 shows the TDCS for ionizing the $2a_1$ state of $CH_4$ and the Ne 2s state at two energies; one at a relatively high energy where the outgoing electrons both have an energy of 20eV (a) and (c) and one for the low energy case where the outgoing electrons have an energy of 5eV (b) and (d). In each case, the data show similar trends for both the molecule and atom. At the higher energy the cross section has a strong intensity in the forward direction which decreases rapidly with higher angles. The TDCS measured for neon only has a small increase for scattering angles beyond 110°, in contrast to $CH_4$, which shows a significant rise at angles greater than 110°. For the low energy case the triple peak structure noted in Fig. 5 is seen in both targets, although for neon the scatter in the data makes this less clear than for $CH_4$. The maximum in the forward direction for neon occurs at higher angles than for $CH_4$. There is now a clear minimum around 115°

for neon, whereas this minimum occurs at ~ 105° in $CH_4$. The cross section for $CH_4$ at higher angles is significantly larger than for forward scattering, in contrast to neon that does not show this effect at angles that are accessible within the spectrometer.

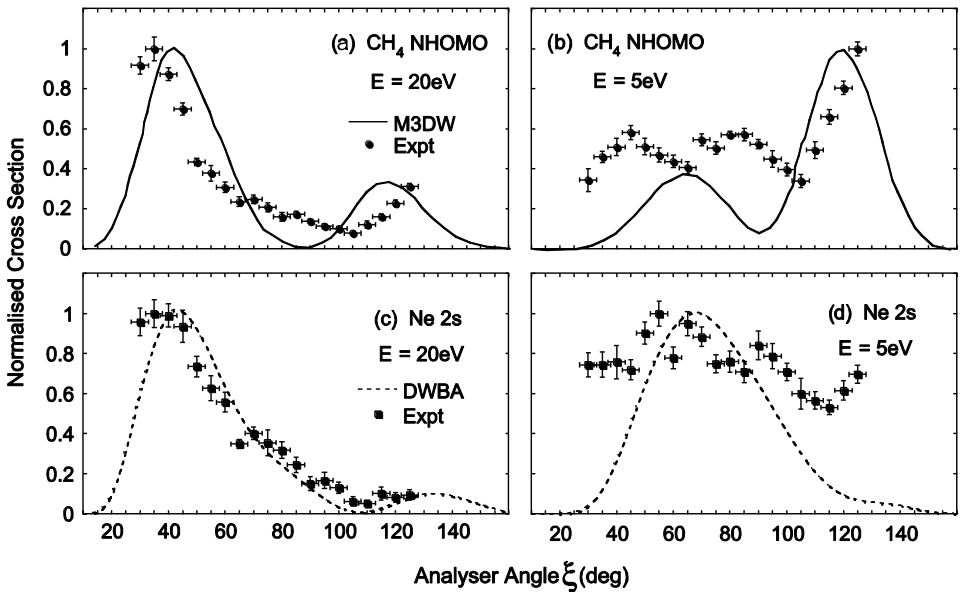


Figure 7: TDCS for the equivalent states within the isoelectronic species, i.e., the $2a_1$ orbital of $CH_4$ and the 2s inner atomic state of Ne. The upper figures show results for the molecule at 20eV and 5eV outgoing energies, as in Figure 4. The bottom panel shows the TDCS from the 2s state inner of neon collected under the same kinematics. The experimental data (points) are compared with theoretical predictions from the distorted wave calculations (solid line) for $CH_4$ and the Distorted Wave Born Approximation (DWBA) (dotted line) for neon.

The qualitative similarities in the experimental cross sections for the two targets corroborate the premise that the target orbitals are similar. The comparison between the data and theory is quite good for neon at the higher energy [Fig. (7c)]. By contrast, at low energies the theoretical TDCS does not emulate the data, and is different for the two targets. With all nuclear charge placed at the center of mass, theory only predicts a single peak for low energy while experiment appears to have a small three-lobe structure superimposed on a large single peak. The small three-lobe structure for Ne indicates that the strong three-lobes found for the $2a_1$ state on $CH_4$ arises from more than scattering

from the H-nuclei. Since theory is not significantly better for the atomic target at low energies, this suggests that the spherical averaging process is not the sole source of discrepancy between experiment and theory, and that other approximations in the calculation must be playing a significant role at these energies, such as using distorted waves calculated on spherically symmetric molecular potentials that do not depend on the orientation of the molecule.

## Conclusions

Experimental (e,2e) data for ionization of methane in the low energy regime using a coplanar symmetric geometry have been compared with a molecular three-body distorted wave approximation (M3DW). A comparison between the $\phi_{Dy}^{OAMO}$ and experiment was made via high energy EMS results. Good agreement was found for both states. However, agreement between theory and experiment is somewhat mixed for low energies and rather surprisingly the best agreement was found for the outermost $1t_2$ molecular state, which has a change in parity through the molecular centre. By contrast, since the $2a_1$ molecular orbital is almost spherical in nature and does not have parity inversion, it was expected that inaccuracies introduced in the spherical averaging process would be minimized from this orbital, so that the theoretical result might be in better agreement with experiment. This was found not to be the case.

A comparison was made between the isoelectronic atomic and molecular cross sections. The theoretical atomic cross sections were in noticeably better agreement with experiment for higher energies but not low energies. This suggests that the molecular nature of the target is not the only cause of disagreement. It may be that the low energies used in these measurements are revealing limitations in the model due to the

approximations that are used. Since the $2a_1$ state of $CH_4$ and the 2s state of neon are both inner states, it may also be that nuclear scattering plays a more predominant role that is not being properly treated. More experimental and theoretical work is clearly necessary to try to explain these differences.

## Acknowledgements

This work was supported by the University of Manchester and the US National Science Foundation under Grant. No. PHY-0757749. K.L.N. would like to thank the Royal Society for a Newton International Fellowship. We would also like to thank Sadek Mohammed Fituri Amami for providing the DWBA Ne 2s cross sections.

## References

1. J Tennyson, Phys. Rep. Physics Lett. **491**, 29 (2010).

2. S. Bellm, J. Lower, R. P. McEachran, E. Weigold, C. Ryan-Andrewson and D. H. Madison, Phys. Rev. A **78**, 062707 (2008).

3. D. V. Fursa, C. J. Bostock and I. Bray, Phys. Rev. A **80** 022717 (2009).

4. J. Colgan, M. Foster, M. S. Pindzola, I. Bray, A. T. Stelbovics, and D. V. Fursa, J. Phys. B. **42**, 145002 (2009).

5. C. J. Colyer, S. M. Bellm, B. Lohmann, G. F. Hanne, O. Al-Hagan, D. H. Madison and C. G. Ning, J. Chem. Phys. **133**, 124302 (2010).

6. C. J. Colyer, M. A. Stevenson, O. Al-Hagan, D. H. Madison, C. G. Ning and B. Lohmann, J. Phys. B. **42**, 235207 (2009).

7. A. Lahmam-Bennani, E. M. S. Casagrande and A. Naja, J. Phys. B. **42**, 235205 (2009).

8. D. S. Milne-Brownlie, S. J. Cavanagh, B. Lohmann, C. Champion, P. A. Hervieux and J. Hanssen, Phys. Rev. A **69**, 032701 (2004).

9. C Champion, C. D. Cappello, S. Houamer, and A. Mansouri, Phys. Rev. A **73**, 012717 (2006).

10. A. Lahmam-Bennani, A. Naja, E. M. S. Casagrande, N. Okumus, C. Dal Cappello, I. Charpentier and S. Houamer, J. Phys. B. **42**, 165201 (2009).

11. K. L. Nixon, A. J. Murray, O. Al-Hagan, D. H. Madison and C. G. Ning, J. Phys. B. **43**, 035201 (2010).

12. C. Kaiser, D. Spieker, J. F. Gao, M. Hussey, A. Murray and D. H. Madison, J. Phys. B. **40**, 2563 (2007).

13. M. J. Hussey and A. J. Murray, J. Phys. B. **38**, 2965 (2005).

14. I. Toth and L. Nagy, J. Phys. B. **43**, 135204 (2010).

15. D. H. Madison and O. Al-Hagan, Journal of Atomic, Molecular, and Optical Physics 2010 367180 (2010).

16. V. M. Sivakumar, A. R. Mohamed, A. Z. Abdullah, and S. P. Chai, J. of Nanomater., **2010**, 395191 (2010).

17. D. J. Fu, X. R. Zeng, J. Z. Zou, L. Li, X. H. Li and F. Deng, J. Alloys Compd. **486**, 406 (2009).

18. X. S. Li, C. W. Magnuson, A. Venugopal, J. H. An, J. W. Suk, B. Y. Han, M. Borysiak, W. W. Cai, A. Velamakanni, Y. W. Zhu, L. F. Fu, E. M. Vogel, E. Voelkl, L. Colombo and R. S. Ruoff, Nano Lett. **10**, 4328 (2010).

19. Z. P. Chen, W. C. Ren, B. L. Liu, L. B. Gao, S. F. Pei, Z. S. Wu, J. P. Zhao and H. M. Cheng, Carbon **48**, 3543 (2010) .

20. F. Wang, J. Mol. Struct. Theochem **678**, 105 (2004).

21. S. A. C. Clark, T. J. Reddish, C. E. Brion, E. R. Davidson and R. F. Frey, Chem. Phys. **143**, 1 (1990).

22. S. T. Hodd, E. Weigold, I. E. McCarthy and P. J. O. Teubner Nature (London) Phys. Sci. **245**, 65 (1973).

23. E. Weigold, S. Dey, A. J. Dixon, I. E. McCarthy and P. J. O. Teubner Chem. Phys. Lett. **41**, (1976).

24. R. Cambi, G. Ciukko, A. Sgamellotti, F. Tarantelli, R. Fantoni, A. Giardini-Guidoni and A. Sergio, Chem. Phys. Lett. **41**, 295 (1981).

25. A. J. Murray, B. C. H. Turton and F. H. Read, Rev. Sci. Instrum. **63**, 3346 (1992).

26. A. J. Murray and F. H. Read, Phys. Rev. A **47**, 3724 (1993).

27. A. J. Murray and D Cvejanovic, J. Phys. B. **36**, (2003).

28. J. F. Gao, J. L. Peacher, and D. H. Madison, J. Chem. Phys. **123**, 204302 (2005).

29. J. F. Gao, D. H. Madison, and J. L. Peacher, J. Chem. Phys. **123**, 204314 (2005).

30. J. F. Gao, D. H. Madison, and J. L. Peacher, J. Phys. B. **39**, 1275 (2006).

31. C. T. Lee, W. T. Yang, and R. G. Parr, Phys. Rev. B **37**, 785 (1988).

32. C. F. Guerra, J. G. Snijders, G. te Velde, and E. J. Baerends, Theor. Chem. Acc. **99**, 391 (1998).

33. S. J. Ward and J. H. Macek, Phys. Rev. A **49**, 1049 (1994).

34. J. B. Furness and I. E. McCarthy, J. Phys. B. **6**, 2280 (1973).

35. J. P. Perdew and A. Zunger, Phys. Rev. B **23**, 5048 (1981).

36. N. T. Padial and D. W. Norcross, Phys. Rev. A **29**, 1742 (1984).

37. E. Weigold and I. E. McCarthy, *Electron Momentum Spectroscopy* (Kluwer/Plenum, New York, 1999).

## II Experimental and theoretical investigation of the triple differential cross section for electron impact ionization of pyrimidine molecules

J D Builth-Williams[1], S M Bellm[1], D B Jones[1], Hari Chaluvadi[2], D H Madison[2], C G Ning[3], B Lohmann[4] and M J Brunger[1,5]

[1] ARC Centre of Excellence for Antimatter-Matter Studies, Flinders University, GPO Box 2100, Adelaide, South Australia 5001, Australia

[2] Department of Physics, Missouri University of Science and Technology, Rolla, MO 65409, USA

[3] Department of Physics and Key Laboratory of Atomic and Molecular NanoSciences of MOE, Tsinghua University, Beijing 100084, People's Republic of China

[4] University of the Sunshine Coast, Maroochydore DC, Queensland 4558, Australia

[5] Institute of Mathematical Sciences, University of Malaya, 50603 Kuala Lumpur, Malaysia

### Abstract

Cross-section data for electron impact induced ionization of bio-molecules are important for modelling the deposition of energy within a biological medium and for gaining knowledge of electron driven processes at the molecular level. Triply differential cross sections have been measured for the electron impact ionization of the outer valence $7b_2$ and $10a_1$ orbitals of pyrimidine, using the (e,2e) technique. The measurements have been performed with coplanar asymmetric kinematics, at an incident electron energy of 250 eV and ejected electron energy of 20 eV, for scattered electron angles of $-5^o$, $-10^o$ and

-15$^{o}$. The ejected electron angular range encompasses both the binary and recoil peaks in the triple differential cross section. Corresponding theoretical calculations have been performed using the molecular 3-body distorted wave model and are in reasonably good agreement with the present experiment.

## Introduction

Studies of the electron-impact ionization of bio-molecules provide important information on the role of electrons in causing damage to DNA in biological systems. It is now well established that low energy secondary electrons produced by high energy primary radiation are responsible for much of the damage to DNA in living tissue[1,2]. In order to predict cellular damage it is desirable to model the trajectories of primary and secondary particles through a biological medium. This can be done by calculating the path along which the primary and secondary particles move as they pass through matter, known as their charged particle track structures[3-6]. Detailed information is required on the initial spatial distribution of events involving both ionization and excitation along the charged particles path. Differential cross sections are an important source of this information as they enable a complete three-dimensional description of the deposition of energy as a function of angle[5]. In the majority of track structure simulations in biological media, the focus is on water[3, 6] as the primary species in the system, but the inclusion of contributions from other species present is needed for a more complete description of the process. Due to the challenging nature of performing measurements and calculations of cross-sectional data for electron interactions with larger molecules, there are currently limited data for targets of biological interest.

Pyrimidine ($C_4H_4N_2$) is an important molecule of biological significance. It possesses a six membered ring structure belonging to the group of diazines, where the

two nitrogen atoms in the ring are located in the meta positions. The molecular point group of pyrimidine is $C_{2v}$. The pyrimidine molecule is of particular interest because it forms the fundamental structure in several nucleobase ring systems, and it is because of this structural similarity that it has been used as a model compound to investigate electron collisions with DNA constituents[7-9]. Indeed, two of the four nucleobases found in DNA, that is cytosine and thymine, as well as the RNA base uracil are pyrimidine derivatives.

The power of the electron-electron coincidence (e,2e) technique for investigating the ionization dynamics of atoms and molecules is well recognized[10]. In an (e,2e) experiment information about the collision of an incident electron with an atomic or molecular target is obtained by measuring the energy and momenta of the outgoing electrons in time coincidence. The technique can be used to provide spatial information about the scattering direction of electrons. A key objective of the present study is to further our understanding of electron interactions with bio-molecules, using smaller molecules to compare directly with the components of larger biological systems. While measuring cross sections for isolated molecules in the gas phase can, of course, only approximate what occurs in biological systems, it is good starting point and has proven to be a useful approach[11-13].

Despite the fact that many dynamical (e,2e) studies of atomic systems have been reported, low-energy (e,2e) studies of molecules have not been as numerous. Indeed, while there has been an increased interest in these studies over the last decade, both theoretical and experimental studies have mostly been limited to smaller targets. Recently molecules including methane[14, 15] and formic acid[16] have been investigated. Studies concerning larger molecules such as component molecules of DNA and RNA are rare,

and include tetrahydrofuran[17] and theoretical studies on thymine[18]. Difficulties in the theoretical calculations arise from the fact that the orientation of the molecule is not commonly determined by experiment and an averaging over all molecular orientations must be incorporated into the theoretical approach. Furthermore, the theoretical approach must include a multicentred wave function. This is in contrast to the much simpler atomic cases where atoms have only a single scattering centre and spherically symmetric wave functions[19].

While to the best of our knowledge the present study represents the first dynamical (e, 2e) investigation of pyrimidine, the bound electronic structure has previously been probed by electron momentum spectroscopy (EMS). Ning *et al* have reported EMS measurements of the complete valence region of pyrimidine at incident electron energies of 600 eV and 1500 eV, and compared their measured results with Hartree Fock and density functional theory (DFT) calculations[20]. Shojaei *et al* have also recently reported an extensive theoretical study of its valence electronic structure, ionization spectrum and electron momentum distributions[21]. The valence electronic structure of pyrimidine and a number of its halogenated derivatives have also recently been investigated using ultraviolet photoelectron spectroscopy and *ab inito* quantum chemical methods[22].

## Experimental Details

The electron impact induced single ionization of a ground state pyrimidine molecule, $C_4H_4N_2$, can be described by:

$$e^-(E_i,\mathbf{k}_i) + C_4H_4N_2 \rightarrow C_4H_4N_2^+ + e^-(E_a,\mathbf{k}_a) + e^-(E_b,\mathbf{k}_b), \quad (1)$$

where $E_i$, $E_a$, $E_b$ and $\mathbf{k}_i$, $\mathbf{k}_a$, $\mathbf{k}_b$ are the kinetic energies and momenta of the incident, scattered and ejected electrons, respectively.

The triple differential cross section (TDCS) is represented by:

$$\frac{d^5\sigma}{d\Omega_a d\Omega_b dE_b}, \tag{2}$$

and it is a measure of the probability that after ionization of a target species by a projectile with energy $E_i$ and momentum $\mathbf{k}_i$, two electrons will be produced with energies $E_a$ and $E_b$ and momenta $\mathbf{k}_a$ and $\mathbf{k}_b$ into the solid angles $\Omega_a$ and $\Omega_b$. The momentum transferred to the target is:

$$\mathbf{K} = \mathbf{k}_i - \mathbf{k}_a. \tag{3}$$

In the present study, coplanar asymmetric measurements were performed using a conventional coincidence spectrometer. The experimental apparatus has previously been described in detail[17, 23] and so only a brief overview will be given here.

An incident beam of electrons is produced by thermionic emission from a tungsten filament and is collimated and transported to the interaction region using five cylindrical electrostatic lens elements. The resulting incident electron beam energy resolution is approximately 0.5 eV. At the interaction region the electron beam crosses a molecular target beam. The target beam enters the interaction region through a 0.7 mm internal diameter stainless steel capillary. In the current configuration of the apparatus, the capillary and thus the target beam are oriented parallel to the scattering plane, which is defined by the momentum vectors of the incident and measured outgoing electrons.

Table 1 Binding energies for the outer valence region of pyrimidine in eV. The error in the Gaussian peak location for the present data is quoted in brackets. The orbital assignments, calculations and EMS data are from Ning *et al*[20]. PES data are from Potts *et al.*[33].

| Orbital | Type | Present Results (eV) | PES (eV) [33] | EMS (eV)[20] | OVGF (eV)[33] |
|---|---|---|---|---|---|
| $7b_2$ | nσ | 9.8 (0.2) | 9.8 | 9.8 | 9.83 |
| $2b_1$ | π | 10.5 (0.6) | 10.5 | 10.5 | 10.4 |
| $11a_1$ | nσ | 11.3 (0.2) | 11.2 | 11.3 | 11.36 |
| $1a_2$ | π | | 11.5 | | 11.28 |
| $10a_1$ | σ | 13.9 (0.1) | 13.9 | 14.1 | 14.49 |
| $1b_1$ | π | | | | 14.49 |
| $6b_2$ | σ | | 14.4 | | 14.63 |
| $9a_1$ | σ | 15.4 (0.3) | 15.8 | 15.7 | 16.25 |
| $5b_2$ | σ | 17.0 (0.9) | 17.0 | 17.5 | 17.26 |
| $8a_1$ | σ | 17.7 (0.4) | 17.7 | | 18.28 |
| $7a_1$ | | 19.4 (0.2) | | 20.6 | |

The higher energy (scattered) and lower energy (ejected) outgoing electrons are both detected in separate hemispherical energy analysers, each comprising a 5-element electrostatic entrance lens system, hemisphere and channel electron multiplier detector. (e,2e) events are identified using standard coincidence timing procedures[24] from the relative arrival times of electrons at the two detectors and background events are subtracted using standard statistical methods. The two electron energy analysers are mounted on independently rotatable turntables concentric with the interaction region. In dynamical TDCS measurements, the scattered electron is detected at a fixed (small) forward angle with respect to the incident electron beam direction. Ejected electron angular distributions are measured by scanning the ejected electron energy analyser and detecting electrons at a number of different angles within the scattering plane. In the current measurements the coincidence energy resolution of the system is approximately

1.1 eV (FWHM), as determined from a measurement of the helium 1s binding energy peak.

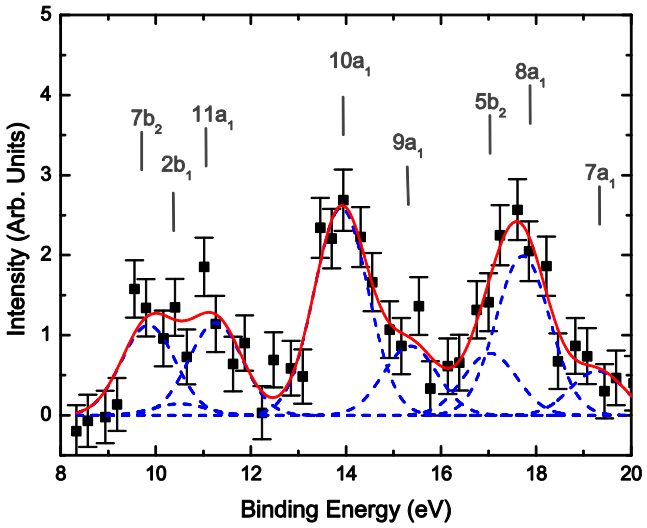


Figure 1 Measured binding energy spectrum for the outer valence region of pyrimidine, obtained at an incident energy of 250 eV (see text for details). The data are fitted with a sum of Gaussian functions using the coincidence energy resolution as the peak width.

Pyrimidine is a liquid at room temperature with sufficient vapour pressure at room temperature to perform our measurements. The pyrimidine sample 99% (Sigma-Aldrich, Australia) was treated with several freeze-pump-thaw cycles prior to use to remove absorbed gases. To prevent possible condensation of pyrimidine within the sample lines, which may contribute to instability in the rate of flow of the sample into the vacuum chamber, the sample lines, and vacuum chamber were heated to approximately 40$^{o}$C throughout the measurements.

## Theoretical Framework

The molecular 3-body distorted wave (M3DW) approximation has been presented in previous publications[24-26], so that only a brief outline of the theory will be presented. The TDCS for the M3DW is given by:

$$\frac{d^5\sigma}{d\Omega_a\Omega_b dE_b} = \frac{1}{(2\pi)^5}\frac{k_a k_b}{k_i}|T|^2 \quad (4)$$

Where $\vec{k}_i$ , $\vec{k}_a$, and $\vec{k}_b$ are the wave vectors for the initial, scattered and ejected electrons. The scattering amplitude is given by:

$$T = \left\langle \chi_a^-(\vec{k}_a, \mathbf{r}_1)\chi_b^-(\vec{k}_b, \mathbf{r}_2)C_{scat-eject}(r_{12}^{ave})\,|V - U_i|\,\phi_{DY}^{OA}(\mathbf{r}_2)\chi_i^+(\vec{k}_i, \mathbf{r}_1)\right\rangle \quad (5)$$

where $r_1$ and $r_2$ are the coordinates of the incident and the bound electrons, $\chi_i, \chi_a$, and $\chi_b$ are the distorted waves for the incident, scattered, and ejected electrons, respectively, and $\phi_{DY}^{OA}(r_2)$ is the initial bound-state Dyson molecular orbital averaged over all orientations. The molecular wave functions were calculated using DFT along with the standard hybrid B3LYP[27] functional by means of the ADF 2007 (Amsterdam Density Functional) program[28] with the triple-zeta with two polarization functions Slater type basis set. For the $7b_2$ orbital, the average of the absolute value of the Dyson wave function is taken since the normal average is zero[15]. The factor $C_{scat-eject}(r_{12}^{ave})$ is the Ward-Macek average Coulomb-distortion factor between the two final state electrons[29], $V$ is the initial state interaction potential between the incident electron and the neutral molecule, and $U_i$ is a spherically symmetric distorting potential which is used to calculate the initial-state distorted wave for the incident electron $\chi_i^+(\vec{k}_i, \mathbf{r}_1)$.

The Schrödinger equation for the incoming electron wave function is given by:

$$(T + U_i - \frac{k_i^2}{2})\chi_i^+(\vec{k_i}, r) = 0 \qquad (6)$$

where $T$ is the kinetic energy operator and the '+' superscript on $\chi_i^+(\vec{k_i}, \mathbf{r})$ indicates outgoing wave boundary conditions. The initial state distorting potential contains three components $U_i = U_s + U_E + U_{CP}$, where $U_s$ contains the nuclear contribution plus a spherically symmetric approximation for the interaction between the projectile electron and the target electrons which is obtained from the quantum mechanical charge density of the target. $U_E$ is the exchange potential of Furness and McCarthy (corrected for sign errors)[30] which approximates the effect of the continuum electron exchanging with the passive bound electrons in the molecule, and $U_{CP}$ is the correlation-polarization potential of Perdew and Zunger[31, 32].

The final state for the system is approximated as a product of distorted waves for the two continuum electrons times the average Coulomb-distortion factor. The final state distorted waves are calculated as the initial state except that the final state spherically symmetric static distorting potential for the molecular ion is used for $U_s$.

## Results and Discussion

Figure 1 shows the present binding energy spectrum for the outer valence region of pyrimidine. The incident and ejected electron energies were fixed at 250 eV and 20 eV, respectively, while the scattered electron energy was scanned across a range of energies. The detection angles for the scattered and ejected electrons were selected to be -15$^o$ and 70$^o$, respectively. As noted earlier, the experimental coincidence energy resolution under the chosen conditions was estimated to be 1.1 eV FWHM, from the

width of the helium 1s binding energy peak measured under the same kinematics. The binding energy spectrum has been fitted with a sum of eight Gaussian functions of a fixed width, which corresponds to the experimental coincidence energy resolution. Note that as our coincidence energy resolution is much larger than the natural widths of the various orbitals[33-37], this is a reasonable approximation in this case.

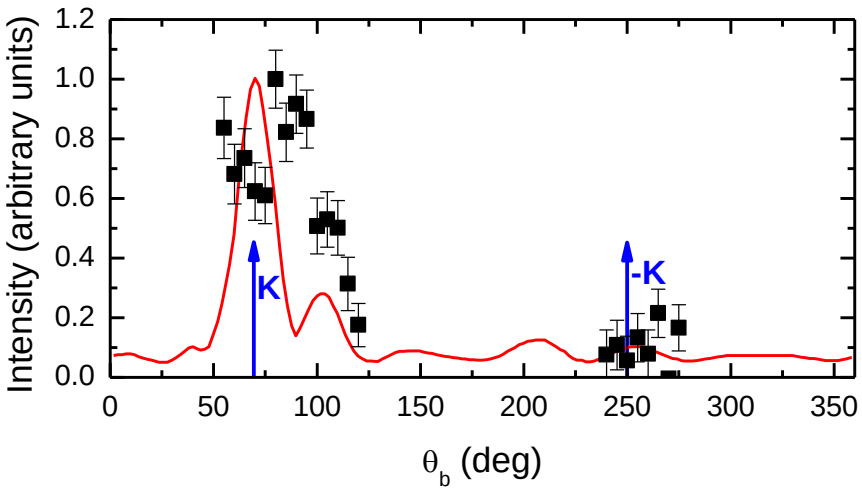


Figure 2 Plot of the triple differential cross sections for ionization of the $7b_2$ orbital of pyrimidine, with $E_0$=250 eV and $E_b$=20 eV. The scattered electron detection angle is -15° and the corresponding momentum transfer is |K|=1.12 au. Points are the experimental data. Solid curve (red): M3DW calculation taking the average of the absolute value of the Dyson wave function. The positions of the momentum transfer vector, K, and –K are indicated by the arrows.

The valence electronic structure of pyrimidine is relatively well characterised. Photoelectron spectra of pyrimidine have been recorded using synchrotron radiation[33], as well as HeI[34, 35, 37] and HeII[36] radiation. Table I shows the binding energy determined for each orbital, as well as the binding energies determined in previous EMS[20] and photoelectron spectroscopy (PES)[33] studies which are in good agreement with the present results. We note that to facilitate their study of β parameters in the PES study by Potts *et al*, pyrimidine was assigned in the $C_s$ point group rather than the $C_{2v}$ group[33]. It should

also be noted that although $C_{2v}$ point group was adopted, a different notation has been used to label the orbitals in some of the previous pyrimidine PES studies.[22,36] The highest occupied molecular orbital (HOMO) is the $7b_2$ orbital which has a binding energy of 9.8 eV. With our coincidence energy resolution this cannot be fully resolved from the next highest $2b_1$ orbital. Note that the $7b_2$ orbital of pyrimidine can be considered as being essentially a non-bonding orbital associated with the N atoms[38]. The largest peak in the spectrum shown in Fig. 1, at a binding energy of 13.9 eV, is assigned as being predominantly due to ionization of the $10a_1$ orbital although contributions from the $1b_1$ and $6b_2$ orbitals are also likely to be present.

Experimental and theoretical TDCSs for the outermost $7b_2$ orbital of pyrimidine at a scattering angle of $-15^o$ are presented in Figure 2. The measurements were performed at a relatively low incident electron energy of 250 eV and the energy for the ejected electron was chosen to be 20 eV. As the energy separation between the HOMO and the next highest occupied molecular orbital is only 0.7 eV, well below the 1.1 eV FWHM coincidence resolution of our apparatus, we reiterate that the data in the present measurements most likely contains contributions from both orbitals. The uncertainties on the present $7b_2$ TDCS are statistical and are at the one standard deviation level.

Conventionally the angular distributions are divided into two regions[23]. These are the angular region between $0^o$ and $180^o$, which is known as the binary region, and the region between $180^o$ and $360^o$ which is named the recoil region. The binary region may contain strong signatures of the orbital structure whereas the recoil region contains structure arising from processes in which the ejected electron undergoes an initial binary collision and then subsequent elastic backscattering from the residual ion core. The

present experimental $7b_2$ orbital binary peak data appears (see Fig. 2) to have a double peak type structure with a local minimum in the angular range very close to the momentum transfer direction. The slight shift of the binary peak, to larger scattering angles, away from the momentum transfer direction is likely caused by Coulomb repulsion between the final state electrons. A double peak type structure in the binary peak of atomic orbitals is characteristic of a *p*-type orbital and reflects the momentum probability density distribution of electrons in these orbitals[39]. The $7b_2$ orbital is of N 2p character[33], thus the observed structure most likely reflects the 2*p* nature of the molecular orbital. The M3DW predicts a double binary peak as well but the peak positions are shifted to larger scattering angles by about 200 and the second peak has a much lower intensity than the experimental data.

The M3DW calculation also predicts the relative magnitudes of the $7b_2$ orbital binary and recoil peaks quite well. As the experimental data are relative they are only attributed absolute values by normalization to the M3DW theory to give the best visual fit in the binary peak region. The size of the recoil peak is small, indicating that there is not a large amount of interaction of the ejected electron with the molecular ion. This is expected as the kinematics are close to bound Bethe ridge conditions. On the Bethe ridge the kinematics satisfy the requirement that all momentum is transferred to the bound, target electron during the collision. Under such conditions, the collision kinematics correspond to a binary e–e collision, where the ion plays no role, and practically no recoil lobe is expected. Interestingly, the HOMO binary peak here also appears quite narrow. This is in contrast to previous dynamical (e,2e) studies on molecules, including for

tetrahydrofuran[17], formic acid[16], water[40], and methane[14], under similar kinematics in which very broad binary peaks have been observed for ionization of the HOMO.

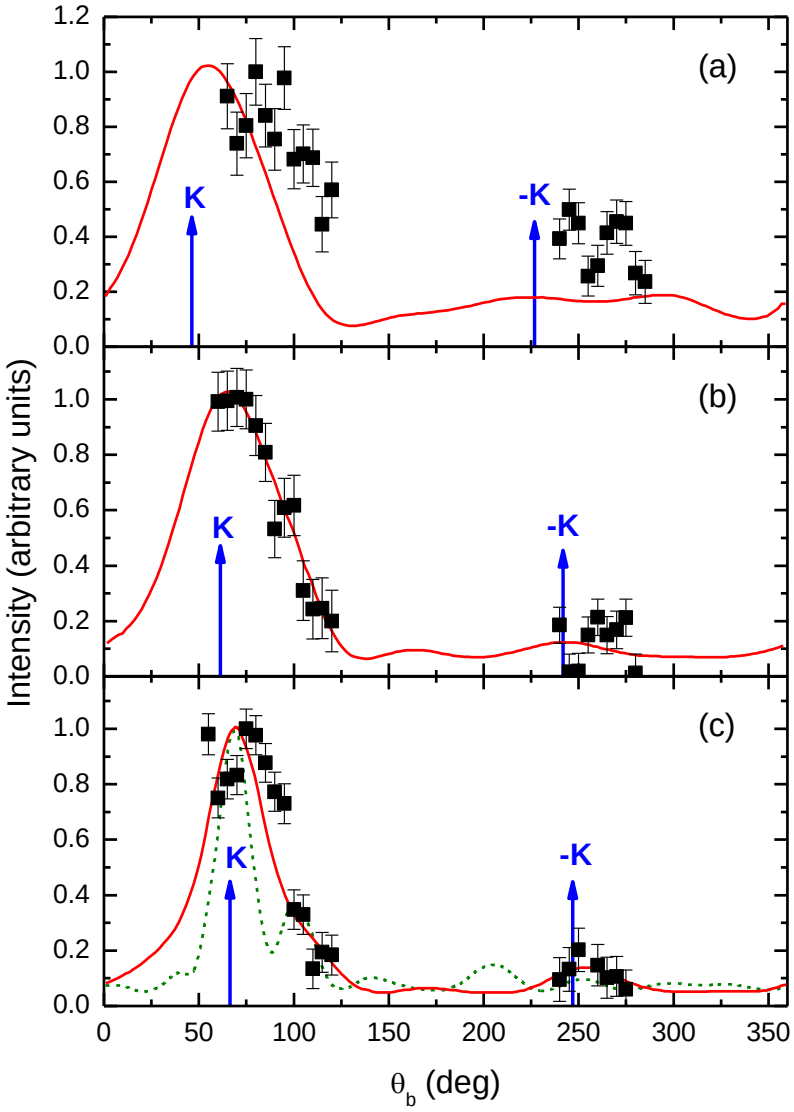


Figure 3 Plot of the triple differential cross sections for ionization of the 10a1 orbital of pyrimidine, with $E_0$=250 eV and $E_b$=20 eV. The scattered electron detection angles and corresponding momentum transfers are (a) -5°, |K|=0.47 au, (b) -10°, |K|=0.78 au and (c) -15°, |K|=1.12 au. Points are the experimental data. Solid curve (red): M3DW calculation. Dashed curve (green): M3DW calculation taking the average of the absolute value of the Dyson wave function. The positions of the momentum transfer vector, K, and –K are indicated by the arrows.

Triple differential cross sections for the $10a_1$ orbital of pyrimidine, at scattered electron angles of $-5^o$, $-10^o$ and $-15^o$, are shown in Figures 3(a)-(c). These measurements were also performed at an incident electron energy of 250 eV and the energy of the ejected electron was 20 eV. Again absolute values are assigned to the experimental data by normalization of the data set to the corresponding M3DW calculation to achieve the best visual fit. For the smallest scattering angle of $-5^o$, the binary peak is somewhat broader than in Fig. 2. As the momentum transfer is increased with increasing scattered electron angle, the binary peak is seen to become narrower. This observation is supported by our M3DW results. All the TDCSs for the $10a_1$ orbital indicate a single binary peak consistent with it being an s-type orbital, a result consistent with the classification given in table I. The EMS study by Ning *et al.*, however, observed a *p*-type momentum distribution at this binding energy[20]. This is likely to be caused by contributions from the $1b_1$ and $6b_2$ orbitals as with the coincidence energy resolution of their apparatus they were unable to separate contributions from these orbitals. While this is also true in our case, it appears from Fig. 3 that with the present kinematics the contribution from the $1b_1$ and $6b_2$ orbitals to the $10a_1$ TDCS is not so severe. Once more it appears that there is very little interaction of the ejected electron with the molecular ion as the $10a_1$ recoil peaks are small in magnitude.

Contrary to the case for the $7b_2$ orbital, where the absolute value of the Dyson wave function is averaged (as taking the average of the molecular wave function would be zero for this symmetry), the totally symmetric nature of the $10a_1$ orbital allows its wave function to be averaged over all orientations. The two types of calculations are compared in Figure 3(c), the method averaging the wave function clearly giving a

superior result to the method averaging the absolute value of the wave function. Note that to facilitate comparison, the calculation where the absolute value of the wave function is averaged has been normalized to the calculation averaging the wave function at the maximum of the binary peak. For the scattering angles of $-10^{o}$ and $-15^{o}$ very good qualitative agreement is seen between the M3DW theory and the experimental data. The calculations predict both the shape of the binary peak and the ratio of the binary to recoil peaks very well. Note also that Coulomb repulsion between the final state electrons causes a slight shift of the binary peak, to larger scattering angles, away from the momentum transfer direction.

Agreement between the M3DW calculation and experimental data is not quite as good at the scattering angle of $-5^{o}$, with the M3DW somewhat underestimating the width of the binary peak. It is possible that this extra width in the experimental cross section is due to contributions from the other unresolved $1b_1$ and $6b_2$ orbitals that are likely to be present. Although the magnitude of the calculated recoil peak is larger than for $-10^{o}$ and $-15^{o}$, it is still not as large as that observed in the experimental data. As discussed in a previous publication[17], a similar situation for DWBA type calculations was also observed for tetrahydrofuran and methane[41] for larger impact parameter collisions. Toth and Nagy showed that the magnitude of the recoil peak is related to the nuclear term in the static potential[41] and an underestimation of the recoil peak was attributed to a spreading of the nuclear charge over a spherical shell leading to a nuclear interaction that is too weak.

While good qualitative agreement is observed between the M3DW calculation and experimental data, absolute cross section measurements are needed to assess how close the magnitudes of the predicted TDCSs are to the true values. Unfortunately,

placing TDCS data on an absolute scale has traditionally been a difficult process[42, 43]. A simple method for absolute (e,2e) measurements was recently reported[43], however due to the high density of molecular orbitals such measurements would still be very difficult to perform for a molecular target of the complexity of pyrimidine.

## Conclusions

Experimental and theoretical dynamical (e,2e) results were presented for the pyrimidine molecule, which is a model compound to investigate electron interactions with the DNA bases thymine and cytosine and the RNA base uracil. The measured binding energies and orbital assignments were found to be in good agreement with the available EMS and PES data. Experimental TDCSs for both orbitals investigated exhibited a narrow binary peak at all scattered electron angles with the exception of $-5^{o}$ for the $10a_1$ orbital. The experimental data were also compared with results from theoretical cross sections obtained using the M3DW method. The M3DW calculations taking an average of the molecular wave function gave much better agreement with the experimental data than when the average of the absolute value of the wave function was employed in the calculation. The M3DW calculation predicted a narrower binary peak in the TDCS for the scattering angle of $-5^{o}$ for the $10a_1$ orbital, than is observed in the experimental data. This is likely due to contributions from the $1b_1$ and $6b_2$ orbitals to the experimental data. However, overall we conclude that the M3DW calculations are in rather good qualitative agreement with the experimental data especially given the complicated nature of the molecular target. The good agreement between experiment and theory strongly supports the use of M3DW caculations as input in charged-particle track structure modelling.

**Acknowledgements**

This work was supported by the Australian Research Council Centre of Excellence for Antimatter-Matter Studies and by the US National Science Foundation (NSF) (Grant. No. PHY-1068237). The author C.N. would like to acknowledge the support of the National Natural Science Foundation of China (NNSFC) (contract No. 10704046).

## References

1.B. Boudaïffa, P. Cloutier, D. Hunting, M. A. Huels and L. Sanche, Science **287** (5458), 1658-1660 (2000).

2.F. Martin, P. D. Burrow, Z. Cai, P. Cloutier, D. Hunting and L. Sanche, Physical Review Letters **93** (6), 068101-068104 (2004).

3.M. Fuss, A. Munoz, J. C. Oller, F. Blanco, P. Limao-Vieira, C. Huerga, M. Tellez, M. J. Hubin-Fraskin, K. Nixon, M. Brunger and G. Garcia, in *XXVI International Conference on Photonic, Electronic and Atomic Collisions*, edited by A. E. Orel, A. F. Starace, D. Nikolic, N. Berrah, T. W. Gorczyca, E. Y. Kamber and J. A. Tanis (IOP Publishing Ltd, Bristol, 2009), Vol. 194, pp. 012028.

4.D. T. Goodhead, International Journal of Radiation Biology **65** (1), 7 - 17 (1994).

5.H. Nikjoo, S. Uehara, D. Emfietzoglou and F. A. Cucinotta, Radiat. Meas. **41** (9-10), 1052-1074 (2006).

6.A. Munoz, F. Blanco, G. Garcia, P. A. Thorn, M. J. Brunger, J. P. Sullivan and S. J. Buckman, International Journal of Mass Spectrometry **277** (1-3), 175-179 (2008).

7.A. Zecca, L. Chiari, G. Garcia, F. Blanco, E. Trainotti and M. J. Brunger, J. Phys. B-At. Mol. Opt. Phys. **43** (21), 215204 (2010).

8.J. B. Maljković, A. R. Milosavljević, F. Blanco, D. Šević, G. García and B. P. Marinković, Physical Review A: Atomic, Molecular, and Optical Physics **79** (5), 052706 (2009).

9.P. Palihawadoma, J. P. Sullivan, M. J. Brunger, C. Winstead, V. McKoy, G. Garcia, F. Blanco and S. J. Buckman, Phys. Rev. A (2011).

10.A. Lahmam-Bennani, J. Phys. B **24** (10), 2401-2442 (1991).

11.S. Ptasinska, S. Denifl, P. Scheier and T. D. Mark, Journal of Chemical Physics **120** (18), 8505-8511 (2004).

12.P. Swiderek, Angew. Chem. Int. Ed. **45** (25), 4056-4059 (2006).

13.R. D. White and R. E. Robson, Physical Review Letters **102** (23) (2009).

14.A. Lahmam-Bennani, A. Naja, E. M. S. Casagrande, N. Okumus, C. Dal Cappello, I. Charpentier and S. Houamer, J. Phys. B-At. Mol. Opt. Phys. **42** (16), 165201 (2009).

15.K. L. Nixon, A. J. Murray, H. Chaluvadi, C. Ning and D. H. Madison, Journal of Chemical Physics **134** (17), 174304 (2011).

16.C. J. Colyer, M. A. Stevenson, O. Al-Hagan, D. H. Madison, C. G. Ning and B. Lohmann, J. Phys. B-At. Mol. Opt. Phys. **42** (23), 235207 (2009).

17.C. J. Colyer, S. M. Bellm, B. Lohmann, G. F. Hanne, O. Al-Hagan, D. H. Madison and C. G. Ning, The Journal of Chemical Physics **133** (12), 124302-124307 (2010).

18.C. Dal Cappello, Z. Rezkallah, S. Houamer, I. Charpentier, P. A. Hervieux, M. F. Ruiz-Lopez, R. Dey and A. C. Roy, Physical Review A **84** (3), 032711 (2011).

19.D. H. Madison and O. Al-Hagan, Journal of Atomic, Molecular, and Optical Physics **2010**, 24 (2010).

20.C. G. Ning, K. Liu, Z. H. Luo, S. F. Zhang and J. K. Deng, Chem. Phys. Lett. **476** (4-6), 157-162 (2009).

21.S. H. R. Shojaei, B. Hajgato and M. S. Deleuze, Chem. Phys. Lett. **498** (1-3), 45-51 (2010).

22.S. J. Cavanagh and B. Lohmann, J. Phys. B-At. Mol. Opt. Phys. **32** (12), L261-L270 (1999).

23.E. Weigold and I. E. McCarthy, *Electron Momentum Spectroscopy*. (Kluwer Academic/Plenum, New York, 1999).

24.J. F. Gao, D. H. Madison and J. L. Peacher, Journal of Chemical Physics **123** (20), 204314 (2005).

25.J. F. Gao, D. H. Madison and J. L. Peacher, Physical Review A **72** (3), 032721 (2005).

26.J. F. Gao, J. L. Peacher and D. H. Madison, Journal of Chemical Physics **123** (20), 204302 (2005).

27.C. Lee, W. Yang and R. G. Parr, Phys. Rev. B **37** (2), 785 (1988).

28.C. F. Guerra, J. G. Snijders, G. te Velde and E. J. Baerends, Theor. Chem. Acc. **99**, 391 (1998).

29.S. J. Ward and J. H. Macek, Physical Review A **49** (2), 1049-1056 (1994).

30.J. B. Furness and I. E. McCarthy, J. Phys. B-At. Mol. Opt. Phys. **6** (11), 2280-2291 (1973).

31.J. P. Perdew and A. Zunger, Physical Review B **23** (10), 5048-5079 (1981).

32.N. T. Padial and D. W. Norcross, Physical Review A **29** (4), 1742-1748 (1984).

33.A. W. Potts, D. M. P. Holland, A. B. Trofimov, J. Schirmer, L. Karlsson and K. Siegbahn, J. Phys. B-At. Mol. Opt. Phys. **36** (14), 3129-3143 (2003).

34.M. N. Piancastelli, P. R. Keller, J. W. Taylor, F. A. Grimm and T. A. Carlson, J. Am. Chem. Soc. **105** (13), 4235-4239 (1983).

35.W. von Niessen, W. P. Kraemer and G. H. F. Diercksen, Chem. Phys. **41** (1-2), 113-132 (1979).

36.R. Gleiter, E. Heilbronner and V. Hornung, Helvetica Chimica Acta **55** (1), 255-274 (1972).

37.L. Asbrink, C. Fridh, B. O. Jonsson and E. Lindholm, International Journal of Mass Spectrometry and Ion Physics **8** (3), 215-227 (1972).

38.M. Stener, P. Decleva, D. M. P. Holland and D. A. Shaw, J. Phys. B-At. Mol. Opt. Phys. **44** (7), 075203 (2011).

39.A. Lahmam-Bennani, H. F. Wellenstein, A. Duguet and M. Rouault, J. Phys. B **16** (1), 121 (1983).

40.D. S. Milne-Brownlie, S. J. Cavanagh, B. Lohmann, C. Champion, P. A. Hervieux and J. Hanssen, Phys. Rev. A **69** (3), 032701-032704 (2004).

41.I. Tóth and L. Nagy, J. Phys. B **43** (13), 135204 (2010).

42.A. Lahmambennani, M. Cherid and A. Duguet, J. Phys. B-At. Mol. Opt. Phys. **20** (11), 2531-2544 (1987).

43.L. R. Hargreaves, M. A. Stevenson and B. Lohmann, Measurement Science & Technology **21** (5), 055112 (2010).

## III Low energy measurements of $CH_4$ and neon in the perpendicular plane

Kate L Nixon[1], Andrew James Murray[1], Hari Chaluvadi[2], Sadek Amami[2], Don H Madison[2] and Chuangang Ning[3]

[1]Photon Science Institute, School of Physics and Astronomy, University of Manchester, Oxford Road, Manchester M13 9PL, United Kingdom

[2]Department of Physics, Missouri University of Science and Technology, Rolla, Missouri 65409, USA

[3]Department of Physics and Key Laboratory of Atomic and Molecular Nano-Sciences of MOE, Tsinghua University, Beijing 100084, People's Republic of China

### Abstract

Low energy experimental and theoretical triple differential cross sections for the highest occupied molecular orbital of methane ($1t_2$) and for the 2p atomic orbital of neon are presented and compared. These targets are iso-electronic, each containing 10 electrons and the chosen orbital within each target has p-electron character. Observation of the differences and similarities of the cross sections for these two species hence gives insight into the different scattering mechanisms occurring for atomic and molecular targets. The experiments used perpendicular, symmetric kinematics with outgoing electron energies between 1.5 eV and 30 eV for $CH_4$ and 2.5 eV and 25 eV for neon. The experimental data from these targets are compared with theoretical predictions using a distorted wave Born approximation. Resonably good agreement is seen between the experiment and theory for neon while mixed results are observed for $CH_4$. This is most likely due to approximations of the target orientation made within the model.

## Introduction

Electron impact ionisation collisions at low energies are important in a number of fundamental areas. These include plasma etching in industry, to the study of natural atmospheric phenomena as well as cancer therapy by radiation treatments. In order to understand the underlying physical process in these areas, a robust understanding of the collision is necessary. Experimental measurements provide data for specific collision parameters from a particular target. By developing comprehensive theoretical models of the collision that are rigorously tested by experiment, accurate predictions for a range of collision parameters from a multitude of targets can then be made. Precise experimental data are hence required to aid in the development of the theoretical models.

(e,2e) experiments control the projectile electron momentum and define the momentum of the electrons resulting from the collision. As such, these kinematically complete experiments provide the most detailed data against which theory can be compared. This field has provided a rich source of information on atomic targets, with good agreement being found between experiment and theory for a range of different atoms. By contrast, the number of molecules that have been investigated is still relatively small, and new models are currently under development. This is due to the more complex nature of molecules compared to atoms. Molecules have spatially distributed nuclei resulting in multiple scattering centres, which means that the wave-functions associated with the electron distribution within the molecule are not spherically symmetric. This reduction in symmetry leads to further complications, since the orientation and alignment of the molecule with respect to the scattering geometry must also be considered. Additionally, the energy levels within molecules are often more closely spaced than in

atoms, resulting in neighbouring orbitals that may not be resolvable by experiment. Despite these theoretical and experimental challenges, detailed electron impact ionisation studies from molecules have been emerging over the past decade.

The molecular target in this current study is methane ($CH_4$), which is the smallest hydrocarbon and so is a relatively simple molecule. It has five atoms, with ten electrons. The molecule has tetrahedral symmetry and only two valence energy levels. The $1t_2$ level is the highest occupied molecular orbital (HOMO) and is a triply degenerate, p-like orbital. The next highest occupied molecular orbital ($2a_1$) has almost spherical symmetry, and has s-like character. These orbitals are separated in energy by ~ 9eV, allowing data to be obtained from the individual orbitals without contamination. Recent measurements from $CH_4$ using scattered electron energies of 500 eV have been reported [1] and corresponding distorted wave Born approximation (DWBA) calculations [2] show good agreement at these higher energies. The data presented here are low energy triple differential cross sections (TDCS) using symmetric energy sharing, where both outgoing electrons leave the collision with equal energy. Perpendicular kinematics were used in which the momentum of the incident projectile electron is orthogonal to the detection plane containing the two outgoing electrons (see Figure 1). In order for both outgoing electrons to leave the collision in this plane, it is necessary for multiple scattering to occur. This geometry hence provides a stringent test of theory. Additionally, marked differences have been observed between atomic helium and molecular $H_2$ in this plane, in contrast to results taken in a coplanar geometry where the cross sections were similar.[3] Since He and $H_2$ have the same number of electrons and protons, these results indicate

that measurements in the perpendicular plane provide a more sensitive test of the structure of the target than data taken in a coplanar geometry.

To further understand the measurements from $CH_4$, the resulting TDCS is compared with that from neon. Neon is the iso-electronic atom to $CH_4$, both species having 10 electrons. By comparing the atomic and molecular cross sections, similarities in the TDCS may be attributable to a similar electronic structure, while differences may arise due to the molecular nature of the target.

A previous study from the NHOMO ($2a_1$) orbital of $CH_4$ in a coplanar geometry yielded poor statistical accuracy due to very low signal at these energies,[4] and so the TDCS for the outermost orbital of the two species are presented here, i.e. the $1t_2$ orbital of $CH_4$ and the corresponding 2p orbital of Ne.

This paper is structured as follows. Section experimental apparatus describes the pertinent details of the apparatus used to collect the data. The theoretical framework used to model the collision is then detailed in Sec. theoretical frame work. Results from experimental measurement and theoretical predictions are presented and discussed in Sec results and discussions. Section conclusions summarises this study and maps out future work that is needed.

## Experimental Apparatus

The fully computer controlled and computer optimised (e,2e) spectrometer at the University of Manchester was used in this work. This apparatus has been described elsewhere [5] so only the salient points are discussed here. The spectrometer consists of an electron gun with an energy resolution of ~ 600 meV, two electron analysers, a gas jet

and a Faraday cup. The electron analysers are mounted on individual turntables so that they can be independently rotated around the interaction region. The detection plane is defined by these analysers (see Figure 1). In this study the spectrometer was configured in a perpendicular geometry where the momentum of the incident electron is perpendicular to the detection plane ( $\psi$=90°). The data are symmetric as the outgoing electrons were detected with equal energies, i.e., $E_1 = E_2$, and the only angle of relevance in this plane is the angle between the analysers, $\phi = \xi_1 + \xi_2$ .

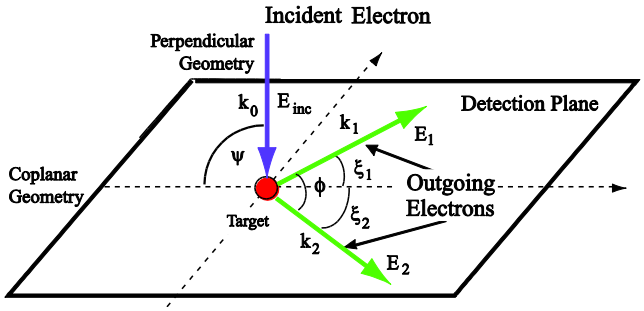


Figure 1: Diagram of the geometry used in this study. A perpendicular geometry ($\psi$=90°) is defined when the momentum of the incident electron is perpendicular to that of the outgoing electrons, i.e.,the detection plane. In the perpendicular geometry only the mutual angle ($\varphi = \xi_1 + \xi_2$ ) is relevant.

High purity $CH_4$ or neon was admitted into the interaction region through a gas jet. The flow of the target gas was controlled by a needle valve. Typical operating pressures for $CH_4$ and Ne were $1.2 \times 10^{-5}$ Torr and $2.2 \times 10^{-5}$ Torr, respectively. Small incident electron beam currents, typically ~120 nA, were used for $CH_4$ in order to maintain a good signal to background ratio. Higher currents of 300 nA were used for neon.

The spectrometer was operated under computer control throughout data collection. The electrostatic lenses in the analysers were optimised at each new angle to ensure maximum signal. The energy of the incident electron beam was calibrated at the beginning of each new data set by locating the peak in the coincidence binding energy spectrum. The two highest occupied molecular orbitals of $CH_4$ are well separated, by ~ 9eV. The experimental energy resolution of ~1.4eV easily ensures there is no contamination in the measured data from the neighbouring orbital, as is often the case for molecular targets.[6-8]

The data have not been placed on an absolute scale due to the low energies used in this study. Molecular targets may have a dramatic influence on the behaviour of the electron beam at these energies [9] and so it is not accurate to assume that the electron beam density remains constant between measurements as the energy is changed or for different target species, as is essential in the normalisation methods applied by others at higher energies [10,11]. Consequently, the data presented here are normalised to unity at the highest data point for each set. Each data set is generated from an average of many sweeps around the detection plane. The error bars on the TDCS represent the standard error derived from this average. The uncertainties on the scattering angle are due to the pencil angle of the incident electron beam, and the acceptance angles of the outgoing electron analysers. This is estimated to be ±5°.

The experimental data for neon have been published previously [12]. The data are re-presented here so that a direct comparison can be made between the two isoelectronic species.

## Theoretical Framework

The molecular 3-body distorted wave (M3DW) approximation [or atomic 3-body distorted wave (3DW) approximation] has been detailed in previous publications [13-15] so only a brief outline is given here. The triple differential cross section (TDCS) for the M3DW is giving by:

$$\frac{d^5\sigma}{d\Omega_a d\Omega_b dE_b} = \frac{1}{(2\pi)^5}\frac{k_a k_b}{k_i}|T|^2 \qquad (1)$$

where $\vec{k}_i$, $\vec{k}_a$, and $\vec{k}_b$ are the wave vectors for the initial, scattered and ejected electrons. The scattering amplitude is given by:

$$T_{dir} = \left\langle \chi_a^-(\vec{k}_a,\mathbf{r}_1)\, \chi_b^-(\vec{k}_b,\mathbf{r}_2)\, C_{\text{scat-eject}}(r_{12})\, |V-U_i|\, \phi_{DY}^{OA}(\mathbf{r}_2)\, \chi_i^+(\vec{k}_i,\mathbf{r}_1)\right\rangle \qquad (2)$$

where $r_1$ and $r_2$ are the coordinates of the incident and the bound electrons, $\chi_i$, $\chi_a$, and $\chi_b$ are the distorted waves representing the incident, scattered, and ejected electrons, respectively, and $\phi_{DY}^{OA}(\mathbf{r}_2)$ is the initial bound-state Dyson molecular orbital averaged over all orientations, The molecular wave-functions were calculated using density functional theory along with the standard hybrid B3LYP [Ref. 16] functional by means of the ADF 2007 (Amsterdam Density Functional) program [17] with the TZ2P (triple-zeta with two polarization functions) Slater type basis sets. For the $1t_2$ state, the average of the absolute value of the Dyson wave-function is taken prior to the collision, since the normal average is zero due to parity of the wave-function [4].

For the Ne atom, the same matrix element (2) is evaluated except the Dyson orbital is replaced by a Hartree-Fock 2p wave-function. The factor $C_{\text{scat-eject}}(r_{12})$ is the Ward-Macek average Coulomb-distortion factor between the two final state electrons [18], *V* is the initial state interaction potential between the incident electron and neutral

molecule, and $U_i$ is a spherically symmetric distorting potential which is used to calculate the initial-state distorted wave for the incident electron $\chi_i^+(\vec{k}_i, \mathbf{r}_1)$.

The Schrödinger equation for the incoming electron wave-function is given by

$$(T + U_i - \frac{k_i^2}{2})\chi_i^+(\vec{k_i}, r) = 0, \quad (3)$$

where T is the kinetic energy operator and the '+' superscript on $\chi_i^+(\vec{k}_i, \mathbf{r}_1)$ indicates outgoing wave boundary conditions. The initial state distorting potential contains three components $U_i = U_s + U_E + U_{CP}$. $U_s$ is the static potential that contains the nuclear contribution and a spherically symmetric approximation for the interaction between the projectile electron and the target electrons which is obtained from the quantum mechanical charge density of the target. $U_E$ is the exchange potential of Furness-McCarthy (corrected for sign errors) [Ref. 19] which approximates the effect of the continuum electron exchanging with the passive bound electrons in the molecule. Finally, $U_{CP}$ is the correlation-polarization potential of Perdew and Zunger [20], and Padial and Norcross. [21]

The final state for the system is approximated as a product of distorted waves for the two continuum electrons multiplied by the average Coulomb-distortion factor. The final state distorted waves are calculated as the initial state, except that the final state spherically symmetric static distorting potential for the molecular ion (or atomic ion) is used for *Us*.

## Results

### A. Predicted scattering signatures using a classical model

A recent investigation by Al-Hagan et al. [3] considers a simple classical picture of the ionisation of atoms and molecules in the perpendicular plane that is validated using quantum mechanical calculations. These authors provide an explanation for features observed in the measured crosssections when the experiments do not determine the orientation of a molecular target. Predictions were given for (i) atomic targets, (ii) molecular targets that have a nucleus at the centre of mass, and (iii) molecular targets that do not have a nucleus at the centre of mass. Experimental and theoretical data from He, $H_2$ and $CO_2$ with $E_1 = E_2 = 10$ eV were used in their study. It was predicted that molecules with no nucleus at the centre of mass should produce a minimum contribution to the cross section at angles corresponding to the outgoing electrons emerging back to back, i.e. at $\varphi = 180°$. This prediction results from the model averaging over all possible orientations of the molecule prior to the collision (as is adopted in the calculations used in this paper), so that the nuclear charge appears as a thin 'shell' of charge with a diameter set by the inter-nuclear distance. In these averaging models, electrons that collide inside the resulting nuclear shell cannot experience any force from the nuclei, and so only a binary collision will occur (no re-collision from the nucleus then being possible). In this case the TDCS in the perpendicular plane should only present peaks at $\varphi \sim 90°,270°$, as was observed for $H_2$. The model further suggests that molecular targets that do have a nucleus at the centre of mass should then yield a backscattering signature similar to atomic targets, since nuclear re-scattering can then occur. This prediction was confirmed in their data for $CO_2$, which produced a TDCS similar in structure to that of helium, with peaks at $\varphi \sim 90°,270°$ (due to binary collisions) and a third peak at 180° (due to re-

scattering of one of the electrons from the nucleus). Since $CH_4$ has a carbon atom at the centre of mass of the molecule, this simple classical model predicts that $CH_4$ should produce a 3- peak TDCS, with significant cross-section at $\varphi = 180°$.

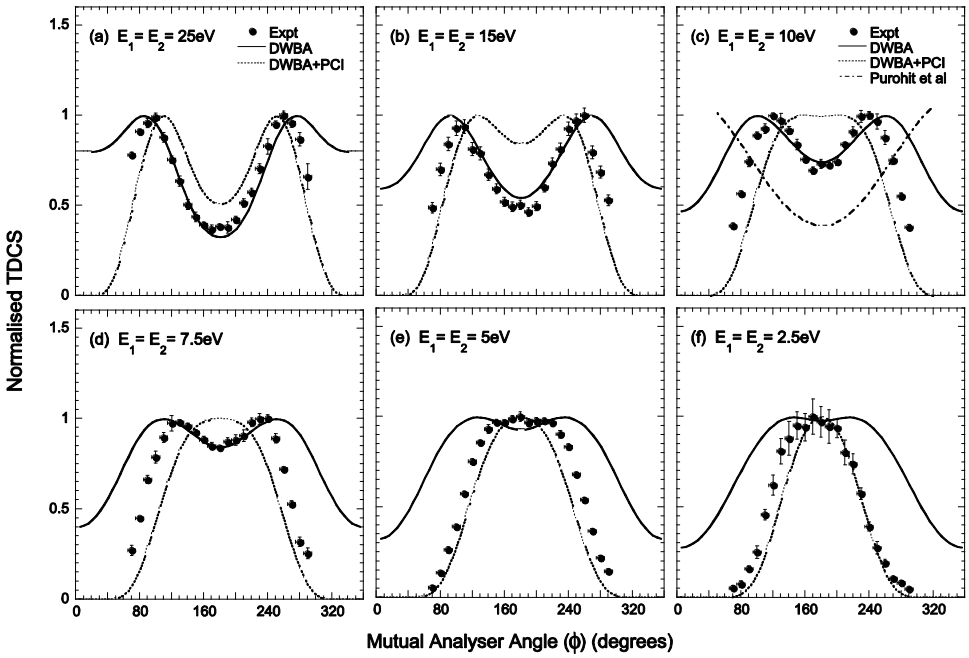


Figure 2: Experimental and theoretical TDCS for the 2p orbital of neon. Incident energies of 5 eV to 50 eV above the ionisation potential (IP=21.6eV) were used, as indicated on the plots. Two theoretical predictions are shown for all energies; DWBA with no PCI included (solid line) and 3DW (dashed line) where PCI is treated using the Ward-Macek approximation. An additional theoretical curve is shown in (c) following the calculation of Purohit et al. [22]. The experimental and theoretical data have been independently normalised to unity at the peak of the TDCS for each energy.

**B. 2p orbital of neon**

The experimental and theoretical TDCS for the valence 2p orbital of neon are shown in Figure 2. The theoretical data have been calculated in the DWBA framework. Two curves are shown that represent different calculations. The first is a basic DWBA calculation (DWBA). The second (3DW) has post-collisional interactions (PCI) included by using the Ward-Macek approximation [18]. The result of an independent theoretical

study by Purohit et al. [22] is also shown for an incident electron energy 20 eV above the ionisation potential.

The structure of the data has been discussed previously [12]. Briefly, a double peak structure is observed at high energies, with a minimum at φ = 180° in contrast to both the prediction of the simple model described in section A, and the experimental results from helium [12]. As the energy decreases the two peaks move closer together giving a narrower distribution, and the local minimum at φ = 180° becomes shallower. At the lowest energy studied here ($E_1 = E_2 = 2.5$ eV), a single peak is observed. This peak will include a contribution due to PCI between the two outgoing electrons [23], since at these low energies the longer interaction time between the outgoing electrons results in them asymptotically being driven apart.

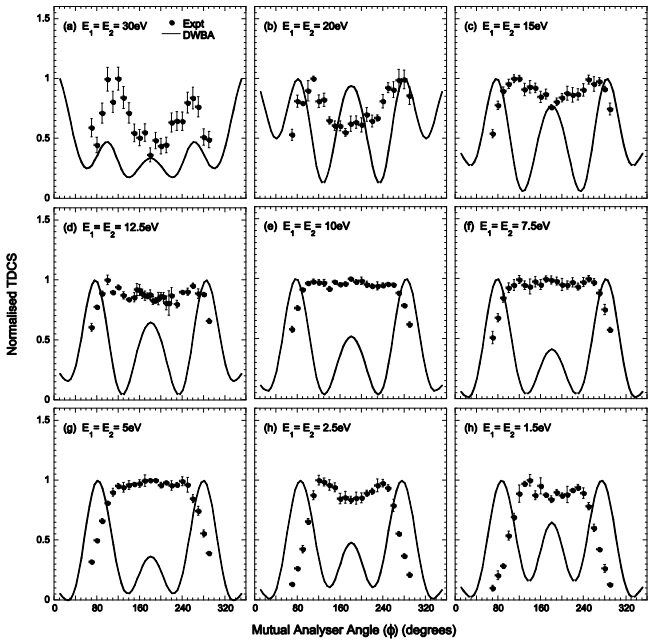


Figure 3: Experimental and theoretical DWBA TDCS for the $1t_2$ HOMO state of $CH_4$. Incident energies of 3 eV to 60 eV above the ionisation potential (IP ~ 14eV) were used, as indicated on the plots. The experimental and theoretical data have been independently normalised to unity at the peak for each energy.

It is interesting that the simple classical picture [3] already appears to fail for this target. The absence of a defined peak at φ = 180° may be attributable to the proposed nuclear re-scattering mechanism having a much smaller probability than for helium, compared with the binary mechanism that gives rise to the peaks on either side. This hypothesis is strengthened by the 3DW model that also predicts a minimum at φ = 180°, in agreement with the data. From a classical viewpoint, it would be expected that nuclear scattering would be weaker for neon since the classical impact parameters for elastic scattering into the perpendicular plane would be five times larger for neon than helium.

Consequently, it appears that the physical effects leading to the shape of the cross section is different for this case. The fact that both the DWBA and 3DW predict a minimum at 180° indicated that the minimum is not related to the electron-electron interaction in the final state.

The prediction from the DWBA calculation (i.e., without PCI) shows unphysically high flux when the electrons emerge at the same angle, i.e., at the mutual angles φ = 0°and φ = 360°. This clearly shows the importance of PCI, as is included in the 3DW prediction. PCI can also be attributed to the narrowing of the TDCS around φ = 180° as the energy is lowered. This reduction in width is due to the electrons that emerge from the interaction region repelling each other.

The correlation between experimental data and the theoretical predictions is interesting. At high energy, the DWBA calculation predicts the depth of the minimum at φ = 180° with more accuracy than the 3DW calculation, which also predicts too narrow a distribution at these energies. This may indicate that the contribution due to PCI is too

strong in the model. Conversely, at the lowest energy the 3DW calculation is far more successful at predicting the width of the distribution. Neither model emulates the success that was found for helium.

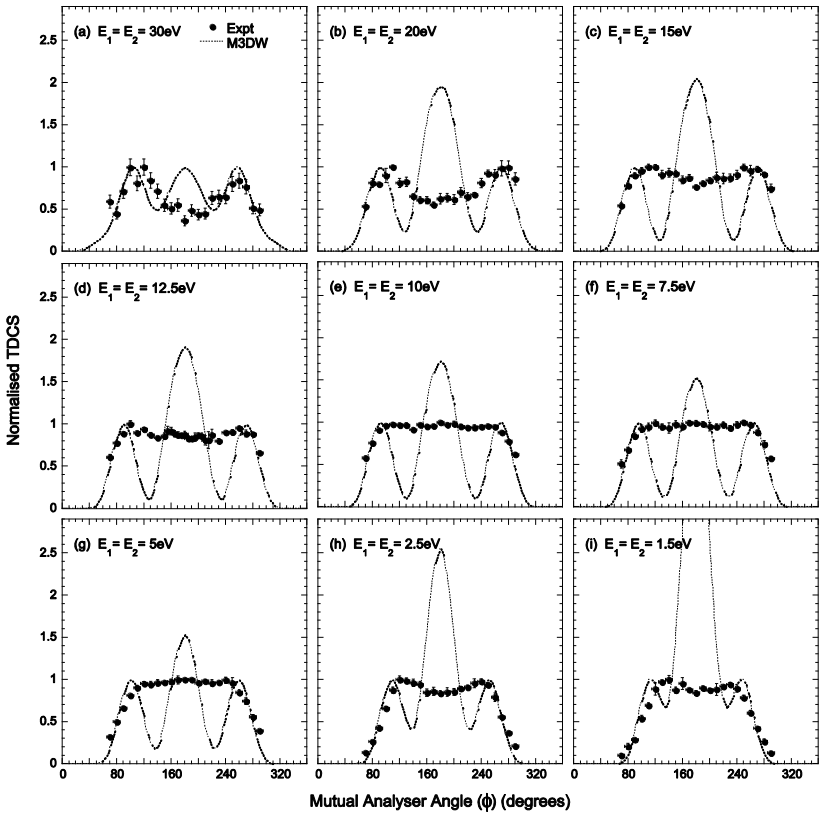


Figure 4: Experimental and theoretical (M3DW) TDCS for the $1t_2$ HOMO state of $CH_4$. The experimental data has been normalised to unity at the maximum intensity, while the theoretical data is normalised to unity at the side peaks. For details, see text.

In addition to the predictions given here, Figure 2(c) also shows the DWBA calculation by Purohit et al. [22]. This calculation used a spin averaged static exchange potential, includes PCI via the Gamow factor and employs a polarization potential in the incident channel only. Only one calculation for neon in the perpendicular plane was reported by these authors, at outgoing electron energies $E_1$=$E_2$=10 eV. Their calculation predicts a minimum at $\varphi = 180°$, as is observed. By contrast, their predicted cross section

increases in both directions towards φ = 0°and φ = 360°, and their minimum is broader and deeper than is seen in the experimental data.

**C. $1t_2$ state of methane**

The experimental and theoretical TDCS for the HOMO of $CH_4$ (the $1t_2$ state), are shown in Figures 3 and 4. Figure 3 compares the data to the DWBA model, whereas Figure 4 shows a comparison with the M3DW model. The HOMO of $CH_4$ is a triply degenerate state consisting of three p-like orbitals. These orbitals have parity inversion through the centre of symmetry, which is also the centre of mass in $CH_4$. To allow for parity inversion, the present models use the absolute value of the orbital wave-function to generate an averaged wave-function over all orientations of the molecule. This is used here since the averaging procedure would produce a zero wave-function if parity inversion was included. It has been found that the orientationally averaged molecular wave-function used for this state is of reasonably good quality [4] when compared with experimentally measured EMS data [24] at high energies.

The data shows a two-peak structure at the highest energy used here, i.e. $E_1$=$E_2$=30 eV as shown in figures 3(a) and 4(a). The peaks are located symmetrically about φ = 180°, at angles of φ = 110° and φ = 260°. A minimum is observed between the two peaks with a magnitude ~ 0.45 of the peaks. This is similar to that observed for the valence states of neon, argon and krypton [12]. As the energy of the outgoing electrons is decreased, the two peaks remain approximately in the same position and the local minimum fills in. In figures (d)-(g), the distribution is wide, flat and almost featureless. Evidence of a faint triple peak structure may be observed. As the energy is lowered further the total angular width of the cross section decreases, and a small two-peak

structure is again seen at the two lowest energies. Here the two peaks are found at φ = 120° and φ = 240°, and the minimum at φ = 180° has an intensity ~ 0.85 of the peak height.

Both DWBA and M3DW models predict well-resolved triple peak structures at the majority of energies measured. The peak at φ = 180° seen in the theoretical results emulates the prediction of the classical model described in Al-Hagan et al. [3]. Initially consider the DWBA prediction as in Figure 3. At high energies the calculation shows unphysical intensity at φ = 0° and 360°, which is due to the absence of PCI in the model, as seen for neon in Figure 2. The model predicts a triple peak structure at the lower energies, the width of the cross-section being overestimated at almost all energies by this calculation.

The predictions from the M3DW calculation that includes PCI using the Ward-Macek approximation [18] are shown in Figure 4. In this figure the data are normalised to unity at the two side peaks. The agreement in width of the TDCS between experiment and theory is much more satisfactory for all energies, and the unphysical cross-section at φ = 0° and 360° is now eliminated due to inclusion of PCI. There is, however, a discrepancy in the number of peaks that are predicted, and the large relative magnitude of the TDCS at φ = 180° predicted by the model is not observed.

Once again, the TDCS generated by this model is in good agreement with that expected from the classical model outlined in Sec. IV A, with three clearly defined peaks and with a large central peak at φ = 180° (as observed for helium). The magnitude of the predicted peak at φ = 180° indicates that re-scattering from the carbon nucleus is much

stronger than for the iso-electronic neon atom at similar energies. This probably results from the fact that the classical impact parameters for elastic scattering into the perpendicular plane are smaller for the molecule than they are for the atom.

A similar discrepancy regarding the number of discrete peaks predicted by theory was noted for $H_2O$ in the perpendicular plane [9]. In these experiments the excess energy remained constant at 20 eV and the energy sharing between the two outgoing electrons was varied. In the three cases studied for this target, the experimental distribution was relatively flat as is seen here for $CH_4$, in contrast to theory that predicted a well-defined triple peak structure.

**D. Comparison between the iso-electronic species**

The experimental distributions for the two iso-electronic analogues neon and $CH_4$, show some similarities in the shape of the cross-section. Differences, particularly at intermediate and low energies, are also observed. To summarise; at is high energies both targets display a double peak structure. Also, in both cases the local minimum is filled in as the energy decreased. For neon, the width of the distribution narrows as the energy is lowered, and the angular distribution shows a small flat section at $E_1 = E_2 = 5$ eV where the TDCS transitions between a double peak structure and a single peak. In contrast, the width of the $CH_4$ distribution remains essentially constant until $E_1=E_2=5$ eV. The TDCS of $CH_4$ is relatively flat and featureless over the range of outgoing electron energies from 12.5 eV to 5 eV, while the distributions for neon always show a double peak structure until $E_1 = E_2=5$ eV. At the lowest energies used here, neon presents a single peak, while $CH_4$ shows a shallow double peak structure. At these energies the width of the $CH_4$ distribution starts to reduce.

Comparison with the theoretical results for these two species show large differences. For all but the lowest energy, a minimum is predicted at $\varphi = 180°$ for neon. Conversely, a maximum is predicted at $\varphi = 180°$ for $CH_4$. Indeed, this maximum dominates the predicted TDCS when PCI is included, in contrast to what is observed in the experiment.

## Conclusions

In comparing the theoretical predictions for neon to the data, it is seen that neither the DWBA nor the 3DW models provide an accurate description over the entire energy range investigated here. At high energies the DWBA model accurately predicts the depth of the minimum at $\varphi = 180°$, but overestimates the width of the distribution. At low energies inclusion of PCI narrows the width around $\varphi = 180°$ so as to be in reasonably good agreement with the data, as is expected. In a similar way, inclusion of PCI for $CH_4$ narrows the width of the distribution. This produces good agreement with the width of the distribution over all energies, although a large peak at $\varphi = 180°$ is predicted that is not observed.

Much better agreement between experiment and theory is found for Ne than $CH_4$. $CH_4$ is clearly a more complex target than neon. This additional complexity is reflected in the evolution of the TDCS with energy. The data for neon shows a double peak at high energies that narrows to a single peak as the energy is lowered. The 3DW calculation shows the same transition, except the single peak occurs at a higher energy than experiment. The TDCS for $CH_4$ also starts with a double peak at high energies. The total angular width of the distribution however remains unchanged until $E_1 = E_2 = 5$ eV at which point the width decreases. The M3DW correctly predicts the width of the peak for

all energies. As the energy is lowered however, the experimental minimum at φ = 180° fills in to yield a broad, flat topped distribution while the M3DW predicts a maximum at φ = 180° which becomes larger with decreasing energy.

The most obvious discrepancy between data and theory is the number of clearly resolved peaks predicted for $CH_4$. The peak at φ = 180° is predicted to be significantly enhanced in the M3DW model in contrast to what is observed. There is perhaps a small triple peak between E=12.5 eV and 7.5 eV in the data, however this is poorly defined. It would be interesting to investigate if the featureless cross section in the data is due to an incoherent summation of cross sections from the different molecular orientations that occur in the experiment, or if it is due to a quantum mechanical effect that is not being reproduced in the theory. To establish this, the model needs to calculate the TDCS for different orientations of the target prior to the collision, and then average the resulting cross sections over all possible orientations of the target. This is a challenging and computationally intensive calculation, however it would provide the most accurate comparison with the data, and would most accurately test the models that are being developed.

In conclusion, it is clear that much has yet to be done to resolve the differences that are seen between theory and experiment at these incident energies. It is important to establish a robust theory for collisions with molecules at these energies since it is here that the cross section for ionization is highest, and so it is in this energy regime where most collisions occur in nature. The contrasts that have been observed between the iso-electronic targets of neon and $CH_4$ show that conclusions can be made about the nature of

the collision for molecular targets. It is clear however that a full calculation that does not include orientation averaging prior to the collision is now required.

## Acknowledgements

This work was supported by the U.S. National Science Foundation (NSF) under Grant. No. PHY-1068237. The author C.N. would like to acknowledge the support of the National Natural Science Foundation of China (NNSFC) under contract No. 10704046. K.L.N. would like to thank the Royal Society for a Newton International Fellowship held at the University of Manchester.

## References

1. O Al-Hagen, C Kaiser, D H Madison and A J Murray, Nature Phys 5 (2009) 59

2. K L Nixon, A J Murray, H Chaluvadi, C Ning and D H Madison, J Chem Phys 134 (2011) 174304

3. A J Murray, B C H Turton and F H Read, Rev Sci Inst 63 (1992) 33465

4. C J Colyer, S M Bellm, B Lohmann, G F Hanne O Al-Hagan, D H Madison, C G Ning, J Chem Phys 133 (2010) 124302

5. C J Colyer, M A Stevenson, O Al-Hagan, D H Madison, C G Ning and B Lohmann, J Phys B 42 (2009) 235207

6. A Naja, E M Staicu-Casagrande, A Lahmam-Bennani, M Nekkab, F Mezdari, B Joulakain, O Chuluunbaatar and D H Madison, J Phys B 40 (2007) 3775

7. K L Nixon, A J Murray, O Al-Hagan, D H Madison and C Ning, J Phys B 43 (2010) 035201

8. L R Hargreaves, M A Stevenson and B Lohmann, Meas Sci Tech 21 (2010) 055112

9. L R Hargreaves, M A Stevenson and B Lohmann, J Phys B 43 (2010) 205202

10. K L Nixon, C Kaiser and A J Murray, J Phys B 43 (2010) 085202

11. J Gao, D H Madison and J L Peacher, J Chem Phys 123 (2005) 204314

12. J Gao, D H Madison and J L Peacher, Phys Rev A 72 (2005) 032721

13. J Gao, D H Madison and J L Peacher, J Chem Phys 123 (2005) 204302

14. C. Lee, W Yang, and R G Parr, Phys Rev B 37 (1988) 785

15. C F Guerra, J G Snijders, G te Velde and E J Baerends Theor Chem Acc 99 (1998) 391

16. S J Ward and J H Macek, Phys Rev A 49 (1994) 1049

17. J B Furness and I E McCarthy, J Phys B 6 (1973) 2280.

18. J P Perdew and A Zunger, Phys Rev B 23 (1981) 5048

19. N T Padial and D W Norcross, Phys Rev A 29 (1984) 1742

20. G Purohit, A S Bhullar and K K Sid, Ind. J Phys B 77 (2003) 177

21. G Wannier, Phys Rev 90 (1953) 817

22. S A C Clarke, T J Reddish, C E Brion, E R Davidson and R F Frey, Chem Phys 143 (1990)

## IV Dynamical (e,2e) studies of tetrahydrofurfuryl alcohol

S M Bellm[1], J D Builth-Williams[1], D B Jones[1], Hari Chaluvadi[2], D H Madison[2], C G Ning[3], F Wang[4], X Ma4, B Lohmann[5] and M J Brunger[1,6]

[1]ARC Centre of Excellence for Antimatter-Matter Studies, Flinders University, GPO Box 2100, Adelaide, South Australia 5001, Australia

[2]Department of Physics, Missouri University of Science and Technology, Rolla, MO 65409, USA

[3]Department of Physics and State Key Laboratory of Low-Dimensional Quantum Physics, Tsinghua University, Beijing 100084, China

[4]Faculty of Life and Social Science, Swinburne University of Technology, P.O. Box 218, Hawthorn, Melbourne, Victoria 3122, Australia

[5]University of the Sunshine Coast, Maroochydore DC, Queensland 4558, Australia

[6]Institute of Mathematical Sciences, University of Malaya, 50603 Kuala Lumpur, Malaysia

### Abstract

Cross section data for electron scattering from DNA is important for modelling radiation damage in biological systems. Triply differential cross sections for the electron impact ionization of the highest occupied outer valence orbital of tetrahydrofurfuryl alcohol, which can be considered as an analogue to the deoxyribose backbone molecule in DNA, have been measured using the (e,2e) technique. The measurements have been

performed with coplanar asymmetric kinematics at an incident electron energy of 250 eV, an ejected electron energy of 20 eV and at scattered electron angles of -5$^o$, -10$^o$ and -15$^o$. Experimental results are compared with corresponding theoretical calculations performed using the molecular 3-body distorted wave (M3DW) model. Some important differences are observed between the experiment and calculations.

## Introduction

In recent years, extensive research has been undertaken into the study of radiation damage in biomolecular systems[1,2]. Monte Carlo track structure simulations are a useful tool to map the path along which primary and secondary species travel as they pass through a biological medium. Such simulations call for a complete set of differential cross sections for both the primary particles and target materials and the secondary particles that are generated. Most track structure simulations focus on water[3,4] as it is the predominant species in living organisms. However, in order to describe the process in a more complete way, the contribution from other species present should also be included in these models[5].

The data obtained by experimentally measuring selected cross sections provides an important means of testing the theoretical calculations which are used to derive the extensive cross section data needed as input in radiation damage models. In the (e,2e) technique, a projectile electron with well-defined energy and momentum ionizes an atomic or molecular target. The scattered projectile and ejected target electron are detected in time coincidence with their energies and momenta determined, yielding a multiply-differential cross section termed the triple differential cross section (TDCS).

Depending on the kinematics employed, the method can be used to determine information about the ionization dynamics of the atomic and molecular targets[6] as well as

to reveal details about the bound electronic structure of the target. In the latter case the kinematics are usually known as electron momentum spectroscopy (EMS)[7]. Both theoretical and experimental dynamical (e,2e) studies on molecules are comparatively scarce, as a result of some of the considerable challenges involved. For theory these include the description of a multi-centred target, and for experiment the difficulties in resolving different molecular states which are often very closely spaced in energy. We note that while measuring cross sections for isolated molecules in the gas phase, as in the present measurements, can only approximate what occurs in biological systems, it has nonetheless been shown to be a useful initial approach[8-10].

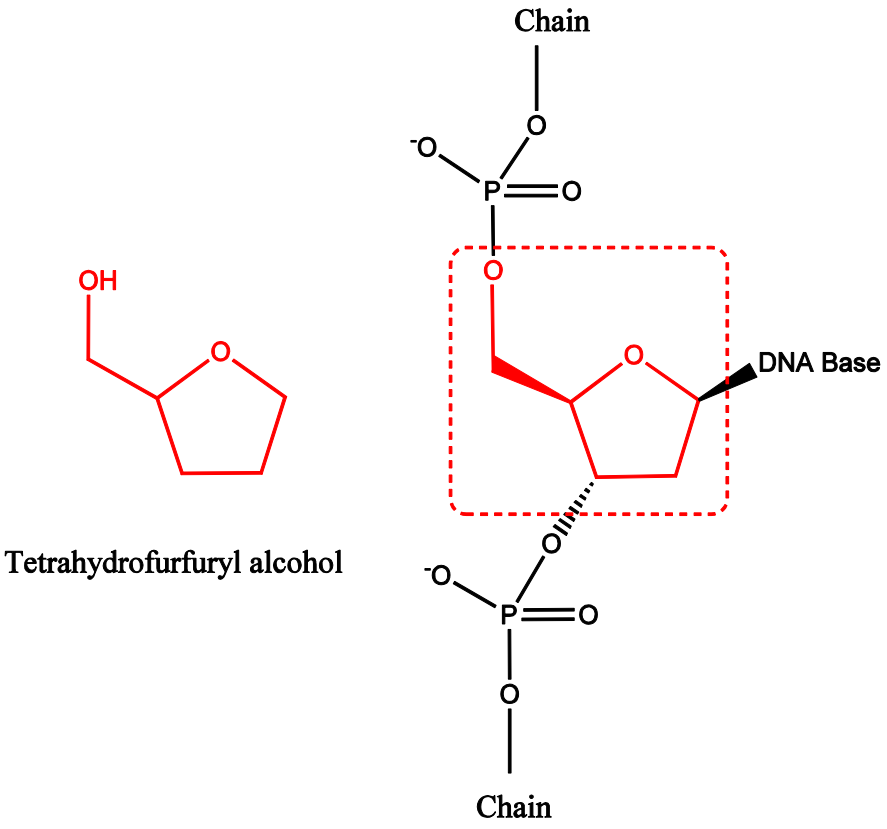


Figure 1.The structure of the THFA molecule and a segment of the sugar-phosphate backbone of a single strand of DNA.

The sugar deoxyribose is an important molecule in biomolecular systems. Indeed, the sugar-phosphate backbone which is the major structural component in DNA is formed by alternating deoxyribose sugar and phosphate groups as is shown schematically in Figure 1. Thus, largely due to the biological significance of deoxyribose, a number of studies have been undertaken to investigate electron interactions with the deoxyribose analogue molecules: tetrahydrofuran (THF), tetrahydrofurfuryl alcohol (THFA) and 3-hydroxytetrahydrofuran (3HTHF). These include measurements of elastic differential cross-sections (DCS's) for THF,[11-14] THFA[15] and 3HTHF[16,17]. Total cross sections for electron and positron scattering from THF,[18-20] 3HTHF,[21] and THFA[22,23] (Refs. 22 and 23) have also been measured. Triple-differential cross sections, however, provide the most complete information about the details of the ionization of atomic and molecular targets, which is essential to modelling the deposition of energy in biological matter. Triply differential cross-sections (TDCS's) have recently been measured for THF using the (e,2e) technique[24]. To the best of our knowledge the present data are, however, the first TDCS's reported for electron impact ionization of THFA.

The structure of the paper is as follows. In the next Section we describe our experimental apparatus and measurement techniques. Thereafter, in Section experimental apparatus, some details pertaining to the current theoretical computations are provided. In Section results and discussions we present our results and a discussion of those results, before some conclusions from the present investigations are drawn.

## Experimental Appartus

Triple differential cross section measurements were performed in coplanar asymmetric geometry using a conventional coincidence spectrometer. As the

experimental apparatus has been described in detail in Refs. 24 and 25, only a brief description will be provided here.

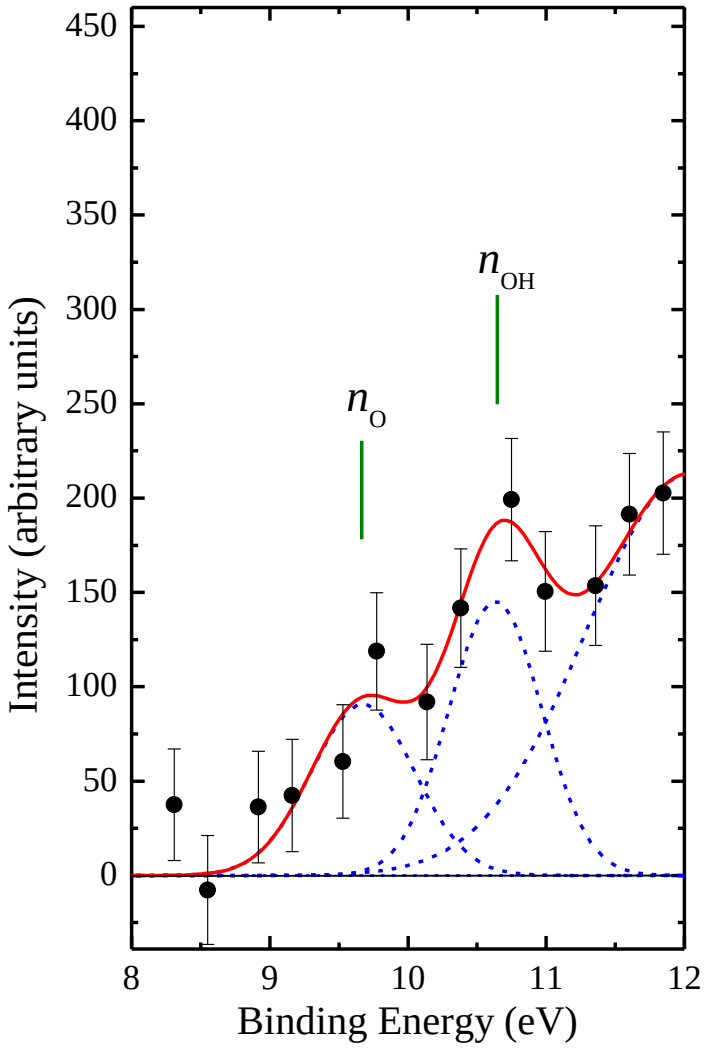


Figure 2. Measured binding energy spectrum for the outer valence region of THFA showing the HOMO (28a) and NHOMO (27a). The data have been fitted with a sum of Gaussian functions, using a convolution of the coincidence binding energy resolution and the vibrationally broadening width of the molecular orbitals to define the peak width parameters.

Electrons are produced by thermionic emission from a tungsten filament. Five cylindrical electrostatic lens elements are used to collimate and transport the electrons to the interaction region. The resulting electron beam energy resolution is approximately 0.5 eV (FWHM). The electron beam then crosses a molecular target beam formed by the effusion of THFA molecules through a 0.7 mm internal diameter stainless steel capillary.

THFA is a liquid with a relatively low vapour pressure at room temperature; however, it still has sufficient vapour pressure to perform our measurements without directly heating the sample. The THFA sample 99% (Sigma-Aldrich, Australia) was treated with several freeze-pump-thaw cycles prior to use to remove absorbed gases. To prevent possible condensation of THFA within the sample lines, which may contribute to instability in the rate of flow of the sample into the vacuum chamber, the sample lines and vacuum chamber were heated to approximately $40^{o}$C throughout the measurements.

For the present measurements, the gas capillary and hence the molecular target beam is oriented perpendicular to the scattering plane, which is defined by the momentum vectors of the incident and measured outgoing electrons. The higher energy (scattered) and lower energy (ejected) outgoing electrons are both detected in hemispherical electron energy analysers, each comprising a 5-element electrostatic entrance lens system, hemispherical selector and channel electron multiplier detector. The two electron energy analysers are mounted on independently rotatable turntables concentric with the interaction region. Coincidence timing procedures[26] are used to identify, from the relative arrival times of the electrons at the two detectors, if the two detected electrons are correlated and originate from the same scattering event. Background events are subtracted using standard statistical methods. The detection

energies of the hemispherical electron energy analyzers have been calibrated using the $L_{2,3}M_{2,3}M_{2,3}$ Auger spectrum of argon,[27] whilst the angular calibration of the analyzers has been determined using the well-defined minimum in the differential cross section for elastic scattering of 60 eV electrons from argon.[28]

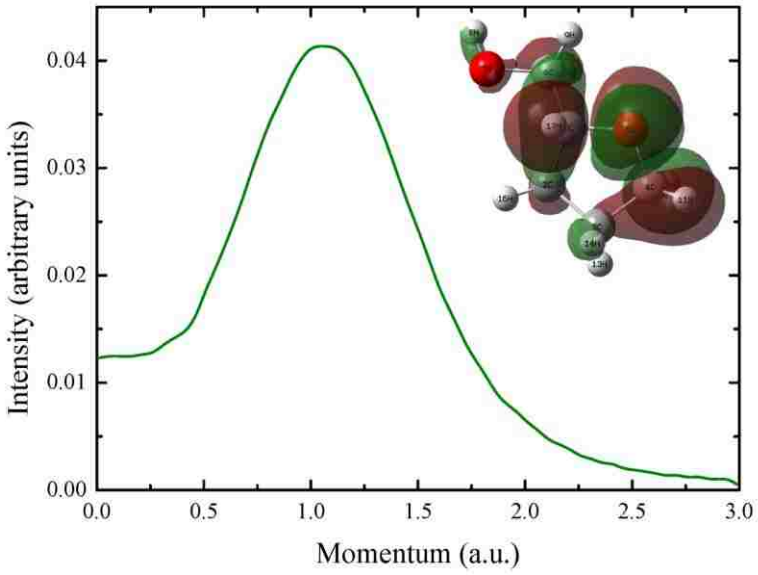


Figure 3. The momentum density probability distribution for the HOMO of THFA and the molecular orbital electron density distribution for the HOMO (inset).

In dynamical TDCS measurements, the scattered electron is detected at a fixed forward angle ($\theta_a$) with respect to the incident electron beam direction, while ejected electron angular distributions are measured by scanning the ejected electron energy analyser and detecting electrons at a number of different ejected electron angles ($\theta_b$) within the scattering plane. The experiments were performed at an incident electron energy of 250 eV and an ejected electron energy of 20 eV. The energy of the scattered electron is determined by conservation of energy such that:

$$E_i = E_a + E_b + \varepsilon_b \quad (1)$$

where $E_i$, $E_a$ and $E_b$ are the kinetic energies of the incident, scattered and ejected electrons, respectively, and $\varepsilon_b$ is the binding energy of the orbital that is ionized.

The TDCS is represented by:

$$\frac{d^5\sigma}{d\Omega_a d\Omega_b dE_b} \quad (2)$$

and it is a measure of the probability that after ionization of a target species by a projectile with energy $E_i$ and momentum $\mathbf{k}_i$, two electrons will be produced with energies $E_a$ and $E_b$ and momenta $\mathbf{k}_a$ and $\mathbf{k}_b$ into the solid angles $\Omega_a$ and $\Omega_b$. The momentum transferred to the target is:

$$\mathbf{K} = \mathbf{k}_i - \mathbf{k}_a . \quad (3)$$

To establish that the instrument was functioning correctly, the TDCS for the ionization of the helium 1s orbital was measured and compared to convergent close coupling (CCC) calculations under the same kinematics[29], which are known to produce accurate results.

## Theoretical Framework

### A. Valence ionization energies and momentum profiles

Quantum mechanical calculations have been undertaken of the momentum profile of the highest occupied molecular orbital (HOMO) of THFA. The chemical structure of THFA is indicated in Fig. 1. Geometry optimizations were performed using the hybrid density functional theory (DFT) model of B3LYP/DGTZVP[30,31]. The DGTZVP basis set of Godbout *et al* [32] has been proven to be a good basis set for orbital momentum distribution calculations[33], which can also be applied to larger molecules[34]. The ionization potential energies of THFA are calculated using the outer valence Green

function OVGF/DGTZVP model. The $i^{th}$ momentum-space wave function $\Phi_i(\mathrm{p})$ of THFA is produced according to the Dirac transformation theory[30], in which the electrons in the $i^{th}$ molecular orbital can be transformed from the coordinate space representation

$$\Phi_i(p,\theta) = (2\pi)^{-3/2} \int_r \exp(-i\vec{\mathrm{p}} \cdot \vec{\mathrm{r}}) \psi_i(\vec{\mathrm{r}}) d\vec{\mathrm{r}} \,. \tag{4}$$

Here the coordinate space wave function $\psi_i(\mathrm{r})$ is obtained within a Kohn-Sham orbital approximation from electronic structure calculations employing the B3LYP/DGTZVP model using the GAUSSIAN 09 computational chemistry package[35]. The momentum profile $\rho(p)$ is then generated by averaging the orbital density over the unknown orientation of the molecule

$$\rho(p) = \int \Phi_i(\vec{p})^* \Phi_i(\vec{p}) d\Omega, \tag{5}$$

**B. Triple differential cross sections**

The molecular 3-body distorted wave (M3DW) approximation has also been presented in previous publications[36-38], so only a brief outline of the theory will be presented. The TDCS for the M3DW is giving by:

$$\frac{d^5\sigma}{d\Omega_a d\Omega_b dE_b} = \frac{1}{(2\pi)^5} \frac{k_a k_b}{k_i} \left( |T_{dir}|^2 + |T_{exc}|^2 + |T_{dir} - T_{exc}|^2 \right), \tag{6}$$

where $\vec{k}_i$, $\vec{k}_a$, and $\vec{k}_b$ are the wave vectors for the initial, scattered and ejected electrons, $T_{dir}$ is the direct scattering amplitude, and $T_{exc}$ is the exchange amplitude. The direct scattering amplitude is given by:

$$T_{dir} = \left\langle \chi_a^-(\vec{k}_a, \mathbf{r}_1) \chi_b^-(\vec{k}_b, \mathbf{r}_2) C_{scat-eject}(r_{12}^{ave}) \,|\, V - U_i \,|\, \phi_{DY}^{OA}(\mathbf{r}_2) \chi_i^+(\vec{k}_i, \mathbf{r}_1) \right\rangle. \tag{7}$$

Here $r_1$ and $r_2$ are the coordinates of the incident and the bound electrons, $\chi_i, \chi_a,$ and $\chi_b$ are the distorted waves for the incident, scattered and ejected electrons, respectively, and $\phi_{DY}^{OA}(r_2)$ is the initial bound-state Dyson molecular orbital averaged over all orientations. Under the frozen orbital approximation, Dyson orbital can be well approximated using the initial bound Kohn-Sham orbital. The molecular wave functions were calculated using DFT along with the standard hybrid B3LYP (Ref. 31) functional by means of the ADF 2007 (Amsterdam Density Functional) program[39] with the TZ2P (triple-zeta with two polarization functions) Slater type basis sets. The factor $C_{scat-eject}(r_{12}^{ave})$ is the Ward-Macek average Coulomb-distortion factor between the two final state electrons,[40] $V$ is the initial state interaction potential between the incident electron and the neutral molecule, and $U_i$ is a spherically symmetric distorting potential which is used to calculate the initial-state distorted wave for the incident electron $\chi_i^+(\vec{k}_i, \mathbf{r}_1)$. For the exchange amplitude $T_{exc}$, particles 1 and 2 are interchanged in eq. (7).

The Schrödinger equation for the incoming electron wave-function is given by:

$$(T + U_i - \frac{k_i^2}{2})\chi_i^+(\vec{k_i}, r) = 0 \quad , \qquad (8)$$

where $T$ is the kinetic energy operator and the '+' superscript on $\chi_i^+(\vec{k}_i, \mathbf{r})$ indicates outgoing wave boundary conditions. The initial state distorting potential contains three components $U_i = U_s + U_E + U_{CP}$, where $U_s$ contains the nuclear contribution plus a spherically symmetric approximation for the interaction between the projectile electron and the target electrons which is obtained from the quantum mechanical charge density of the target. The nuclear contribution to $U_s$ is the interaction between the projectile

electron and all the 17 nuclei averaged over all orientations. Averaging the nuclei over all orientations is equivalent to putting the nuclear charge on a thin spherical shell whose radius is the distance of the nuclei from the center of mass (CM). For THFA, there is no nucleus at the CM and the closest nucleus to the CM is a carbon at 1.15 $a_0$ from the CM. Consequently, the first nuclear sphere has a charge of 6 with a radius of 1.15 $a_0$. The next sphere is another carbon atom with charge 6 and a radius of 2.24 $a_0$, while the following sphere is an oxygen atom with charge 8 and a radius of 2.61 $a_0$. This process continues for the 17 nuclei and the last one is a hydrogen atom with charge 1 and a radius of 6.53 $a_0$.

$U_E$ is the exchange potential of Furness-McCarthy (corrected for sign errors)[41] which approximates the effect of the continuum electron exchanging with the passive bound electrons in the molecule, and $U_{CP}$ is the correlation-polarization potential of Perdew and Zunger[42,43].

The final state for the system is approximated as a product of distorted waves for the two continuum electrons times the average Coulomb-distortion factor. The final state distorted waves are calculated as the initial state except that the final state spherically symmetric static distorting potential for the molecular ion is used for $U_s$.

Results are presented for the M3DW described above as well, as the standard DWBA (distorted wave Born approximation). The DWBA is identical to the M3DW except that the PCI (post collision interaction) term, $C_{scat-eject}(r_{12}^{ave})$, is omitted in the evaluation of the direct and exchange amplitudes.

## Results and Discussion

Figure 2 shows the measured binding energy spectrum for the outer valence region of THFA. The incident electron energy was 250 eV. Ejected electrons were detected at an energy of 20 eV, while the energy of the scattered electrons was varied. The scattered and ejected electrons were detected at fixed angles of $-10^{o}$ and $90^{o}$, respectively. The instrumental binding energy resolution under the chosen conditions was estimated to be 1.1 eV FWHM, from the width of the helium 1s binding energy peak measured under the same kinematics. The binding energy spectrum has been fitted with a sum of three Gaussian functions of fixed width. As the instrumental binding energy resolution is comparable to the natural line width of the orbitals observed in photoelectron spectra of THFA[44], the width of the individual peaks in the Gaussian fitting was determined by adding the coincidence resolution and the natural widths of each molecular orbital in quadrature.

A THFA molecule contains a five membered heterocyclic furanose ring which undergoes pseudorotation. This is an internal motion that involves out-of-plane ring puckering vibrations which occur in a way that makes the phase of the puckering rotate about the ring.[45] Twenty possible conformations of THFA may be produced through pseudorotation in the gas phase.[46] The molecular structure of THFA in the gas phase has been investigated by electron diffraction and ab initio methods,[46] which suggested the presence of two conformers with abundances of 84 ± 8% and 16 ± 8%. Hence in practice the population of our THFA beam is essentially dominated by one conformer. In the most stable conformers the O-H group is directed toward the ring oxygen and seems to be stabilised by hydrogen bonding.

The HOMO 28a, appears at an electron binding energy of 9.6 ±0.6 eV, 0.9 eV lower in energy than the next highest occupied molecular orbital (NHOMO). With our coincidence energy resolution, we are unable to completely resolve the HOMO from the NHOMO (see Fig. 2). The present results are in good agreement with the appearance energy measured for the THFA parent cation of $9.43 \pm 0.12$ eV[47] and with previous photoelectron spectroscopy measurements[44]. The HOMO and NHOMO correspond to ionization from the ether $(n_0)$ and hydroxyl $(n_{OH})$ oxygen lone pair orbitals, respectively[44].

The calculated momentum density probability distribution for the HOMO of THFA is presented in Figure 3. The profile suggests that the HOMO of THFA is predominantly a p-type molecular orbital. The inset in Fig. 3 shows the orbital electron density distribution for the HOMO (28a) and also indicates that the HOMO of THFA is dominated by out-of-plane contributions of 2p electrons from atoms on the ring. Such a p-type orbital would normally lead us to anticipate the binary peak in our TDCS possessing a double lobe structure. However, Figure 3 does suggest a quite significant intensity at small momenta which, if due to some sort of s-p hybridisation, might complicate the situation.

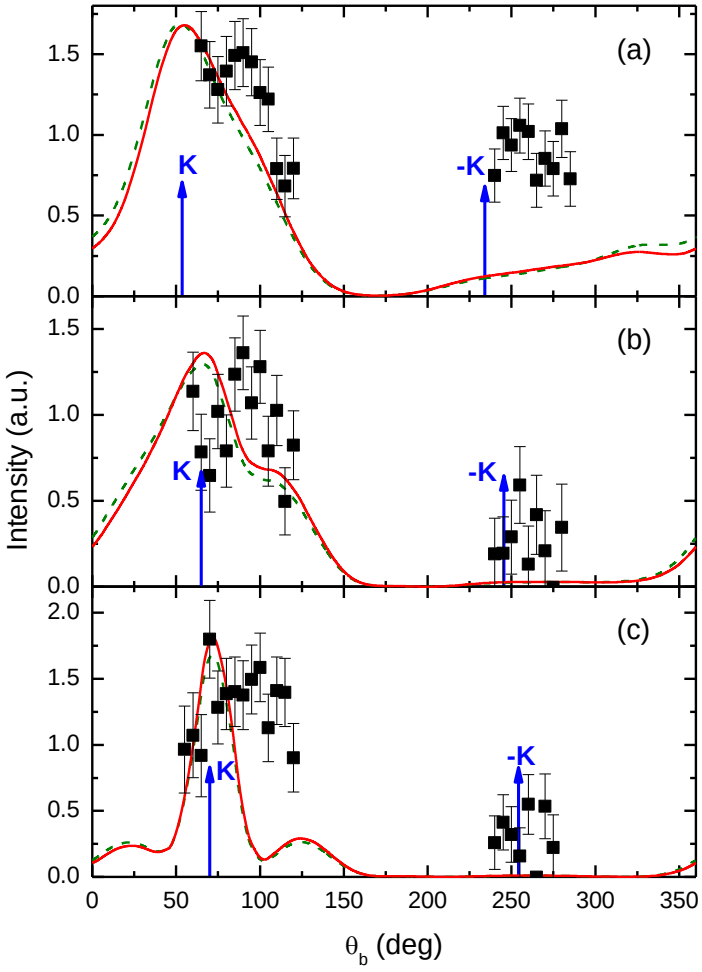


Figure 4. The triple differential cross sections for ionization of the HOMO of THFA with $E_0$=250 eV and $E_b$=20 eV. The scattered electron detection angles and corresponding momentum transfers are (a) –5°, |K|=0.45 au, (b) –10°, |K|=0.77 au and (c) –15°, |K|=1.12 au. The positions of the momentum transfer vector, +K, and –K are indicated by the arrows. Points are the experimental data. Solid curve (red): M3DW calculation for the HOMO. Dashed curve (green) DWBA calculation for the HOMO (see text for details).

Figures 4(a)-(c) show the present experimental and theoretical TDCS results for the HOMO of THFA. The relatively large error bars on the experimental data result from the small magnitude of the coincidence cross section. Traditionally the angular distributions are divided into two regions, the binary region ranging from 0° to 180° and

the recoil region which ranges from 180° to 360°. In the binary region, structure is attributed to single binary collisions and depending upon the kinematics, may contain strong signatures of the orbital structure[48]. In contrast, in the recoil region structure arises from processes in which the ejected electron produced by an initial binary collision undergoes subsequent recoil scattering from the target nucleus. The distributions have a binary lobe centred close to the momentum transfer direction (+**K**) and a recoil lobe pointing in the opposite direction (–**K**). Coulomb repulsion between the final state electrons causes a slight shift of the binary peak, to larger scattering angles, away from the momentum transfer direction

Two theoretical calculations are presented in Fig. 4. The solid line (red) denotes the M3DW calculation and the dashed (green) line the DWBA calculation. As the experimental data are only relative they are attributed absolute values by normalization to the M3DW theory to give the best visual fit in the binary peak region. Measuring absolute TDCS data is not a straightforward process[49,50]. Although a relatively simple method for absolute (e,2e) measurements was recently described in the literature[50], due to the high density of molecular orbitals here, such measurements would be very difficult to apply to a target like THFA. The main difference between the M3DW and DWBA calculations is that the PCI between the scattered and ejected electrons is not included in the evaluation of the direct and exchange amplitudes in the DWBA calculation. However, there appears very little difference between the two calculations suggesting that the inclusion of PCI in the model is relatively unimportant under these kinematics.

The size of the recoil peak for the scattered electron angles of $-10^{o}$ and $-15^{o}$ in Fig. 4(b) and 4(c) is small, indicating that there is not a large amount of interaction of the

ejected electron with the molecular ion. The recoil peak at the scattered electron angle of -5$^o$ is greater in magnitude relative to the binary peak, both in the experimental data and theoretical calculations. However, the theory does significantly underestimate the recoil intensity here as well as at both the other scattered electron angles investigated, which is likely due to insufficient weak nuclear scattering being included in the calculations. This is caused by spreading the nuclear charge over a spherical shell when averaging the nuclei over all orientations, resulting in a nuclear interaction that is too weak.

Table 1. Ionization energies for the outer valence region of THFA. Calculations have been performed using the OVGF/DGTZVP model. The spectroscopic pole strength for each orbital is given in parentheses. The error in the ionization energy for the present experimental data is ±0.6 eV. The PES data are from Ibanescu *et al.*[45]

| Orbital | OVGF/DGTZVP (eV)[a] | Present results (eV) | PES (eV) (Ref. 45) |
|---|---|---|---|
| 28a | 9.79 (0.91) | 9.8 | 9.81 |
| 27a | 10.93 (0.91) | 10.7 | 10.60 |
| 26a | 11.47 (0.91) | | |
| 25a | 11.86(0.91) | | |
| 24a | 12.09 (0.91) | | |
| 23a | 12.41 (0.91) | | |
| 22a | 13.24 (0.91) | | |
| 21a | 14.03 (0.91) | | |
| 20a | 14.37 (0.91) | | |
| 19a | 14.65 (0.90) | | |
| 18a | 15.62 (0.91) | | |
| 17a | 16.39 (0.90) | | |

The binary peak in the experimental data shown in Fig. 4(b) for the scattered electron angle of -10$^o$ shows the suggestion of a dip in the distribution around the momentum transfer direction. As double peak structures are characteristic of ionization of atomic p-states, the dip in the distribution suggests that this structure may result from ionization of p-type orbitals. This is consistent with the HOMO being largely a p-type

molecular orbital as is indicated by the momentum density probability distribution in Fig. 3. However, the dip is not particularly evident in Fig. 4(c) at the scattered electron angle of -15$^{o}$ where it might be expected to be more pronounced as it is closer to Bethe ridge kinematics. On the Bethe ridge, the kinematics satisfy the requirement that all momentum is transferred to the bound, target electron during the collision and the ion essentially acts as a spectator. We previously suggested that the small recoil peak intensity observed for some molecular targets, in particular CHCOOH and THF, relative to H2O was due to the lack of a charge center at the molecule's center of mass.[24, 52] An alternative explanation has been proposed by Xu et al.,[53] which is that rather than being related to the geometry of the target this observation more simply results from the momentum profile of the orbitals investigated and the kinematics being close to the Bethe ridge. Following from this argument, as a consequence of the momentum profile of the HOMO of THFA having non-zero intensity at zero momentum (see Fig. 3), in the region of the Bethe ridge the recoil peak intensity should be relatively small. This is similar to the HOMO for CHOOH and THF which also have momentum profiles with significant non-zero intensity at zero momentum.[54, 55] In contrast, the very strongly p-like momentum profiles[56] investigated for H2O exhibit a much larger recoil peak relative to the binary peak.[57]

The M3DW and DWBA calculations show a multi-peaked structure in the binary region in Fig. 4(c), with a narrow binary peak centred close to +**K** and two smaller shoulders. The calculated binary peaks in Fig. 4(a) and Fig. 4(b), while much broader than that in 4(c,) are still centred close to +**K**. In contrast the experimental binary peaks appear shifted to significantly larger ejected electron emission angles. As noted earlier, we are unable to completely resolve the HOMO from the NHOMO so that some

inconsistency between theory and experiment may arise from contributions from the NHOMO to the measured TDCS.

The binary peaks in the present experimental measurements appear quite broad, which appears to be characteristic of TDCS measurements for a number of molecular targets. Comparably broad binary peaks have also been observed in experimental studies for molecules including water[51], formic acid[52], methane[53] and nitrogen[54] under similar kinematics. Broad binary peaks were also observed for TDCS measurements of the HOMO of THF[24]. Note that THF and THFA are very similar in structure. Both are five membered heterocyclic ether compounds and in THFA, a hydrogen atom on the alpha-carbon is substituted by a $CH_2OH$ group. Interestingly much narrower binary peaks have been observed both for ionization of the HOMO in pyrimidine[55] and for the inner valence orbitals thymine[56], again under similar kinematics. This observation is possibly related to the structure of the molecular rings in pyrimidine and thymine, which are both six membered ring type structures. Pyrimidine belongs to the group of diazines and contains two nitrogen atoms which are located at the meta- positions in the ring and thymine is a pyrimidine derivative.

## Conclusions

We have presented experimental and theoretical TDCS measurements for THFA, which is an important analogue molecule for the deoxyribose molecule found in DNA. The measured binding energies are in good agreement with previous PES data and quantum chemical calculations. The measured TDCSs at all three scattered electron detection angles investigated exhibit a quite broad binary peak, with only a suggestion for the double-lobed structure we anticipated from a p-type orbital. Although the theoretical width of the binary peak was quite broad and similar to the experimental data for electron

detection angles of $-5^0$ and $-10^0$, for $-15^o$ theory is significantly narrower than the experimental measurements. The TDCSs at scattered electron detection angles of $-15^o$ and $-10^o$ showed a small recoil peak relative to the magnitude of the binary peak, indicating that there is very little interaction between the ejected electron and the target ion under these kinematical conditions. In contrast at $-5^o$ there is considerable intensity in the recoil peak. Only a small difference was observed between the M3DW and DWBA calculations, suggesting that post collision interaction effects were unimportant in the kinematical conditions of this investigation. While our theory indicates that PCI effects are unimportant here, the shift in the binary peak away from K in our experimental data might suggest that PCI is in fact playing a role in the collision dynamics. Further investigation into this apparent contradiction is needed.The calculations significantly underestimated the recoil peak intensity observed at all scattered electron detection angles studied, which is attributed to spreading of the nuclear charge over a spherical shell leading to a nuclear interaction that is too weak. The calculations performed within the M3DW model were generally in satisfactory agreement with the experimental data. which is perhaps not surprising given the complexity of the molecular target and the inability to completely resolve the HOMO from the NHOMO in the experimental measurements. Further work is needed to probe the discrepancies highlighted above.

## Acknowledgements

This work was supported by the Australian ResearchCouncil Centre of Excellence for Antimatter-Matter Studies, an Australian Research Council Discovery Project grant and by the U.S. National Science Foundation (NSF) under Grant. No. PHY-1068237. The author C.N. would like to acknowledge the support of the National Natural Science

Foundation of China (NNSFC) under Contract No. 10704046. One of us (M.J.B.) also thanks the University of Malaya for his "Distinguished Visiting Professor" appointment. F.W. acknowledges the National Computational Infrastructure (NCI) at the Australian National University for an award under the "Merit Allocation Scheme" for supercomputing facilities.

## References

1. L. Sanche, Eur. Phys. J. D 35, 367 (2005).

2. L. Sanche, Mass Spectrom. Rev. 21, 349 (2002).

3. A. Munoz, F. Blanco, G. Garcia, P. A. Thorn, M. J. Brunger, J. P. Sullivan, and S. J. Buckman, Int. J. Mass. Spectrom. 277, 175 (2008).

4. A. G. Sanz, M. C. Fuss, A. Munoz, F. Blanco, P. Limao-Vieira, M. J. Brunger, S. J. Buckman, and G. Garcia, Int. J. Radiat. Biol. 88, 71 (2012).

5. M. U. Bug, W. Y. Baek, and H. Rabus, Int. J. Radiat. Biol. 88, 137 (2012).

6. A. Lahmam-Bennani, J. Phys. B 24, 2401 (1991).

7. I. E. McCarthy and E. Weigold, Rep. Prog. Phys. 51, 299 (1988).

8. S. Ptasinska, S. Denifl, P. Scheier, and T. D. Mark, J. Chem. Phys. 120, 8505 (2004).

9. P. Swiderek, Angew. Chem., Int. Ed. 45, 4056 (2006).

10. R. D. White and R. E. Robson, Phys. Rev. Lett. 102, 230602 (2009).

11. A. R. Milosavljevic, A. Giuliani, D. Sevic, M. J. Hubin-Franskin, and B. P. Marinkovic, Eur. Phys. J. D 35, 411 (2005).

12. C. S. Trevisan, A. E. Orel, and T. N. Rescigno, J. Phys. B 39, L255 (2006).

13. M. G. P. Homem, R. T. Sugohara, I. P. Sanches, M. T. Lee, and I. Iga, Phys. Rev. A 80, 032705 (2009).

14. C. J. Colyer, V. Vizcaino, J. P. Sullivan, M. J. Brunger, and S. J. Buckman, New J. Phys. 9, 41 (2007).

15. A. R. Milosavljevic, F. Blanco, D. Sevic, G. Garcia, and B. P. Marinkovic, Eur. Phys. J. D 40, 107 (2006).

16. V. Vizcaino, J. Roberts, J. P. Sullivan, M. J. Brunger, S. J. Buckman, C. Winstead, and V. McKoy, New J. Phys. 10, 053002 (2008).

17. A. R. Milosavljevic, F. Blanco, J. B. Maljkovic, D. Sevic, G. Garcia, and B. P. Marinkovic, New J. Phys. 10, 103005 (2008).

18. A. Zecca, C. Perazzolli, and M. J. Brunger, J. Phys. B 38, 2079 (2005).

19. P. Mozejko, E. Ptasinska-Denga, A. Domaracka, and C. Szmytkowski, Phys. Rev. A 74, 012708 (2006).

20. M. Fuss, A. Munoz, J. C. Oller, F. Blanco, D. Almeida, P. Limao-Vieira, T. P. D. Do, M. J. Brunger, and G. Garcia, Phys. Rev. A 80, 052709 (2009).

21. A. Zecca, L. Chiari, A. Sarkar, and M. J. Brunger, J. Phys. B 41, 085201 (2008).

22. P. Mozejko, A. Domaracka, E. Ptasinska-Denga, and C. Smytkowski, Chem. Phys. Lett. 429, 378 (2006).

23. A. Zecca, L. Chiari, G. Garcia, F. Blanco, E. Trainotti, and M. J. Brunger, New J. Phys. 13, 115001 (2011).

24. C. J. Colyer, S. M. Bellm, B. Lohmann, G. F. Hanne, O. Al-Hagan, D. H. Madison, and C. G. Ning, J. Chem. Phys. 133, 124302 (2010).

25. S. J. Cavanagh and B. Lohmann, J. Phys. B 32, L261 (1999).

26. E. Weigold and I. E. McCarthy, Electron Momentum Spectroscopy (Plenum, New York, 1999).

27. L. O. Werme, T. Bergmark, and K. Siegbahn, Phys. Scr. 8, 149 (1973).

28. R. Panajotovic, D. Filipovic, B. Marinkovic, V. Pejcev, M. Kurepa, and L. Vuskovic, J. Phys. B 30, 5877 (1997).

29. I. Bray, personal communication (2011).

30. A. D. Becke, J. Chem. Phys. 98, 5648 (1993).

31. C. Lee, W. Yang, and R. G. Parr, Phys. Rev. B 37, 785 (1988).

32. N. Godbout, D. R. Salahub, J. Andzelm, and E. Wimmer, Can. J. Chem.70, 560 (1992).

33. F. Wang, J. Phys. Chem. A 107, 10199 (2003).

34. A. Ganesan, F. Wang, and C. Falzon, J. Comput. Chem. 32, 525 (2011).

35. M. J. Frisch, G. W. Trucks, H. B. Schlegel et al., GAUSSIAN 09, Revision A.02, Gaussian, Inc., Wallingford, CT, 2009.

36. J. F. Gao, D. H. Madison, and J. L. Peacher, J. Chem. Phys. 123, 204314 (2005).

37. J. F. Gao, D. H. Madison, and J. L. Peacher, Phys. Rev. A 72, 032721 (2005).

38. J. F. Gao, J. L. Peacher, and D. H. Madison, J. Chem. Phys. 123, 204302 (2005).

39. C. F. Guerra, J. G. Snijders, G. te Velde, and E. J. Baerends, Theor. Chem. Acc. 99, 391 (1998).

40. S. J. Ward and J. H. Macek, Phys. Rev. A 49, 1049 (1994).

41. J. B. Furness and I. E. McCarthy, J. Phys. B 6, 2280 (1973).

42. J. P. Perdew and A. Zunger, Phys. Rev. B 23, 5048 (1981).

43. N. T. Padial and D. W. Norcross, Phys. Rev. A 29, 1742 (1984).

44. D. H. Madison and O. Al-Hagan, Journal of Atomic, Molecular, and Optical Physics 2010, 367180 (2010).

45. B. C. Ibanescu, O. May, A. Monney, and M. Allan, Phys. Chem. Chem.Phys. 9, 3163 (2007).

46. D. O. Harris, G. G. Engerholm, C. A. Tolman, A. C. Luntz, R. A. Keller, H. Kim, and W. D. Gwinn, J. Chem. Phys. 50, 2438 (1969).

47. K. B. Borisenko, S. Samdal, I. F. Shishkov, and L. V. Vilkov, J. Mol. Struct. 448, 29 (1998).

48. A. R. Milosavljevic, J. Kocisek, P. Papp, D. Kubala, B. P. Marinkovic, P.Mach, J. Urban, and S. Matejcik, J. Chem. Phys. 132, 104308 (2010).

49. H. Ehrhardt, K. Jung, G. Knoth, and P. Schlemmer, Z. Phys. D 1, 3 (1986).

50. A. Lahmam-Bennani, M. Cherid, and A. Duguet, J. Phys. B 20, 2531 (1987).

51. L. R. Hargreaves, M. A. Stevenson, and B. Lohmann, Meas. Sci. Technol.21, 055112 (2010).

52. C. J. Colyer, M. A. Stevenson, O. Al-Hagan, D. H. Madison, C. G. Ning, and B. Lohmann, J. Phys. B 42, 235207 (2009).

53. S. Xu, X. Ma, S. Yan, and P. Zhang, J. Chem. Phys. 136, 237101 (2012).

54. K. L. Nixon, W. D. Lawrance, and M. J. Brunger, Chem. Phys. Lett. 474, 23 (2009).

55. C. G. Ning, Y. R. Huang, S. F. Zhang, J. K. Deng, K. Liu, Z. H. Luo, and F. Wang, J. Phys. Chem. A 112, 11078 (2008).

56. R. Cambi, G. Ciullo, A. Sgamellotti, C. E. Brion, J. P. D. Cook, I. E. McCarthy, and E. Weigold, Chem. Phys. 91, 373 (1984).

57. D. S. Milne-Brownlie, S. J. Cavanagh, B. Lohmann, C. Champion, P. A. Hervieux, and J. Hanssen, Phys. Rev. A 69, 032701 (2004).

58. A. Lahmam-Bennani, A. Naja, E. M. S. Casagrande, N. Okumus, C. Dal Cappello, I. Charpentier, and S. Houamer, J. Phys. B 42, 165201 (2009).

59. A. Naja, E. M. Staicu-Casagrande, A. Lahmam-Bennani, M. Nekkab, F. Mezdari, B. Joulakian, O. Chuluunbaatar, and D. H. Madison, J. Phys. B 40, 3775 (2007).

60. J. D. Builth-Williams, S. M. Bellm, D. B. Jones, H. Chaluvadi, D. H. Madison, C. G. Ning, B. Lohmann, and M. J. Brunger, J. Chem. Phys.136, 024304 (2012).

61. S. M. Bellm, C. J. Colyer, B. Lohmann, and C. Champion, Phys. Rev. A 85, 022710 (2012).

## V Low energy (e, 2e) study from the $1t_2$ orbital of $CH_4$

S. Xu,[1,2] Hari Chaluvadi,[3] X. Ren,[2] T. Pflüger,[2] A. Senftleben,[2] C. G. Ning4, S. Yan,[1] P. Zhang,[1] J. Yang,[1] X. Ma,[1] J. Ullrich,[2,5] D. H. Madison[3] and A. Dorn[2]

[1]Insititute of Modern Physics, Chinese Academy of Sciences, Lanzhou 730000, China

[2]Max-Planck-Institut für Kernphysik, Saupfercheckweg1, 69117 Heidelberg, Germany

[3]Department of Physics, Missouri University of Science and Technology, Rolla, Missouri 65409, USA

[4]Department of Physics and State Key Laboratory of Low-Dimensional Quantum Physics, Tsinghua University,Beijing 100084, China

[5]Physikalisch-Technische Bundesanstalt, Bundesallee 100, 38116 Braunschweig, Germany

### Abstract

Single ionization of the methane ($CH_4$) $1t_2$ orbital by 54eV electron impact has been studied experimentally and theoretically. The measured triple differential cross sections cover nearly a $4\pi$ solid angle for the emission of low energy electrons and a range of projectile scattering angles. Experimental data are compared with theoretical calculations from the distorted wave Born approximation and the molecular three-body distorted wave models. It is found that theory can give a proper description of the main features of experimental cross section only at smaller scattering angles. For larger

scattering angles, significant discrepancies between experiment and theory are observed. The importance of the strength of nuclear scattering from the H-nuclei was tested by reducing the distance between the carbon nuclei and the hydrogen nuclei and improved agreement with experiment was found for both the scattering plane and the perpendicular plane.

## Introduction

Electron impact single ionization of atomic and molecular targets is a fundamental process which is important in a wide range of science and technology, such as plasmas physics, chemistry of planetary atmospheres and radiation damage of living tissues. Detailed information about this process can be obtained from the kinematically complete experiments, or (e, 2e) experiments, which determine the momentum vectors of all continuum particles (i.e. initial state of the projectile electron and the two final state electrons after ionization). From such measurements, triple differential cross sections (TDCSs) can be deduced to provide the most rigorous test of theoretical models.

Previous (e, 2e) studies about the collision dynamics mainly focused on atomic targets[1-5], and works dedicated to the molecular targets are scarce because of difficulties in both experiment and theory. On the experimental side, the closely-spaced electronic states of molecules are difficult to be resolved[6-10]. On the theoretical side, the multi-center nature makes calculations more complicated compared to atomic targets. In addition, the target molecules are randomly oriented in most of the experiments, thus theoretical results need to be averaged over all the possible orientations to allow comparison with experiment[7]. In spite of such challenges, different molecules such as $H_2$,[11, 12] $N_2$,[13-15] $H_2O$,[16-18] $CO_2$[19] have been studied experimentally, and several theoretical models, such as

the Brauner, Briggs, and Klar (BBK) model[7], the time dependent close coupling (TDCC) model,[20, 21] and the molecular 3-body distorted wave (M3DW) model[6, 8, 10, 22, 23] coupled with the orientation-averaged molecular orbital approximation (OAMO)[24], have been adapted to molecular targets.

Most of the previous (e, 2e) experiments were performed under the so-called coplanar asymmetric geometry, in which the energy and angular location of the scattered electron are fixed, and the emitted electron is detected in the scattering plane defined by the momentum vectors of the projectile and scattered electron. Binary and recoil peaks are found to be the dominant features in the cross sections for all atomic and molecular targets in a wide projectile energy range. Good agreement between theory and experiment has been achieved for atomic targets, especially for the simplest atoms such as H[1, 2] and He[3, 4]. However, for molecular targets, there are some difficulties for theory to reproduce the most basic features, such as the relative size of the recoil to the binary peak. Lohmann and coworkers measured the TDCSs for single ionization of different orbitals of $H_2O$ by 250 eV electron impact and observed very large recoil peaks[16]**.** These were well reproduced by the BBK model in a later publication[17]. To further examine the BBK theory, Lahmam-Bennani and coworkers applied the BBK model to single ionization of $CH_4$ with incident electron energy around 600 eV. They found that the experimental TDCSs exhibited again a large recoil peak which was not reproduced by BBK theory[7]. The authors attributed the large recoil scattering to the particular kinematics under which the electron-nucleus interaction is strong, but such interaction is not properly considered in the BBK theory. Toth and Nagy[9] showed that a strong electron-nucleus interaction can be simulated by localizing the H nuclei closer to the center of mass in their spherical shell

approximation of the nuclear potential, and good agreement with experiment was achieved[9]. Such method was then adopted to $N_2$ in a recent publication[15]. The calculation agrees well with experiment for outer molecular orbitals, but cannot reproduce the large recoil peak for the inner $2\sigma_g$ orbital. In a recent study on $H_2$ it was shown both experimentally and theoretically that shortening the internuclear distance increases the binding potential and, hence, the relative contribution of recoil scattering.[25]

The M3DW is a model that has been widely employed in (e, 2e) studies for various molecular targets under different kinematics. A review of this work is contained in Ref. 22. Lohmann and coworkers measured the TDCSs for the complex CHOOH[6] and tetrahydrofuran[8] targets, and compared their results with M3DW calculations. The measurement showed that for the emitted electron energy of 10 eV, the relative size of the recoil to the binary peak decreases as the scattering angle increases, and is much smaller than that observed in ionization of water under similar kinematics. The authors attributed these to the special molecular configurations of the two targets. For both targets, there is no nucleus at the center-of-mass, which suggests that the electron-nuclei interaction might not be as strong as that for molecules with nuclei located at/around the center-of-mass, such as $H_2O$. However, since the same trend of the relative size of the recoil to the binary peak is observed for ionization of the outmost orbitals of single center atomic targets He[4], Ne[5] and Xe[5] under similar kinematics, this may indicate that the nuclear configuration is not the only/dominant cause of this phenomenon. The M3DW calculation agrees well with the experiment for large scattering angles where the recoil peak is small, but does not reproduce the large recoil peak for small scattering angles.

Recently, Nixon *et al.*[10] performed low energy (e, 2e) studies of $CH_4$ for the symmetric coplanar geometry. For ionization of the $1t_2$ state, the location of the small angle peak and the relative sizes of the small and large angle peaks were qualitatively reproduced by the M3DW, but the theory predicted the large angle peak at smaller angles than observed in experiment. For ionization of the $2a_1$ state, the M3DW was in better agreement with experiment for high energies than low energies and for low energies experiment found 3 peaks while theory only had 2 peaks. They also compared ionization of the $2a_1$ state of $CH_4$ with the 2s state of neon. For neon, there was excellent agreement between experiment and theory for high energy while for low energy experiment found more peaks than theory similar to the methane $2a_1$ results. This suggests that the molecular nature of the target is not the only cause of the disagreement between theory and experiment, and that the nuclear scattering may also play a dominant role that is not being properly treated.

There are also some experiments that have been performed for out-of-plane geometries. For example, Al-Hagan and coworkers analyzed the cross section for the geometry where both final state electrons are emitted in the plane perpendicular to the incoming beam[12]. The TDCSs in this geometry exhibited different features for the isoelectronic targets He and $H_2$. A strong peak for back-to-back emission of electrons was observed for He, while a minimum was observed for $H_2$. The authors introduced a multi-scattering process to explain such difference. The origination of the difference was attributed to different nuclear configurations of the two center $H_2$ molecule and the one center He atom. The authors concluded that all the molecules with a nucleus in the center-of-mass, such as $CH_4$, should behave in a similar way as He. However, a recent

study[23] showed that this prediction failed for the isoelectronic targets Ne and $CH_4$ which are more complicated than the targets discussed in Ref. 12. Ren *et al.* measured the 3D TDCSs for He and $H_2$ using the reaction microscope. Their study showed that the strong back-to-back emission of two outgoing electrons for (e, 2e) of He is mainly due to the overlap of the binary and recoil lobes.[26]

In short, previous (e, 2e) studies show that the molecular configurations of the targets influence the features of the TDCSs in both the coplanar and out-of-plane geometries. $CH_4$ is the simplest hydrocarbon molecule present in nature. It is a benchmark molecule with a nucleus at the center-of-mass. Thus electron-$CH_4$ collisions represent an ideal system to investigate the influence of molecular configurations on the electron emission patterns in the (e, 2e) process.

In this paper, we explore single ionization of the $1t_2$ orbital of $CH_4$ by 54 eV electron impact. By employing the advanced reaction microscope technique, TDCSs under different geometries were measured and compared with M3DW and DWBA calculations.

## Experiment

### A.Experimental apparatus

The experiment was performed with a reaction microscope that was specially designed for (e, 2e) studies. Details of the experimental procedure were given in previous publications[27, 28]. In brief, a pulsed electron beam with energy of 54 eV crosses the $CH_4$ supersonic gas jet, and causes single ionization of the target. Using the uniform electric and magnetic fields, the charged fragments in the final state are extracted and directed to the two individual time and position sensitive detectors. In this way, a large part of the

$4\pi$ solid angle is covered for final state particles (100 % for the detection of $CH_4^+$ ions and 80 % for electrons with energy lower than 20 eV). The momentum components of the recoil ion and the electrons along the projectile direction (longitudinal components) can be determined from the time of flight of each particle from the collision region to the respective detector, while the transverse momentum can be obtained from the position and the time of flight information recorded by the detectors. For recoil ions, since the so called time-focusing condition[28, 29] is employed in the spectrometer, the longitudinal momentum has a much higher resolution (0.4 a.u.) compared to the transverse component (1.2 a.u.). It should be emphasized that the TDCSs are deduced directly from the momenta of the two outgoing electrons without relying on the recoil ion momentum, thus the angular resolution is not influenced by the temperature of the heavy target. Experimentally a large range of the final state phase space is recorded simultaneously. Thus, in the offline data analysis particular scattering geometries of interest are selected by choosing those events which fulfill particular conditions concerning, e.g. the fast electron scattering angle or the energy partitioning between both electrons in the final state. The resolution for obtaining the target electron binding energy is around 6 eV during the present experiment. Since the $CH_4^+$ ion is only produced from the $(1t_2)^{-1}$ state,[30] the contribution from the higher ionization/ionization-excitation states can be well separated from $(1t_2)^{-1}$ by coincidence measurement of the $CH_4^+$ ion. It should, however, be noted that ionization from the $(1t_2)$ orbital can yield other fragments as well that have not been studied in this work.

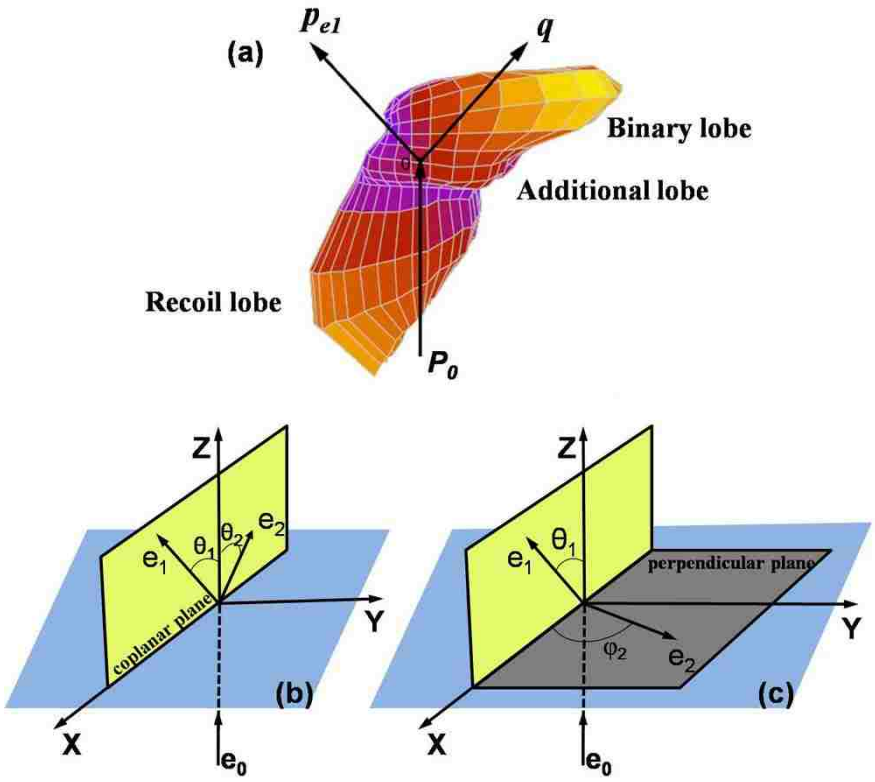


Figure. 1. (a) TDCS for (e, 2e) of $1t_2$ orbital of $CH_4$ as a function of the emission angle of the slow electron with kinetic energy of $E_2$=10 eV. The scattering angle of the fast electron is fixed to $\theta_1$=-55$^o$; (b) and (c): coplanar and perpendicular plane geometries used for the present studies. See text for details.

**B. Definition of geometries**

Figure 1(a) is an example of the measured three-dimensional (3D) polar plot of the TDCS for single ionization of the $1t_2$ orbital of $CH_4$. The scattering angle of the fast electron is fixed at $\theta_1$=55$^o$, while the emission angle of the slow electron with energy 10eV covers a large range of the full $4\pi$ solid angle. In such diagrams, the TDCS for emission to a particular direction is proportional to the distance between the origin and the point on the surface of the 3D plot intersected by the electron's emission direction. In order to get a reduced scattering of the data points in this 3D plot, the count in each unit is summed with the neighboring units. The cross section pattern is dominated by the

binary and recoil lobes which are universal in the (e, 2e) process. An additional structure is observed between the binary and recoil lobes. This lobe may arise from high-order effects which would be particularly important at low incident energy[10].

To make a more quantitative comparison between experiment and theory, we define two different geometries, the coplanar geometry shown in figure 1(b) and the perpendicular plane geometry in figure 1(c). The energy ($E_1$) and scattering angle of the scattered (faster) electron ($\theta_1$) and the energy of the emitted (slower) electron ($E_2$) are fixed for both geometries. For the coplanar geometry in figure 1(b), the slow electron is detected in the scattering plane defined by the momenta of the fast scattered electron and the incident projectile. The TDCS is given as a function of the scattering angle of the slow electron ($\theta_2$) measured clockwise relative to the incident beam direction. For perpendicular plane geometry in figure 1(c), the slow electron is detected in the plane perpendicular to the incident electron beam. The TDCS is plotted as a function of the angle ($\varphi_2$) between the momentum vector of the slow electron and the projection of the fast electron momentum onto the perpendicular plane. The intersection of the two planes corresponds to $\theta_2 = 90^o\,(270^o)$ in the coplanar plane, and $\varphi_2 = 180^o\,(0^o)$ in the perpendicular plane. For both geometries, the cross sections are integrated over an angular range of $\pm 10^o$ above and below the defined plane.

## Theoretical Framework

The molecular 3-body distorted wave (M3DW) approximation has been presented in previous publications[31-33] so only a brief outline of the theory will be presented. The TDCS for the M3DW is giving by:

$$\frac{d\sigma}{d\Omega_a d\Omega_b dE_b} = \frac{1}{(2\pi)^5}\frac{k_a k_b}{k_i}\left(|T_{dir}|^2 + |T_{exc}|^2 + |T_{dir} - T_{exc}|^2\right), \qquad (49)$$

Where $\vec{k}_i$, $\vec{k}_a$, and $\vec{k}_b$ are the wave vectors for the initial, scattered and ejected electrons, $T_{dir}$ is the direct scattering amplitude, and $T_{exc}$ is the exchange amplitude. The direct scattering amplitude is given by:

$$T_{dir} = \left\langle \chi_a^-(\vec{k}_a, \mathbf{r}_1)\chi_b^-(\vec{k}_b, \mathbf{r}_2)C_{scat-eject}(r_{12}^{ave})\,|V - U_i|\,\phi_{DY}^{OA}(\mathbf{r}_2)\chi_i^+(\vec{k}_i, \mathbf{r}_1)\right\rangle, \qquad (50)$$

Where $r_1$ and $r_2$ are the coordinates of the incident and the bound electrons, $\chi_i, \chi_a$, and $\chi_b$ are the distorted waves for the incident, scattered, and ejected electrons, respectively, and $\phi_{DY}^{OA}(r_2)$ is the initial bound-state Dyson molecular orbital averaged over all orientations. The molecular wave functions were calculated using density functional theory along with the standard hybrid B3LYP[34] functional by means of the ADF 2007 (Amsterdam Density Functional) program[35] with the TZ2P (triple-zeta with two polarization functions) Slater type basis sets. For the $1t_2$ state, the average of the absolute value of the Dyson wave-function is taken prior to the collision since the normal average is zero due to parity of the wave-function.[10]

The factor $C_{scat-eject}(r_{12}^{ave})$ is the Ward-Macek average Coulomb-distortion factor between the two final state electrons,[36] $V$ is the initial state interaction potential between the incident electron and the neutral molecule, and $U_i$ is a spherically symmetric distorting potential which is used to calculate the initial-state distorted wave for the

incident electron $\chi_i^+(\vec{k}_i, \mathbf{r}_1)$. For the exchange amplitude $T_{exc}$, particles 1 and 2 are interchanged in the final state wavefunction (left hand side) in eq. (2).

The Schrödinger equation for the incoming electron wave-function is given by:

$$(T + U_i - \frac{k_i^2}{2})\chi_i^+(\vec{k}_i, r) = 0, \qquad (51)$$

where $T$ is the kinetic energy operator and the '+' superscript on $\chi_i^+(\vec{k}_i, \mathbf{r})$ indicates outgoing wave boundary conditions. The initial state distorting potential contains three components $U_i = U_s + U_E + U_{CP}$, where $U_s$ contains the nuclear contribution plus a spherically symmetric approximation for the interaction between the projectile electron and the target electrons which is obtained from the quantum mechanical charge density of the target. The nuclear contribution to $U_s$ consists of a charge of +6 at the center of mass and a charge of +4 located on a thin spherical shell at the equilibrium distance of 2.06 a.u. relative to the center of mass. $U_E$ is the exchange potential of Furness-McCarthy (corrected for sign errors)[37] which approximates the effect of the continuum electron exchanging with the passive bound electrons in the molecule, and $U_{CP}$ is the correlation-polarization potential of Perdew and Zunger.[38, 39]

The final state for the system is approximated as a product of distorted waves for the two continuum electrons times the average Coulomb-distortion factor. The final state distorted waves are calculated as for the initial state except that the final state spherically symmetric static distorting potential for the molecular ion is used for $U_s$.

Results will be presented for the M3DW described above as well as the standard distorted wave Born approximation (DWBA). The DWBA is identical to the M3DW except that the post collision interaction (PCI) term $C_{scat-eject}(r_{12}^{ave})$ is omitted in the evaluation of the direct and exchange amplitudes.

## Results and Discussion

### A. TDCSs under coplanar geometry

Since the ionization energy for the $1t_2$ state is 14 eV, the two final state electrons have 40 eV to share when the incident electron has energy of 54 eV. Several energy pairs ($E_1$, $E_2$) were analyzed where $E_1$ is the energy of the faster electron and $E_2$ the slower with $E_1 + E_2 = 40$ eV. For each energy pair, different scattering angles $\theta_1$ of the fast final state electron were selected ranging from $15^0$ to $55^0$. Figure 2 compares theoretical and experimental coplanar results for three different energy pairs and faster electron scattering angles of $15^0$ and $20^0$.

The experimental data exhibit the normal binary peak at small angles and recoil peak at large angles. The vertical line on each figure at small scattering angles indicates the classical momentum transfer direction and the line at large angles is the location of the classical recoil direction (i.e., the opposite of the momentum transfer direction). Since the ionized $1t_2$ orbital has p-character with a minimum of the bound momentum wave function at zero momentum, the binary peak can show a split structure with two maxima when the reaction kinematics is close to the region of the Bethe ridge. It is possible that the observed splits of the binary peaks in both the experimental data and the theoretical curves are due to the p-character of the $1t_2$ orbital.

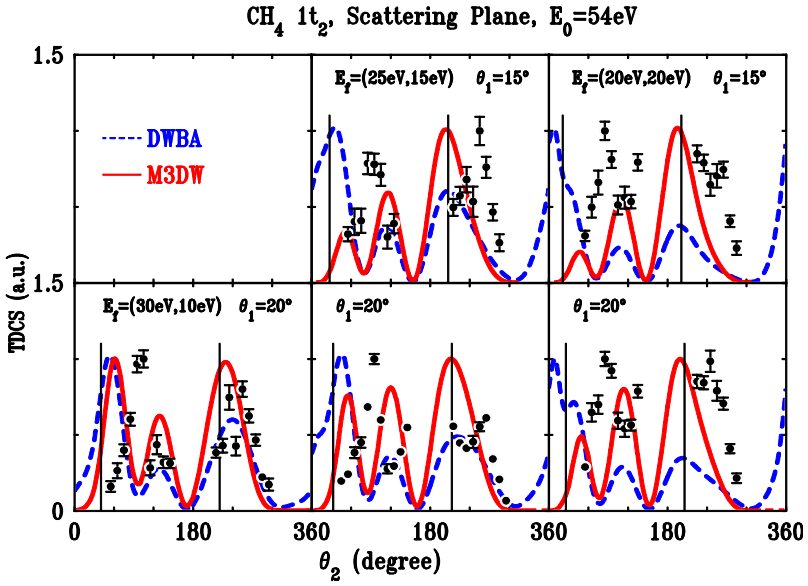


Figure. 2. TDCSs for the scattering plane geometry. The emission angle of the faster final state (scattered) electron is $15^{o}$ and $20^{o}$, while the emitted electron energy ranges between 10 eV and 20 eV. The experimental data are the black circles and the theoretical results are the DWBA (dashed curve) and M3DW (solid curve). The horizontal axis is the observation angle for the slower (ejected) electron. The vertical line at small ejection angles is the direction of classical momentum transfer and the vertical line at larger ejection angles is the direction of the classical recoil peak. The experimental and theoretical data have been normalized to unity independently at the maximum for each curve.

This has been seen for higher incident electron energies for ionization of 2*p* state of Ne.[39] However, for the atomic case, the double peaks become a single peak as the incident electron energy is lowered to those of the present experiment[39] due to the enhanced influence of high order effects. In Sec. C, we will show that the second binary peak is suppressed when scattering from the nuclei is made stronger. So this peak may be more strongly related to nuclear scattering than the 2*p* structure of the molecular wavefunctions. At higher incident-electron energies, one would expect that the binary peak should be close to the momentum transfer direction and the recoil peak should be close to the opposite direction. For the low energies considered in this work, it is seen that the experimental binary peak is significantly shifted to larger angles. In principle,

this could be the result of the PCI between the ejected electron and the scattered electron which in the diagrams in Figure 2 is fixed at the angle $(360^o - \theta_1)$. The precise position of the recoil peak cannot be well judged since it is only partly in the experimentally accessible angular range. Nevertheless, while theory predicts recoil peaks fairly well contered at the direction opposite to the momentum transfer, the experimental recoil lobes extend to larger angles, in particular, for equal energy sharing of the final state electrons.

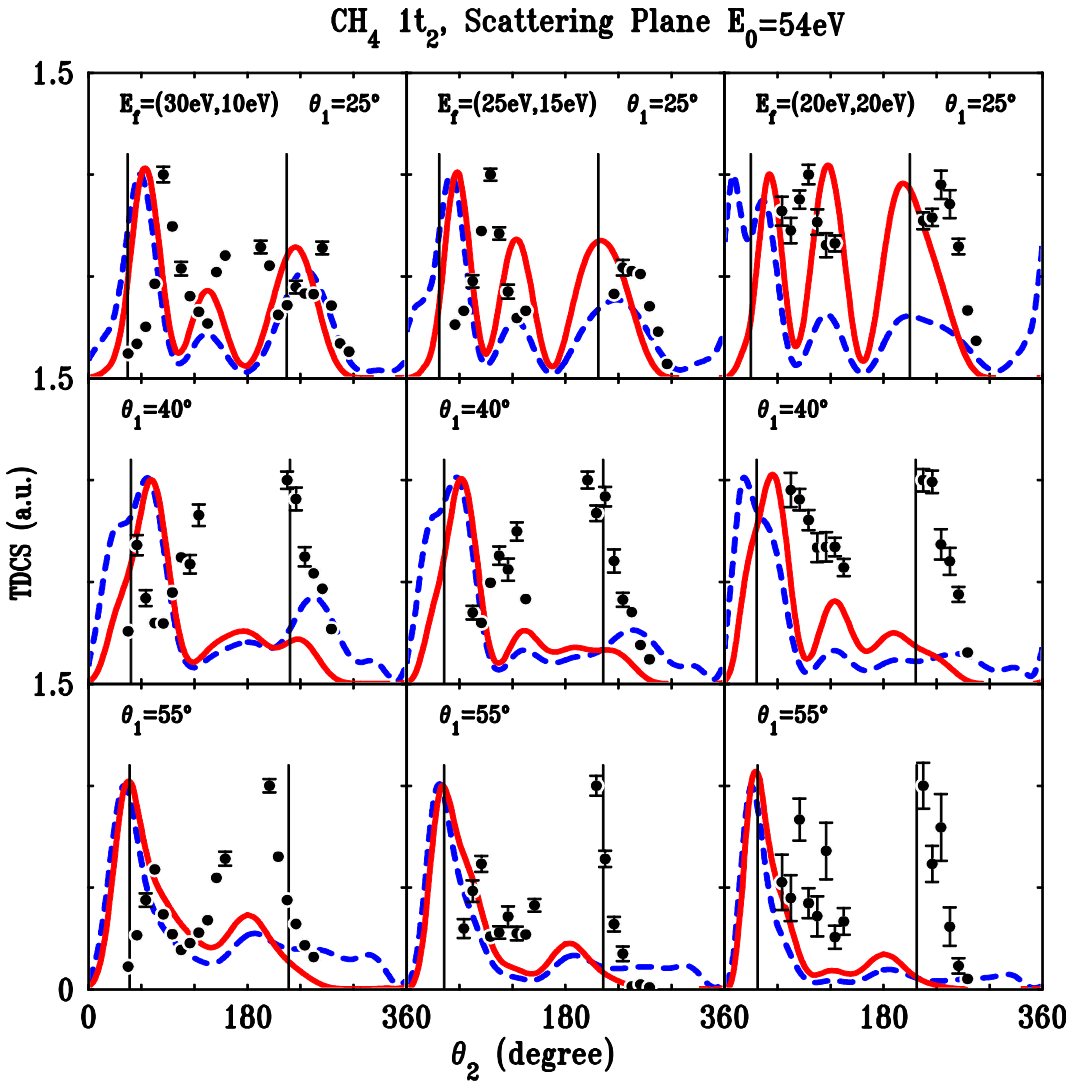


Figure. 3. Same as Figure 2 except for faster final state (scattered) electron angles of $25^o$, $40^o$ and $55^o$.

Some information on the mechanisms underlying the experimental cross section patterns can be gained from comparison with theory. Both calculations show a significant shift of the binary peaks away from the momentum transfer direction. Although the DWBA does not contain PCI directly in the T-matrix, the phenomenon is indirectly taken into account by the distorted wave description, i.e. the higher-order projectile target interactions in the initial and final states must play a key role for this shift. The comparison with the M3DW calculation which contains PCI directly in the T-matrix, shows that the role of PCI is a suppression of the cross section in the vicinity of the scattered projectile direction $(360^o - \theta_1)$. As expected this effect is weak for the most asymmetric energy sharing (30 eV, 10 eV), where the DWBA and M3DW results are similar in the momentum transfer direction. On the other hand for equal energy sharing, PCI is strong and gives rise to a significant reduction and a shift of the small angle binary peak while the magnitude of the large angle peak at about 120° is increasing. Experimentally the binary peaks are observed at even larger angles. Finally, both theories show the recoil peak at a position roughly opposite to momentum transfer direction and do not show the apparent shift of the experimental peaks to larger angles. The large magnitude of the recoil peak, which is similar in size to the binary peak in most cases is reproduced. The best overall agreement of experiment and theory is observed for the most asymmetric energy sharing case (30 eV, 10 eV) with $\theta_1=20^o$.

Figure 3 contains the same comparison between experiment and theory for fast electron scattering angles of $25^0$, $40^0$, and $55^0$. For these larger scattering angles, the experimental TDCSs is still dominated by the binary and recoil peaks with the recoil

peaks as large as or larger than the binary peaks. In a recent study on the low energy (e, 2e) of Ar,[40] a new structure is observed in the projectile backwards direction. It is also possible that the peaks around 180° observed in the present study (e.g. for (30 eV, 10 eV) and $\theta_1$=25°) originates from the same mechanisms. For the two largest angles, the experimental recoil peaks are close to the classical recoil direction. With increasing $\theta_1$, the theoretical calculations evolve into a single binary peak very close to the classical binary direction. In Sec. C, we will show that the second binary peak is suppressed when scattering from the H-nuclei is made stronger. With increasing $\theta_1$, the projectile electron penetrates closer to the center of mass. Consequently, the reduction of the second binary peak seen here with increasing $\theta_1$ is probably due to increased importance of nuclear scattering as a result of smaller impact collisions. Both the theoretical binary and recoil peaks occur at smaller angles than in experiment.

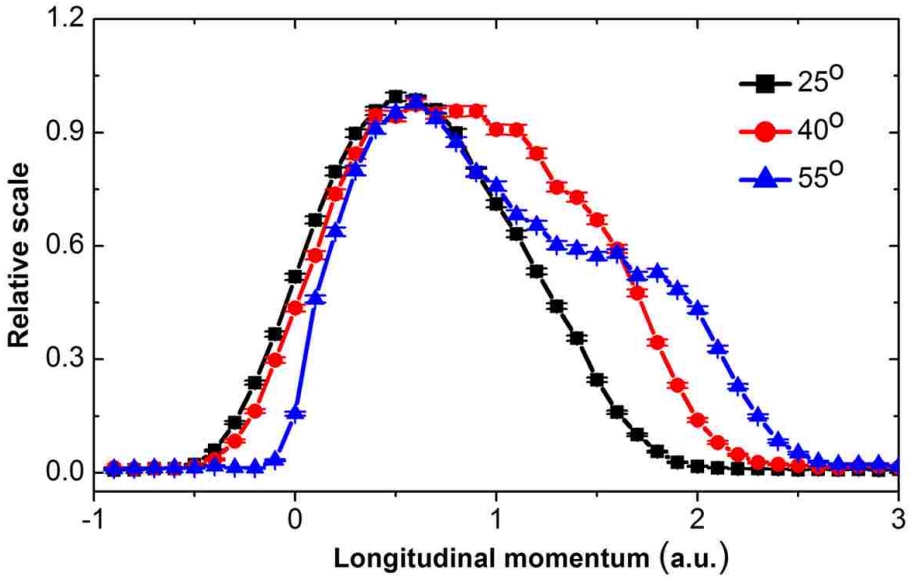


Figure 4. Longitudinal momentum distributions at different scattering angles. The curves are intergrated over all the emitted electron energy of $e_2$.

The recoil peak arises from a process in which the emitted electron produced by the binary collision is scattered backward by the nucleus. Thus the increased experimental recoil peak may be attributed to an increased interaction between the emitted electron and the target nuclei. While the emitted electron is scattered backward, momentum will be transferred to the recoil ion simultaneously. Consequently, the momentum distribution of the recoil ion provides direct information revealing how strong the electron-nuclei interaction is. As mentioned before, the advanced reaction microscope technique makes it possible to obtain the longitudinal momentum distribution of the recoil ions with a relative high resolution (0.4 a.u.). Figure 4 shows the longitudinal momentum distributions of the recoil ions at scattering angles of $\theta_1 = 25^o$, $40^o$ and $55^o$ respectively.

Figure 4 shows that, as the scattering angle increases, the longitudinal momentum distribution extends toward the larger momentum side (right-hand side), which indicates that the electron-nuclei interaction becomes stronger. In two recent studies for CHOOH[6] and tetrahydrofuran[8], the relative size of the recoil to binary peak was found to decrease as the scattering angle increased. The authors suggested that this trend is due to the fact that there is no nucleus in/near the center-of-mass for both of these targets. For $CH_4$, the carbon nucleus is located at the center of the tetrahedron defined by the four protons. If we consider this process under the classical Rutherford scattering model, increasing the scattering angle indicates that the impact parameter of this collision process reduces, which means that the binary collision happens closer to the carbon nucleus. Thus, it stands to reason that the interactions between the target nuclei and the electrons should increase.

Finally, it can be concluded that increasing the relative size of the recoil to the binary peak of the TDCS in the scattering plane is due to an increased electron-nuclei interaction as the scattering angle increases. However, there are no experimental TDCSs for the molecules without a nucleus in the center of mass (for example $N_2$) under the same kinematics available for comparison. Consequently, it is hard to estimate from experiment how strong the molecular configurations influences the electron-nuclei interaction is.

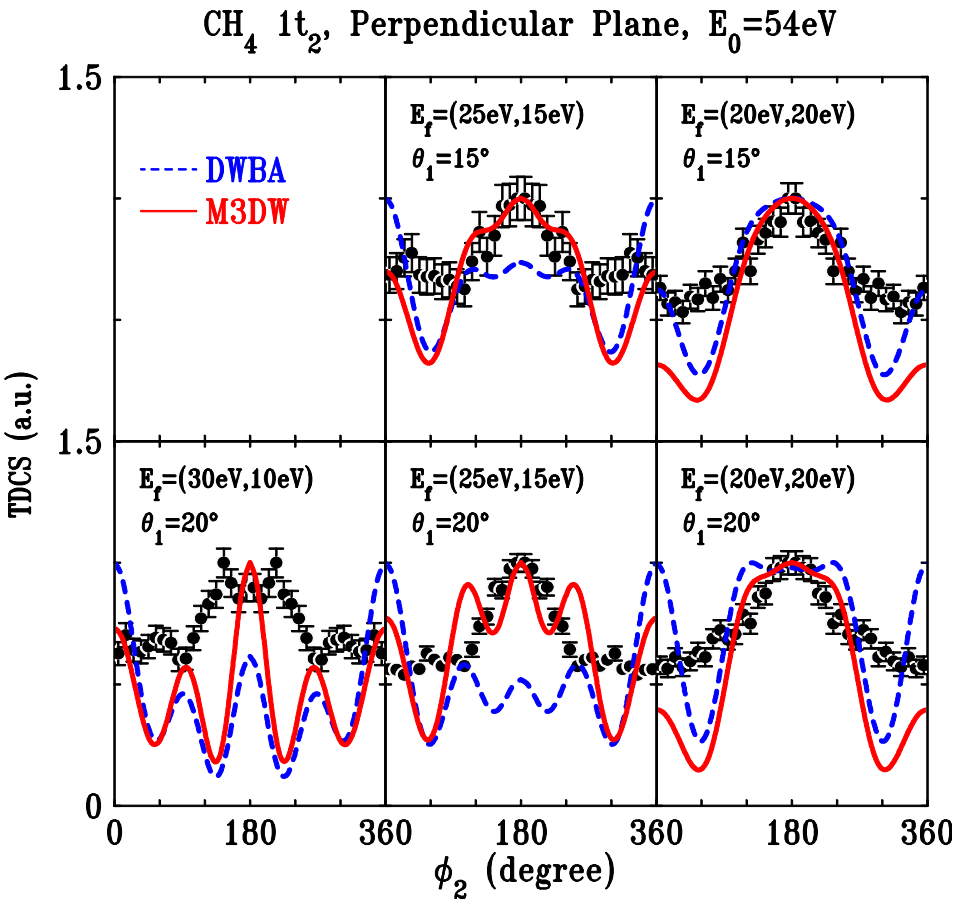


Figure. 5. Same as Figure 2 except for the perpendicular plane.

Comparing with theory, the agreement tends to be better for small scattering angles, and it get worse as the scattering angle increases in the scattering plane. This is

consistent with the observations in Ref. 10 where better agreement was found for the forward peaks in the coplanar symmetric geometry employed in Ref. 10. These forward peaks correspond to small scattering angle events. For the backward peaks, which correspond to the events with larger scattering angle and stronger nuclei scattering, obvious discrepancy between theory and experiment is observed. Finally and on a more positive side, the present theoretical ratios of binary to recoil peak heights are reasonably good for scattering angles out to $\theta_1 = 25^o$.

**B. TDCSs under perpendicular geometry**

The collision dynamics at low incident energies are far away from the impulsive regime and higher order effects are expected to be important. Since the TDCS in the coplanar plane is dominated by the binary and recoil lobes, out-of-plane geometries such as perpendicular plane defined in part II are good choices for investigation of higher order contributions. Figure 5 shows the TDCSs in the perpendicular plane with same kinematics as in Figure 2. The cross sections should be symmetrical about $180^o$. However, in some cases the experimental TDCSs show a deviation of around 10% between the equivalent points. which seems to be a systematic effect with the experiment. The data have been averaged for equivalent points to make a more effective comparison with calculations. It can be seen from figure 5 that the experimental cross section has a maximum for $180^0$ emission angle which corresponds to the ejected electron being emitted in the scattering plane on the opposite side of the beam direction as the scattered electron and a minimum for $0^0$ ($360^0$) which corresponds to the ejected electron being emitted in the scattering plane on the same side of the beam direction as the scattered electron. The M3DW theoretical calculations also predict a maximum for $180^0$ scattering but with more structure than seen in the data. The M3DW results are in better agreement

with experiment than the DWBA and the DWBA tends to predict cross sections that are too large for $0^0$ ($360^0$).

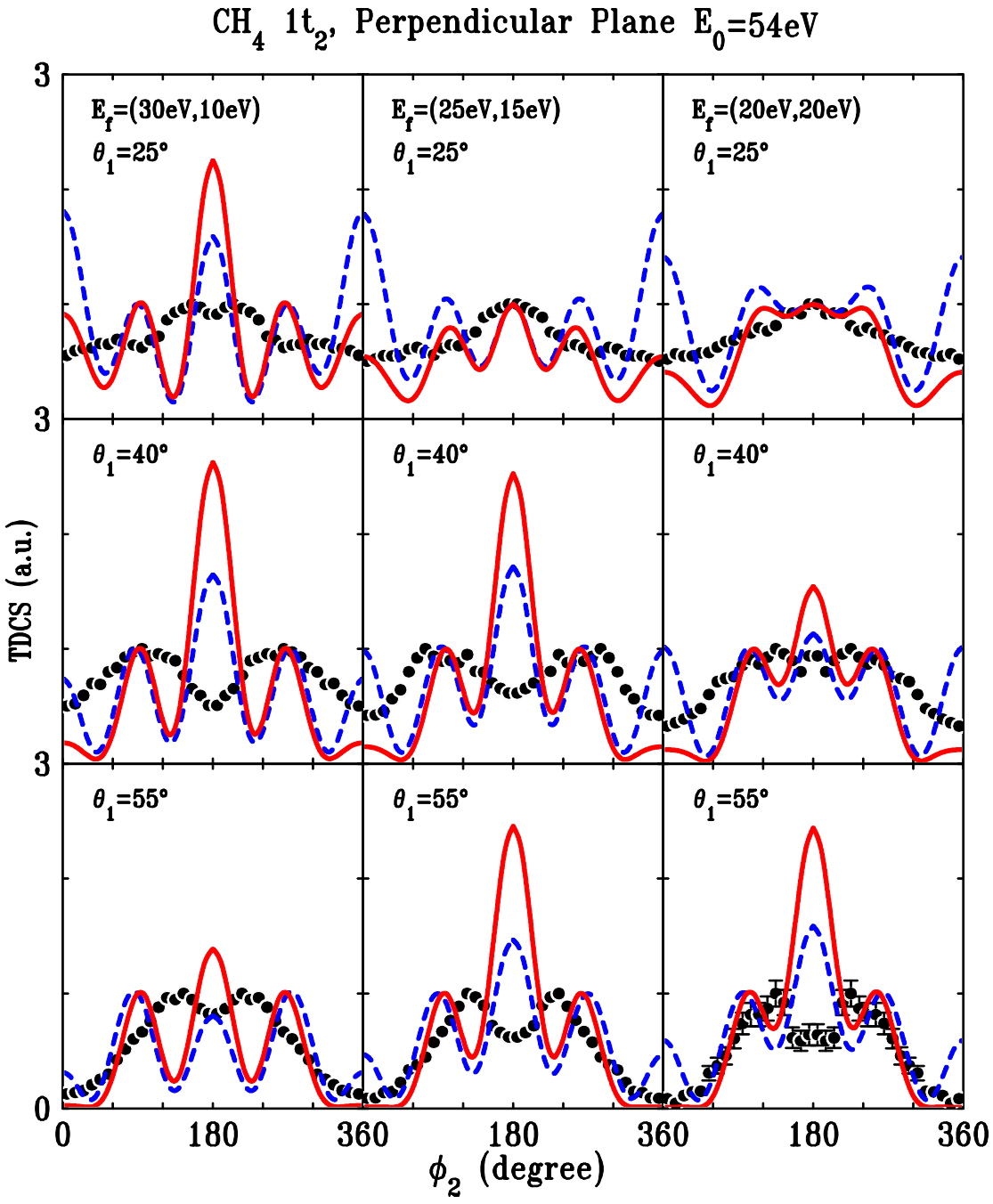


Figure. 6. Same as Figure 3 except for the perpendicular plane.

Figure 6 shows the TDCSs in the perpendicular plane with the same kinematics as in Figure 3. There is very little structure in the experimental data except that the $180^0$ maximum turns into a shallow minimum with increasing fast electron scattering angle. The experimental data for $\theta_1 = 55^0$ is very reminiscent of the Al-Hagan *et al.* results for ionization of $H_2$ with both final state electrons being detected in the perpendicular plane (i.e. $\theta_1 = 90^0$).[12] In that work, results for ionization of $H_2$ were compared with the equivalent cross sections for ionization of He. For $H_2$, peaks were found near $90^0$ and $270^0$ and a minimum was found for $180^0$ scattering. as shown in that work that the $90^0$ and $270^0$ peaks resulted from elastic scattering. For He, peaks were found for angles in the vacinity of $90^0$ and $270^0$ as well as $180^0$. It was shown in that work that the $90^0$ and $270^0$ peaks resulted from elastic scattering into the perpendicular plane followed by a binary collision in the perpendicular plane. The minimum at $180^0$ for $H_2$ was attributed to very small impact parameter binary collisions taking place between the two nuclei where the average nuclear attraction would be zero. The strong maximum for He was attributed to the strong attraction resulting from small impact parameters with the nuclear charge located at the center of mass. Al-Hagan *et al.*[12] predicted that ionization of any molecule with a nucleus at the center of mass should have 3 peaks in the perpendicular plane at $90^0$, $180^0$ and $270^0$ just like both theoretical calcultions predict for the present case.

Very recently, Nixon *et al.*[23] published low energy TDCS for ionization of $CH_4$ and Ne where both final state electrons were detected in the perpendicular plane. In that work, the energy of the incident electron was varied and both final state electrons were detected with the same energy. Their experimental results for (20eV, 20eV) and $\theta_1 = 90^0$ is very similar to the present results for (20eV, 20eV) and $\theta_1 = 55^0$ of Figure 6. Likewise,

the theoretical DWBA and M3DW results presented in that work are similar to the results shown in Figure 6 with three peaks near $90^0$, $180^0$ and $270^0$ as predicted by Al-Hagan *et al.*[12] but not found in the experiment. For electron energies above about 12 eV, Nixon *et al.*[23] found two peaks near $90^0$ and $270^0$ similar to the two peaks found in the present work for $\theta_1 = 40^0, 55^0$ and predicted by the theory. The intriguing question remains why both experiments find very little backscattering from the highly charged nucleus located at the center of mass while the theory predicts very strong backscattering.

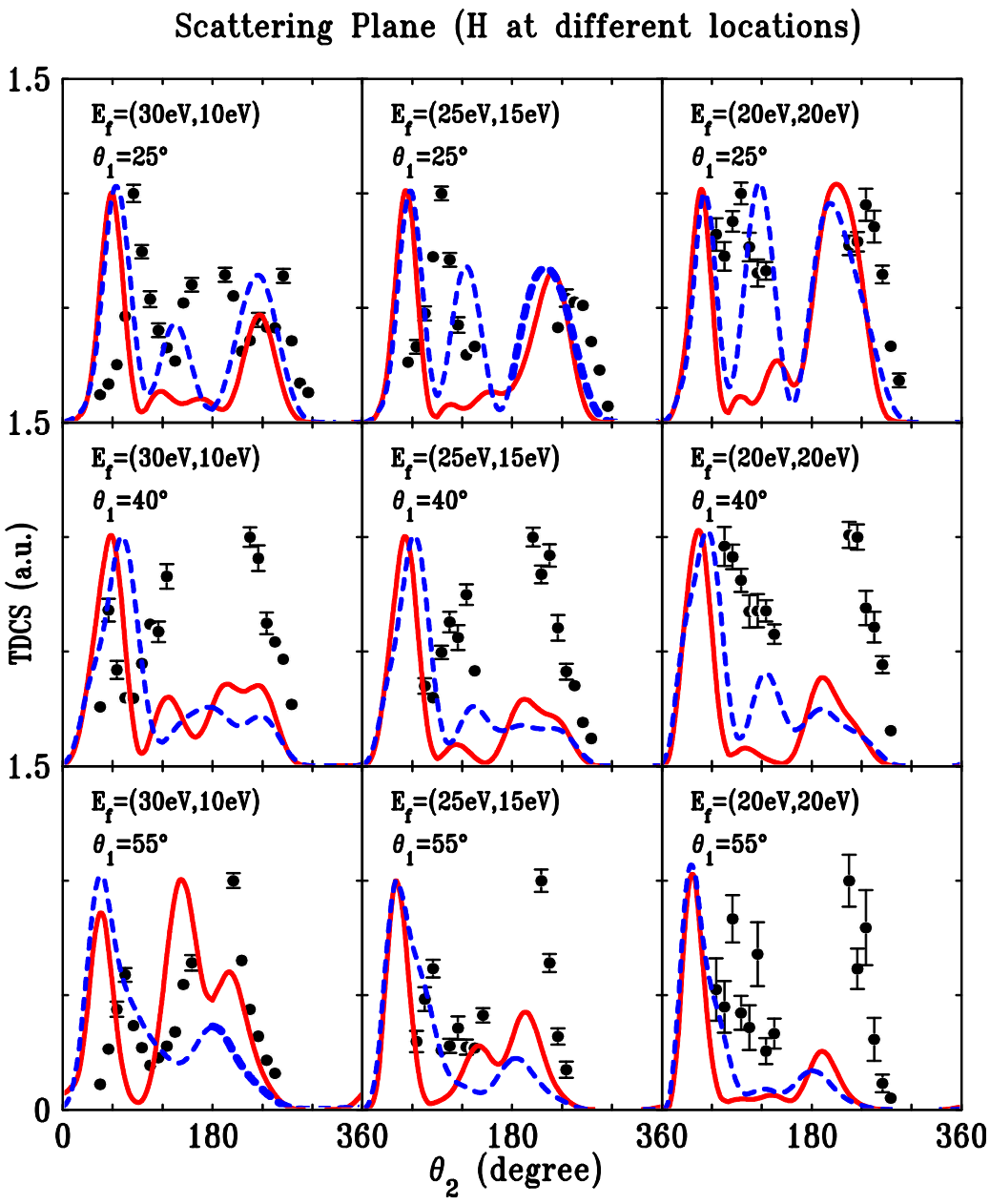


Figure. 7. Same as Figure 3 except for different theoretical curves. The theoretical results are the M3DW with the H nuclei 2.06 a.u. from the C nucleus (dashed curve) and M3DW with the H nuclei 0.8 a.u. from the C nucleus (solid curve).

### C. The reduced C-H distance calculations

Toth and Nagy[9] reported a DWBA calculation very similar to the present work for high energy ionization of $CH_4$ and compared their results with the coplanar experimental data of Lahman-Bennani *et al.*[7] They noted that the standard DWBA predicted recoil

lobes that were too small compared to experiment which they attributed to a weak scattering from the H nuclei. Recall that in the present spherically symmetric model, the four H nuclei are uniformly distributed on a thin spherical shell of radius 2.06 a.u. They showed that, by decreasing this radius (and presumably increasing the strength of the attractive potential felt by the target electrons), they could increase the recoil lobe and achieve good agreement with experiment. Recently, an experimental verification of the increasing recoil contribution with decreasing inter-nuclear separation was found in molecular hydrogen.[25] Since the recoil lobes calculated with the H-shell radius of 2.06 a.u. for coplanar scattering and $\theta_1 = 40^0, 55^0$ are significantly smaller than experiment, we decided to try reducing the H radii to see if this would help. It is important to note that the electronic wavefuntions are not changed in these calculations. The only thing changed is the nuclear contribution to the distorting potential (i.e., the radius of the sphere with charge +4 is changed but everything else is unchanged).

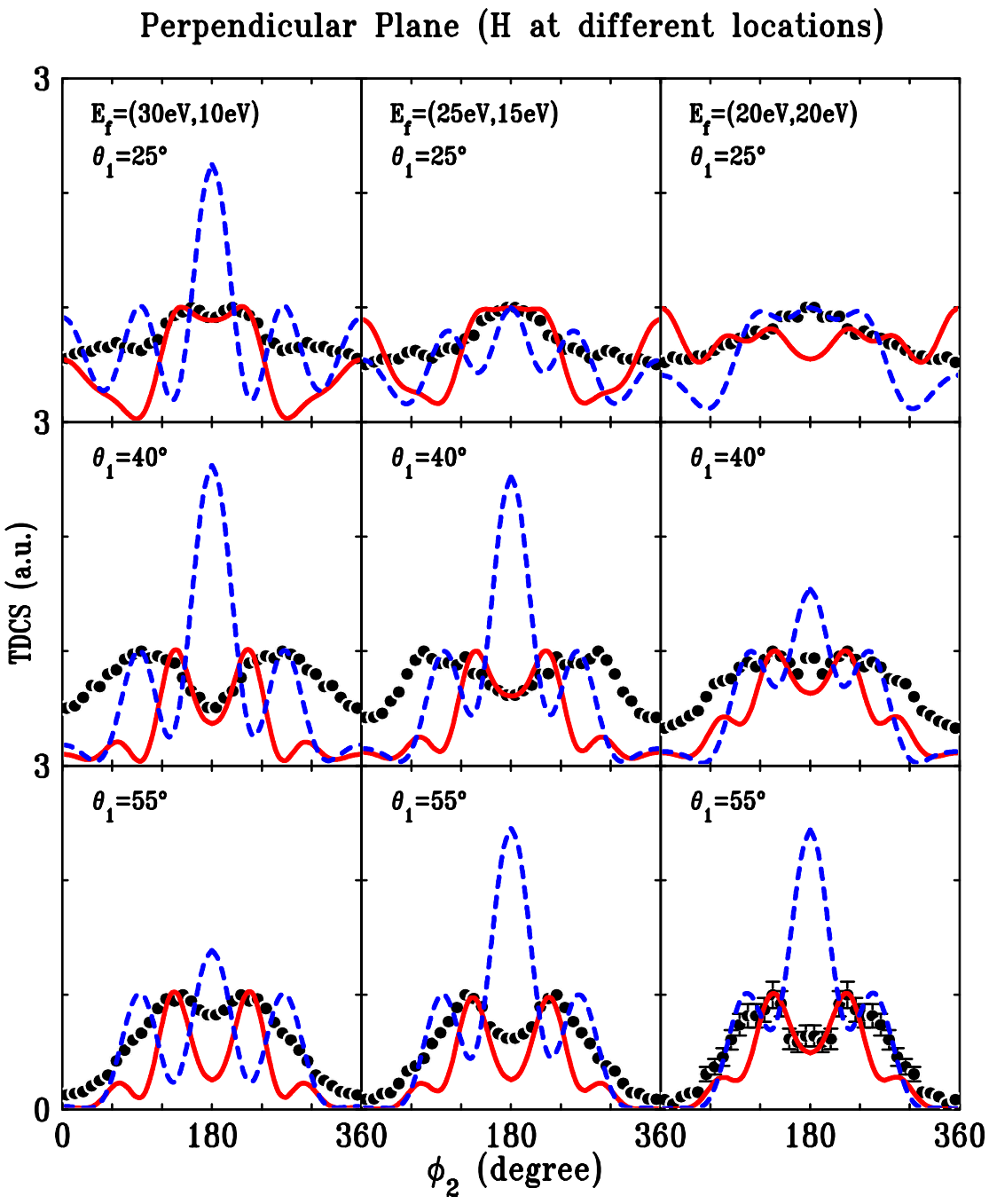


Figure. 8. Same as Figure 7 except for the perpendicular plane.

Figure 7 shows the effect of reducing the H-shell radius to 0.8 a.u. for coplanar kinematics and the larger faster electron scattering angles presented in Figure 3. We found that, for coplanar scattering, the size of the sphere did not have a large effect on the

ratio of binary to recoil lobes. The only important change from making the H-sphere smaller was to significantly reduce the right-hand side of the split binary peak to the point of essentially eliminating it. Although the results for the recoil peak are disappointing, they seem reasonable since the classical impact parameters for these scattering angles range between 5 and 11 a.u. such that a sphere of 2 a.u. looks the same as a point charge at the center classically. It is interesting to note that the second peak was suppressed by changing the strength of the scattering from the nuclei. Since the p-type wavefunctions were not changed in this calculation, these results suggest that the split lobe binary peak more closely related to nuclear scattering than p-type structure of the wavefunction.

Although it would seem senseless to make the nuclear interaction stronger for the perpendicular plane since the present results indicate that the interaction with the nuclei is already too strong, we tried it anyway and the results are shown in Figure 8 for the larger scattering angles. Surprisingly, increasing the strength of the H-nuclear interaction changed the large backscattering peak to a minimum consistent with the experimental data. Now the agreement with experiment is not perfect but at least reasonable. Obviously the simple classical models are not able to explain this behavior and we are evidently seeing some kind of quantum interference effect. By using different size radii for different scattering angles, we could obtain even better agreement with experiment but we do not think that it is appropriate to push this model that far (it seems too much like curve fitting.). On the other hand, since agreement with experiment was improved in both the scattering plane and perpendicular plane (contrary to expectation), we think that there may be some important physics contained herein. In any event, these results indicate that the cross sections are strongly dependent on the nuclear configuration. It is

also imaginable that detecting electron ionization events coincident with the creation of a $CH_4^+$ ion selects ionization events that take place at certain nuclear geometries covered by the methane ground state nuclear wave function. Other configurations will consequently lead to dissociation after removal of a $1t_2$ electron. The specific geometries leading to bound methane ions do not have to employ symmetrically arranged protons, i.e. the C-H bonds might have different lengths, as the ground state of the methane ion has a reduced symmetry due to Jahn-Teller distortions.[41]

## Conclusions

Experimental (e, 2e) measurements for ionization of the $1t_2$ orbital of $CH_4$ induced by 54 eV electron-impact have been compared with DWBA and M3DW theoretical calculations. Up to a fast electron scattering angle of $\theta_1=25^o$ experiment and theory were in qualitative agreement concerning the relative magnitudes of the binary and recoil peaks. Remaining differences were the positions of the split binary peak and the recoil peak, which in experiment were observed at larger angles than predicted by theory. In the coplanar plane, the experimental relative size of the recoil peak to the binary peak increases as the scattering angle becomes larger while the theoretical recoil peak decreased in magnitude. Overall the agreement between experiment and theory was better for the smaller faster electron scattering angles. The importance of the strength of nuclear scattering from the H-nuclei was tested by reducing the distance between the carbon nuclei and the hydrogen nuclei and improved agreement with experiment was found for both the scattering plane and the perpendicular plane. This indicates that the averaging process of uniformly distributing a charge of +4 on a thin spherical shell unphysically dilutes the role of the hydrogen nuclei. The present study highlights the importance of the electron-nuclei interaction for the (e, 2e) process. Both the experimental and theoretical

results exhibited a double binary peak which is seen for ionization of atomic 2*p* states at much higher incident electron energies. Increasing the strength of the scattering from the nuclei suppressed the second binary peak so the double binary peak seems to be more strongly related to nuclear scattering than the 2*p* structure of the molecular wavefunctions. Further experimental and theoretical works focusing on this issue are necessary.

## Acknowledgements

This work is partly supported by the US National Science Foundation under Grant. No. PHY-1068237 and by the National Natural Science Foundation of China under Grants Nos. 10979007, 10674140 and 10704046. S.X. is grateful for support from the CAS-MPS doctor training program, and helpful discussion from Dr. Toth and Professor Nagy.

## References

[1]T. N. Rescigno, M. Baertschy, W. A. Isaacs, and C. W. McCurdy, Science **286**, 2474 (1999).

[2]I. Bray, Phys. Rev. Lett. **89**, 273201 (2002).

[3]A. T. Stelbovics, I. Bray, D. V. Fursa, and K. Bartschat, Phys. Rev. A **71**, 052716 (2005).

[4]M. Dürr, C. Dimopoulou, A. Dorn, B. Najjari, I. Bray, D. V. Fursa, Z. Chen, D H Madison, K Bartschat, and J. Ullrich, J. Phys. B **39**, 4097 (2006).

[5]M. A. Stevenson, L. R. Hargreaves, B. Lohmann, I. Bray, D. V. Fursa, K. Bartschat, and A. Kheifets, Phys. Rev. A **79**, 012709 (2009).

[6]C. J. Colyer, M. A. Stevenson, O. Al-Hagan, D. H. Madison, C. G. Ning, and B. Lohmann, J. Phys. B **42**, 235207 (2009).

[7]A. Lahmam-Bennani, A. Naja, E. M. Staicu Casagrande, N. Okumus, C. Dal Cappello, I. Charpentier, and S. Houamer, J. Phys. B. **42**, 165201 (2009).

[8]C. J. Colyer, S. M. Bellm, B. Lohmann, G. F. Hanne, O. Al-Hagan, D. H. Madison, and C. G. Ning, J. Chem. Phys. **133**, 124302 (2010).

[9]I. Tóth, and L. Nagy, J. Phys. B **43**, 135204 (2010).

[10]K. L. Nixon, A. J. Murray, H. Chaluvadi, C. Ning, and D. H. Madison, J. Chem. Phys. **134**, 174304 (2011).

[11]D. S. Milne-Brownlie, M. Foster, J. Gao, B. Lohmann, and D. H. Madison, Phys. Rev. Lett. **96**, 233201 (2006).

[12]O. Al-Hagan, C. Kaiser, D. Madison, and A. J. Murray, Nat. Phys. **5**, 59 (2009).

[13]J. P. Doering, and J. Yang, Phys. Rev. A **54**, 3977 (1996).

[14]A. Naja, E. M. Staicu-Casagrande, A. Lahmam-Bennani, M. Nekkab, F. Mezdari, B. Joulakian, O. Chuluunbaatar, and D. H. Madison, J. Phys. B **40**, 3775 (2007).

[15]I. Tóth, and L. Nagy, J. Phys. B **44**, 195205 (2011).

[16]D. S. Milne-Brownlie, S. J. Cavanagh, B. Lohmann, C. Champion, P. A. Hervieux, and J. Hanssen, Phys. Rev. A **69**, 032701 (2004).

[17]C. Champion, C. D. Cappello, S. Houamer, and A. Mansouri, Phys. Rev. A **73**, 012717 (2006).

[18]K. L. Nixon, A. J. Murray, O. Al-Hagan, D. H. Madison, and C. Ning, J. Phys. B **43**, 035201 (2010).

[19]M. J. Hussey, and A. J. Murray, J. Phys. B **38**, 2965 (2005).

[20]J. Colgan, M. S. Pindzola, F. Robicheaux, C. Kaiser, A. J. Murray, and D. H. Madison, Phys. Rev. Lett. **101**, 233201 (2008).

[21]A. Senftleben, O. Al-Hagan, T. Pflüger, X. Ren, D. Madison, A. Dorn, and J. Ullrich, J. Chem. Phys. **133**, 044302 (2010).

[22]D. H. Madison, and O. Al-Hagan, J. At. Mol. and Opt. Phys. **2010**, 367180 (2010).

[23]K. L. Nixon, A. J. Murray, H. Chaluvadi, S. Amami, D. H. Madison, and C. Ning, J. Chem. Phys. **136**, 094302 (2012).

[24]J. Gao, D. H. Madison, and J. L. Peacher, J. Chem. Phys. **123**, 204314 (2005).

[25]A. Senftleben, T. Pflüger, X. Ren, B. Najjari, A. Dorn, and J. Ullrich, J. Phys. B **45**, 021001 (2012).

[26]X. Ren, A. Senftleben, T. Pflüger, A. Dorn, J. Colgan, M. S. Pindzola, O. Al-Hagan, D. H. Madison, I. Bray, D. V. Fursa, and J. Ullrich, Phys. Rev. A **82**, 032712 (2010).

[27]S. Xu, X. Ma, X. Ren, A. Senftleben, T. Pflüger, A. Dorn, and J. Ullrich, Phys. Rev. A **83**, 052702 (2011).

[28]J. Ullrich, R. Moshammer, A. Dorn, R. Dörner, L. P. H. Schmidt, and H. Schmidt-Böcking, Rep. Prog. Phys. **66**, 1463 (2003).

[29]W. C. Wiley, and I. H. McLaren, Rev. Sci. Instrum. **26**, 1150 (1955).

[30]X. Liu, and D. E. Shemansky, J. Geophys. Res. **111**, A04303 (2006).

[31]J. Gao, J. L. Peacher, and D. H. Madison, J. Chem. Phys. **123**, 204302 (2005).

[32]J. Gao, D. H. Madison, and J. L. Peacher, Phys. Rev. A **72** (2005).

[33]J. Gao, D. H. Madison, and J. L. Peacher, J. Chem. Phys. **123**, 204314 (2005).

[34]C. Lee, W. Yang, and R. G. Parr, Phys. Rev. B **37** (1988).

[35]C. F. Guerra, J. G. Snijders, G. t. Velde, and E. J. Baerends, Theor. Chem. Acc. **99** (1998).

[36]S. J. Ward, and J. H. Macek, Phys. Rev. A **49**, 1049 (1994).

[37]J. B. Furness, and I. E. McCarthy, J. Phys. B: At. **6**, 2280 (1973).

[38]J. P. Perdew, and A. Zunger, Phys. Rev. B **23**, 5048 (1981).

[39]N. T. Padial, and D. W. Norcross, Phys. Rev. A **29**, 1742 (1984).

[40]X. Ren, T. Pflüger, J. Ullrich, O. Zatsarinny, K. Bartschat, D. H. Madison, and A. Dorn, Phys. Rev. A **85**, 032702 (2012).

[41]R. F. Frey, and E. R. Davidson, J. Chem. Phys. **88**, 1775 (1988).

## VI Young's Double Slit Interference for Quantum Particles

Zehra Nur Ozer[1], Hari Chaluvadi[3], Melike Ulu[1], Mevlut Dogan[1], Bekir Aktas[2], and Don Madison[3]

[1]*Department of Physics, e-COL Laboratory, Afyon Kocatepe University, 03200, Afyonkarahisar, Turkey*

[2]*Department of Physics, Gebze High Technology Institute, Gebze, Turkey*

[3]*Department of Physics, Missouri S&T, Rolla, Missouri, USA*

### Abstract

For the last 50 years, there has been considerable interest in the possibility of observing the equivalence of a Young's double-slit wave interference at the quantum level for diatomic molecules. For electron-impact ionization of diatomic molecules, indirect evidence for this type of interference has been found by changing the energy (wavelength) of the ejected electron while keeping the incident projectile scattering angle fixed. The present work represents an experimental and theoretical collaboration to better understand the physics of this type of interference. In addition to examining the effect of changing the ejected electron energy for a fixed scattered projectile angle, we have also examined the effect of keeping the ejected electron energy fixed while varying the projectile scattering angle. Model calculations are performed for three different types of possible two-center interference effects, and it is found that the most important one is diffraction of the projectile off two scattering centers.

### Introduction

In the famous Young's double slit experiment, the wave nature of light was demonstrated by observing the constructive and destructive interference pattern resulting from two light waves emitted from two closely spaced slits. In 1966 Cohen and Fano [1]

suggested a quantum mechanical equivalent in which light incident on the double slits is replaced by light incident on and ionizing a diatomic molecule. Cohen and Fano [1] considered the two atoms in the molecule as independent absorbers of light which then became two separate sources for the emission of photoelectrons which would then produce an interference pattern. Due to particle-wave duality, similar interference effects should be expected if the incident light is replaced by particles and in 2001, Stolterfoht et al. [2] reported evidence for interference effects for $Kr^{34+}$ ionizing $H_2$ in which the ejected electrons were detected but the scattered projectiles were not. These cross section measurements were doubly differential in the energy and angle of the ejected electron so we will label them DDCS(electron). In the Cohen and Fano [1] model where the interference arises from electron waves being emitted from two different centers, one would expect that the important parameter would be how the wavelength of the emitted electron compared to the slit separation (i.e., internuclear distance) so measurements were performed as a function of the electron energy (i.e., wavelength).

Since the first DDCS(electron) measurements were reported for heavy particle impact, there have been a large number of papers published for different heavy projectiles and different energy ranges [3-9]. However, all these measurements were performed as a function of the ejected electron energy. More recently, Alexander et al. [10] measured cross sections for 75-keV proton impact ionization of $H_2$. They performed a DDCS(projectile) measurement where the energy and angle of the scattered proton is measured instead of the ejected electron. They showed that the interference effects were more sensitive to the angular dependence of the scattered projectile than to the energy dependence of the ejected electron. Egodapitiya *et al*. [11] showed that, for heavy

particles, one can control the perpendicular width of the projectile wave packet such that either both scattering centers are exposed to the beam ($H_2$ scattering) or only one scattering center is exposed (H scattering) and interference effects are seen when both centers are exposed and no interference is seen when only one center is exposed. Using this technique, Sharma *et al.* [12] showed that one can simultaneously measure cross sections for atomic hydrogen and molecular hydrogen and get the interference effects in a single measurement without relying on any theoretical calculations or second independent experiment.

Electrons as projectiles should be better than heavy particles for investigating interference effects since they have larger de Broglie wavelengths for identical velocities and are more easily deflected. Also, it is much easier to measure fully differential cross sections [normally called triply differential cross sections (TDCS)], which should be more sensitive to interference than DDCS measurements. For TDCS measurements, the energy and angular location of both final state electrons are simultaneously determined. Murray *et al*. [13] were the first to look for interference effects in low energy TDCS measurements for electron-impact ionization of $H_2$ and they found no evidence for interference.

Cohen and Fano [1] pointed out that, since the measured cross sections typically fall by orders of magnitude as a function of electron energy, the interference effects can be seen more readily by taking a ratio of the molecular cross section to the corresponding atomic cross sections. This ratio is called the interference factor ($I$), and the idea is that the cross section for a diatomic molecule should be equal to the atomic cross section times the interference factor, which should be an oscillating function that exhibits the

constructive and destructive interference effects. Stia *et al*. [14] examined the interference factor for electron-impact ionization of $H_2$ and they found that the TDCS interference factor for electron-impact ionization could be approximated the same as Cohen and Fano [1] found for photoionization:

$$I^{CF} = \frac{\sigma_{H_2}}{2\,\sigma_H} = 1 + \frac{\sin(QD)}{QD} \qquad (52)$$

Here $\mathbf{Q} = \mathbf{k}_0 - \mathbf{k}_a - \mathbf{k}_b$ is the momentum transferred to the residual (recoil) ion, $\mathbf{k}_0, \mathbf{k}_a$ and $\mathbf{k}_b$ are the momentum of the incident, scattered and ejected electrons, respectively, and $D$ is the equilibrium internuclear distance in the target molecule (1.4 a.u. for $H_2$). All molecular orientations have been averaged in the evaluation of Eq. (1).

Typical (*e*,2*e*) TDCS measurements plotted as a function of the ejected electron angle for a fixed projectile scattering angle exhibit a large peak for small ejection angles and a smaller peak for large ejection angles. (Although we do not know which electron is the projectile and which one is ejected, for discussion purposes we will refer to the faster final-state electron as the scattered projectile and the slower electron as the ejected electron.) The small-angle peak is called the binary peak, since it is normally close the classical billiard ball angle for a collision between the incident electron and an electron at rest. The large-angle peak is called the recoil peak and it is attributed to electrons backscattered from the nucleus. Depending on the kinematics, the interference factor of Eq. (52) predicts that the molecular recoil peak should be either suppressed or enhanced relative to the atomic one.

Milne-Brownlie *et al*. [15] measured TDCS for 250-eV electron-impact ionization of $H_2$ and three different ejected electron energies. For the kinematics of their

experiment, Eq. (52) predicts that the recoil peak for $H_2$ should be suppressed relative to the atomic cross section and this was verified by their experiment. Milne-Brownlie *et al*. [15] just looked at the relative sizes of the binary and recoil peaks and not directly at the interference factor *I*. Next Casagrande *et al.* [16] performed a similar experiment for higher energies (~600 eV) and they looked directly at the experimental interference factor of Eq. (52), which predicted suppression of the recoil peak for some energies and enhancement for other energies, and they found good agreement with $I^{CF}$.

Consequently, the current situation for electron-impact TDCS is that existing measurements of the interference parameter *I* are in good agreement with $I^{CF}$, which is based upon the assumption that the two atoms in the molecule are independent absorbers of energy which then became two separate sources for the emission of electrons which then produce an interference pattern.

Both of the TDCS studies reported so far were performed for an ejected electron energy scan for a fixed projectile scattering angle similar to the DDCS(electron) studies for heavy projectiles. As mentioned above, Alexander *et al*. [10] showed from DDCS(projectile) measurements that interference effects were more sensitive to scanning the projectile scattering angle than to scanning the ejected electron energy for proton collisions. In the Cohen-Fano model, the incident projectile (or light) is just a source of energy which is transferred to the atoms, causing them to become an electron-emitter, and one would expect a weak dependence on the projectile scattering angle and a strong dependence on the ejected electron wavelength. If the projectile scattering angle is more important than the ejected electron energy, the current model of interference resulting from electron waves emitted from two centers would come into question.

Here we report a study of the interference factor I for 250-eV electron-impact ionization for both an energy scan with a fixed projectile angle and a projectile angle scan with a fixed ejected electron energy. We find that the interference factor: (1) has significantly more structure than predicted by $I^{CF}$ and (2) there is a stronger dependence on projectile scattering angle than on ejected electron energy. These results indicate that the current model is incomplete and that additional two-center effects are important for these energies. We investigate three possible two-center effects: (1) an incident electron diffracted by two scattering centers; (2) a scattered projectile in the field of two scattering centers; and (3) an ejected electron in the field of two scattering centers. We find that the most important double-slit effect is the incident electron diffracted by two scattering centers.

To validate our experimental results, we chose the same kinematics as Milne-Brownlie *et al*. [15] for the energy scan and we followed the same procedure as both Milne-Brownlie *et al*. [15] and Casagrande *et al.* [16], who compared the molecular $H_2$ results to atomic He instead of atomic H. From an experimental point of view, using He is obviously desirable due to the difficulty of measuring atomic H cross sections. However, the implicit assumption is that single-center scattering effects are the same for both H and He such that the interference factor ratio contains only double-scattering effects. To our knowledge, this assumption has never been checked. Our results provide some indirect evidence for the validity of this assumption.

## Experimental Apparatus and Procedure

This apparatus has been used before in several experiments [17-20] by Albert Crowe's group in Newcastle. The experimental apparatus, acquired from a UK grant, was moved to Afyon Kocatepe University, Turkey, in 2007 and is now used in electron-

electron coincidence experiments. The experimental setup and procedure are in principle identical to those used by Sise *et al.* [21]. The description of the apparatus can be divided into (a) the implementation of the general principles of the electron spectrometer with special features for the electronic detection and (b) the data acquisition systems. The electron spectrometer consists of an electron gun, two hemispherical analyzers and a Faraday cup. All these components are housed in a vacuum chamber with a base pressure of ≈8 x $10^{-8}$ mbar. The spectrometer is kept in the vacuum chamber with μ-metal shielding, which reduces the surrounding magnetic fields in addition to the Helmholtz coils.

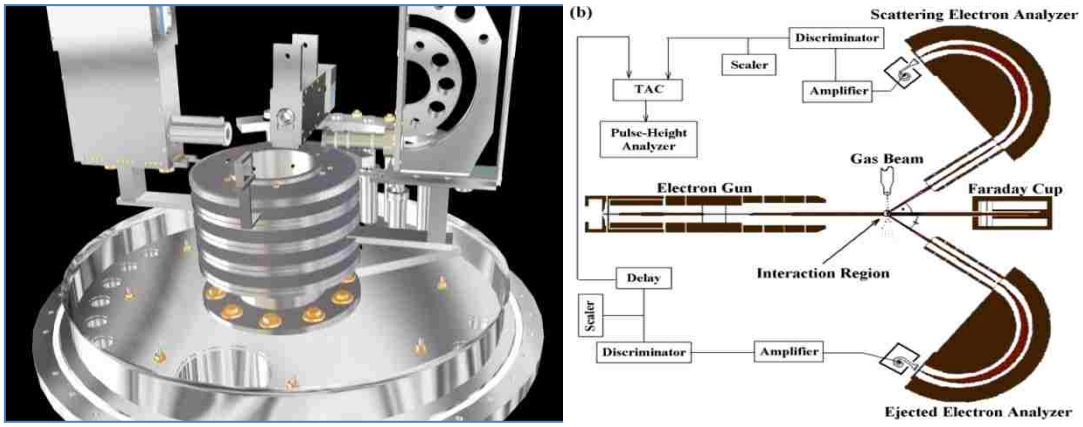


Figure. 1. Sketch of electron spectrometer. The main components are: (a) electron gun, two electron analyzers and Faraday cup; and (b) coincidence electronics used to accumulate the coincidence timing spectrum at each set of kinematics.

Figure 1(a), shows a schematic representation of the present experimental apparatus. The energy of the electron beam could be varied between 40 and 350 eV, with an energy width resolution less than 0.6 eV. The typical electron-beam currents used in these experiments ranged from 3 to 5 μA, as detected on the Faraday cup.

The electron beam was crossed perpendicularly with a gas beam, formed by a nozzle with 2 mm diameter. In a well defined electric field configuration, the electrons

are projected onto the electron analyzers. The two electron analyzers are located on separate turntables inside the vacuum chamber which can rotate around the detection plane. The effective angular range is limited by the presence of the Faraday cup in forward angles and the electron gun in the backward angles. To reduce the angular limitations, a small Faraday cup is placed onto the large Faraday cup which allows us to measure scattering angles down to 35 degrees.

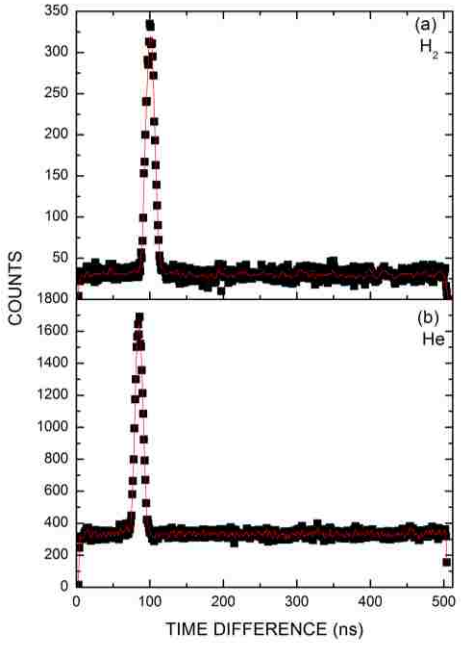


Figure. 2.Typical coincidence peaks for $H_2$ (a) and He (b) for $E_0$=250 eV,$E_b$=50 eV, $\Theta_a$=-15$^0$.

The method used for computerized data collection and analysis has also been described in detail in [21, 22]. The electron beam is produced by the electron gun via a filament crossed with the gas. The two outgoing electrons are detected using hemispherical electron analyzers with channel electron multipliers (CEM), [Fig. 1(b)]. The signals acquired from the CEMs are processed via amplifier and discriminator circuits. The two time-correlated electrons are detected in coincidence. The output pulses

from the coincidence electronics are recorded via a Trump-PCI interface card as a time spectrum which contains the true coincidence signal. Results were recorded by computer software (Maestro) and saved before the analyzer is rotated to another angle. The true coincidence count rate was determined in an usual way, from the difference between true-plus-random and random coincidence rates. The statistical accuracy of the true coincidence data was determined by the uncertainty in the measurement of both the true and random coincidence counts. The interaction region must be precisely positioned at the center of the rotation of the analyzers and the electron gun (50 mm away from the interaction region).

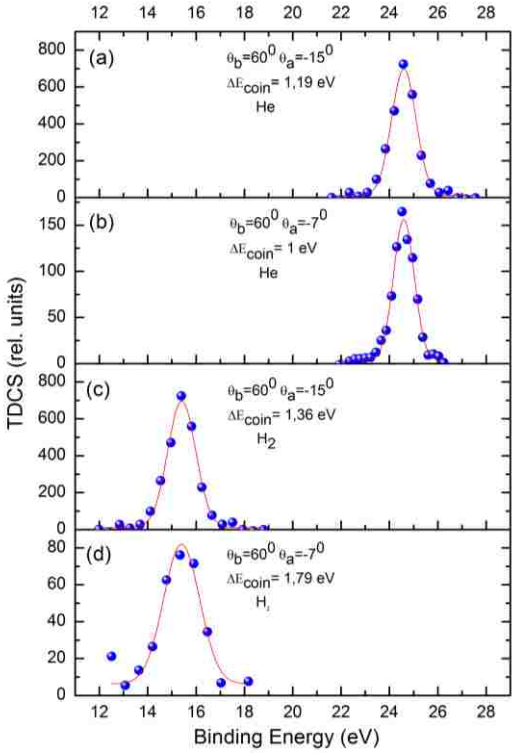


Figure 3. Binding energy spectra for He and $H_2$. The kinematics are $E_0$=250 eV and $E_b$=50 eV. Panels (a) and (b) show He binding energy spectra for projectile scattering angles of $-15^0$ and $-7^0$. Panels (c) and (d) show the binding energy spectra for $H_2$ also for projectile scattering angles of $-15^0$ and $-7^0$.

To establish the kinematics for the measurement, the incident and ejected electron energies were chosen and the scattered electron energy was determined by energy conservation:

$$E_0 = E_a + E_b + V_1 \quad (53)$$

Here ($E_0$, $E_a$, $E_b$) are the incident, scattered and the ejected electron energies, respectively, and $V_1$ is the ionization potential (24.6 eV for He and 15.4 eV for $H_2$).

Measurements in the study were obtained using an asymmetric coplanar geometry. In this geometry, the two outgoing and the incident electrons are all in the same plane. Figure 2 shows a coincidence peak obtained for $H_2$ and He for the same kinematics. The width of the coincidence peak at half maximum (FWHM), under the same conditions for both targets, is approximately 12 ns.

The uniform background in the coincidence spectra is caused by the arrival of fully uncorrelated electrons in the detectors. The peak that is superimposed on these background contributions is the coincidence peak for the fully correlated events. Figure 3 presents the binding energy spectra that show the coincidence count rates as a function of scattered electron energy for He and $H_2$ targets. The $H_2$ binding energy spectrum is broader than the He spectrum, as was also seen in Refs. [15, 16]. The ejected electron energy is 50 eV for both cases. Binding energy spectrum were recorded for each energy and projectile scattering angle.

## Theoretical Framework

The most sophisticated current theories for electron impact molecular ionization process are the first born approximation in which the two-center continuum wave approximation with correct boundary conditions is applied in both the incident and exit channels [23], the molecular three-body distorted wave approximation (M3DW) coupled

with an orientation-averaged molecular orbital approximation [24], and the time dependent close coupling (TDCC) approximation [25]. Al-Hagan *et al*. [26] showed that the M3DW method yielded good agreement with experimental TDCS data for $H_2$ and this is the theoretical approach we will use here.

The molecular three-body distorted wave (M3DW) approximation has been presented in previous publications [27-29] so only the main points of the theory will be presented. The triple differential cross section (TDCS) for the M3DW is given by

$$\frac{d\sigma}{d\Omega_a d\Omega_b dE_b} = \frac{1}{(2\pi)^5}\frac{k_a k_b}{k_i}\left(|T_{dir}|^2 + |T_{exc}|^2 + |T_{dir} - T_{exc}|^2\right) \qquad (54)$$

where $\vec{k}_i$, $\vec{k}_a$, and $\vec{k}_b$ are the wave vectors for the initial, scattered and ejected electrons, $T_{dir}$ is the direct scattering amplitude, and $T_{exc}$ is the exchange amplitude. The direct scattering amplitude is given by:

$$T_{dir} = \left\langle \chi_a^-(\vec{k}_a, \mathbf{r}_1)\chi_b^-(\vec{k}_b, \mathbf{r}_2)C_{scat-eject}(r_{12}^{ave})\,|V - U_i|\,\phi_{DY}^{OA}(\mathbf{r}_2)\chi_i^+(\vec{k}_i, \mathbf{r}_1)\right\rangle \qquad (55)$$

where $r_1$ and $r_2$ are the coordinates of the incident and the bound electrons, $\chi_i, \chi_a$, and $\chi_b$ are the distorted waves for the incident, scattered, and ejected electrons, respectively, and $\phi_{DY}^{OA}(r_2)$ is the initial bound-state Dyson molecular orbital averaged over all orientations. The factor $C_{scat-eject}(r_{12}^{ave})$ is the Ward-Macek average Coulomb-distortion factor between the two final state electrons [30], *V* is the initial state interaction potential between the incident electron and the neutral molecule, and $U_i$ is a spherically symmetric distorting potential which is used to calculate the initial-state distorted wave for the

incident electron $\chi_i^+(\vec{k}_i, \mathbf{r}_1)$. For the exchange amplitude $T_{exc}$, particles 1 and 2 are interchanged in Eq. (4).

The Schrödinger equation for the incoming electron wave-function is given by

$$(T + U_i - \frac{k_i^2}{2})\chi_i^+(\vec{k}_i, r) = 0 \qquad (56)$$

where $T$ is the kinetic energy operator and the '+' superscript on $\chi_i^+(\vec{k}_i, \mathbf{r})$ indicates outgoing wave boundary conditions. The initial state distorting potential contains three components $U_i = U_s + U_E + U_{CP}$, where $U_s$ contains the nuclear contribution plus a spherically symmetric approximation for the interaction between the projectile electron and the target electrons, which is obtained from the quantum-mechanical charge density of the target. The charge density is $2|\phi_{DY}|^2$ (the 2 is for double occupancy and the original non-averaged Dyson orbital is used). The nuclear contribution to $U_s$ is the interaction between the projectile electron and the two nuclei averaged over all orientations. Averaging the nuclei over all orientations is equivalent to putting the nuclear charge of 2 on a thin spherical shell whose radius is the distance of the nuclei from the center of mass (c.m.) (0.7 $a_0$).

$U_E$ is the exchange potential of Furness-McCarthy (corrected for sign errors) [31] which approximates the effect of the continuum electron exchanging with the passive bound electrons in the molecule, and $U_{CP}$ is the correlation-polarization potential of Perdew and Zunger [32] (see also Padial and Norcross [33]).

In Eq. (4), the final state for the system is approximated as a product of distorted waves for the two continuum electrons $(\chi_a^-, \chi_b^-)$ times the Ward-Macek average Coulomb-distortion factor $C_{scat-eject}$. The final-state distorted waves are calculated the same as the initial state except that the final state charge density is used to calculate $U_s$. The final state charge density is obtained the same as the initial state except that the occupancy number is unity. Additional details can be found in Madison and Al-Hagan [24].

## Results and Discussion

Figures 4 and 5 compare the experimental and theoretical TDCS for 250-eV electron-impact ionization of He and $H_2$. On each figure, the left hand column is the energy scan for a fixed projectile scattering angle of $15^0$ and the right hand column is a scattered projectile angular scan for a fixed ejected electron energy of 50 eV. The typical binary peaks for small ejection angles and recoil peaks for large ejection angles are evident from the figures (although the recoil peaks tend to be very small for these kinematics). The theoretical and experimental results are normalized to unity at the binary peak. The solid circles are the present results and the stars are the results of Milne-Brownlie *et al*. [15]. It is seen that the present experimental results are in very good agreement with those of Milne-Brownlie *et al*. [15] with the possible exception of the He recoil peak for 15 eV. However, the Milne-Brownlie *et al*. [15] measurements were made for 10 eV, which is inaccessible for us so we have plotted their 10-eV results with our 15-eV results.

It is seen that overall there is also very good agreement between experiment and theory. The only significant disagreement between experiment and theory is seen for the

He recoil peak for $7^0$ in the angular scan. The disagreement with the Milne-Brownlie *et al*. [15] recoil peak for He 15 eV in the energy scan is not due to the energy difference mentioned above. We calculated M3DW TDCS for 10-eV ejected electron energy (same as the data) and our theoretical results are noticeably smaller than the Milne-Brownlie et al. [15] recoil peak and closer to the present 15-eV recoil peak. We would also note that there is a small difference between the two experiments for the 20-eV He binary peak position and the theoretical results are in excellent agreement with the present measurements.

Looking only at the TDCS angular distributions, one cannot see anything remarkably different between the energy scan and angular scan. To see the possible effects of Young's-type interference, we need to look at the ratio of the molecular cross section to the atomic cross section to get the interference factor I. Figure 6 shows the theoretical and experimental I factors for the energy and angular scans (using He for the denominator). We have arbitrarily normalized theory to unity at one of the peaks and experiment to the best visual fit to theory. Also shown is the Cohen-Fano of Eq. (52) (dashed blue curve).

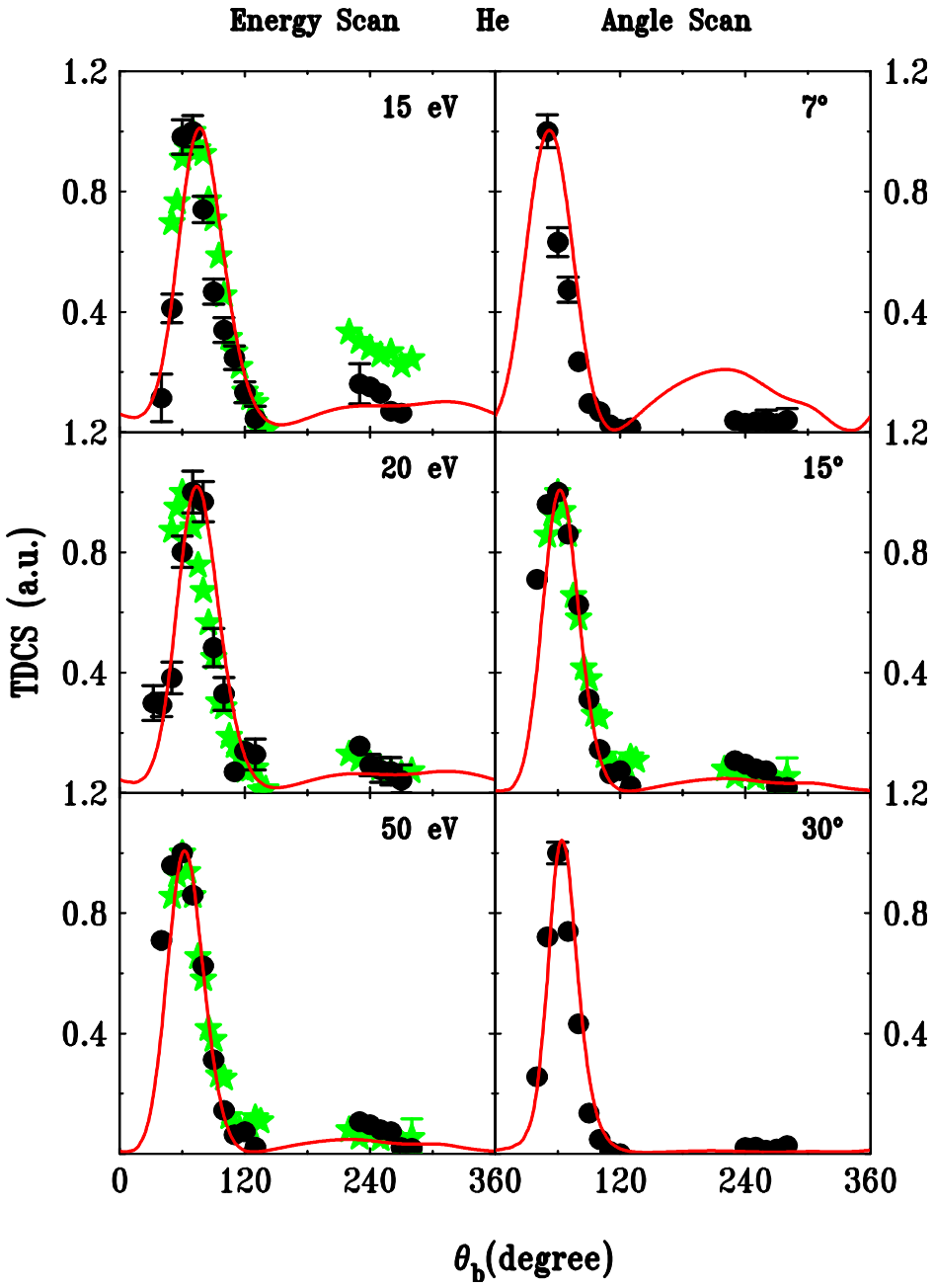


Figure 4 TDCS for 250-eV electron impact ionization of He as a function of the ejected electron angle $\theta_b$. For the left-hand column, the projectile scattering angle is $\theta_a=15^0$ and the energy of the ejected electron is noted. For the right-hand column, the ejected electron energy is 50 eV and the projectile scattering angle is noted. Solid circles- present data, stars- data of Milne-Brownlie et al. [15], and solid (red) curve- 3DW.

Overall, there is a qualitative agreement with $I^{CF}$. As mentioned above, Casagrande et al. [16] presented these same ratios for higher electron energies (~600 eV)

and they found good agreement with the shape of the simple $I^{CF}$ factor in their energy scan results. However, from Fig. 6 it is seen that both experiment and theory exhibit a much more complicated structure, particularly for the binary region for the present kinematics. In general, there is very good agreement between the M3DW *I* factor and experiment.

In the energy scan, the M3DW *I* factors have a triple-peak structure for the binary region. Although the first peak is in an angular range inaccessible to experiment, the other two peaks lie mostly in the measured angular range. For the two lower energies, there is sufficient scatter in the data so that all one can say is that the data is consistent with the possibility of two peaks. However, for the 50-eV case, it is clear that the experiment also has two peaks, although the second experimental peak appears to be smaller than the predicted theoretical one. For the recoil peak angular range, both experiment and the M3DW predict a greater suppression relative to the binary peak than that predicted by the $I^{CF}$ factor.

Comparing the I factors for the energy scan and angular scan, it is seen that the I-factor changes more dramatically with changing angle than with changing energy. For the energy scan, there are three peaks in the binary region for all three cases and, with increasing energy, the only noticeable changes are relative peak heights and a small change in peak location. For the angle scan, on the other hand, the M3DW I factor has two peaks at 70, three peaks at 150, and only a single peak with a shoulder at 300 and the experimental data exhibit this same structure!

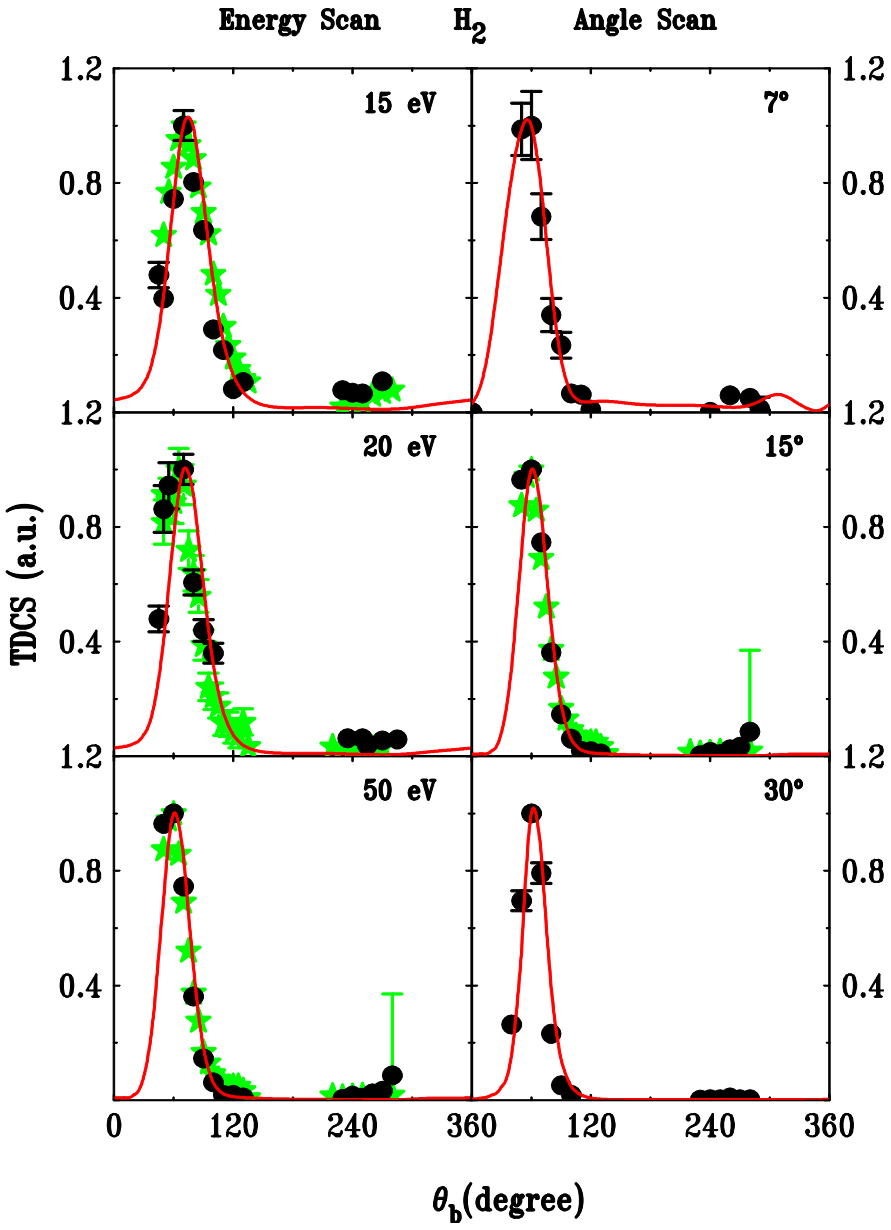


Figure 5. Same as Fig. 4 except for ionization of $H_2$.

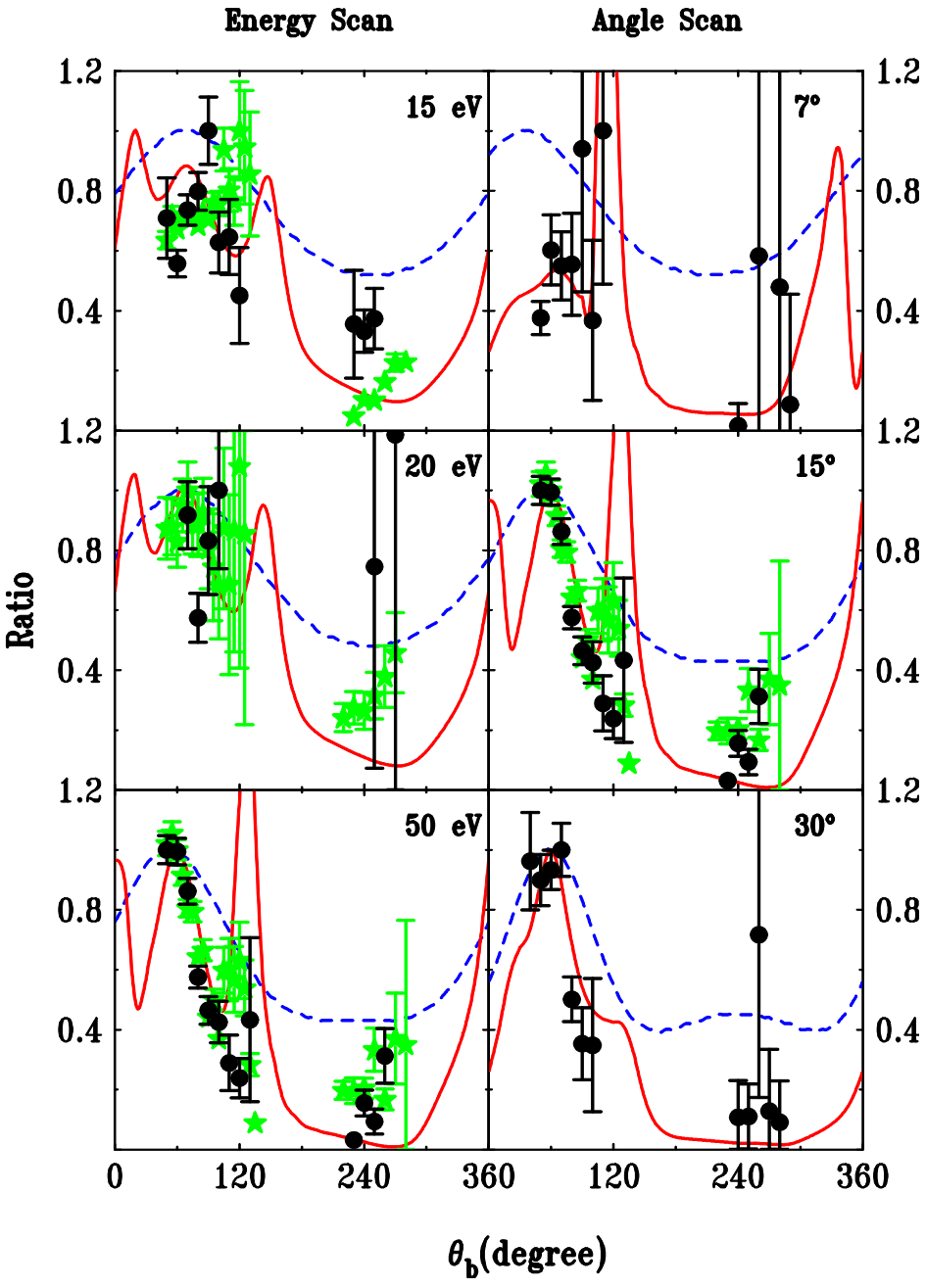


Figure 6 Interference factor for 250-eV electron impact ionization of $H_2$ and He as a function of the ejected electron angle $\theta_b$. For the left hand column, the projectile scattering angle is $\theta_a=15^0$ and the energy of the ejected electron is noted. For the right-hand column, the ejected electron energy is 50 eV and the projectile scattering angle is noted. Solid circles- present data, stars- data of Milne-Brownlie *et al*. [15], solid (red) curve- M3DW, and dashed (blue) curve- $I^{CF}$.

Previously, the observation of a suppressed recoil peak for molecular $H_2$ was thought to be sufficient evidence indicating Young's-type interference [15]. Here we see a much larger and more interesting consequence of interference with significant structure in the binary region which has not been seen before. The important question concerns the physical effects which cause this structure. Obviously, there are going to be a lot of different types of interference effects contributing to any quantum mechanical calculation. Presumably, taking the ratio of the molecular to atomic cross sections isolates the molecular double slit effects. However, the $I^{CF}$ factor attributed to the ejected electron being emitted from two nuclear centers is just one of the possible molecular double-slit interference effects. A second possible interference effect is the diffraction of the incoming projectile from two scattering centers, and a third possibility is the motion of the scattered projectile in the field of two scattering centers.

One of the big advantages of the present perturbation approach lies in the fact that different physical effects like this can be isolated in the calculation. For example, the effect of the ejected electron being emitted from two scattering centers can be modeled by performing a helium calculation except replace the ejected electron distorted wave $\chi_b^-(\vec{k}_b, \mathbf{r}_2)$ calculated using a helium-ion potential with a $H_2$ distorted wave calculated using the $H_2$-ion potential. Likewise, the effect of the scattered projectile being emitted from two scattering centers can be modeled by performing a helium calculation except replace the scattered electron distorted wave $\chi_a^-(\vec{k}_a, \mathbf{r}_1)$ calculated using a helium-ion potential with a $H_2$ distorted wave calculated using the $H_2$-ion potential. Finally, the effect of the incident electron diffracting from two scattering centers can be modeled by performing a helium calculation, except replace the initial channel helium wavefunctions

with molecular wavefunctions (i.e., molecular bound-state wavefunction and the incident channel distorted wave calculated using the neutral molecular distorting potential).

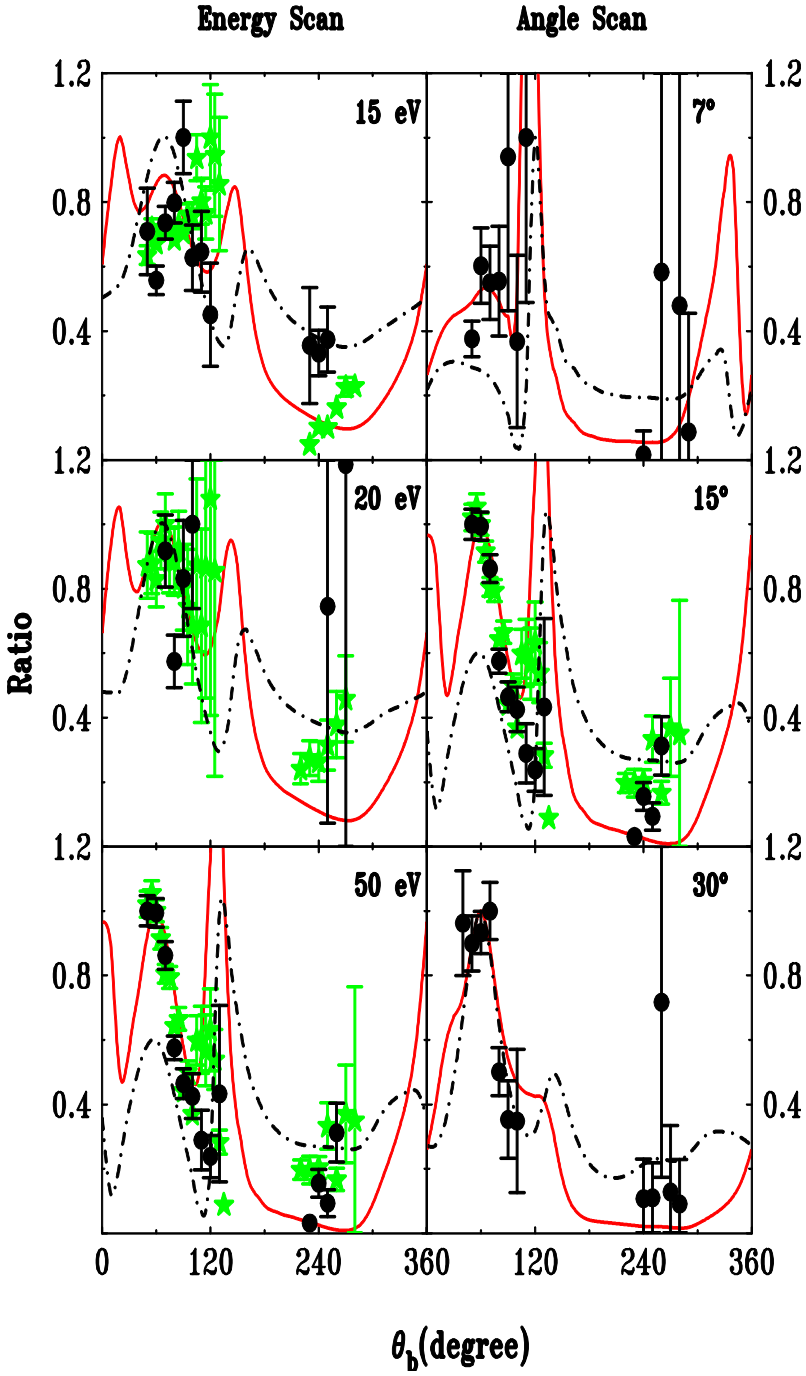


Figure 7. Same as Fig. 6 except that the solid (red) curve is the full M3DW calculation, and the solid (black) curve is the model calculation with the only molecular contribution being the diffraction of the incident projectile from two scattering centers.

We have performed these three different model calculations and the results clearly demonstrate that the most important process is the diffraction of the incident electron from two scattering centers. In Fig. 7, the *I* factor is presented for the full molecule calculation (solid red curve) and the model calculation treating only the initial state as a molecule (dot-dashed black curve). It is seen that the two calculations yield very similar *I* factors, which means that most of the double-slit interference effects contributing to the structure in the *I* factor is contained in the diffraction of the incoming projectile from two scattering centers.

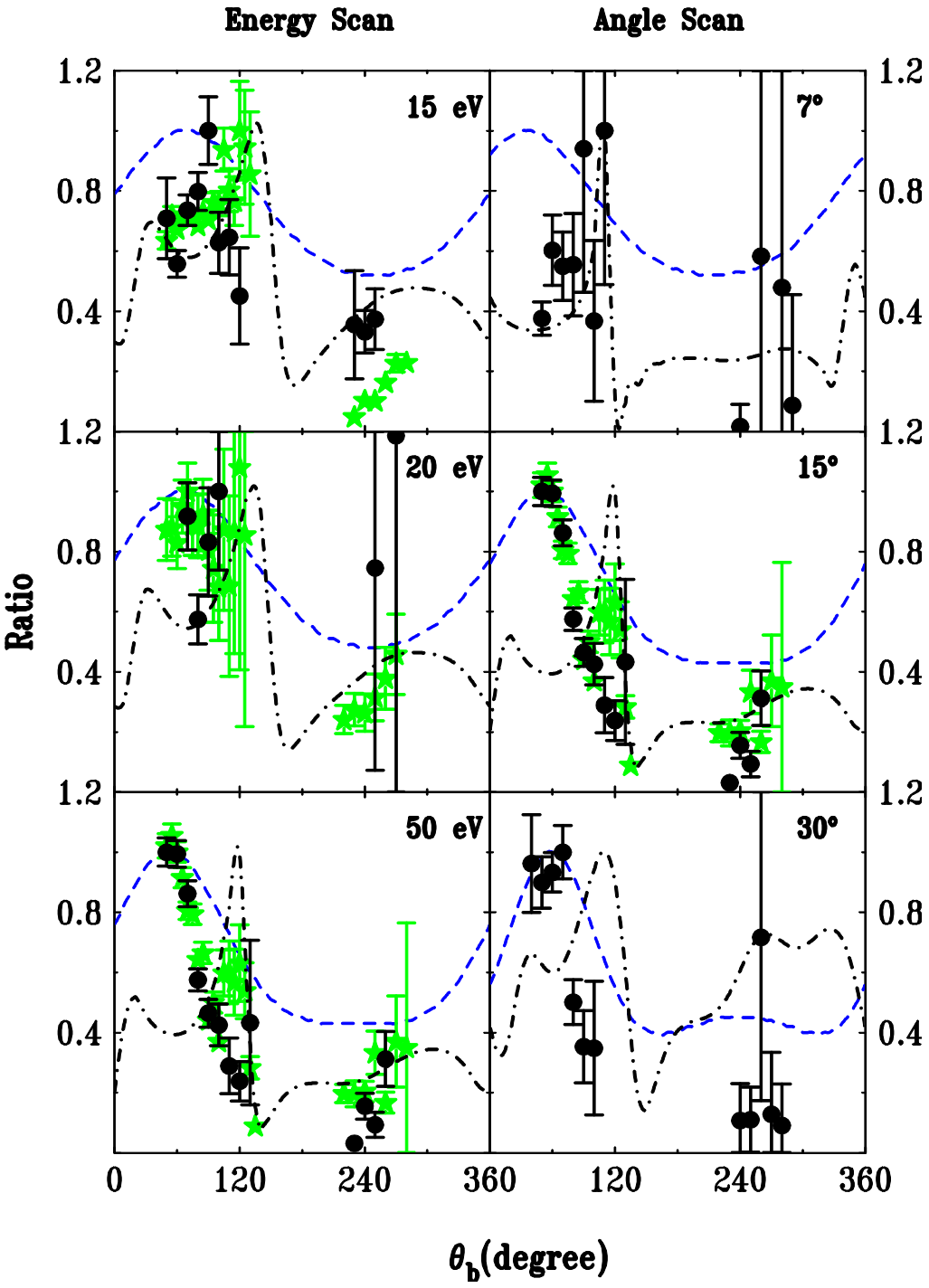


Figure 8. Same as Fig. 6 except that the dashed-dot curve is the model calculation with the only molecular contribution being the emission of the ejected electron from two scattering centers and the dashed (blue) curve is $I^{CF}$.

It is also interesting to compare the *I* factor by treating just the ejected electron as a molecular wave with $I^{CF}$, since they are presumably modeling the same physical effects. This comparison is contained in Fig. 8 where it is seen that the two calculations yield very different results. Although $I^{CF}$ was valid for 600-eV electrons [16], it is clearly not a good approximation for the present energies.

## Conclusion

This paper presents experimental and theoretical results for 250-eV electron-impact ionization of He and $H_2$. Results were presented for (1) an ejected electron energy scan of 15, 20 and 50 eV for a fixed projectile scattering angle of $15^0$ and for (2) a projectile angular scan of $7^0$, $15^0$, and $30^0$ for a fixed ejected electron energy of 50 eV.

We have examined the *I* factor and we found that the *I* factor has significantly more structure than $I^{CF}$ and that it is more sensitive to the angle scan than to the energy scan. The Cohen-Fano model where the two atoms in the molecule are independent absorbers of energy which then became two separate sources for the emission of electrons was previously believed to accurately describe Young's-type interference effects for electron-impact TDCS of diatomic molecules. Here we see that, while there is an overall qualitative agreement with $I^{CF}$, both experiment and theory predict a much more complicated interference pattern in the binary peak region.

We separately examined the three different types of contributions to the microscopic double-slit interference pattern and found that the most important contribution comes from the incident projectile diffracting from two scattering centers. We also compared the contribution of the ejected electron being emitted from two scattering enters with $I^{CF}$, which presumably contains the same physical effects, and

found that the results were very different, indicating that $I^{CF}$ is not a good approximation for the kinematics considered here.

Obviously, any quantum-mechanical calculation can and will have multiple different types of interference effects contributing to the final results. The main idea of the *I* factor introduced by Cohen-Fano is that all of the non–two-center interference effects can be eliminated by dividing by the atomic cross section. Here, as in previous works, we have divided by atomic He cross sections instead of atomic H cross sections. Obviously, the practical problem is that experimental atomic H cross sections are very hard to measure. For several of the heavy-particle DDCS measurements referenced here [2–5,9,10], theoretical atomic H cross sections were used and that work has been criticized as not representing a clean comparison between experiment and theory. Using He allows for a clean comparison between experiment and theory. Helium is also appealing since it has the same number of electrons and protons as $H_2$. The only downside is that one cannot be sure that all of the non–two-center interference effects will have been divided out. Even if this is not the case, the comparison with theory is still valid. What will not be valid is our assumption that the observed structure results only from the three different types of possible two-center interference effects which we have identified. In Fig. 7, the solid (red) curve represents all the interference structure not contained in He (whether it be two-center or not). The dashed-dot curve represents the effect of the incident projectile diffracting from two scattering centers. The similarity of these two curves would indicate that most, if not all, of the structure seen in the solid (red) curve stems from two-center effects.

**Acknowledgements**

This work was supported by the Scientific and Technological Research Council of Turkey (TUBITAK) through grant 109T738. The theoretical work of H.C. and D.M. was supported by US National Science Foundation under Grant. No. PHY-1068237.

**References**

1. H. D. Cohen, and U. Fano, Phys. Rev. **150**, 30 (1966).
2. N. Stolterfoht, B. Sulik, V. Hoffmann, B. Skogvall, J.Y. Chesnel, J. Rangama, F. Fremont, D. Hennecart, A. Cassimi, X. Husson, A.L. Landers, J.A. Tanis, M.E. Galassi, and R. D. Rivarola, Phy. Rev. Lett. **87**, 023201 (2001).
3. N. Stolterfoht *et al.*, Phys. Rev. A **67**, 030702 (R) (2003).
4. S. Hossain, A.L. Landers, N. Stolterfoht, and J.A. Tanis, Phy. Rev. A **72**, 010701(2005).
5. D. Misra, U. Kadhane, Y.P. Singh, P.D. Tribedi, P. Fainstein, and P. Richard, Phy. Rev. Lett. **92**, 153201 (2004).
6. C. Dimopoulou et al., Phy. Rev. Lett. **93**, 123203 (2004).
7. O. Kamalou, J.Y. Chesnel, J. Hanssen, R.C. Stia, O.A. Fojon, R.D. Rivarola, and F. Fremont, Phy. Rev. A **71**, 010702(R) (2005).
8. D. Misra *et al.*, Phys. Rev. A **74**, 060701 (R) (2006).
9. J. Tanis et al., Phy. Rev. A **74**, 022707 (2006).
10. J.S. Alexander, A.C. LaForge, A. Hasan, Z.S. Machavariani, M.F. Ciappina, R.D. Rivarola, D.H. Madison and M. Schulz, Phys. Rev. A **78**, 060701(R) (2008).
11. K. N. Egodapitiya, S. Sharma, A. Hasan, A. C. Laforge, D. H. Madison, R. Moshammer, and M. Schulz, Phys. Rev. Lett. **106**, 153202 (2011).
12. S. Sharma, A. Hasan, K. N. Egodapitiya, T. P. Arthanayaka, G. Sakhelashvili, and M. Schulz, Phys. Rev. A **86**, 022706 (2012).
13. A.J. Murray, M.J. Hussey, C. Kaiser, J. Gao, J.L. Peacher, and D.H. Madison, Journal of Electron Spectroscopy and Related Phenomena **161**, 11 (2007).
14. C. R. Stia, A. O. Fojon, P. F. Weck, J. Hanssen, and R. Rivarola, J. Phys. B. **36**, L257 (2003).
15. D.A. Milne-Brownlie, M. Foster, J. Gao, B. Lohmann, and D.H. Madison, Phy. Rev. Lett. **96**, 233201 (2006).
16. E. M. Casagrande, A. Lahmam-Bennani, and D. H. Madison, J. Phys. B, **41,** 025204 (2008).
17. M. Dogan, and A. Crowe, J. Phys. B **33**, L461 (2000).
18. M. Dogan, and A. Crowe, J. Phys. B **35**, 2773 (2002).
19. M. Stevenson, and A. Crowe, J. Phys. B **37**, 2493, (2004).

20. M. Dogan, A. Crowe, K. Bartschat and P J Marchalant, J. Phys. B **31**, 1611 (1998).

21. O. Sise, M. Dogan, I. Okur and A. Crowe, Phys. Rev. A **84**, 022705 (2011).

22. M., Dogan, M., Ulu, O., Sise, J. Elect. Spect. Rel. Phen., 161, 58-62, (2007).

23. C. R. Stia, A. O. Fojon, P. F. Weck, J. Hanssen, B. Joulakian, and R. Rivarola, Phys. Rev. A **66**, 052709 (2002).

24. D.H. Madison and O. Al-Hagan, Journal of Atomic, Molecular, and Optical Physics 2010, 367180, (2010).

25. J. Colgan, M.S. Pindzola, F. Robicheaux, C. Kaiser, A.J. Murray, and D.H. Madison, Phys. Rev. Lett. **101**, 233201 (2008).

26. Ola Al-Hagan, Christian Kaiser, Don Madison and Andrew Murray, *Nature Physics* **5**, 59 (2009).

27. J. Gao, D.H. Madison, and J.L. Peacher, *J. Chem. Phys.* **123** 204314 (2005).

28. J. Gao, D.H. Madison, and J.L. Peacher, *Phys. Rev.* A **72** 032721 (2005).

29. J. Gao, D.H. Madison, and J.L. Peacher, *J. Chem. Phys*. **123** 204302 (2005).

30. S.J. Ward and J.H. Macek, *Phys. Rev*. A **49** 1049 (1994).

31. J.B. Furness and I.E. McCarthy, *J.Phys. B* **6** 2280 (1973).

32. J.P. Perdew and A. Zunger, *Phys. Rev.* B **23** 5048 (1981).

33. N.T. Padial and D.W. Norcross, *Phys. Rev*. A **29** 1742 (1984).

# VII Low energy (e,2e) coincidence studies from $NH_3$: Results from experiment and theory

Kate L Nixon[1], Andrew James Murray[1], Hari Chaluvadi[2], Chuangang Ning[3], James Colgan[4], and Don H. Madison[2]

[1]Photon Science Institute, School of Physics & Astronomy, University of Manchester, Manchester M13 9PL, Unied Kingdom.

[2]Department of Physics, Missouri University of Science and Technology, Rolla MO 65409, USA

[3]Department of Physics, State Key Laboratory of Low-Dimensional Quantum Physics, Tsinghua University, Beijing 100084, China

[4]Theoretical Division, Los Alamos National Laboratory, Los Alamos, NM 87545

## Abstract

Experimental and theoretical triple differential cross sections (TDCS) from ammonia are presented in the low energy regime with outgoing electron energies from 20 eV down to 1.5 eV. Ionization measurements from the $3a_1$, $1e_1$ and $2a_1$ highest occupied molecular orbitals were taken in a coplanar geometry. Data from the $3a_1$ and $1e_1$ orbitals were also obtained in a perpendicular plane geometry. The data are compared to predictions from the distorted wave Born approximation and molecular-three-body distorted wave models. The cross sections for the $3a_1$ and $1e_1$ orbitals that have *p*-like character were found to be similar, and were different to that of the $2a_1$ orbital which has s-like character. These observations are not reproduced by theory, which predicts the structure of the TDCS for all orbitals should be similar. Comparisons are also made to results from experiment and theory for the iso-electronic targets neon and methane.

## Introduction

The ionization of atoms and molecules by electron impact is important in many fundamental and applied areas. A full and detailed understanding of this process is however still incomplete. The technique of (e,2e) spectroscopy [1] provides the most comprehensive data from these electron impact ionization processes, since the experiments are kinematically complete. As such, sophisticated theoretical models describing these types of collision are most rigorously tested against (e,2e) data. Current state of the art models for atomic targets include relativistic and non-relativistic distorted wave Born approximations (DWBA) [2,3], time dependant close coupling (TDCC) [4] and convergent close coupling (CCC) theories [5], and R-matrix with pseudo-states models [6]. These calculations now provide good agreement with experiment over a wide energy range for lighter targets. Only the TDCC and DWBA models have been applied to molecular targets, the TDCC model currently being restricted to hydrogen. New theories are hence required to predict the ionization of more complex molecules. Many of the current predictions are based upon the DWBA. The molecular three-body distorted wave approximation (M3DW) [7] used in the present studies employs the Ward-Macek factor to include post-collision interactions. Alternatively Champion et al. [8] use three Coloumb waves to model the final state, often referred to as the BBK method. Toth and Nagy have developed a total screening model for their direct transition matrix elements [9].

The challenges that occur for ionization models from molecular targets are considerable, as the electron collision with a molecule gives rise to many additional complexities that need to be carefully considered. Most obvious of these is that the nuclei are distributed throughout the molecule, which leads to a reduction in symmetry of the

interaction compared to that for an atom. Given that the target molecules are also randomly aligned in almost all experimental studies, this presents a major challenge to any theory that wishes to directly compare to experiment. Additionally, since each atom within a molecule may act as a scattering centre, the collision dynamics are considerably more complex. Other properties unique to molecules include their internal rotational and vibrational degrees of freedom, which also may need to be considered. Many molecules have orbitals that are closely spaced in energy, and they may be liquids or solids under normal temperature and pressures. These complexities can be addressed by careful choice of the target under consideration, and by employing molecular beam ovens to yield sufficient vapour pressure in the interaction region to allow accurate experimental data to be obtained.

Ammonia ($NH_3$) is an excellent target to study from both experimental and theoretical aspects. It is gaseous at room temperature and has three well-separated orbitals (with ionization potentials of ~11, 16.74 and 27.74 eV) [R10], making measurements from individual states straightforward to conduct and analyze. Furthermore, since ammonia is a relatively simple molecule with only four atoms and ten electrons, this should aid in reducing the complexity of the theoretical computations.

Accurate wavefunctions for $NH_3$ are available using standard quantum chemical software packages, as established most recently by Zhu et al. [11]. Calculations of the momentum distributions derived from these wavefunctions were compared to electron momentum spectroscopy (EMS) data to confirm their quality. It has also been shown recently that a single centred molecular orbital can reproduce high-energy EMS data, suggesting that multi-centred wavefunctions may not be necessary in this regime [12].

Recent low energy or dynamical (e,2e) studies have highlighted the importance of electron-nuclei interactions in electron impact ionisation collisions [13,14]. These investigations show that spherical averaging of the nuclear frame can produce unrealistically low nuclear density for the atoms located away from the centre of mass (CM), i.e., the nuclear charge of such atoms is distributed on a sphere of radius equal to the distance between the CM and the nucleus. In turn this results in theory underestimating the scattering from these nuclei in the molecule. Improvement in agreement between experiment and theory was seen by increasing the nuclear contribution to the distorting potential, achieved through a reduction of the radius of the equivalent sphere of charge. This method demonstrates that important physical processes are probably being masked by the spherical averaging process.

The aim of the present study is to evaluate the influence various parameters have on the scattering dynamics. Initially the effect of the orbital character is assessed by comparing and contrasting the data from the two outermost orbitals of $NH_3$, which both have *p*-like character. The results are then compared to data from the third outermost orbital, that has *s*-like character. To assess the influence of the molecular structure, the data from $NH_3$ is then compared to results from the iso-electronic targets neon (Ne) and methane ($CH_4$). By studying neon, a comparison can be made between experimental and theoretical data without the added complexities introduced by a molecular target. This provides a baseline from which to assess the predictions for the different molecules. The M3DW model for the molecules contains the same scattering physics as for neon, but adopts a more complex molecular wavefunction for both the neutral molecule and ion. The model also includes a spherical averaging process to allow for the random

orientation of the molecules in the experiment. Finally, by comparing data from both atomic and molecular species, the influence of the nuclear frame on the scattering process can be ascertained. This is possible since methane and ammonia have a similar frame, with the light H nuclei separated from the heavier atom, whereas neon has all of the nuclear charge located at a single point in space.

By systematically assessing the effect of these parameters on the ionization process, the strengths and weaknesses of the models can be determined. This will allow further improvement and refinement of the models to increase the accuracy of the predictions. A steady improvement of the early atomic interaction models was achieved through systematic and detailed comparison to experimental (*e*,2*e*) data. It is expected that such improvements will also accrue for these new theories describing interactions with molecular targets, through a similar rigorous comparison to different species.

This paper is presented as follows. After this introduction the structure and orbitals of ammonia are briefly discussed in Sec molecular structure of ammonia. Section the experimental apparatus outlines key features of the (*e*,2*e*) spectrometer used to determine the triple differential cross sections (TDCS), and Sec. theoretical framework describes the models used to generate the predicted cross sections. Results from experiment and theory are compared in Sec. results and discussion. Data from coplanar scattering are given in Sec. A, and results from the perpendicular plane geometry are in section B. Conclusions from this work, together with suggestions for future studies are in Sec. conclusions

## Molecular Structure of Ammonia

Prior to considering electron impact ionization from $NH_3$, it is useful to describe the molecular structure and introduce the orbital labeling conventions used in this paper.

The structure of ammonia falls into the $C_{3v}$ group, having a trigonal pyramidal geometry. The centre of mass (CM) for this molecule does not correspond to the position of the nitrogen atom. This has a bearing on the calculations that are presented below, which average the molecular structure over all orientations prior to modelling the collision. This averaging (as described in Sec. IV ) is performed around the CM. For $NH_3$ this results in a nuclear charge structure consisting of two concentric thin spheres of charge: an *outer* sphere due to the hydrogen nuclei which is ~2 A° in diameter, and an *inner* spherical shell due to the nitrogen nucleus which is ~0.13 A° in diameter. Since no nuclei reside at the centre of mass of the molecule, the interior of the inner spherical charge shell is then field-free. Electrons that enter this small region will therefore not be deflected.

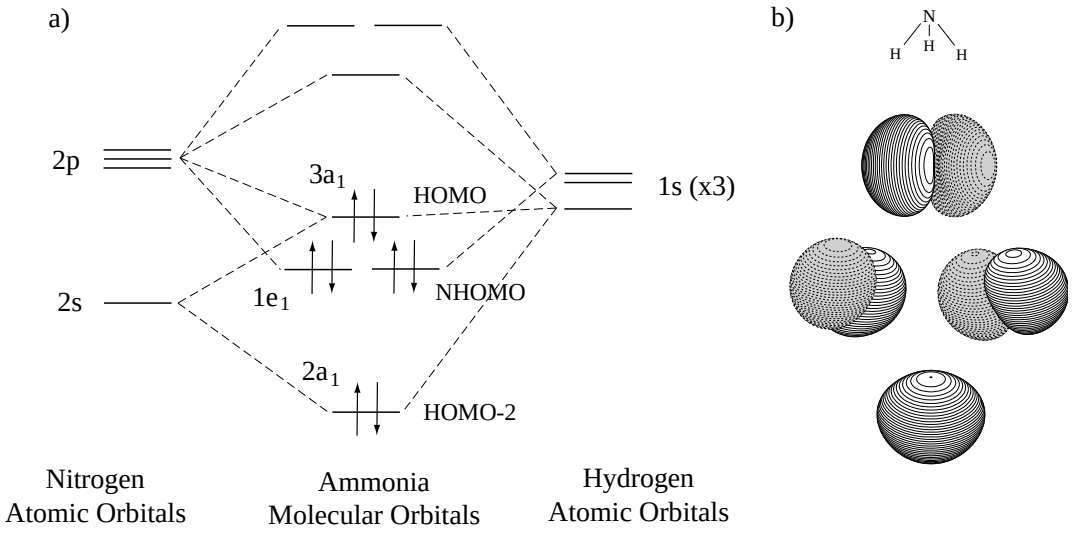


Figure 1. (a) Molecular orbital diagram of the valence orbitals of $NH_3$. (b) Corresponding spatial orbital representations generated with Gaussian03 [15] for the four valence orbitals. The diagram shows the $3a_1$ highest occupied molecular orbital is anti-bonding with p-like character. The $1e_1$ state is doubly degenerate, consisting of two molecular orbitals with p-like character. By contrast, the $2a_1$ HOMO-2 state has s-like character.

Molecular orbital theory gives rise to three valance energy levels (see Figure 1). The highest energy level (or highest occupied molecular orbital, HOMO) is singly

degenerate and has $3a_1$ symmetry, so it behaves according to the operations of the A1 symmetry label within the character table for $NH_3$. [16] In these orbital configurations the 'a' denotes it is a singly degenerate orbital, whereas the 'e' denotes a doubly degenerate orbital. The subscript 1 indicates the orbital is symmetric with reflection through a $\sigma_v$ mirror plane (i.e., vertical through the N and H and dissecting the H-N-H bond angle), whereas the leading number '3' indicates it is the 3rd orbital of this type in the molecule.

The $3a_1$ orbital is a non-bonding orbital and is attributed to the lone pair of electrons on the nitrogen atom. Both electron momentum spectroscopy measurements [11,17] and *ab initio* [11] calculations show it has dominant *p*-like characteristics. The second energy level, or next highest occupied molecular orbital (NHOMO or HOMO-1) is a doubly degenerate bonding level with $1e_1$ symmetry. Again, this orbital is found to have significant *p*-like character from EMS measurements [17]. The third energy level, HOMO-2, is a singly degenerate bonding orbital, and has *s*-like character in contrast to the outer orbitals.

While these characteristics and symmetry labels are derived from simple molecular orbital theory, they can be helpful in interpreting the data and are important in the calculations. The different characteristics of the orbitals have a significant effect when averaging the target wavefunctions over all possible orientations prior to the collision, since parity inversion of *p*-character states would largely cancel contributions to the scattering process unless carefully considered. By contrast, wavefunctions of *s*-character do not suffer from parity inversion, and so the orientation averaging of these wavefunctions is more straightforward. A fuller discussion of these effects and their consequences is presented in Sec. conclusions.

## The Experimental Apparatus

The experimental data presented here were taken using the fully computer controlled and optimised (*e*,2*e*) spectrometer in Manchester. This spectrometer is described in Ref. 18 and so only the pertinent details are given here. The spectrometer can operate over a range of geometries from a coplanar geometry, where the incident electron is in the same plane as the two outgoing electrons ($\gamma = 0°$), to the perpendicular geometry where the incident electron is orthogonal to the detection plane ($\gamma = 90°$) (see Figure 2).

The incident electron beam was produced by a two-stage electron gun that had an energy resolution ~0.6 eV. The electron analyzers were mounted on individual turntables that enabled them to rotate independently around the detection plane. The experiments described here used a *doubly symmetric* geometry with $E_1 = E_2 = E$ and $\chi_1 = \chi_2 = \chi$ (see Figure 2). The TDCS was obtained by measuring the ionization probability for a range of angles $\chi$ for a given energy $E$. Data in the perpendicular plane is presented in terms of the mutual angle $\phi = \chi_1 + \chi_2$ since this is the only relevant angle in this geometry.

The ammonia target gas was admitted into the interaction region via a gas jet. The flow of ammonia was regulated by a needle valve so that the vacuum in the chamber was raised from a base pressure of ~6x10$^{-7}$ Torr to $2.2 \times 10^{-5}$ Torr. An incident electron beam current of 120 nA was used for measurements from the $3a_1$ and $1e_1$ orbitals and this was reduced to 50 nA when collecting data from the $2a_1$ state. These low beam currents were particularly important for the $2a_1$ state, due to the small cross-section from this orbital. This allowed acceptable accumulation rates to be delivered while maintaining good signal to background ratios.

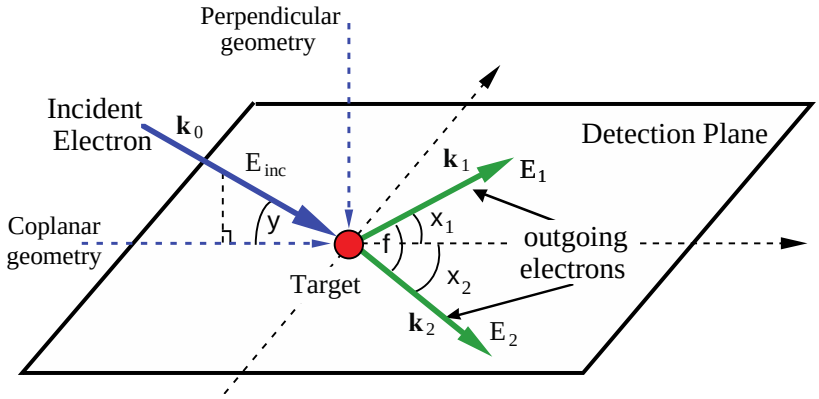


Figure 2: Schematic diagram of the scattering geometry. A coplanar geometry is defined when the momenta of the incident and scattered electrons lie in the detection plane ($\gamma = 0°$). The analyser angles $\xi_1$ and $\xi_2$ are measured with respect to the projection of the incident electron momentum in this plane. A perpendicular geometry is defined when the incident electron momentum is orthogonal to the detection plane ($\gamma = 90°$).

The electrostatic focussing lenses in the analyzers were optimised under computer control, so as to allow for any small misalignment as they rotated around the detection plane. The energy of the spectrometer was calibrated at the start of each new experiment by tuning the incident electron energy to the peak in the coincidence binding energy spectrum. The three valence orbitals of ammonia are energetically well separated (11, 16.5 and 26.3eV respectively) [10] and so were easily resolved within the energy resolution of the spectrometer (~1.4eV in these experiments). As such, the measured TDCS was uncontaminated by contributions from neighbouring orbitals.

The data presented here have been individually scaled to unity at the highest point in the cross section, since absolute measurements were not obtained. Each dataset was generated from an average of several sweeps of the analyzers around the detection plane. The uncertainty in the TDCS as presented here is then the standard error derived from this averaging process. Angular uncertainties are due to the pencil angle of the incident

electron beam and acceptance angle of the analyzers. This was estimated to be around ~±3°.

## Theoretical Framework

The M3DW approximation has been presented in previous publications [7, 19, 20] so only a brief outline of the theory will be presented. The TDCS for the M3DW is given by:

$$\frac{d\sigma}{d\Omega_a d\Omega_b dE_b} = \frac{1}{(2\pi)^5}\frac{k_a k_b}{k_i}\left(|T_{dir}|^2 + |T_{exc}|^2 + |T_{dir} - T_{exc}|^2\right) \quad (57)$$

where $\vec{k}_i$, $\vec{k}_a$, and $\vec{k}_b$ are the wave vectors for the initial, scattered and ejected electrons, $T_{dir}$ is the direct scattering amplitude, and $T_{exc}$ is the exchange amplitude. The direct scattering amplitude is given by:

$$T_{dir} = \left\langle \chi_a^-(\vec{k}_a, \mathbf{r}_1)\chi_b^-(\vec{k}_b, \mathbf{r}_2)C_{scat-eject}(r_{12}^{ave})\,|V - U_i|\,\phi_{DY}^{OA}(\mathbf{r}_2)\chi_i^+(\vec{k}_i, \mathbf{r}_1)\right\rangle \quad (58)$$

where $r_1$ and $r_2$ are the coordinates of the incident and the bound electrons, $\chi_i, \chi_a$, and $\chi_b$ are the distorted waves for the incident, scattered, and ejected electrons, respectively, and $\phi_{DY}^{OA}(r_2)$ is the initial bound-state Dyson molecular orbital averaged over all orientations. As mentioned in the introduction, averaging states of odd parity would lose most of the information contained in the wavefunction due to cancellation. Consequently, we average the absolute value of the wavefunction instead. Under the frozen orbital approximation, the Dyson orbital can be approximated using the initial bound Kohn-Sham orbital. The molecular wave functions were calculated using density functional theory (DFT) along with the standard hybrid B3LYP [21] functional by means of the

ADF 2007 (Amsterdam Density Functional) program [22] with the TZ2P (triple-zeta with two polarization functions) Slater type basis sets.

The factor $C_{scat-eject}(r_{12}^{ave})$ is the Ward-Macek average Coulomb-distortion factor between the two final state electrons [23], $V$ is the initial state interaction potential between the incident electron and the neutral molecule, and $U_i$ is a spherically symmetric distorting potential which is used to calculate the initial-state distorted wave for the incident electron $\chi_i^+(\vec{k}_i, \mathbf{r}_1)$.

Details about the calculation of initial and final state distorted waves can be found in Madison and Al-Hagan [24]. For the exchange amplitude $T_{exc}$, particles 1 and 2 are interchanged in the final state wavefunction in Eq. (2). However, for equal final state energies and angles, $T_{exc} = T_{dir}$ so it is not necessary to calculate both amplitudes.

We label results as obtained from Eq. (2) as M3DW. Results will also be presented for Ne which are calculated similarly (using the same computer code) except that atomic wavefunctions and distorted waves are used. The atomic results are labeled 3DW. We will also show some results of the standard DWBA. The DWBA results are calculated identically to M3DW or 3DW except that the final state Coulomb interaction factor $C_{scat-eject}$ (normally called the post collision interaction (PCI)) is not included in the evaluation of the T-matrix.

## Results and Discussion

Results are presented for a coplanar geometry in Sec. A, and for the perpendicular plane geometry in section B. As noted above, the three outermost orbitals were studied in a coplanar geometry, whereas data from only the two outermost orbitals were obtained in the perpendicular plane due to the very small cross sections in this plane. The results are

also compared to data from the iso-electronic targets neon [25,26] and methane, [27,28], as were obtained previously in this spectrometer. This allows contrasts to be seen between targets that carry the same overall nuclear and electronic charge, but which have quite different structures.

**A Coplanar geometry**

**A.1. The HOMO $3a_1$ state**

Experimental and theoretical TDCS for the $3a_1$ HOMO state of ammonia are presented in Figure 3 for six different energies ranging from $E = E_1 = E_2$ = 20 eV to 2.5 eV. The energy of the outgoing electrons is shown on individual plots. The ionization binding energy of this orbital is ~11 *eV*, and it has *p*-like character.

At the higher energies with outgoing electron energies $E$ = 20 eV and 15 eV, the data are dominated by a large cross section in the forward scattering direction ($x < 90°$), compared to that seen in the backward direction ($x > 90°$). As the energy is lowered towards $E$ = 2.5 eV the TDCS inverts to yield higher cross sections in the backward direction compared to forward scattering. The cross section in the backward direction is usually attributed to multiple scattering involving the nuclear core. This mechanism is more probable at lower energies since the electrons interact with the nucleus for a longer time, increasing the probability of the backward scattering, as is observed.

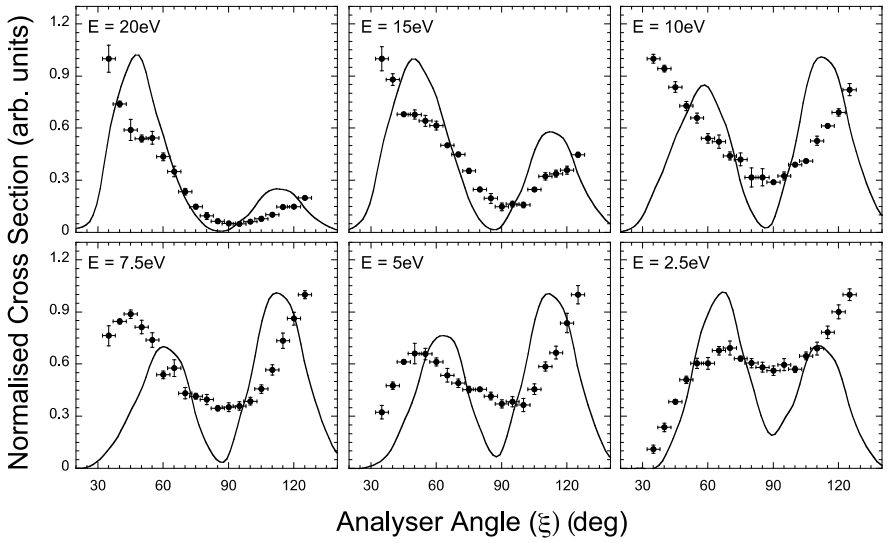


Figure 3: TDCS from the $3a_1$ HOMO state of ammonia for coplanar symmetric kinematics. The energies of the outgoing electrons are shown in the respective plots. The experimental data (dots) and results from the molecular three-body distorted wave approximation (lines) are shown. The experimental and theoretical data have been independently normalised to unity at the peak for each energy.

An additional effect normally observed in this energy regime is a migration of the forward peak towards $\chi = 90°$ as the energy decreases. This angular shift occurs due to PCI between the outgoing electrons, brought about by their Coulomb repulsion. PCI plays an increasing role as the energy of the outgoing electrons is lowered, since they have more time to interact. PCI is also strongest when the outgoing electrons have equal energies, as in these measurements. The Coulomb repulsion between the electrons emerging from the interaction region effectively drives them apart, so that they emerge at a greater relative angle in the asymptotic region. This phenomenon is clearly observed in the data at the three lowest energies in Figure 3, with the peak moving from $\chi \sim 45°$ for $E$ = 7.5 eV to $\chi \sim 70°$ for $E$ = 2.5 eV. PCI should also cause the backward scattering peak

to migrate towards $\chi = 90°$. This latter movement cannot be verified in the current data, as the peak in this region is outside the range that can be measured.

An additional structure appears in the experimental data at the two highest energies, with the forward scattering peak exhibiting a shoulder in the cross section for $\chi \sim 50°$. In atomic targets such as argon, "dips" are frequently found in the small angle peak which are attributed to the momentum probability of the *p*-like target orbital being zero at the origin [29].

Overall the agreement between the experimental data and the theoretical prediction is fair, with most of the trends observed in the data also being reproduced by theory. The dominant forward and backward structures observed in the experiment are reproduced by theory, with the position of the minimum between the forward and backward peak being well represented. The forward peak movement towards $\chi = 90°$ as the energy is lowered is also reproduced. The calculated forward scattering peak is seen to steadily migrate from $\chi \sim 47°$ to 67° as the outgoing electron energy is decreased from 20 eV to 2.5 eV. By contrast, theory predicts that the backward scattering peak should remain static at $\chi \sim 110°$ for all these energies.

Despite the structural agreement between experiment and theory, the peak positions are not well reproduced. The position of the forward scattering peak is overestimated at all energies apart from at $E$ = 2.5 eV, and the position of the backward peak is consistently underestimated for all energies. Theory also does not predict the shoulder in the forward scattering peak as is observed at higher energies. Except for $E$ = 2.5 eV, theory does predict qualitatively the relative magnitudes of the forward and

backward peaks with the forward peak becoming smaller and the backward peak growing with decreasing energy.

### A.2. The $1e_1$ HOMO-1 state

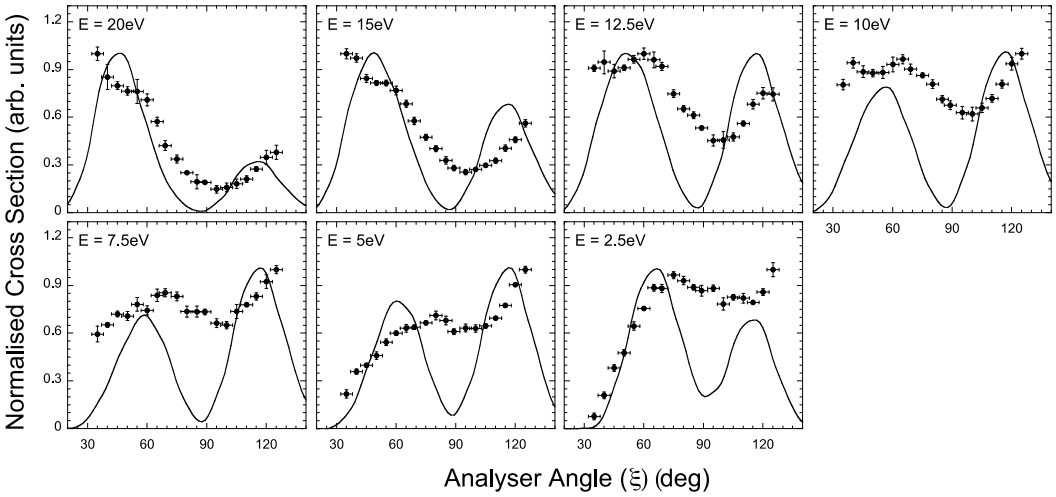


Figure 4. As for Figure 3, for the $1e_1$ HOMO-1 state of $NH_3$.

The TDCS for the $1e_1$ HOMO-1 state are shown in Figure 4 at seven different energies. The $1e_1$ state has *p*-like character and is doubly degenerate, consisting of two bonding orbitals of equal energy (Figure 1). The ionisation potential for this orbital is ~16.74 eV.

As for the $3a_1$ state, at higher energies the data shows a large forward peak compared to backward scattering. The relative strength of the cross section in the backward direction increases as the energy is lowered, except for $E$ = 2.5 eV. At high energies, the shoulder seen in the $3a_1$ data becomes more pronounced and becomes a "dip" at $\chi \sim 50°$, for energies around $E$ = 10 eV. As the energy decreases the forward peak again moves to higher angles; however in this orbital the shift is larger with the peak being between $\chi = 70°$ and 80° for energies from $E$ = 7.5 eV to 2.5 eV. This shift in the peak position also effects the position of the minimum between forward and backward

peaks, which occurs at a higher angle in the $1e_1$ state compared to the $3a_1$ state. The minimum is significantly shallower in this orbital compared to the outermost orbital.

The theoretical calculations for the $3a_1$ HOMO and $1e_1$ HOMO-1 states are very similar. As a consequence, agreement between experiment and theory for the $1e_1$ state is less satisfactory than for the $3a_1$ state, since none of the differences between orbitals described above are reproduced by theory.

The calculation does predict a shift of the forward scattering peak towards $\chi = 90°$ as the energy decreases, but does not accurately predict the magnitude of this shift. Theory consequently overestimates the position of the peak at high energies and underestimates the position at low energies. As for the outer orbital, the calculation consistently underestimates the position of the backward scattering peak. The position of the minima that was well reproduced for the $3a_1$ state is also underestimated for the $1e_1$ orbital. In both cases the magnitude of the minimum in the cross section is poorly reproduced. As with the $3a_1$, the calculation predicts that the relative intensity of the peak in the backward direction compared to the forward peak increases as the energy is lowered similar to the data, apart from at the lowest energy of $E$ = 2.5 eV.

### A.3. Comparison to iso-electronic targets $CH_4$, $NH_3$ and Ne with orbitals of p-character

Figure 5 shows representative TDCS data for the three iso-electronic targets $CH_4$[27], $NH_3$, and Ne[25], with all orbitals having p-like character. For each target, data for outgoing electron energies of E = 20 eV and E = 5 eV are depicted. A similar trend in the TDCS is seen for the molecular targets; however neon shows quite different structures at both energies. At E = 20 eV the neon cross section exhibits a small third peak at $\xi \sim 85°$ , with two local minima at $\xi \sim 70°$ and $\xi \sim 105°$. The forward cross

section clearly peaks at $\xi \sim 35°$ and does not show the "dip" structure seen for the molecular targets and as has been observed in neon at much higher energies [25]. The data from $CH_4$ at this energy show a "dip" in the cross section in the forward direction which is more pronounced than the $NH_3$ structure and occurs at a lower scattering angle. The ratio of forward to backward cross sections in both $CH_4$ and $NH_3$ are similar across all three orbitals.


Figure 5. TDCS for orbitals with *p*-like character from the iso-electronic series $CH_4$,[27] $NH_3$ and Ne[25]. For each target results for two energies are given: the top row gives data for outgoing electron energies of 20 eV while the bottom row shows data with outgoing energies of 5 eV. At left is the TDCS for the $1t_1$ HOMO state of $CH_4$, the middle columns show results from the $3a_1$ and $1e_1$ states of $NH_3$ and the right column gives data from the $2p$ state of Ne. The experimental data is compared to distorted wave theoretical predictions; M3DW for the molecular targets and 3DW for the atomic target.

At low energies the neon cross section does not show increased intensity in the backward direction, but is dominated by a forward peak at $\chi = 65°$. A small structure is seen at $\chi \sim 95°$ which may be the evolution of the central peak at $\chi \sim 85°$ seen at the higher energy; however the cross section at higher scattering angles monotonically decreases beyond this point. The structure of the cross section in neon is unusual, as most

other targets show a greater intensity in the backward region compared to forward scattering at these low energies [25], and as is predicted by the 3DW theory.

The data shown in Figure 5 indicate that the molecular nature of the targets plays a significant role in the scattering kinematics. It also appears that the different geometries of $CH_4$ and $NH_3$ do not impact greatly under these kinematic conditions. This is perhaps not surprising as the change in bond length and bond angle is relatively small between $CH_4$ and $NH_3$, as is the change in nuclear charge of the central atom. Comparison between experiment and theory for neon in Figure 5 shows reasonable agreement at the higher energy with the calculation accurately predicting the forward scattering peak, and also predicting a small peak at $\xi \sim 85°$ . By contrast, the theoretical prediction at the low energy displays the trend of increased intensity in the backward region, but is opposite to the experimental data. It is surprising that the theory agrees better with experiment for low energy molecular targets than atomic targets since fewer approximations are made in the calculation for atomic targets.

Xu *et al.* [13] recently suggested that the dip in the cross section seen at forward angles may be related to a nuclear scattering phenomenon, rather than simply being due to the *p*-like character of the orbital. However, since this dip is seen for all *p*-like orbitals in methane and ammonia as shown above, and yet is absent in the corresponding *s*-like orbitals in these targets (see Figure 7), it would appear that the underlying physical phenomena giving rise to the dip needs further investigation.

### A.4. Ionization from the $2a_1$ state

The third orbital studied here is the $2a_1$ state, which has *s*-like character. Calculations for this orbital are expected to be more accurate, since uncertainties introduced through the orientation averaging process should be largely eliminated for *s*-

states, since they have approximately spherical electron distributions, and since their wavefunctions do not change under parity inversion. This expectation was contradicted in the study of methane [27] however, where the outermost *p*-character orbital gave better agreement between experiment and theory than the HOMO-1 state, which has *s*-character.

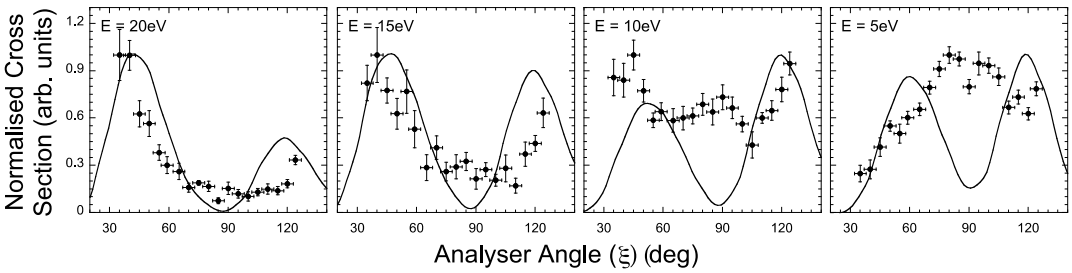


Figure 6. As for Figure 2, for the $2a_1$ state of $NH_3$.

Figure 6 shows the new results for the HOMO-2 ($2a_1$ state) in $NH_3$. The data show significantly more scatter than for the higher orbitals, due to the lower cross section. At the higher energies a similar cross section to that for the outermost orbitals is observed. Once again a higher intensity is seen for forward scattering compared to the backscatter region, with the peaks are separated by a minimum at $\xi \sim 90°$. The forward scattering peak shows no evidence of the structure seen for the HOMO and HOMO-1 states. As the energy is lowered, an additional peak emerges around $x = 90°$, which is most evident at $E$ = 10 eV. A three-peak structure is also observed for the iso-electronic targets neon [25] and $CH_4$ [27] at this energy (see Figure 7). This middle peak emerges from the background as the energy is lowered, and is not due to a migration of either the forward or backward scattering peaks, as might be caused by PCI. In the previous study of methane [27], this peak was attributed to a new scattering mechanism.

The calculated cross sections are similar in shape to that for the two outermost orbitals. At high energy, theory predicts atomic-like behaviour with a high forward scattering peak, a small backward peak, and a deep minimum in between similar to the data. The model again predicts that the relative intensity of the backward peak increases with decreasing energy, the minimum between the peaks shifting slightly in angle and increasing slightly in relative intensity. Experiment and theory are in better agreement for the two highest energies than was found for the two outermost orbitals. However as for the two outermost orbitals, the calculation overestimates the position of the forward peak and underestimates that of the backward scattering peak. At lower energies, theory fails to predict the increasing intensity of the cross section in the middle region around $x = 90°$ and does not predict the third peak that is observed. At the lowest energy of $E$ = 5 eV the data shows a maximum where theory predicts a minimum.

**A.5. Comparison between orbitals of s-character in the iso-electronic targets**

Figure 7 shows representative TDCS data for the three iso-electronic targets $CH_4$,[27] $NH_3$ and Ne,[25] with all orbitals having *s*-like character. For each target, data for outgoing electron energies of $E$ = 20 eV and $E$ = 5 eV are depicted. The data shown in Figure 7 indicate that scattering from s-like orbitals under these kinematic conditions is similar at $E$ = 20 eV, irrespective of the iso-electronic target and energy. At $E$ = 5 eV the cross sections for $CH_4$ and Ne both show a triple peak structure while that of $NH_3$ is dominated by a central peak at $\xi = 90°$. Note that $NH_3$ also gives a triple peak structure at $E$ = 10 eV. For all targets with *s*-like character, the theoretical calculation for $E$ = 20 eV shows reasonable agreement with the data. By contrast, at the lower energies little agreement is found. This may be in part due to the low energies that are used, since distorted wave theories typically have difficulty modelling the collision in this regime.

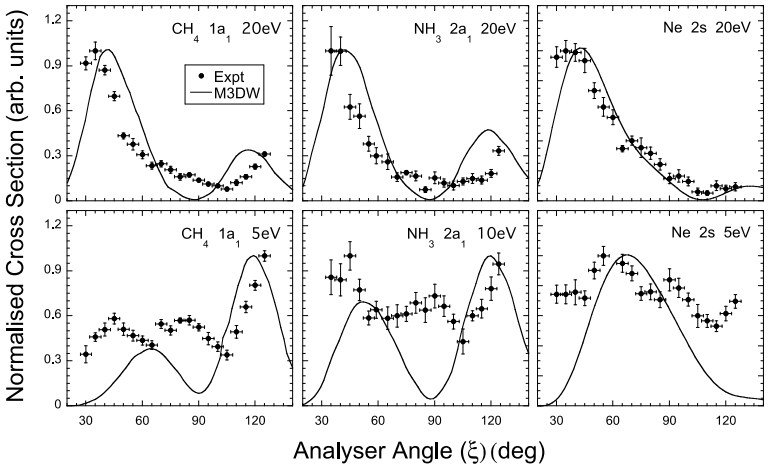


Figure 7. TDCS for orbitals of *s*-like character for the three iso-electronic targets using different outgoing electron energies. The left plots are from the $2a_1$ (HOMO-1) of $CH_4$,[27] the $2a_1$ (HOMO-2) for $NH_3$ is shown in the central plots, and the 2*s* orbital of neon[25] is shown in the right-hand plots. The energies in each case are shown on the respective plots.

**B. Scattering into the perpendicular plane**

The experimental apparatus in Manchester has the capability to measure the ionization cross section over a wide range of geometries, as shown in Figure 2. The perpendicular plane ($\gamma = 90°$) was hence selected to further this study, since scattering into this plane requires a strong interaction to occur between the incident electron and target nuclei [26, 30]. As such, scattering into this geometry maximises the sensitivity to these nuclear interactions. Further, only the mutual angle between the outgoing electrons $\phi = \chi_1 + \chi_2$ has meaning in this plane, due to rotational symmetry around the incident electron beam direction.

Data from the two outermost orbitals of $NH_3$ are presented below. No results from the $2a_1$ HOMO-2 state were obtained due to the very low scattering cross section into the perpendicular plane for this orbital. The data are compared to DWBA and M3DW models

over a range of energies from $E$ = 20 eV to $E$ = 1.5 eV , and are also compared to data from the iso-electronic targets $CH_4$[28] and Ne[26] in this energy regime.

**B.1. Ionization from the $3a_1$ state in the perpendicular plane**

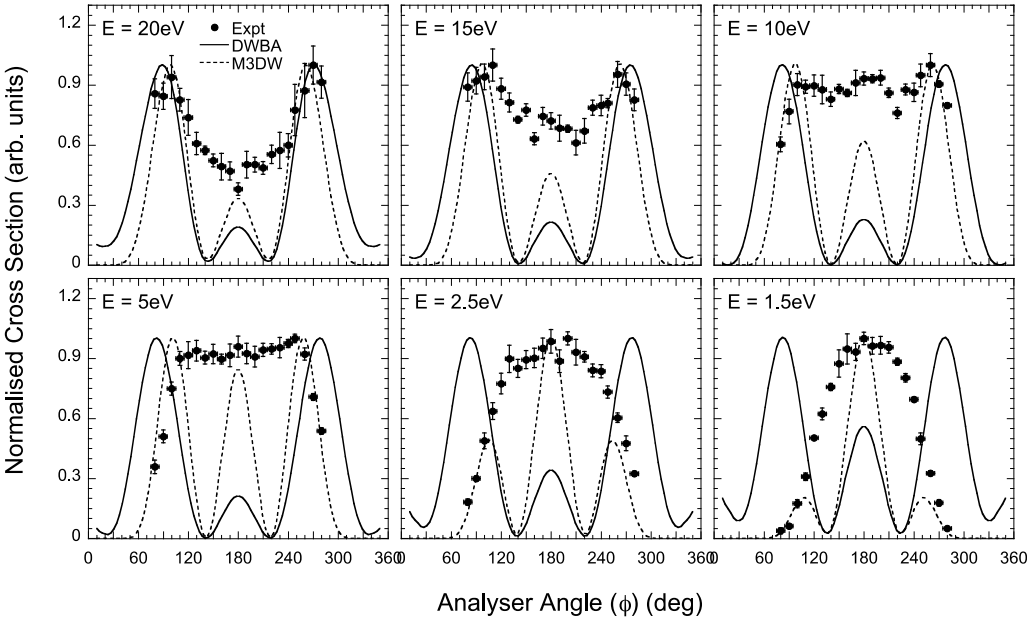


Figure 8: TDCS from the $3a_1$ state (HOMO) of ammonia in perpendicular kinematics. The energies of the outgoing electrons are shown in the respective plots. The experimental data (dots) and prediction from a distorted wave Born approximation (dashed lines) and molecular three-body distorted wave approximation (solid lines) are shown. The data and theoretical curves have been independently normalised to unity at their peak for each energy.

Figure 8 shows data in the perpendicular plane for the HOMO $3a_1$ state of $NH_3$ at six energies from $E$ = 20 eV to 1.5eV. Predictions from the DWBA and M3DW that includes PCI are also shown for comparison.

At $E$ = 20 eV the data show a two-peak symmetric structure with a deep minimum at $f = 180°$, the peaks being located at $f = 90°$ and $f = 270°$. As the energy decreases, the position of the two peaks remains approximately constant; however the local minimum at $f = 180°$ becomes shallower. At $E$ = 10 eV a small third peak at

$f = 180°$ appears, although this is difficult to see clearly. As the energy is lowered to $E$ = 5 eV, the width of the distribution narrows and the cross section remains flat over a wide range of angles between the edges of the distribution. At still lower energies the cross section evolves into a single distribution centred at $f = 180°$. A similar single-peak structure is seen in this geometry for helium at low energies [31], and this has been attributed to the dominance of PCI between the outgoing electrons [32] at these energies. It may be that PCI is also playing a significant role for the molecular target.

Both DWBA and M3DW calculations predict three well-resolved peaks as seen in Figure 8, in contrast to the data. Al-Hagan et al. [30] compared perpendicular plane cross sections for ionization of $H_2$ and He and they found two peaks for $H_2$ and three peaks for He. They showed that the two peaks near $\phi = 90^0$ and $\phi = 270^0$ resulted from elastic scattering in the perpendicular plane for both $H_2$ and He and that the third peak at $\phi = 180^0$ resulted from backscattering from the central nucleus for He with no peak for $H_2$ due to the fact that there was no nucleus at the CM. Further they predicted that one should always find three peaks for molecules that had a nucleus at the CM and two peaks for molecules that did not have a nucleus at the CM. Although there is no nucleus at the CM for $NH_3$, the nitrogen nucleus is close enough to the CM that one might expect three peaks as predicted. Interestingly, theory predicts the three peaks while the experiment only has two for the higher energies.

The DWBA theory predicts a small, unphysical intensity at $f = 0°$ and $f = 360°$ since PCI is not included. At the higher energies the DWBA predicts two dominant peaks at $f = 90°$ and $f = 270°$ with a small central peak at $f = 180°$. As the energy is lowered the calculated peaks remain in the same position and the small central peak increases in

intensity. The M3DW model (which includes PCI) predicts the two outer peaks to be slightly closer together at $f \sim 100°$ and $f \sim 260°$ at the highest energy. As the energy decreases, the outer peaks move toward $f = 180°$ and the intensity of the central feature increases until it becomes the dominant peak in qualitative agreement with experiment. Since the M3DW calculation includes PCI (in contrast to the DWBA model), it appears that PCI is making a significant contribution to the relative intensity of the central peak, and contributes to the shift in position of the outer peaks. The M3DW is in better agreement with the data in terms of the position of the outside peaks and width of the distribution.

**B.2. Ionization from $1e_1$ state**

Figure 9 presents the results from the 1e1 state, again at six energies from E = 20 eV to E = 1.5 eV. Once again the data and calculations are independently normalised to unity at the peak. The observations made for the 3a1 state are largely applicable to the data in Figure 9, as the results from both states are similar. This is consistent with the coplanar data, where orbitals of the same character produced similar cross sections. In the perpendicular plane experiments for the $1e_1$ state the highest energy was E = 15 eV, although the theoretical calculations extend to 20 eV. At E = 15 eV a twin-peak structure is again seen with a shallow minimum at $\phi$=180° as seen for the HOMO orbital. In contrast to measurements from the $3a_1$ state, the peaks in the $1e_1$ state data steadily move closer to $f = 180°$ as the energy is reduced. At low energies the distribution has merged into a single peak at $f = 180°$ as seen for the HOMO orbital.

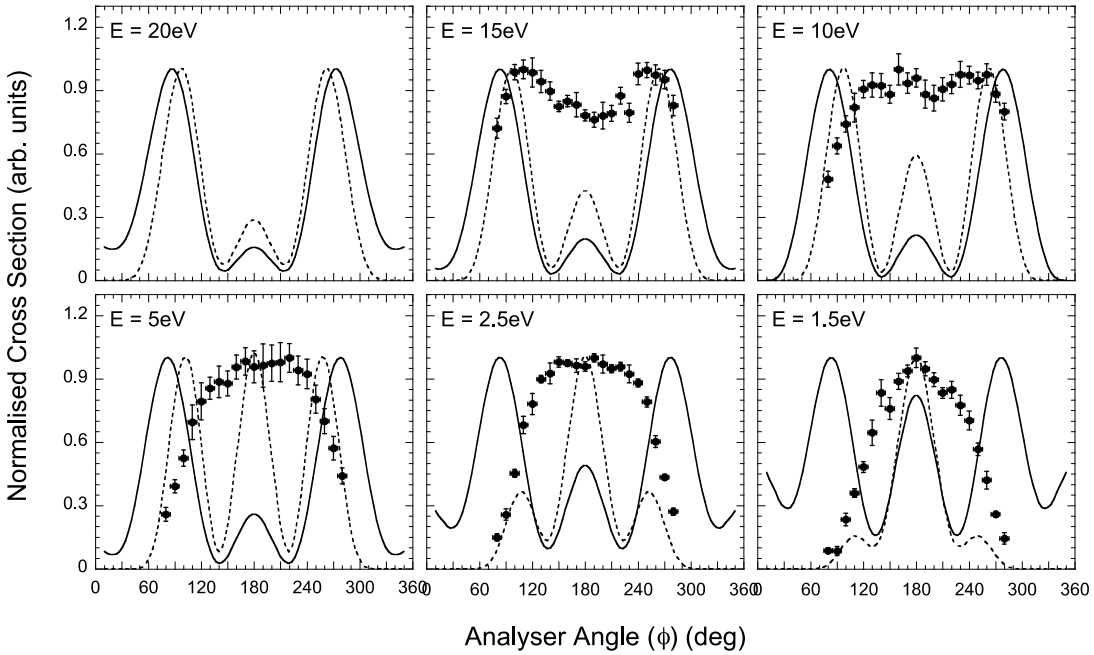


Figure. 9. As for Figure 8, for the $1e_1$ state (HOMO-1) of $NH_3$

The DWBA model once again predicts finite intensity at $f = 0°$ and $f = 360°$, since PCI is not included. The M3DW calculation is almost identical in shape for the $3a_1$ and $1e_1$ states. This model once again accurately models the overall width of the distribution; however, it fails to predict the structure in the data and shows three peaks at all energies, with a dominant central peak for lower energies.

***3. Orbitals of p-like character in the iso-electronic targets (perpendicular plane geometry)***

Figure 10 shows the TDCS in the perpendicular plane for $CH_4$, $NH_3$ and Ne for orbitals with *p*-like structure. Data at three different energies are shown for each target, from a high energy ($E$ = 20 eV or 25 eV) down to low energy ($E$ = 2.5 eV or 1.5 eV). A comparison between the outermost orbital cross sections in the perpendicular plane for Ne and $CH_4$ was presented in Nixon *et al.* [26] and so will not be repeated here. In brief,

the data for neon is subtly different to that for $CH_4$ and is relatively well represented by the theory.

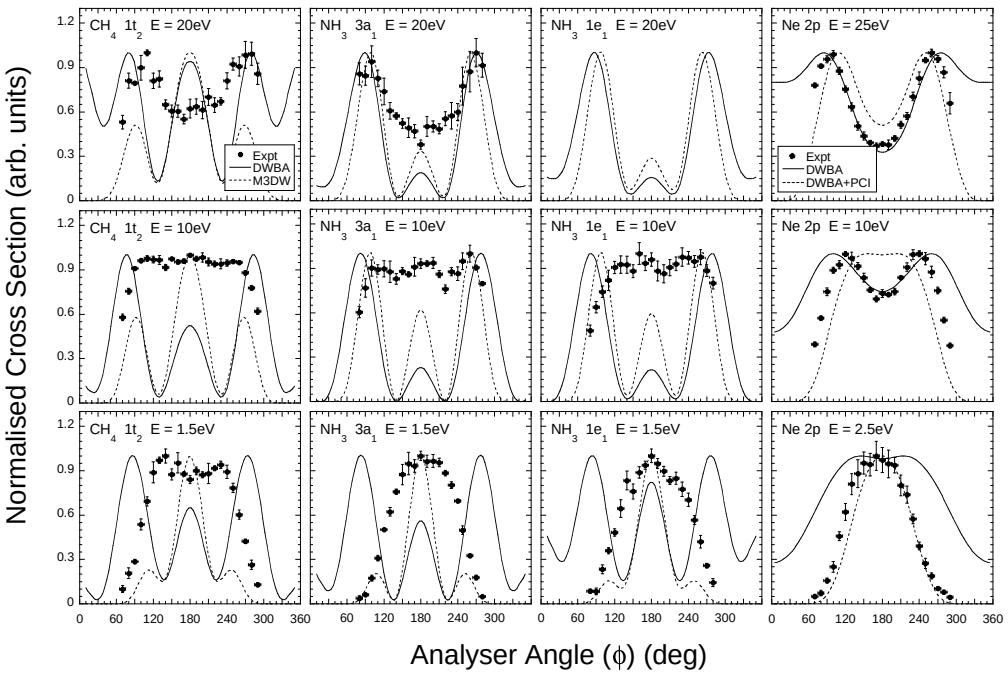


Figure. 10. TDCS in the perpendicular plane for orbitals with *p*-like character for the iso-electronic series. The left hand panels show data for the HOMO orbital of $CH_4$,[28] the middle two columns show data for the HOMO and HOMO-1 orbitals of $NH_3$, respectively, and the right hand column shows the data from Ne[26]. For each target three energy regimes are shown, labelled on the individual plots.

From Figure 10 it can be seen that similar results are obtained for all three *p*-like orbitals in $CH_4$ and $NH_3$, while neon exhibits slightly different behaviour. The cross sections for neon do not evolve into a wide distribution with a relatively flat top as for the molecules, but rather show movement of the two peaks towards each other as the energy is lowered. At the lowest energy a single peak is again observed.

It is interesting to note for neon that the calculation which does not include PCI appears to fit the data well at both $E$ = 25 eV and $E$ = 10 eV in the region near $f = 180°$

while overestimating the cross section for small and large angles where PCI is most important. Inclusion of PCI (solid line) yields qualitative agreement with the shape of the data for $E$ = 25 eV and very good agreement with the data for the lowest energy $E$ = 2.5 eV. As the energy is lowered, the two theoretical peaks including PCI merge to a single peak by $E$ = 10eV in contrast to experiment. PCI is clearly important for this target in this energy regime; however, it appears that the energetic effects of this interaction need to be more carefully considered. Overall, agreement between experiment and theory for neon is much better than for the molecular targets. This suggests that in the perpendicular plane the treatment of the molecular nature of the target has a stronger influence on the level of agreement between the calculation and the data.

## Conclusions

Experimental (e,2e) data for the ionisation of $NH_3$ have been presented for both coplanar and perpendicular plane geometries, and have been compared to predictions from distorted wave Born approximation and molecular three-body distorted wave calculations. The outer three orbitals of $NH_3$ were selected for this study. Agreement between experiment and theory is mixed. For the coplanar geometry some agreement is found at higher energies for all three orbitals; however this is less satisfactory at lower energies. The $3a_1$ and $1e_1$ states both have *p*-like character and their measured cross sections are similar. The cross-sections for ionization from these orbitals are similar to that of the outermost orbital of methane, which also has *p*-like character. Significant differences are found in the HOMO-2 orbital when compared with the outer orbitals. This is due to the different character of the orbital, which is *s*-like. Orbitals with *s*-like character in the iso-electronic targets neon and methane also show similar features to the data from the $2a_1$ orbital in ammonia. It appears that, in a coplanar geometry, the

character of the orbitals plays a dominant role in describing the interaction, rather than the nuclear structure of the target.

In the perpendicular geometry a similar set of data is presented for the two outermost orbitals of $NH_3$, which is again similar to data from $CH_4$. A closer agreement with experiment is found for the M3DW calculation than the DWBA calculation, due to the inclusion of PCI. However, in all of the iso-electronic species that have been investigated to date (neon[26], ammonia, methane[28], and water [33]), theory predicts considerably more structure than is observed. It would again appear that the orbital symmetry is playing a dominant role in controlling the ionization cross-section, compared to differences in the structure of the target.

These observations are not reflected in the calculations, since the structural predictions for all three orbitals in ammonia are remarkably similar. This would suggest that the models are at present dominated by the scattering dynamics from the nuclei, and not enough emphasis is being attributed to the electron distribution within the individual target orbital. This observation brings into question the OAMO (orientation averaged molecular orbital) approximation for these targets.

## Acknowledgements

K.L.N. would like to thank the Royal Society for a Newton International Fellowship at the University of Manchester. We would like to thank the technicians in the Schuster laboratory for providing excellent support for the experimental apparatus. This work was partly supported by the US National Science Foundation under Grant. No. PHY-1068237 and by the National Natural Science Foundation of China under Grant No. 11174175. Computataional work was performed with Institutional Computing resources made available through Los Alamos National Laboratory.

## References

1.I. E. McCarthy and E. Weigold, Rep. Prog. Phys. 54, 789 (1991).

2.A. Prideaux and D. H. Madison, Phys. Rev. A 67, 052710 (2003).

3.R. Srivastava, T. Zup, R. P. McEachran, and A. D. Stauffer, J. Phys. B 25, 1073 (1992).

4.M. S. Pindzola, F. Robicheaux, S. D. Loch, J. C. Berengut, T. Topcu, J. Colgan, M. Foster, D. C. Griffin, C. P. Ballance, D. R. Schultz, T. Minami, N. R. Badnell, M. C. Witthoeft, D. R. Plante, D. M. Mitnik, J. A. Ludlow, and U. Kleiman, J. Phys. B 40, R39 (2007).

5.I. Bray and A. T. Stelbovics, Phys. Rev. Lett. 69, 53 (1992).

6.O. Zatsarinny and K. Bartschat, Phys. Rev. A 85, 062710 (2012).

7.J. Gao, D. H. Madison, and P. L. Peacher, J. Chem. Phys. 123, 204302 (2005).

8.C. Champion, C. Dal Capello, S. Houamer, and A. Mansouri, Phys. Rev. A 73, 012717 (2006).

9.I. Toth and L. Nagy, J. Phys. B 43, 135204 (2010).

10.M. S. Banna and D. A. Shirley, J. Chem. Phys. 63, 4759 (1975).

11.J. S. Zhu, Y. R. Miao, J. K. Deng, and C. G. Ning, J. Chem. Phys. 137,174305 (2012).

12.Z. Rezkallah, S. Houamer, C. Dal Capello, I. Charpentier, and A. C. Roy, Nucl. Instrum. Methods Phys. Res. B 269, 2750 (2011).

13.S. Xu, H. Chaluvadi, X. Ren, T. Pfluger, C. G. Ning, S. Yan, P. Zhang, J. Yang, J. Ullrich, D. H. Madison, and A. Dorn, J. Chem. Phys. 137, 024301 (2012).

14.I. Toth and L. Nagy, J. Phys. B 44, 195205 (2011).

15.M. J. Frisch, G. W. Trucks, H. B. Schlegel et al., GAUSSIAN 03, Gaussian, Inc., Wallingford, CT, 2004.

16.P. Atkins and J. de Paula, Atkins Physical Chemistry, 9th ed. (Oxford University

Press, 2010).

17A. O. Bawagan, R. Muller-Fiedler, C. R. Brion, E. R. Davidson, and C. Boyle, Chem. Phys. 120, 335 (1988).

18A. J. Murray, B. C. H. Turton, and F. H. Read, Rev. Sci. Instrum. 63, 3346 (1992).

19J. Gao, D. H. Madison, and J. L. Peacher, J. Chem. Phys. 123, 204314 (2005).

20J. Gao, D. H. Madison, and J. L. Peacher, Phys. Rev. A 72, 032721 (2005).

21C. Lee, W. Yang, and R. G. Parr, Phys. Rev. B 37, 785 (1988).

22C. F. Guerra, J. G. Snijders, G. te Velde, and E. J. Baerends, Theor. Chem. Acc. 99, 391 (1998).

23S. J. Ward and J. H. Macek, Phys. Rev. A 49, 1049 (1994).

24D. H. Madison and O. Al-Hagan, Journal of Atomic, Molecular and Optical Physics 2010, 367180 (2010).

25K. L. Nixon and A. J. Murray, Phys. Rev. A 87, 022712 (2013).

26K. L. Nixon, A. J. Murray, and C. Kaiser, J. Phys. B 43, 085202 (2010).

27K. L. Nixon, A. J. Murray, H. Chaluvadi, C. Ning, and D. H. Madison,

J. Chem. Phys. 134, 174304 (2011).

28K. L. Nixon, A. J. Murray, H. Chaluvadi, S. Amami, D. H. Madison, and C. Ning, J. Chem. Phys. 136, 094302 (2012).

29G. Stefani, R. Camilloni, and A. Giardini-Guidonu, J. Phys. B 12, 2583 (1979).

30O. Al-Hagan, C. Kaiser, D. H. Madison, and A. J. Murray, Nat. Phys. 5, 59 (2009).

31A. J. Murray and F. H. Read, Phys. Rev. A 47, 3724 (1993).

32G. Wannier, Phys. Rev. 90, 817 (1953).

33K. L. Nixon, A. J. Murray, O. Al-Hagan, D. H. Madison, and C. G. Ning, J. Phys. B 43, 035201 (2010).

## VIII Dynamical (e,2e) investigations of tetrahydrofuran and tetrahydrofurfuryl alcohol as DNA analogues

D. B. Jones,[1,a)] J. D. Builth-Williams,[2] S. M. Bellm,[2] L. Chiari,[2] H. Chaluvadi,[3] D. H. Madison,[3] C. G. Ning,[4] B. Lohmann,[5] O. Ingólfsson,[6] and M. J. Brunger[2,7,b)]

[1]School of Chemical and Physical Sciences, Flinders University, GPO Box 2100, Adelaide, South Australia 5001, Australia.

[2]ARC Centre of Excellence for Antimatter-Matter Studies, Flinders University, GPO Box 2100, Adelaide, South Australia 5001, Australia.

[3]Department of Physics, Missouri University of Science and Technology, Rolla, Missouri 65409, USA.

[4]Department of Physics and Key Laboratory of Atomic and Molecular NanoSciences of MOE, Tsinghua University, Beijing 100084, People's Republic of China.

[5]University of the Sunshine Coast, Maroochydore DC, Queensland 4558, Australia.

[6]Science Institute, University of Iceland, Dunhagi 3, 107 Reykjavik, Iceland.

[7]Institute of Mathematical Sciences, University of Malaya, 50603 Kuala Lumpur, Malaysia.

### Abstract

New triple differential cross section measurements for the electron-impact ionization of the highest occupied molecular orbital of tetrahydrofuran (THF) are reported. Experimental measurements were performed using the (e,2e) technique in asymmetric coplanar kinematics with an incident electron energy of 250eV and an

ejected electron energy of 20eV. With the scattered electrons being detected at -5°, the angular distribution of the ejected electrons in the binary and recoil regions was observed. These measurements are compared with calculations performed within the molecular 3-body distorted wave (M3DW) model, and against previous measurements on THF and tetrahydrofurfuryl alcohol in order to further understand the role the kinematics and structure play in the dynamics of electron impact ionization.

## Introduction

There have been a number of recent studies on positron-induced and electron-induced phenomena from biologically relevant targets [1]. This stems from the fact that such studies are required to develop models to simulate charged-particle induced damage to biological systems. Here the role of electron scattering is particularly important as a large number of low-energy secondary electrons are produced from a single high-energy ionizing particle, with these low-energy electrons capable of inducing damage to DNA through single and double strand breakages [2]. Further, such damage has been found to result from localized electron-interactions with the sub-units of DNA, rather than the bulk structure [3, 4]. This has created a pressing need to characterise the electron scattering mechanisms from key structural moieties found in biological systems. Of particular importance is a knowledge of the electron-impact cross sections that describe the probability of the electron-induced scattering phenomena. Here experimental and theoretical cross sections are particularly useful in simulating charged-particle interactions in the media resembling biological systems.

Given the larger number of complex molecules that are analogous to segments of DNA or other biologically relevant compounds, it is becoming increasingly important to identify and understand the role that adding functional groups or performing chemical

substitutions play in electron-induced phenomena. It is only through an understanding of the influence of structure on collision dynamics that charged-particle induced damage in DNA can be accurately simulated. This is also particularly important for interpreting phenomena observed in complex biological media and identifying the most suitable species for simulating DNA when modeling radiation induced damage.

To facilitate the goal of understanding electron-impact induced phenomena in biological systems, we must go beyond understanding electron-scattering phenomena from single molecules to understanding the importance of molecular structure in electron scattering. We are therefore extending some recent investigations on electron-impact ionization of individual biomolecules (water [5, 6], formic acid [7-9], pyrimidine [10] and thymine [11]) to studies on series of chemically similar molecules. In this respect, an understanding of the sensitivity of the scattering behavior from specific species over a range of kinematical conditions is also pertinent.

In this letter we consider electron-impact ionization of thetrahydrofuran (THF, C4H8O) and tetrahydrofurfuryl alcohol (THFA, C5H12O2). Both THF and THFA resemble structural units of the phosphate deoxyribose backbone of DNA (see Fig. 1). This fact has led to a number of recent studies of electron scattering phenomena from both THF and THFA, which has included electron-impact total [12-16], elastic [16-22], inelastic [22-24] and dissociative electron-attachment [25, 26] scattering cross section measurements. Regarding relatively low-energy electron-impact ionization, Colyer et al. [27-29] performed TDCS measurements for the electron-impact ionization of the highest occupied molecular orbital (HOMO) of THF under asymmetric coplanar kinematics. Here the HOMO for conformationally versatile THF is either the 12a′ (Cs) or 9b (C2)

orbital. In that work [27-29] angular distributions of the ejected electron, with energy Eb = 10 eV, were measured for the electron-impact ionization of the HOMO when the scattered electron was detected at the angles of θa= -5, -10 or -15°, respectively. Here the incident electrons energy was E0 = 250eV. Recently, we performed an electron-impact ionization study of the HOMO of THFA (28a) under similar asymmetric coplanar kinematics [30], although in that study the angular distributions of the ejected electron were measured for an ejected electron energy of 20eV while the scattered electron was again detected at θa = -5, -10 or -15°. Those measurements displayed some similarities to those previously reported for THF, with both species having a significant recoil peak intensity when the scattered electron was detected at θa = -5°. This observation is intriguing as it suggests that the behavior for electron-impact ionization of the HOMOs for THF and THFA may be similar. This result may be somewhat anticipated as the ionized orbitals in both cases are expected to be dominated by contributions from the lone-electron pair located on the oxygen atom forming the five-member ring. However, the different kinematical conditions employed in the THF [27-29] and THFA [30] measurements (see Fig. 2) restricted our ability to fully evaluate the role of structure and kinematics in the electron-impact ionization phenomena. To resolve this issue, we have performed new measurements for THF under kinematical conditions that match those employed for our recent measurements on THFA [30]. Specifically, angular distributions for E0=250eV and 20eV ejected electrons were measured while the detected scattered electron angle was fixed at θa = -5°. By comparing the new TDCS measurements to the earlier measurements of THF [27] we can gain insights into the sensitivity of the electron-impact cross section to the ejected electron energy. Further, we can make a

direct comparison of the new measurements with the existing data for THFA [30] to understand the importance of structure in the scattering dynamics.

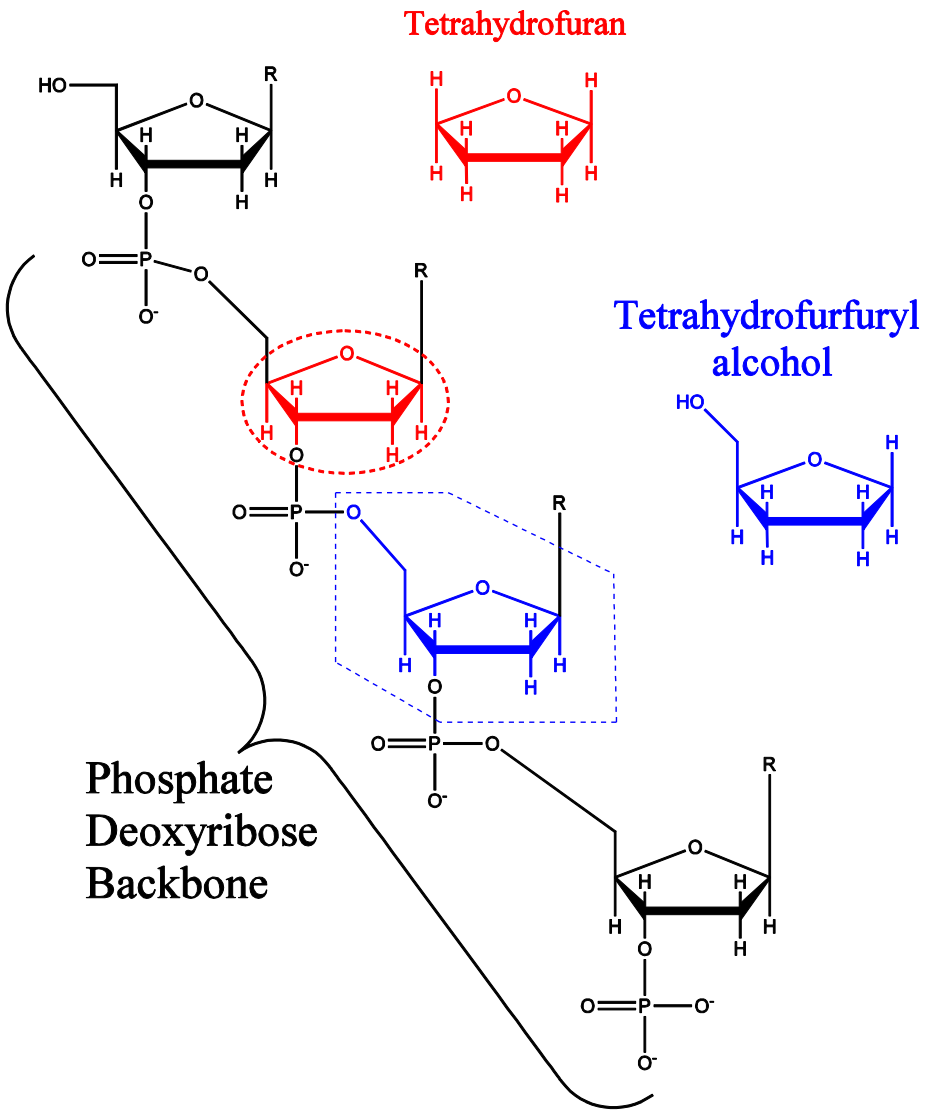


Figure. 1. Schematic diagram of tetrahydrofuran (THF) and tetrahydrofurfuryl alcohol (THFA) as structural analogues to the Phosphate Deoxyribose backbone found in DNA.

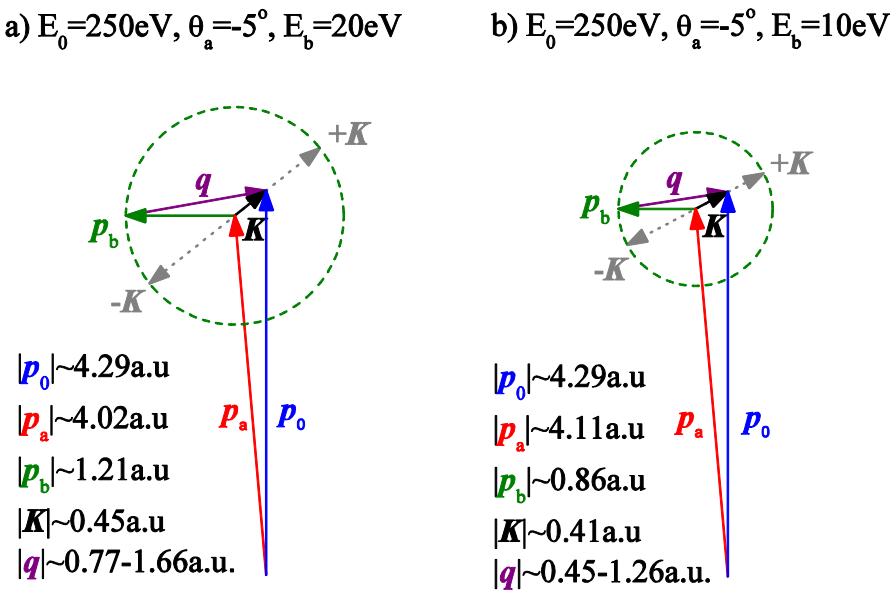


Figure. 2. Schematic diagram of the kinematics employed for the TDCS measurements of (a) THF (present work) and THFA [30] and (b) THF measurements of Coyler et al. [27]. The dashed line in each figure displays the range of ejected electron momentum values with the variation in polar angles. See text for further details.

## Experimental Methods and Theoretical Details

Triple differential cross sections for the kinematically-complete electron-impact ionization of THF, described by

$$e_0^-(E_0, p_0) + THF \rightarrow THF^+(\varepsilon_i) + e_a^-(E_a, p_a) + e_b^-(E_b, p_b), \qquad (1)$$

have been measured under coplanar asymmetric kinematical conditions using a (e,2e) coincidence technique. In equation (1), $E_j$ and $p_j (j = 0, a, \text{or } b)$ are the energies and momenta of the incident, scattered and ejected electrons, respectively. Here the conservation of energy during the collision allows the binding energy of the ionized orbital $\varepsilon_i$ to be determined,

$$\varepsilon_i = E_0 - (E_a + E_b). \qquad (2)$$

Likewise, to conserve momentum the recoiling ion has momentum

$$q = p_0 - (p_a + p_b), \quad (3)$$

after the collision. In the present experiment, as noted previously, the incident electron and ejected electron energies are fixed at $E_0$ = 250eV and $E_b$ = 20eV, respectively. The scattered electron is detected at a fixed polar angle, $\theta_a$ = -5°, made with respect to the incident electron beam direction. Here the scattered electron energy is selected to match the ionization energy of the HOMO of THF. The direction of the scattered electron defines the momentum transferred to the target,

$$K = p_0 - p_a. \quad (4)$$

Under the conditions where the ejected electron is in the direction close to the momentum transfer direction (K+), all momentum transferred to the target is absorbed by the outgoing electron. These collisions are said to be binary in nature. In this binary region, the magnitude of the momentum of the recoiling ion is at its minimum. Alternatively, when the electron is ejected in the direction anti-parallel to the momentum transfer (K-), substantial momentum may be transferred to the nucleus. The recoil momentum is therefore near its maximum. Such collisions are said to be recoil in nature.

The full details of our experimental apparatus and measurement procedure have been described previously [27, 31], so that only a brief summary is presented here. An electron beam of fixed energy, E0 = 250eV, is generated through the thermionic emission of a tungsten filament.

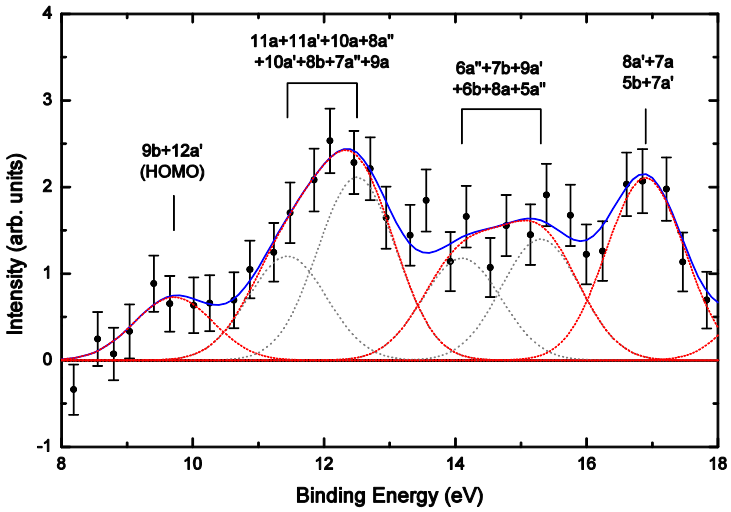


Figure. 3. Measured binding energy spectra (●) for THF obtained for an incident electron energy E0=250 eV. Here the scattered electron was detected at θ_a= -5°, while the ejected electron was detected with Eb=20eV at θ_b= 75°. Also shown are spectral deconvolutions of the measured spectra into contributions from each orbital (— —) and their sum (——). Also shown are the individual (unresolved) Gaussians (·····) that combine to form the larger spectral features. See text for further details.

The emitted electrons are then accelerated, collimated and focused into the interaction region by a 5-element cylindrical lens stack. The electrons interact with a beam of THF introduced through a capillary. Here, a high purity THF sample was degassed by repeated freeze-pump-thaw cycles prior to being introduced into the system. During the measurements, the vacuum chamber and sample gas lines were heated to ~40 °C. Scattered and ejected electrons produced though ionizing collisions with the target beam were detected in separate analyzers. Each analyzer consisted of a 5-element electrostatic lens system, hemispherical energy selector and channel electron multiplier. Using standard coincidence timing techniques, the arrival times of the electrons detected in each analyzer were used to determine if the electrons originated from the same ionization event. In this study the obtained coincidence energy resolution was 1.1 eV (FWHM), as determined from measurements of the Helium 1s binding energy peak. Each

electron analyzer was mounted on an independently rotatable turntable. In the present work, the scattered electron analyzer was fixed at $\theta_a$ = -5°, while the ejected electron analyzer was rotated in the scattering plane defined by the incident and scattered beams. In this way we obtain coincidence angular distributions for the slow ejected electron.

The present experimental data is compared to theoretical calculations obtained within a M3DW (molecular 3-body distorted wave) framework [31-33]. These calculations have been described elsewhere, so only a brief description is repeated here. The triple differential cross section (TDCS) for the M3DW is giving by:

$$\frac{d\sigma}{d\Omega_a d\Omega_b dE_b} = \frac{1}{(2\pi)^5}\frac{k_a k_b}{k_i}\left(|T_{dir}|^2 + |T_{exc}|^2 + |T_{dir} - T_{exc}|^2\right) \qquad (5)$$

where $\vec{k}_i$, $\vec{k}_a$, and $\vec{k}_b$ are the wave vectors for the initial, scattered and ejected electrons, $T_{dir}$ is the direct scattering amplitude, and $T_{exc}$ is the exchange amplitude. The direct scattering amplitude is given by:

$$T_{dir} = \left\langle \chi_a^-(\vec{k}_a, \mathbf{r}_1)\chi_b^-(\vec{k}_b, \mathbf{r}_2)C_{scat-eject}(r_{12}^{ave}) \,|\, V - U_i \,|\, \phi_{DY}^{OA}(\mathbf{r}_2)\chi_i^+(\vec{k}_i, \mathbf{r}_1)\right\rangle \quad (6)$$

where $r_1$ and $r_2$ are the coordinates of the incident and the bound electrons, $\chi_i, \chi_a$, and $\chi_b$ are the distorted waves for the incident, scattered, and ejected electrons respectively, and $\phi_{DY}^{OA}(r_2)$ is the initial bound-state Dyson molecular orbital averaged over all orientations. Under the frozen orbital approximation, the Dyson orbital can be approximated using the initial bound Kohn-Sham orbital. The molecular wave functions were calculated using density functional theory (DFT) along with the standard hybrid B3LYP [34] functional by means of the ADF 2007 (Amsterdam Density Functional) program [35] with the TZ2P (triple-zeta with two polarization functions) Slater type basis

sets. The factor $C_{scat-eject}(r_{12}^{ave})$ is the Ward-Macek average Coulomb-distortion factor between the two final state electrons 30, *V* is the initial state interaction potential between the incident electron and the neutral molecule, and $U_i$ is a spherically symmetric distorting potential which is used to calculate the initial-state distorted wave for the incident electron $\chi_i^+(\vec{k}_i, \mathbf{r}_1)$. For the exchange amplitude $T_{exc}$, particles 1 and 2 are interchanged in eq. (2).

The Schrödinger equation for the incoming electron wave-function is given by:

$$(T + U_i - \frac{k_i^2}{2})\chi_i^+(\vec{k}_i, r) = 0 \qquad (7)$$

where $T$ is the kinetic energy operator and the '+' superscript on $\chi_i^+(\vec{k}_i, \mathbf{r})$ indicates outgoing wave boundary conditions. The initial state distorting potential contains three components $U_i = U_s + U_E + U_{CP}$, where $U_s$ contains the nuclear contribution plus a spherically symmetric approximation for the interaction between the projectile electron and the target electrons which is obtained from the quantum mechanical charge density of the target. The charge density is obtained by summing $2|\phi_{DY}|^2$ over all occupied orbitals (the 2 is for double occupancy and the original non-averaged Dyson orbital is used). The nuclear contribution to $U_s$ is the interaction between the projectile electron and all the 17 nuclei averaged over all orientations. Averaging the nuclei over all orientations is equivalent to putting the nuclear charge on a thin spherical shell whose radius is the distance of the nuclei from the center of mass (CM). For THF, there is no nucleus at the CM and the 4 carbon nuclei and one oxygen nucleus are all about the same distance from the CM. The closest nucleus to the CM is the oxygen at 2.35 $a_0$. Consequently, the first

nuclear sphere has a charge of 8 with a radius of 2.35 $a_0$. The next sphere has 2 carbon with charge 12 and a radius of 2.36 $a_0$. The next sphere has another 2 carbon with charge 12 and a radius of 2.37 $a_0$. The 8 hydrogen nuclei are on 4 spheres of charge 2 located at 3.69, 3.75, 4.10, and 4.21 $a_0$ respectively.

$U_E$ is the exchange potential of Furness-McCarthy (corrected for sign errors) 31 which approximates the effect of the continuum electron exchanging with the passive bound electrons in the molecule, and $U_{CP}$ is the correlation-polarization potential of Perdew and Zunger 32 (see also Padial and Norcross 33).

In Eq. (2), the final state for the system is approximated as a product of distorted waves for the two continuum electrons $(\chi_a^-, \chi_b^-)$ times the Ward-Macek average Coulomb-distortion factor $C_{scat-eject}$. The final state distorted waves are calculated the same as the initial state except that the final state charge density is used to calculate $U_s$. The final state charge density is obtained the same as the initial state except that unity occupancy is used for the active electron orbital. Additional details can be found in Madison and Al-Hagan [40].

In order to offer more quantitative comparisons between THF and THFA, the calculated TDCS for THF are weighted by a 1:1, $C_s$:$C_2$ conformer ratio that is close to the recently observed experimental values [41–43] at room temperature, and is thus representative of the conditions used in our experiments. Lastly, in order to facilitate further quantitative understanding of the observed behavior, spherically averaged orbital momentum profiles have been generated [44] for both THF and THFA from Kohn–Sham orbitals calculated with GAUSSIAN [45].

## Results and Discussion

In Fig. 3, the newly measured binding energy spectrum (BES) for THF is presented. This spectrum was obtained for an incident electron energy $E_0$=250 eV, with the scattered electron being detected at $\theta_a$ = -5° in coincidence with an ejected electron with $E_b$=20eV at $\theta_b$ = 75°. Here the data is accumulated by recording the number of true coincident events as the scattered electron energy was scanned. Note that the features observed in this spectrum are in good accord with results obtained in ultraviolet photoelectron spectroscopy (UPS) [37, 38], Penning ionization electron spectroscopy (PIES) [38], and electron momentum spectroscopy [33, 34]. Interestingly, the BES from the earlier dynamical (e,2e) study [27] shows marked differences to the present spectra. Here those variations relate to the relative intensity of each spectral feature, which highlights the importance of the kinematical conditions to the spectral behavior. Specifically, the BES of Colyer *et al*. (Fig. 3 of Ref. [27]) and the present spectrum are obtained in the binary region with recoil momentum values, $|\boldsymbol{q}|$, of ~0.3 a.u and ~0.8 a.u., respectively. The shift from a lower to higher recoil momentum, value probes different parts of the momentum profile of the ionized orbital. As such, the nature of the ionized orbitals momentum profile dramatically influences the relevant state's contribution to the spectrum [39].

In Fig. 4 (a), measured TDCS for the HOMO of THF (12a′+9b) are presented for $\theta_a$ = -5° and $E_b$=20eV. Initially, we compare the present TDCS for THF shown is Fig. 4 (a) with the results measured previously for THF under different kinematics where $E_b$=10eV (Fig. 5 of Ref. [27]). Here we see a significant reduction in the observed binary to recoil ratio as the ejected electron's energy has increased from 10 to 20eV. Comparing these results to those from the M3DW calculations, we see that the theory gives a much

better prediction of the shape of the binary feature when the ejected electron energy is 20eV. However, the M3DW still fails to reproduce the significant recoil peak intensity observed experimentally in both this work and that of Colyer *et al.* [27].

In order to qualitatively understand this behavior, we expand on the ideas proposed by Xu *et al.* [39]. Here we make reference to the kinematical conditions detailed in Fig. 2 and the momentum profiles for the HOMO (12a′, 9b and conformational averaged 12a′+9b) of THF which are presented in Fig. 5. In both measurements the momentum transfer is small, being ~0.4 a.u. However, this momentum transfer is significantly less than the outgoing electrons momentum, being $|p_b|$=0.86 and 1.21 a.u for $E_b$ = 10 eV and 20 eV, respectively. The ionization process must therefore always rely on linear momentum contributions from the internal momentum of the particles within the target. Note that in the impulsive limit, where no momentum is transferred to the recoiling ion, the momentum of the ionized electron is equal and opposite to the recoil momentum (this is the so-called electron momentum spectroscopy experiment [40]). The momentum profile and recoil momentum magnitude may therefore have a large influence on the scattering dynamics.

In the two kinematical conditions with $E_b$ = 10 or 20 eV the magnitude of the recoil momentum belongs to the ranges of 0.45-1.26 a.u or 0.77-1.66 a.u, respectively. As the THF 12a′+9b momentum profile has a minimum at $|\boldsymbol{q}|$~0.4 a.u and a maximum at $|\boldsymbol{q}|$~1.0 a.u. we may expect a weak intensity for the binary peak and a more significant recoil peak for $E_b$ = 10eV. Conversely, under conditions where the ejected electron leaves with 20eV, the maximum in the momentum profile coincides with the recoil momentum value when the electron is ejected along the momentum transfer direction. The TDCS

should therefore be at its maximum in this binary region. As the momentum distribution decreases in going to higher recoil momentum values, it might be expected that the recoil peak intensity is reduced from that found in the binary region for $E_b$ = 20eV. Such observations are consistent with the experimental binary-to-recoil ratios observed by Colyer *et al.* [27] and in the present work. Thus, the behavior of the momentum profile over the recoil momentum values studied through the defined kinematics provides a qualitative rationale for the experimentally observed binary-to-recoil peak ratios.

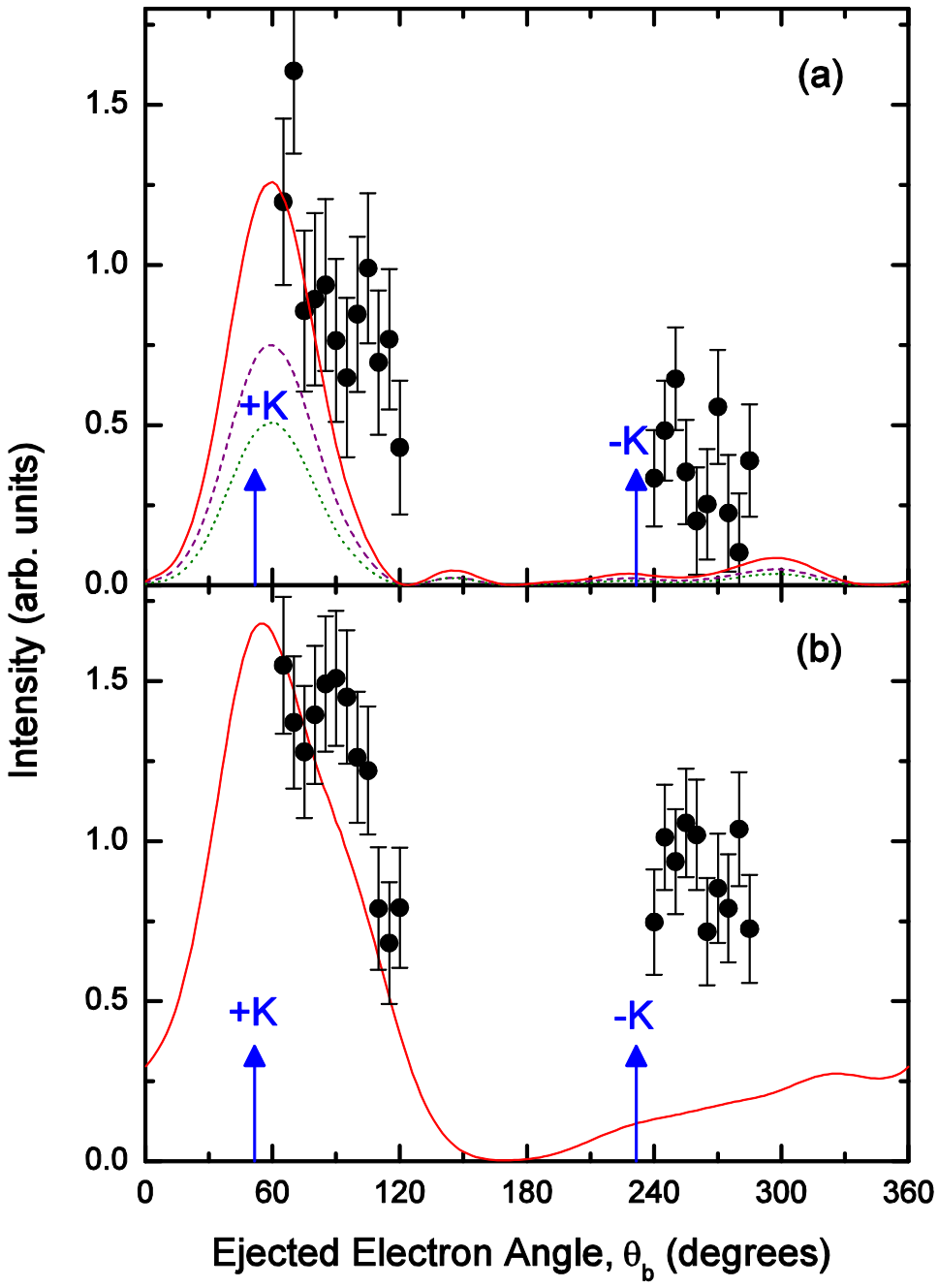


Figure. 4. Triple differential cross sections for the electron-impact ionization of the HOMOs of (a) THF (9b+12a′) and (b) THFA (28a) [30], with E0=250eV and Eb=20eV. Measured experimental data (●). The M3DW calculations (——) are also presented for each orbital or conformational average of contributing orbitals. Also shown are the TDCS contributions from the 12a′ (— —) and 9b (·····) orbitals of THF after being weighted by their respective conformer populations. See text for further details

The TDCS for THF and THFA, measured under identical scattering conditions and shown in fig. 4 (a) and 4 (b), are now discussed. It is immediately apparent from Fig. 4 that the recoil peak for THF is somewhat smaller than that observed previously for THFA. Specifically, the recoil peak of THF is roughly a third of the intensity of the binary peak while for THFA the recoil peak is about half the intensity measured for the binary peak. This behavior is somewhat surprising as the HOMOs for both THF and THFA are structurally expected to be quite similar. Indeed, the momentum profiles of the HOMOs of both THF and THFA, shown in Fig. 5, are essentially identical over the range of recoil momentum values covered by the relevant kinematical conditions, $|\boldsymbol{q}|$~0.8-1.7a.u, of both experiments. With the identical kinematical conditions, the observed variation in the binary-to-recoil ratios suggests that the dynamics of the ionization process must clearly influence the scattering behaviour. In this respect, comparisons between M3DW and distorted-wave Born approximation calculations for both THF (not shown) and THFA [29] have revealed that post-collision interactions between the two outgoing electrons are unimportant under the present kinematics. This perhaps suggests that a better description of the post-collisional interaction between the two-outgoing electrons and the residual ion may therefore be required.

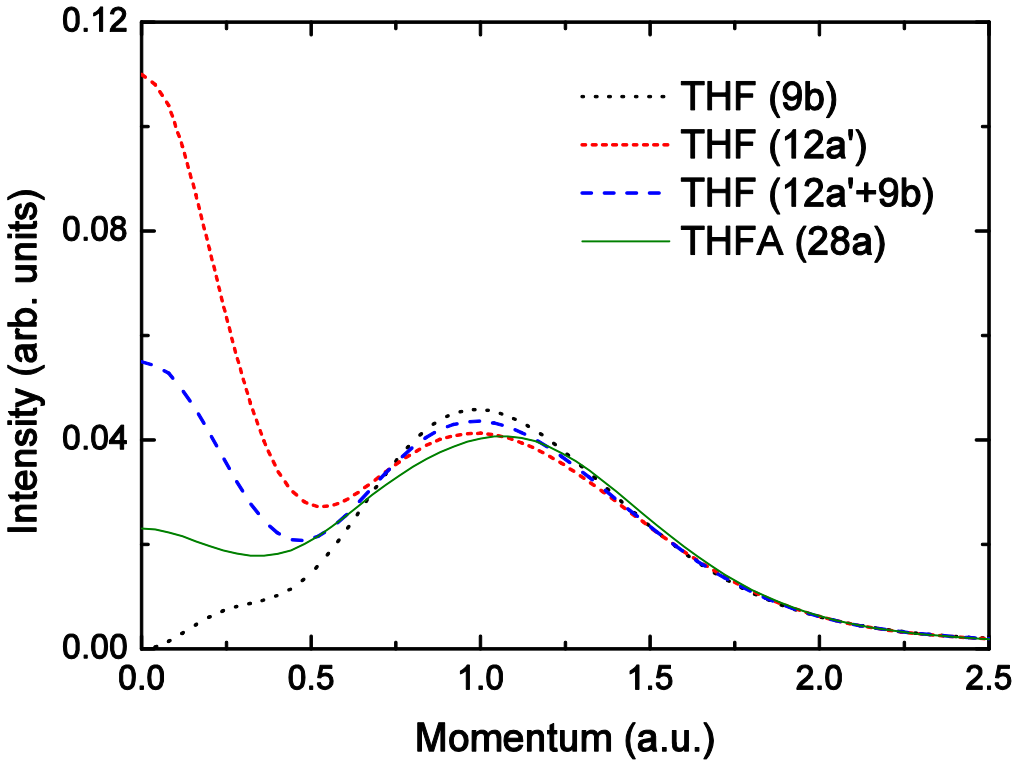


Figure. 5. Momentum profiles for the HOMOs (9b, 12a′ and conformationally averaged 9b+12a′) of THF and 28a of THFA. See text for further details

## Conclusions

By supplementing earlier studies on electron-impact ionization of THF [26], with new experimental measurements and theoretical calculations under kinematical conditions that matched those employed in our previous study of THFA [29], significant insights into the nature of the observed binary-to-recoil ratios have been revealed. The present results for THF, when compared against previous results measured under different kinematical conditions [26], suggest that the relevant orbital momentum profiles may assist us in understanding the observed binary-to-recoil peak ratios for a particular target. However, when the TDCS measurements of THF were compared to those from THFA, it was also apparent that a quantitative understanding of the collision dynamics is also required to explain the observed scattering phenomena.

**Acknowledgements**

This research was supported by the Australian Research Council (ARC) Centre of Excellence for Antimatter-Matter Studies, by the US National Science Foundation under Grant. No. PHY-1068237 (HC and DHM), and by the National Natural Science Foundation of China under Grants No. 11174175 (CGN). DBJ acknowledges financial support provided through an ARC Discovery Early Career Researcher Award (DECRA). O.I. acknowledges support from the Icelandic Centre for Research (RANNIS) and the Research fund of the University of Iceland.

**References**

[1] L. Chiari, M.J. Brunger, A. Zecca, Total cross sections for positron scattering from bio-molecules, in: G. Garcia Gomez-Tejedor, M.C. Fuss (Eds.), Radiation Damage in Biomolecular Systems, Springer, London, UK, 2012, pp. 155–163.

[2] I. Baccarelli, I. Bald, F.A. Gianturco, E. Illenberger, J. Kopyra, Phys. Rep. 508 (2011) 1.

[3] S.M. Pimblott, J.A. LaVerne, Radiat. Phys. Chem. 76 (2007) 1244.

[4] B. Boudaiffa, P. Cloutier, D. Hunting, M.A. Huels, L. Sanche, Science 287 (2000) 1658.

[5] X. Pan, P. Cloutier, D. Hunting, L. Sanche, Phys. Rev. Lett. 90 (2003) 208102.

[6] F. Martin, P.D. Burrow, Z.L. Cai, P. Cloutier, D. Hunting, L. Sanche, Phys. Rev. Lett. 93 (2004) 068101.

[7] D.S. Milne-Brownlie, S.J. Cavanagh, B. Lohmann, C. Champion, P.A. Hervieux, J. Hanssen, Phys. Rev. A 69 (2004) 032701.

[8] C.J. Colyer, M.A. Stevenson, O. Al-Hagan, D.H. Madison, C.G. Ning, B. Lohmann, J. Phys. B: At. Mol. Opt. Phys. 42 (2009) 235207.

[9] J. Builth-Williams, S.M. Bellm, D.B. Jones, H. Chaluvadi, D. Madison, C.G. Ning, B. Lohmann, M.J. Brunger, J. Chem. Phys. 136 (2012) 024304.

[10] S.M. Bellm, C.J. Colyer, B. Lohmann, C. Champion, Phys. Rev. A 85 (2012) 022710.

[11] A. Zecca, L. Chiari, G. Garcia, F. Blanco, E. Trainotti, M.J. Brunger, New J. Phys. 13 (2011) 063019.

[12] A. Zecca, C. Perazzolli, M.J. Brunger, J. Phys. B: At. Mol. Opt. Phys. 38 (2005)2079.

[13] M. Fuss, A. Munoz, J.C. Oller, F. Blanco, D. Almeida, P. Limão-Vieira, T.P.D. Do,M.J. Brunger, G. Garcia, Phys. Rev. A 80 (2009) 052709.

[14] P. Mozejko, E. Ptasinska-Denga, A. Domaracka, C. Szmytkowski, Phys. Rev. A 74 (2006) 012708.

[15] W.Y. Baek, M. Bug, H. Rabus, E. Gargioni, B. Grosswendt, Phys. Rev. A 86 (2012) 032702.

[16] C.J. Colyer, V. Vizcaino, J.P. Sullivan, M.J. Brunger, S.J. Buckman, New J. Phys. 9 (2007) 41.

[17] A.R. Milosavljevic, A. Giuliani, D. Sevic, M.J. Hubin-Franskin, B.P. Marinkovic, Eur. Phys. J. D 35 (2005) 411.

[18] M. Dampc, A.R. Milosavljevic´ , I. Linert, B.P. Marinkovic´ , M. Zubek, Phys. Rev. A 75 (2007) 042710.

[19] A.R. Milosavljevic´ , F. Blanco, D. Šević´ , G. García, B.P. Marinkovic´ , Eur. Phys. J. D 40 (2006) 107.

[20] A. Gauf, L.R. Hargreaves, A. Jo, J. Tanner, M.A. Khakoo, T. Walls, C. Winstead, V. McKoy, Phys. Rev. A 85 (2012) 052717.

[21] M. Allan, J. Phys. B: At. Mol. Opt. Phys. 40 (2007) 3531.

[22] T.P.T. Do, M. Leung, M. Fuss, G. Garcia, F. Blanco, K. Ratnavelu, M.J. Brunger, J. Chem. Phys. 134 (2011) 144302.

[23] M. Dampc, I. Linert, A.R. Milosavljevic´ , M. Zubek, Chem. Phys. Lett. 443 (2007) 17.

[24] B.C. Ibanescu, O. May, A. Monney, M. Allan, Phys. Chem. Chem. Phys. 9 (2007) 3163.

[25] P. Sulzer, S. Ptasinska, F. Zappa, B. Mielewska, A.R. Milosavljevic, P. Scheier, T.D. Mark, I. Bald, S. Gohlke, M.A. Huels, E. Illenberger, J. Chem. Phys. 125 (2006) 044304.

[26] C.J. Colyer, S.M. Bellm, B. Lohmann, G.F. Hanne, O. Al-Hagan, D.H. Madison, C.G. Ning, J. Chem. Phys. 133 (2010) 124302.

[27] C.J. Colyer, S.M. Bellm, G.F. Hanne, O. Al-Hagan, D. Madison, C.G. Ning, B. Lohmann, J. Phys. Conf. Ser. 288 (2011) 012007.

[28] C.J. Colyer, M.A. Stevenson, B. Lohmann, J. Phys.: Conf. Ser. 194 (2009) 052022.

[29] S.M. Bellm, J.D. Builth-Williams, D.B. Jones, H. Chaluvadi, D.H. Madison, C.G. Ning, F. Wang, X.G. Ma, B. Lohmann, M.J. Brunger, J. Chem. Phys. 136 (2012) 244301.

[30] S.J. Cavanagh, B. Lohmann, J. Phys. B: At. Mol. Opt. Phys. 32 (1999) L261.

[31] J. Gao, D.H. Madison, J.L. Peacher, J. Chem. Phys. 123 (2005) 204314.

[32] J. Gao, D.H. Madison, J.L. Peacher, J. Phys. B: At. Mol. Opt. Phys. 39 (2006) 1275.

[33] J. Gao, J.L. Peacher, D.H. Madison, J. Chem. Phys. 123 (2005) 204302.

[34] C. Lee, W. Yang, R.G. Parr, Phys. Rev. B 37 (1988) 785.

[35] C.F. Guerra, J.G. Snijders, G. te Velde, E.J. Baerends, Theor. Chem. Acc. 99 (1998) 391.

[36] S.J. Ward, J.H. Macek, Phys. Rev. A 49 (1994) 1049.

[37] J.B. Furness, I.E. McCarthy, J. Phys. B: Atom. Molec. Phys. 6 (1973) 2280.

[38] J.P. Perdew, A. Zunger, Phys. Rev. B 23 (1981) 5048.

[39] N.T. Padial, D.W. Norcross, Phys. Rev. A 29 (1984) 1742.

[40] D.H. Madison, O. Al-Hagan, J. At. Mol. Opt. Phys. 2010 (2010) 367180.

[41] A. Giuliani, P. Limão-Vieira, D. Duflot, A.R. Milosavljevic, B.P. Marinkovic, S.V. Hoffmann, N. Mason, J. Delwiche, M.J. Hubin-Franskin, Eur. Phys. J. D 51 (2009) 97.

[42] C.G. Ning, Y.R. Huang, S.F. Zhang, J.K. Deng, K. Liu, Z.H. Luo, F. Wang, J. Phys. Chem. A 112 (2008) 11078.

[43] T. Yang, G. Su, C. Ning, J. Deng, F. Wang, S. Zhang, X. Ren, Y. Huang, J. Phys. Chem. A 111 (2007) 4927.

[44] J.P.D. Cook, C.E. Brion, Chem. Phys. 69 (1982) 339.

[45] M.J. Frisch et al., GAUSSIAN 09, Revision B.01, Gaussian Inc., Wallington CT, USA (2010).

[46] K. Kimura, S. Katsuwata, Y. Achiba, T. Yamazaki, S. Iwata, Handbook of HeI Photoelectron Spectra of Fundamental Organic Molecules, Japan Scientific Societies Press, Tokyo, Japan, 1981.

[47] M. Yamauchi, H. Yamakado, K. Ohno, J. Phys. Chem. A 101 (1997) 6184.

[48] S. Xu, X. Ma, S. Yan, P. Zhang, J. Chem. Phys. 136 (2012) 237101.

[49] E. Weigold, I.E. McCarthy, Electron Momentum Spectroscopy, Kluwer Academic/Plenum Publishers, New York, 1999

## IX A dynamical (e,2e) investigation of the structurally related cyclic ethers tetrahydrofuran, tetrahydropyran and 1,4-dioxane

J. D. Builth-Williams,[1] S. M. Bellm,[1] L. Chiari,[1] P. A. Thorn,[1] D. B. Jones,[2,a)] H. Chaluvadi,[3] D. H. Madison,[3] C. G. Ning,[4] B. Lohmann,[5] G. da Silva,[1,6] and M. J. Brunger[1,7,b)]

[1]ARC Centre of Excellence for Antimatter-Matter Studies, Flinders University, GPO Box 2100, Adelaide, South Australia 5001, Australia.

[2]School of Chemical and Physical Sciences, Flinders University, GPO Box 2100, Adelaide, South Australia 5001, Australia.

[3]Department of Physics, Missouri University of Science and Technology, Rolla, Missouri 65409, USA.

[4]Department of Physics, State Key Laboratory of Low-Dimensional Quantum Physics,

Tsinghua University, Beijing 100084, China.

[5]University of the Sunshine Coast, Maroochydore DC, Queensland 4558, Australia.

[6]Department of Physics, Universidade Federal de Mato Grosso, Cuiabá, Mato Grosso, Brazil.

[7]Institute of Mathematical Sciences, University of Malaya, 50603 Kuala Lumpur, Malaysia.

### Abstract

Triple differential cross section measurements for the electron-impact ionization of the highest occupied molecular orbitals of tetrahydropyran and 1,4-dioxane are presented. For each molecule, experimental measurements were performed using the

(e,2e) technique in asymmetric coplanar kinematics with an incident electron energy of 250 eV and an ejected electron energy of 20 eV. With the scattered electrons being detected at -5°, the angular distributions of the ejected electrons in the binary and recoil regions were observed. These measurements are compared with calculations performed within the molecular 3-body distorted wave (M3DW) model. Here reasonable agreement was observed between the theoretical model and the experimental measurements. These measurements are compared with results from a recent study on tetrahydrofuran [Jones *et al.* Chem. Phys. Lett. **572**, 32 (2013)], in order to evaluate the influence of structure on the dynamics of the ionization process across this series of cyclic ethers.

## Introduction

Electron-matter interactions play key roles in the processes relating to terrestrial and atmospheric phenomena and plasma processing.[1] Recently, positron- and electron-interactions in biological systems have attracted significant attention[2, 3] owing to the large number of secondary electrons that are produced from a single ionizing particle.[4] Here the low-energy secondary electrons can deposit energy through ro-vibrational or electronic excitations or induce damage to the system through ionization or dissociative electron attachment processes.[5] In particular, recent studies have revealed that low-energy electron interactions with DNA can induce single and double strand breakage.[6, 7] This has created a pressing demand for electron-impact collision cross section data with biological analogues that can be used for simulating radiation-induced damage to biological media. Further, collision cross section data may also provide clues for understanding radiation-induced phenomena in larger macro-molecular environments.

The experimental difficulties in measuring collision cross sections for many biological species have, however, limited the availability of data. This is particularly true

for solid targets, such as the DNA bases. As such, it is imperative that theoretical models be developed that can accurately simulate data for species for which no experimental data is currently available. In this respect, studies on electron-induced phenomena on series of chemically similar compounds serve as a method for providing benchmark experimental cross section data that can test and assess the limitations of the theoretical models. Such studies represent an important step in understanding how the structure of a species can influence the electron scattering phenomena. In this vane, we have recently extended some of our earlier studies on individual biomolecules[8-14] to chemically similar compounds in an attempt to further understand the role of structure and kinematics on the dynamics of electron-impact ionization.[15]

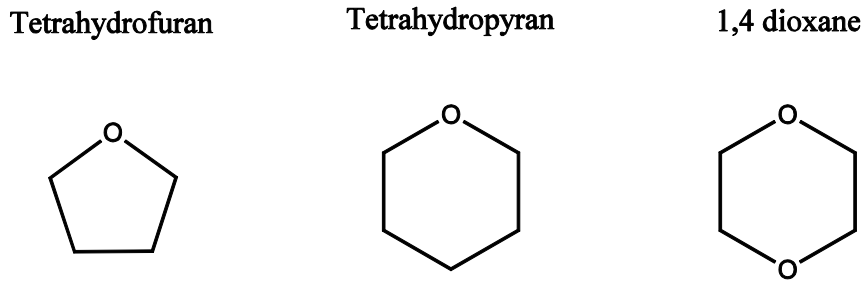


Figure 1. The structure of the cyclic ethers; (a) tetrahydrofuran, (b) tetrahydropyran and (c) 1,4-dioxane.

Building on that work, we present a dynamical (e,2e) investigation to compare the electron-impact ionization process across a series of cyclic ethers: tetrahydrofuran (THF, $C_4H_8O$), tetrahydropyran (THP, $C_5H_{10}O$) and 1,4-dioxane ($C_4H_8O_2$). These species are shown schematically in Fig. 1. Note that previous measurements of total cross sections for electron[16, 17] and positron scattering[18] from series of structurally related cyclic ethers have been useful in establishing trends in their scattering phenomena. Further, they have revealed the potential for constructing functional forms for describing the total scattering

cross section in both the electron and positron scattering cases. As such, a dynamical (e,2e) investigation of these cyclic ethers may provide key insights into the nature of ionization phenomena.

In this paper, we therefore supplement the existing data for electron-impact dynamical ionization of THF,[12-15] with the first dynamical (e,2e) measurements for THP and 1,4-dioxane. Specifically, we present triple differential cross section (TDCS) measurements for the ionization of the highest occupied molecular orbital (HOMO) for each of these species. For these cyclic ethers, the HOMOs are expected to be dominated by the non-bonding out-of-plane lone-electron pair contributions from the oxygen atom(s). With qualitatively similar orbital structures for each target, the present results may thus be expected to provide detailed information into the influence that structure plays on the dynamics of the electron-impact ionization process. For our TDCS measurements, we select kinematical conditions that fall below the bound Bethe-Ridge condition. In our previous work on large biomolecules, these kinematical conditions exhibited the most sensitivity regarding the observed binary to recoil peak ratios.

The paper is organized as follows. In Section experimental method we present our experimental details and measurement techniques. This is followed by a discussion of the theoretical methods employed in Section theoretical details. We next provide a summary of the spectroscopy of the cyclic ethers, and how it impacts on their electron scattering phenomena. Our results are then presented and discussed in Section results and discussion. Following this, the conclusions drawn from this investigation are summarized.

## Experimental Method

Triple differential cross sections for the electron-impact ionization of cyclic ethers have been measured under coplanar asymmetric kinematical conditions using a (e,2e) coincidence technique. These processes are described by

$$e_0^-(E_0, p_0) + T \rightarrow T^+(\varepsilon_i, q) + e_a^-(E_a, p_a) + e_b^-(E_b, p_b), \qquad (1)$$

where the target, $T$, is either THP or 1,4-dioxane. Here $E_j$ and $p_j (j = 0, a, orb)$ are the energies and momenta of the incident, scattered and ejected electrons, respectively. Here the conservation of energy during the collision determines the binding energy $K = p_0 - p_a$ of the ionized orbital,

$$\varepsilon_i = E_0 - (E_a + E_b). \qquad (2)$$

Likewise, the recoil momentum of the target ion is determined by the conservation of momentum,

$$q = p_0 - (p_a + p_b). \qquad (3)$$

In the present experiments, the incident electron and ejected electron energies are fixed at $E_0$ = 250 eV and $E_b$ = 20 eV, respectively. The scattered electron is detected at a fixed polar angle, $\theta_a$ = -5°, made with respect to the incident electron beam direction. The momentum of the scattered electron defines the momentum transferred to the target,

$$K = p_0 - p_a. \qquad (3)$$

Under the conditions where the ejected electron is in a direction close to that of the momentum transfer direction (+*K*), all momentum transferred to the target is absorbed by the outgoing electron. This minimizes the recoil momentum magnitude, and the collisions are said to be binary. Similarly, when the electron is directed in the direction

opposite to that of the momentum transfer (-*K*), the ions' recoil momentum is at its maximum, and the collisions are said to be recoil in nature.

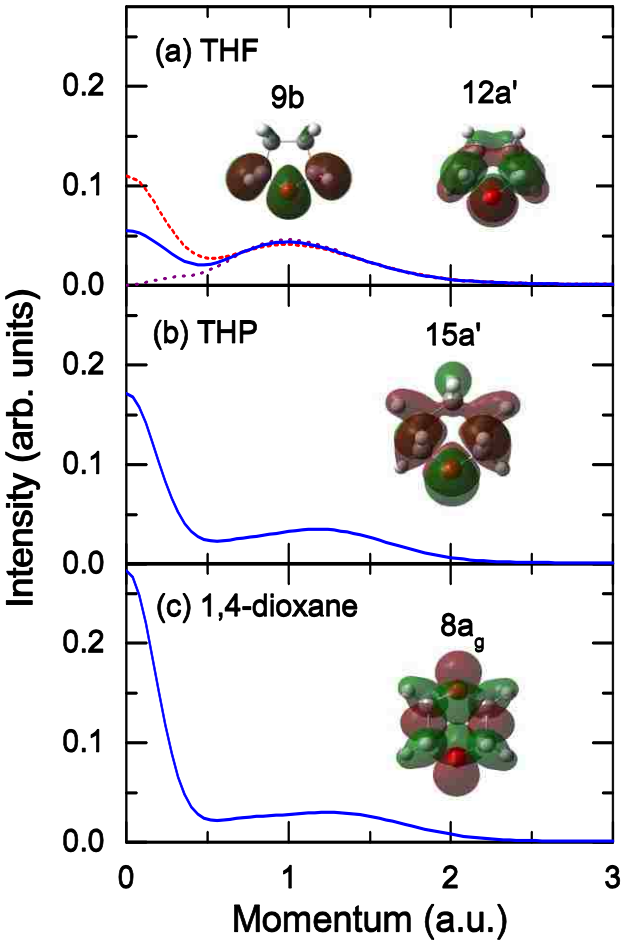


Figure. 2. Momentum profile and spatial representation of the HOMO for each cyclic ether. (a) 9b (· · ·), 12a′ (— —), and the conformational average of the 12a′+9b (——) orbitals of THF; (b) 15a′ orbital of THP; (c) 8ag orbital of 1,4-dioxane. See text for further details

The full details of our experimental apparatus and measurement procedure have been described previously,[13, 19] so only a brief précis is repeated again here. An electron beam of fixed energy, $E_0$ = 250 eV, is generated through the thermionic emission of a tungsten filament. The emitted electrons are then accelerated, collimated and focused into the interaction region by a 5-element cylindrical lens stack. The energy resolution of the

incident electron beam was of the order of ~0.5 eV (FWHM). The electrons now interact with a pure beam of the target molecules (either THP or 1,4-dioxane) introduced through a capillary. Here, high purity samples were degassed by repeated freeze-pump-thaw cycles prior to being introduced into the system. During the measurements, the vacuum chamber and sample gas lines were heated to ~40 °C in order to minimize any absorption onto their surfaces. Scattered (fast) and ejected (slow) electrons, produced in ionizing collisions with the target beam, were detected in separate analyzers, mounted on independently rotatable turntables. Each analyzer consisted of a 5-element electrostatic lens, hemispherical energy selector and channel electron multiplier. Using standard coincidence timing techniques, the arrival times of the electrons detected in each analyzer were used to determine if the electrons originated from the same ionization event.

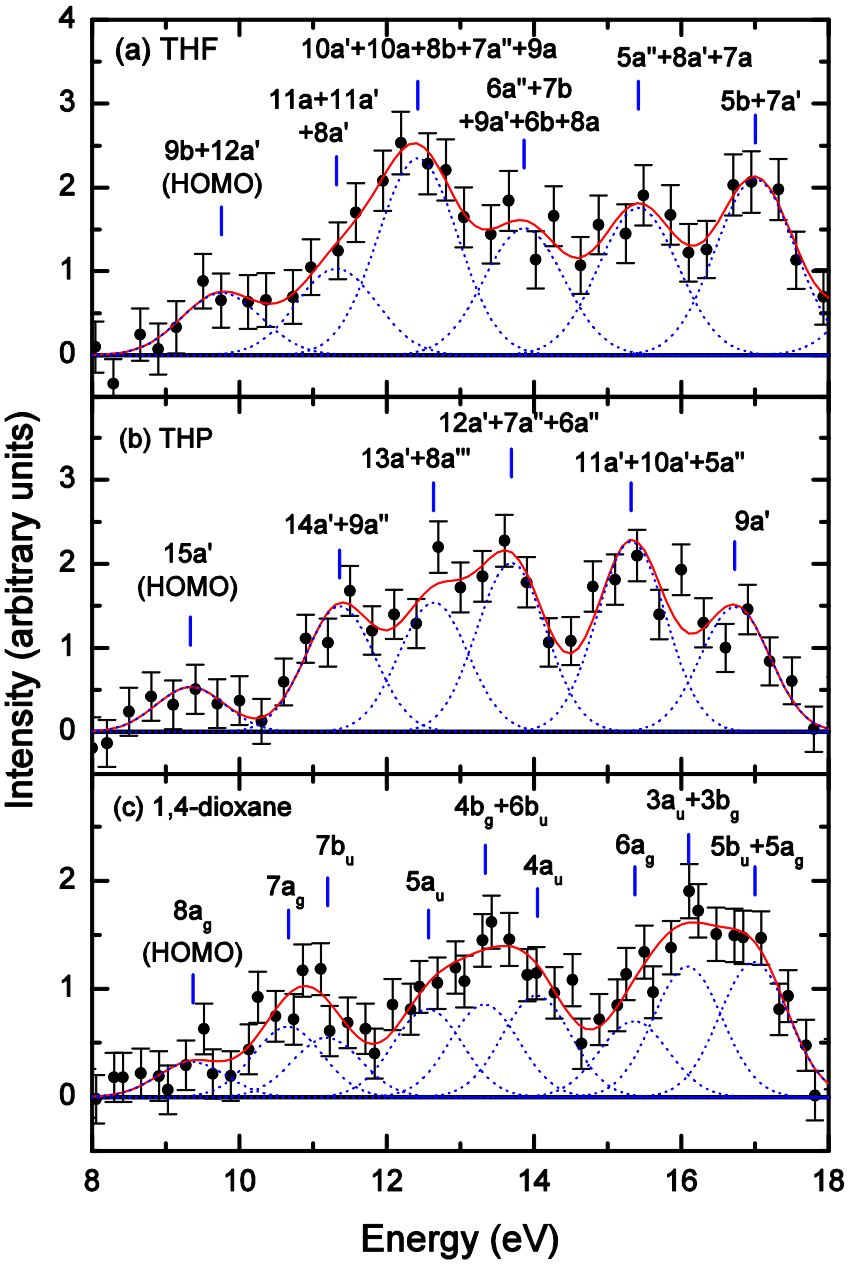


Figure. 3. Measured binding energy spectra (●) for (a) THF, (b) THP, and (c) 1,4-dioxane. Also shown are the spectral deconvolutions of the measured spectra into contributions from each orbital feature (— —) and their sum (——). See text for further details

For each cyclic ether, we measured its binding energy spectrum (BES-see later). These spectra are obtained at $E_0$ = 250 eV and $E_b$ = 20 eV, while the scattered and ejected electron angles are fixed at $\theta_a$ = -10° and $\theta_b$ = 75°, respectively. The BES for each target

is obtained by measuring the number of true coincident events as the scattered electron energy is repeatedly scanned over a range of detection energies. Here the kinematics for the binding energy spectra measurements are selected to approximate bound Bethe ridge kinematics, where $|\boldsymbol{K}|\approx|\boldsymbol{K_b}|$, and we note that the typical coincidence binding energy resolution of the apparatus is 1.1 eV (FWHM) as determined from measurements of the Helium 1s binding energy peak.

In the present work, TDCS for a particular transition are obtained by fixing the scattered electron analyzer at $\theta_a$ = -5° and rotating the ejected electron analyzer in the scattering plane. In this way we obtain angular distributions for the slow ejected electron. Here we again note that the incident electron and ejected electron energies are $E_0$ = 250 eV and $E_b$ = 20 eV, respectively. The selected kinematics for our TDCS study now correspond to those below the bound Bethe-Ridge, and match those employed in our earlier study on THF.[15] Specifically, the magnitude of the momentum transfer, $|\boldsymbol{K}|$ = 0.45 a.u, is much less than the momentum of the ejected electron, $|p_b|$ = 1.21 a.u. As such, a substantial linear momentum contribution to the outgoing electrons must arise from the internal momentum of the particles within the target. Under these conditions, below the bound Bethe-Ridge condition, the magnitude of the momentum transfer and the ejected electron's momentum are comparable to the momentum of the electrons bound to the target. Indeed, this kinematical condition has been most interesting in terms of our earlier dynamical (e,2e) studies on large biomolecules.[8-14]

## Theoretical Details

The present experimental data is compared to theoretical calculations obtained within a M3DW (molecular 3-body distorted wave) framework.[20-22] These calculations

have been described elsewhere, so only a brief description is repeated here. The TDCS for the M3DW is given by

$$\frac{d\sigma}{d\Omega_a d\Omega_b dE_b} = \frac{1}{(2\pi)^5}\frac{k_a k_b}{k_i}\left(|T_{dir}|^2 + |T_{exc}|^2 + |T_{dir} - T_{exc}|^2\right), \quad (5)$$

where $\vec{k}_i$, $\vec{k}_a$, and $\vec{k}_b$ are the wave vectors for the initial, scattered and ejected electrons, respectively, $T_{dir}$ is the direct scattering amplitude, and $T_{exc}$ is the exchange amplitude. The direct scattering amplitude is given by

$$T_{dir} = \left\langle \chi_a^-(\vec{k}_a, \mathbf{r}_1)\chi_b^-(\vec{k}_b, \mathbf{r}_2)C_{scat-eject}(r_{12}^{ave})\,|\,V - U_i\,|\,\phi_{DY}^{OA}(\mathbf{r}_2)\chi_i^+(\vec{k}_i, \mathbf{r}_1)\right\rangle. \quad (6)$$

Here $r_1$ and $r_2$ are the coordinates of the incident and the bound electrons, $\chi_i, \chi_a$, and $\chi_b$ are the distorted waves for the incident, scattered, and ejected electrons respectively, and $\phi_{DY}^{OA}(r_2)$ is the initial bound-state Dyson molecular orbital averaged over all orientations. Under the frozen orbital approximation, the Dyson orbital can be approximated using the initial bound Kohn-Sham orbital. The molecular wave functions were calculated using density functional theory (DFT) along with the standard hybrid B3LYP[23] functional by means of the ADF 2007 (Amsterdam Density Functional) program[24] with the TZ2P (triple-zeta with two polarization functions) Slater type basis sets. The factor $C_{scat-eject}(r_{12}^{ave})$ is the Ward-Macek average Coulomb-distortion factor between the two final state electrons,[25] $V$ is the initial state interaction potential between the incident electron and the neutral molecule, and $U_i$ is a spherically symmetric distorting potential which is used to calculate the initial-state distorted wave for the

incident electron $\chi_i^+(\vec{k}_i, \mathbf{r}_1)$. For the exchange amplitude $T_{exc}$, particles 1 and 2 are interchanged in equation (6).

The Schrödinger equation for the incoming electron wave-function is given by:

$$(T + U_i - \frac{k_i^2}{2})\chi_i^+(\vec{k}_i, r) = 0, \qquad (7)$$

where $T$ is the kinetic energy operator and the '+' superscript on $\chi_i^+(\vec{k}_i, \mathbf{r})$ indicates outgoing wave boundary conditions. The initial state distorting potential contains three components $U_i = U_s + U_E + U_{CP}$, where $U_s$ contains the nuclear contribution plus a spherically symmetric approximation for the interaction between the projectile electron and the target electrons which is obtained from the quantum mechanical charge density of the target. The charge density is obtained by summing $2|\phi_{DY}|^2$ over all occupied orbitals (the 2 is for double occupancy and the original non-averaged Dyson orbital is used). The nuclear contribution to $U_s$ is the interaction between the projectile electron and all the nuclei of the respective molecular target averaged over all orientations. Averaging the nuclei over all orientations is equivalent to putting the nuclear charge on a thin spherical shell whose radius is the distance of the nuclei from the center of mass (CM).

For THP, there is no nuclei at the CM. The closest nuclei to the CM are the 2 carbons at 2.699 $a_0$. Consequently, the first nuclear sphere has a charge of 12 with a radius of 2.699 $a_0$. The next sphere has one oxygen with charge 8 at 2.700 $a_0$. The next sphere has another two carbons with charge 12 at 2.753 $a_0$. The next sphere has one carbon with charge 6 at 2.774 $a_0$. The next sphere has two hydrogens with charge 2 at 3.728$a_0$. The next sphere has one hydrogen with charge 1 at

3.823 $a_0$. The next 6 hydrogen nuclei are on 3 spheres of charge 2 located at 3.827,4.601 and 4.645 $a_0$ respectively, and the next sphere has 1 hydrogen with charge 1 at 4.681 $a_0$.

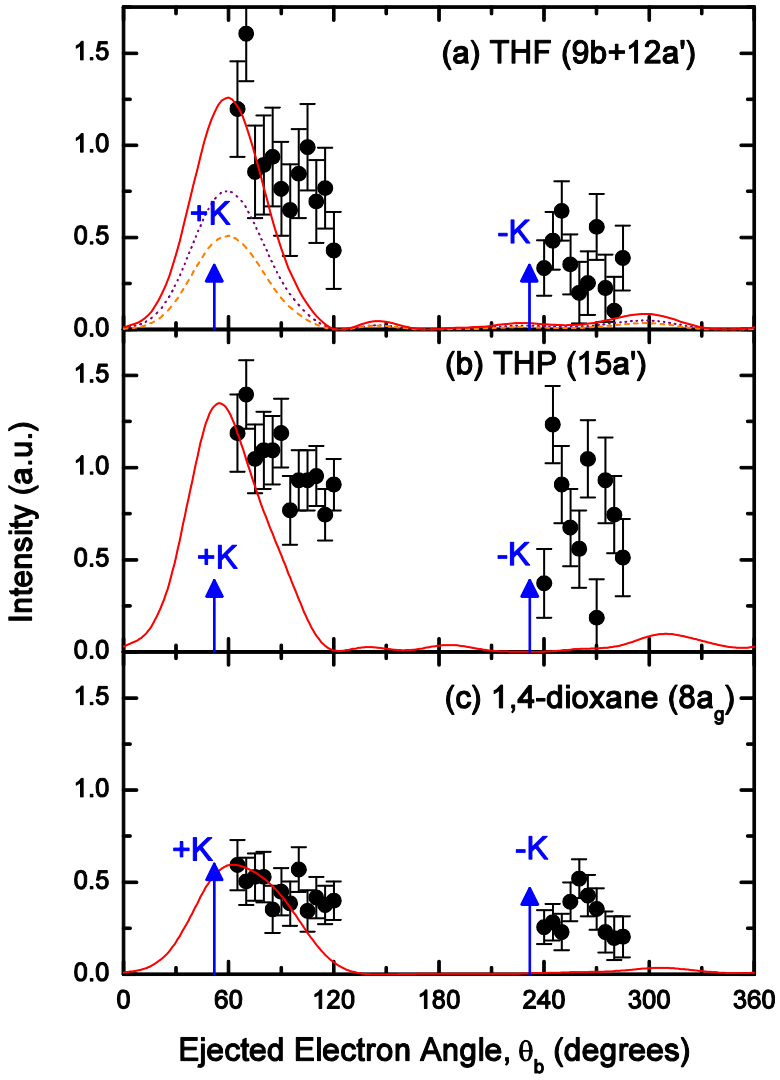


Figure. 4. Triple differential cross sections for the electron impact ionization of the HOMOs of (a) THF (9b+12a′), (b) THP (15a′), and (c) 1,4-dioxane ($8a_g$) with $E_0$=250eV and $E_b$=20eV. Measured experimental data (●). The M3DW calculation results (——) are also presented for each orbital or conformational average of contributing orbitals. Additionally shown are the TDCS contributions from the 9b (— —) and 12a′ (·····) orbitals of THF, after being weighted by their respective conformer populations. See text for further details.

For 1,4—dioxane, also there are no nuclei found at theCM. The first nuclear sphere has 4 carbon nuclei with a total charge of 24 at a radius of 2.639 $a_0$. The next sphere has 2 oxygen nuclei with charge 16 at 2.668 $a_0$, while the 8 hydrogen nuclei are described by 2 spheres of charge 4 with radii of 3.707 and 4.521 $a_0$, respectively. Note that we present the radii to three decimal places to distinguish the closely spaced nuclear spheres, not because we necessarily believe that we have this level of numerical accuracy in our calculations. Note that the corresponding details of our calculations on THF can be found elsewhere,[15]

$U_E$ is the exchange potential of Furness-McCarthy (corrected for sign errors)[26] which approximates the effect of the continuum electron exchanging with the passive bound electrons in the molecule, and $U_{CP}$ is the correlation-polarization potential of Perdew and Zunger [27] (see also Padial and Norcross [28]).

In equation (6), the final state for the system is approximated as a product of distorted waves for the two continuum electrons $(\chi_a^-, \chi_b^-)$ times the Ward-Macek average Coulomb-distortion factor $C_{scat-eject}$. The final state distorted waves are calculated the same as the initial state except that the final state charge density is used to calculate $U_s$. The final state charge density is obtained the same as the initial state except that unity occupancy is used for the active electron orbital. Additional details can be found in Madison and Al-Hagan [29].

To assist in the interpretation of the scattering phenomena, theoretical calculations to optimize the geometries and calculate molecular properties have been performed at the B3LYP/aug-cc-pVDZ level using Gaussian 09.[30] These calculations have been utilized to

generate orbital momentum profiles for each target,[31] with the results being given in Fig. 2.

**Structure and Spectroscopy of Cyclic Ethers**

The structures of the cyclic ethers have attracted considerable interest.[32-35] On the one hand THF has a relatively flat 5-member ring that possesses puckering out of the planar configuration, with the flatness of this ring structure producing a number of conformations that lie close in energy. Further, low potential energy barriers for pseudo-rotation between its conformations enables essentially free rotation between minima.[32, 33] As such, THF exists in conformers with either $C_2$ and $C_s$ symmetry found along the pseudorotation coordinate.[32, 33] On the other hand, it has been well established that both THP and 1,4-dioxane exist in their lowest energy chair conformations.[34, 35] These, respectively, have $C_2$ and $C_{2h}$ symmetries. In the interest of making fruitful comparisons regarding the behavior of these three cyclic ethers, we consider THF through an average over the $C_2$ to $C_s$ conformations; with experimental results having revealed that both conformations exist in near equal proportions at room-like temperatures.[32, 33] As our experiment is performed under room-like temperature conditions, this is a reasonable approximation given the complexity of the calculations. The full details of this averaging approach have been described elsewhere.[15]

Information regarding the ionization of the cyclic ethers has been obtained by ultraviolet photoelectron spectroscopy (PES),[36-38] Penning ionization electron spectroscopy (PIES)[36] and electron momentum spectroscopy.[33, 39] In all the species under consideration, the highest-occupied molecular orbital (HOMO) is well separated from the other orbitals. Here the HOMOs are 9b+12a′, 15a and $8a_g$ for THF, THP and 1,4-dioxane, respectively. The calculated momentum profiles and spatial representation for the HOMO

of each species is presented in Fig 2. Each of these orbitals is dominated by the out-of-plane lone electron pair from the oxygen atom(s). Here the structure of the target allows for varying degrees of interaction between the lone-electron pair and the carbon ring structure, with the non-bonding lone-electron pair interaction with the carbon frame increasing as the structure changes in going from the relatively flat THF molecule to the chair conformation of THP. These interactions are further enhanced in 1,4-dioxane where there are also through-bond interactions that couple the lone-electron pair contributions from each of the oxygen atoms found in the ring. Note that this through-bond interaction energetically splits the molecular orbitals corresponding to the symmetric/asymmetric lone electron pair contributions.

The coupling of the lone-electron pair contributions to the carbon frame are particularly evident from the calculated orbital momentum distributions presented in Fig. 2. Note that our calculated orbital momentum profiles for THF and 1,4-dioxane are in reasonable qualitative agreement with measured orbital momentum profiles from independent electron momentum spectroscopy experiments.[33, 39, 40] To our knowledge, there are no other theoretical or experimental data for the momentum profile of the HOMO of THP with which we can compare our calculation. Here we see that the momentum profiles for each species have two distinct features. Namely, there is the oxygen lone-electron 2p contribution that gives the local maxima about 0.5-1.5 a.u and the σ–contribution from the carbon frame at momentum $|\boldsymbol{p}| \sim 0$ a.u. In Fig. 2 we also see discernible trends in the momentum profiles, with the σ–contribution increasing from THF to THP and then to 1,4-dioxane as the lone-electron pair(s) have larger interactions with the carbon frame. Note that the delocalization of the lone-electron pair through the

carbon frame reduces the overall magnitude of the 2p oxygen contribution and shifts its peak to a higher momentum value. These peak values have intensities of 0.044, 0.035 and 0.030 and are located at 1.00, 1.16 and 1.24 a.u for THF, THP and 1,4,-dioxane, respectively. In 1,4-dioxane, this redistribution of intensity in the momentum profile is also expected to be influenced by the interference effects of having O(2p) contributions located on separated atoms, the so called bond-oscillation phenomenon.[41]

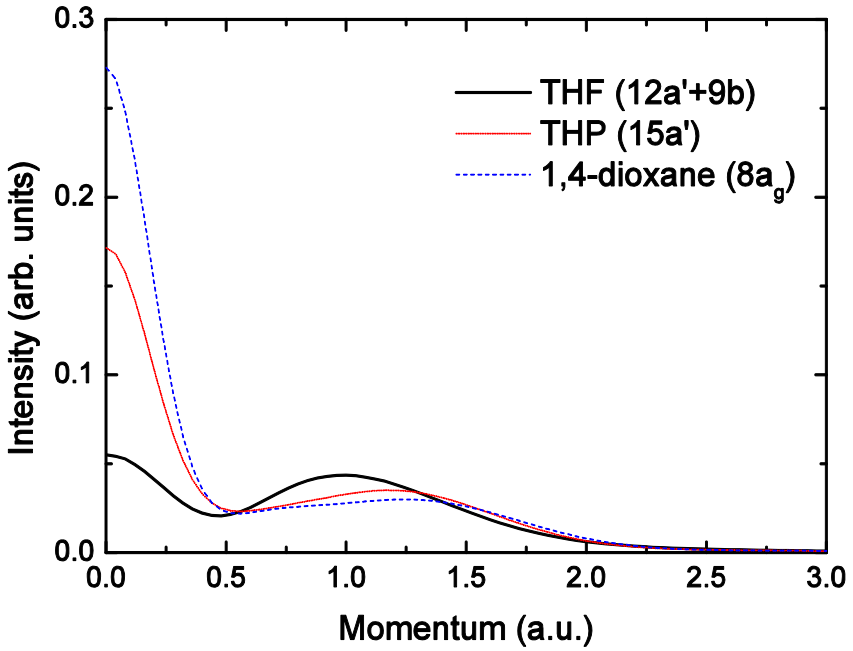


Figure. 5. Momentum profiles for 12a′+9b orbitals of THF (——), the 15a′ orbital of THP (· · ·), and the $8a_g$ orbital of 1,4-dioxane (— —), now plotted on the one graph. See text for further details.

The coupling of the lone-electron pair contributions to the carbon frame are particularly evident from the calculated orbital momentum distributions presented in Fig. 2. Note that our calculated orbital momentum profiles for THF and 1,4-dioxane are in reasonable qualitative agreement with measured orbital momentum profiles from independent electron momentum spectroscopy experiments.[33, 39, 40] To our knowledge,

there are no other theoretical or experimental data for the momentum profile of the HOMO of THP with which we can compare our calculation. Here we see that the momentum profiles for each species have two distinct features. Namely, there is the oxygen lone-electron 2p contribution that gives the local maxima about 0.5-1.5 a.u and the σ–contribution from the carbon frame at momentum $|\boldsymbol{p}| \sim 0$ a.u. In Fig. 2 we also see discernible trends in the momentum profiles, with the σ–contribution increasing from THF to THP and then to 1,4-dioxane as the lone-electron pair(s) have larger interactions with the carbon frame. Note that the delocalization of the lone-electron pair through the carbon frame reduces the overall magnitude of the 2p oxygen contribution and shifts its peak to a higher momentum value. These peak values have intensities of 0.044, 0.035 and 0.030 and are located at 1.00, 1.16 and 1.24 a.u for THF, THP and 1,4,-dioxane, respectively. In 1,4-dioxane, this redistribution of intensity in the momentum profile is also expected to be influenced by the interference effects of having O(2p) contributions located on separated atoms, the so called bond-oscillation phenomenon.[41]

While the structural changes across the series of cyclic ethers significantly effects the momentum distributions, these structural variations may have a minimal bearing on the scattering dynamics in the ionization of the HOMO for these species. Here the localized geometric perturbations surrounding the oxygen atom, in expanding the ring structure to accommodate the additional C atom in going from THF to THP, appears to be negligible. Specifically, the two closest C-atoms to the primary oxygen ionization site have bond distances of 1.43Å, whilst making COC angles of ~111-112° for both THF ($C_2$) and THP. Note that for the THF ($C_s$) conformer, it has the same bond distances with a slightly smaller COC angle of 106°. Further, the CO bond distances and COC angles

are also 1.43 Å and 111°, respectively, for 1,4-dioxane. We note that recent TDCS calculations on methane have revealed that a delocalization of the nuclear charge reduces the electron-nuclei post-collision interaction.[42] Bearing this in mind, perhaps of most importance in understanding ionization scattering dynamics is the proximity of the surrounding nuclei to the primary ionization site. We will examine this notion again later.

## Results and Discussion

In Fig. 3, the binding energy spectrum for each of the cyclic ethers is presented. Recall that all of these BES have been obtained under conditions where the incident electron is 250 eV, the scattered electron is detected at $\theta_a$ = -10°, and the ejected electron is detected at $\theta_b$= 75° with an energy of 20 eV. For each species, we note reasonable agreement regarding the location of features in the binding energy spectra with those previously observed in the PES and PIES experiments.[36, 38] Each binding energy spectrum has been deconvolved using Gaussian functions whose widths represent the combination of the coincidence energy resolution from the experimental apparatus and the line widths of the ionization transitions, as estimated from the respective photoelectron spectra. This deconvolution procedure suggests that the HOMO of THP may be completely resolved from the other molecular orbitals. For THF (conformer independent) and 1,4-dioxane, while PES reveals that the HOMOs are well separated from the next highest occupied molecular orbitals (NHOMO), the limited energy resolution of our spectrometer suggests that the HOMOs may not be completely resolved from the NHOMOs in our measurements on these species. However, the NHOMO contribution to the HOMO peak in the BES would still be very small in these cases.

Figures 4(a)-(c) show the experimental and theoretical TDCS results for the electron impact ionization of the HOMOs of THF, THP and 1,4-dioxane. For each cyclic

ether, the cross sections have been measured with the incident electron having an energy of 250 eV and the scattered electron being detected at $\theta_a$= -5°. Once again the ejected electron is detected with an energy of 20 eV. Note also that our experimental measurements are relative, and to place them on the absolute scale they have been independently normalized to the M3DW theory in each case at $\theta_b$= 65°. While we note that experimental techniques exist for placing the (e,2e) measurements on an absolute scale,[43] such techniques are not possible here owing to the complexity of the ionization spectra for such large molecules. We further note that the quite large statistical uncertainties in our TDCS in Fig. 4 arise from the difficulties in performing coincident measurements under the present kinematical conditions.

Considering Fig. 4, it is immediately apparent that the experimental binary peak for each species is particularly broad. Comparing these experimental results with those calculated, we observe that the width of the binary feature in each species is largely underestimated by the M3DW calculations. A possible exception to this is for 1,4-dioxane, where the M3DW calculation gave a broader peak than that calculated for either THF or THP. Although, even in this case, the M3DW cross section decreases more rapidly in magnitude than the experimental data at the larger ejected electron scattering angles ($\theta_b$= 110-120°) in the binary region. The M3DW calculations of the cyclic ethers in this binary region are also particularly interesting, and those details are now discussed in turn.

Firstly, the magnitude of the cross sections for THF and THP in their binary peaks were calculated to be similar, while the magnitude of 1,4-dioxane is about half that of THF and THP. Despite the similarity of the HOMOs for the cyclic ethers, the distribution

of the lone-electron pair contribution over multiple sites seems to significantly influence the calculated cross section intensity. This variation may have its origins from interference effects, commonly observed in (e,2e) experiments on diatomic molecules,[44, 45] that originate from the two ionization centers of the target acting as coherent sources. However, the complexity of the present target structures limits any quantitative assessment of such effects here. Secondly, the maximum binary cross section intensity is calculated to be at 60°, 55° and 62° for THF, THP and 1,4-dioxane, respectively. Here we note that the momentum transfer direction, under these kinematical conditions, for each of these cyclic ethers is 52°. The M3DW calculation gives larger shifts away from the momentum transfer direction for THF and 1,4-dioxane, than that calculated for THP. Unfortunately, the broad nature and rather large statistical uncertainty, on the experimental data for the binary feature, doesn't allow us to make a quantitative assessment of any possible experimental shift in the binary peak.

Shifting our discussion to the recoil region, prominent recoil peaks are observed in the experimental data for each species. In this case, we observe in Fig. 4 that the strength of these recoil features, relative to that observed for the binary features, changes between the 5- and 6-member rings. For THF the recoil peak is about a third of the intensity of the binary peak, while it is about two-thirds of the intensity of the binary peak for both THP and 1,4-dioxane. Interestingly, the experimental recoil data reveals quite broad flat features for both THF and THP, when the errors on the data are allowed for, while there is evidence of a quite prominent peak centered at $\theta_b$ = 260° for 1,4-dioxane. While significant experimental intensity is observed in the recoil region for each of the cyclic ethers, the M3DW model greatly underestimates the recoil feature intensity for

each species. The absence of any important theoretical recoil peak contribution has also been observed in our earlier studies on large biomolecules.[9, 10, 15] This is attributed to weak electron-nuclear scattering arising from the need to spread the nuclear charge in the calculation over large spherical shells, in order to perform the spherical averaging over the random orientation of the molecule. The key to unlocking this information may involve considering the localized ionization of the lone-electron pair on an oxygen atom, however, such calculations are limited by the complexity in performing scattering computations on open-shell targets.

The trend in the measured binary to recoil ratios across the series of cyclic ethers is also quite interesting. Previously Xu *et al.*[46] have suggested that the origins of the observed binary-to-recoil ratio may be related to the momentum profile of the ionized molecular orbital. In earlier studies on THF,[12-15] the behavior of the binary to recoil ratios, with respect to the variations in kinematical conditions could be qualitatively explained by relating the kinematical conditions to the ionized orbitals momentum profile. However, comparisons between the cross sections of THF and THFA[15] also revealed that the target molecular structure must play a role in the observed binary-to-recoil ratio. The cyclic ethers thus present an opportunity to discover the extent by which orbital momentum profiles may influence the scattering dynamics. In the present work, the geometric perturbations in expanding the 5-member ring structure to accommodate the additional C-atom are negligible in going from THF to THP, such that any contribution arising from electron-nuclei scattering may be similar if the scattering dynamics are dominated by the nuclei closest to the ionization site. We now evaluate if

the momentum profile can provide any clues for explaining the observed binary-recoil ratios in this series of structurally related cyclic ethers.

To assist in this discussion, the orbital momentum profiles of Fig. 2 have now been plotted together in Fig. 5. Under the present kinematics below the bound Bethe-ridge condition, where substantial linear momentum contributions must arise from the internal momentum of the target particles, the range in magnitude of the recoil momentum values covered by the experiment in going from the binary to recoil region is $|\boldsymbol{q}|$ = 0.77-1.66 a.u. Note that under such low-incident electron energy and low momentum transfer collisions, there is no guarantee that the recoil momentum is equal and opposite to the momentum of the bound electron at the time of ionization, as in electron momentum spectroscopy experiments,[47] however it may still provide insight into the observed physical behavior. Considering Fig. 5 in the momentum range 0.77-1.66 a.u., the momentum profile for the HOMO of THF starts at a higher intensity and decreases rather more rapidly than that for the HOMO of either THP or 1,4-dioxane. This observation may thus explain why the recoil peak intensity, relative to that observed for the binary, is lower for THF when compared to THP and 1,4-dioxane. Note also that the similar momentum profiles in this recoil momentum range for THP and 1,4-dioxane may also explain the similar binary to recoil peak intensities observed for those species.

With the clues for the observed scattering behavior between THF and THP possibly being qualitatively described by their respective momentum distributions, it appears as though 5- and 6-member rings exert similar effects on the scattering dynamics. This result may be somewhat expected, as the geometric perturbations in expanding the ring structure to accommodate the additional C-atom may be negligible here. It is

interesting to note that this behavior is markedly different from an earlier comparison between THF and THFA, where the addition of the exocyclic group appeared to perturb the scattering dynamics despite the orbital momentum profiles of the two targets being similar. All of these observations initially suggest that we may be able to separate contributions from the orbital behavior and the scattering dynamics to the measured TDCS. This in particular alludes to the possibility of identifying key structural moieties that can be utilized for the purpose of modeling the scattering dynamics of the ionization process in combination with quantum chemical calculations.

## Conclusion

We have presented results from the first dynamical study of the electron-impact ionization of tetrahydropyran and 1,4-dioxane. Here the measured binding energies for each species were found to be in good agreement with earlier photoelectron spectroscopic measurements. The chosen kinematical conditions enabled a comparison with our earlier measurements on tetrahydrofuran, in order to study the dynamics of the ionization process over a series of structurally related cyclic ethers under kinematics that fall below the bound Bethe ridge conditions. Across this series of cyclic ethers, the binary peak structures were seen to be quite broad with their widths generally being underestimated by our theoretical calculations. For each of the cyclic ethers, significant recoil peak intensity was observed and this was also largely underestimated by the present theoretical calculations. Our calculated orbital momentum profiles suggest that they may yet provide key information into explaining the observed binary-recoil ratios in this kinematic regime. The present results also hint at the possibility for separating the orbital and structural contributions to the scattering phenomena under dynamical (e,2e) conditions.

This would represent an important step in improving quantitative models for ionization phenomena in larger complex systems.

## Acknowledgements

This research was supported by the Australian Research Council (ARC) Centre of Excellence for Antimatter-Matter Studies, by the US National Science Foundation under Grant. No. PHY-1068237 (HC and DHM), and by the National Natural Science Foundation of China under Grant No. 11174175 (CGN). GdS thanks the Brazilian CNq funding agency and Flinders University for financial assistance during his stay in Australia. DBJ gratefully acknowledges support provided through an ARC Discovery Early Career Researcher Award.

## References

1. L. Campbell and M. J. Brunger, Plasma Sources Sci. Technol. **22**, 013002 (2013).

2. L. Chiari, M. J. Brunger and A. Zecca, in *Radiation Damage in Biomolecular Systems*, edited by G. Garcia Gomez-Tejedor and M. C. Fuss (Springer, London, UK, 2012), pp. 155-163.

3. I. Baccarelli, I. Bald, F. A. Gianturco, E. Illenberger and J. Kopyra, Phys. Rep. **508**, 1 (2011).

4. S. M. Pimblott and J. A. LaVerne, Radiat. Phys. Chem. **76**, 1244 (2007).

5. H. D. Flosadóttir, B. Ómarsson, I. Bald and O. Ingólfsson, Eur. J. Phys. D **66**, 13 (2012).

6. B. Boudaiffa, P. Cloutier, D. Hunting, M. A. Huels and L. Sanche, Science **287**, 1658 (2000).

7. X. Pan, P. Cloutier, D. Hunting and L. Sanche, Phys. Rev. Lett. **90**, 208102 (2003).

8. D. S. Milne-Brownlie, S. J. Cavanagh, B. Lohmann, C. Champion, P. A. Hervieux and J. Hanssen, Phys. Rev. A **69**, 032701 (2004).

9. S. M. Bellm, J. D. Builth-Williams, D. B. Jones, H. Chaluvadi, D. H. Madison, C. G. Ning, F. Wang, X. G. Ma, B. Lohmann and M. J. Brunger, J. Chem. Phys. **136**, 244301 (2012).

10. J. D. Builth-Williams, S. M. Bellm, D. B. Jones, H. Chaluvadi, D. Madison, C. G. Ning, B. Lohmann and M. J. Brunger, J. Chem. Phys. **136**, 024304 (2012).

11. C. J. Colyer, M. A. Stevenson, O. Al-Hagan, D. H. Madison, C. G. Ning and B. Lohmann, J. Phys. B: At. Mol. Opt. Phys. **42**, 235207 (2009).

12. C. J. Colyer, M. A. Stevenson and B. Lohmann, J Phys. Conf. Series **194**, 052022 (2009).

13. C. J. Colyer, S. M. Bellm, B. Lohmann, G. F. Hanne, O. Al-Hagan, D. H. Madison and C. G. Ning, J. Chem. Phys. **133**, 124302 (2010).

14. C. J. Colyer, S. M. Bellm, G. F. Hanne, O. Al-Hagan, D. Madison, C. G. Ning and B. Lohmann, J. Phys. Conf. Series **288**, 012007 (2011).

15. D. B. Jones, J. D. Builth-Williams, S. M. Bellm, L. Chiari, C. G. Ning, H. Chaluvadi, B. Lohmann, O. Ingolfsson, D. Madison and M. J. Brunger, Chem. Phys. Lett., (in press) (2013).

16. C. Szmytkowski, A. Domaracka, P. Mozejko and E. Ptasinska-Denga, J. Chem. Phys. **130**, 134316 (2009).

17. C. Szmytkowski and E. Ptasińska-Denga, J. Phys. B: At. Mol. Opt. Phys. **44**, 015203 (2011).

18. A. Zecca, E. Trainotti, L. Chiari, M. H. F. Bettega, S. Sanchez, M. T. Varella, M. A. P. Lima and M. J. Brunger, J. Chem. Phys. **136**, 124305 (2012).

19. S. J. Cavanagh and B. Lohmann, J. Phys. B: At. Mol. Opt. Phys. **32**, L261 (1999).

20. J. Gao, D. H. Madison and J. L. Peacher, J. Chem. Phys. **123**, 204314 (2005).

21. J. Gao, D. H. Madison and J. L. Peacher, J. Phys. B: At. Mol. Opt. Phys. **39**, 1275 (2006).

22. J. Gao, J. L. Peacher and D. H. Madison, J. Chem. Phys. **123**, 204302 (2005).

23. C. Lee, W. Yang and R. G. Parr, Phys. Rev. B **37**, 785 (1988).

24. C. F. Guerra, J. G. Snijders, G. te Velde and E. J. Baerends, Theor. Chem. Acc. **99**, 391 (1998).

25. S. J. Ward and J. H. Macek, Phys. Rev. A **49**, 1049 (1994).

26. J. B. Furness and I. E. McCarthy, J. Phys. B: Atom. Molec. Phys. **6**, 2280 (1973).

27. J. P. Perdew and A. Zunger, Physical Review B **23**, 5048 (1981).

28. N. T. Padial and D. W. Norcross, Phys. Rev. A **29**, 1742 (1984).

29. D. H. Madison and O. Al-Hagan, Journal of Atomic, Molecular, and Optical Physics **2010**, 367180 (2010).

30. M. J. Frisch *et al.*, *Gaussian 09, Revision B.01*, Gaussian Inc., Wallington CT, USA (2010).

31. J. P. D. Cook and C. E. Brion, Chem. Phys. **69**, 339 (1982).

32. A. Giuliani, P. Limão-Vieira, D. Duflot, A. R. Milosavljevic, B. P. Marinkovic, S. V. Hoffmann, N. Mason, J. Delwiche and M. J. Hubin-Franskin, Eur. Phys. J. D **51**, 97 (2009).

33. C. G. Ning, Y. R. Huang, S. F. Zhang, J. K. Deng, K. Liu, Z. H. Luo and F. Wang, J. Phys. Chem. A **112**, 11078 (2008).

34. H. E. Breed, G. Gundersen and R. Seip, Acta Chem. Scand. A **33** 225 (1979).

35. D. M. Chapman and R. E. Hester, J. Phys. Chem. A **101**, 3382 (1997).

36. M. Yamauchi, H. Yamakado and K. Ohno, J. Phys. Chem. A **101**, 6184 (1997).

37. T. Kobayashi and S. Nagakura, Bull. Chem. Soc. Jap. **46**, 1558 (1973).

38. K. Kimura, S. Katsuwata, Y. Achiba, T. Yamazaki and S. Iwata, *Handbook of HeI Photoelectron Spectra of Fundamental Organic Molecules* (Japan Scientific Societies Press, Tokyo, Japan, 1981).

39. T. C. Yang, C. G. Ning, G. L. Su, J. K. Deng, S. F. Zhang, X. G. Ren and Y. R. Huang, Chin. Phys. Lett. **23**, 1157 (2006).

40. T. Yang, G. Su, C. Ning, J. Deng, F. Wang, S. Zhang, X. Ren and Y. Huang, J. Phys. Chem. A **111**, 4927 (2007).

41. N. Watanabe, X. Chen and M. Takahashi, Phys. Rev. Lett. **108**, 173201 (2012).

42. I. Tóth and L. Nagy, J. Phys. B: At. Mol. Opt. Phys. **43**, 135204 (2010).

43. L. R. Hargreaves, M. A. Stevenson and B. Lohmann, Meas. Sci. Technol. **21**, 055112 (2010).

44. D. S. Milne-Brownlie, M. Foster, J. Gao, B. Lohmann and D. H. Madison, Phys. Rev. Lett. **96**, 233201 (2006).

45. L. R. Hargreaves, C. Colyer, M. A. Stevenson, B. Lohmann, O. Al-Hagan, D. H. Madison and C. G. Ning, Phys. Rev. A **80**, 062704 (2009).

46. S. Xu, X. Ma, S. Yan and P. Zhang, J. Chem. Phys. **136**, 237101 (2012).

47. E. Weigold and I. E. McCarthy, *Electron Momentum Spectroscopy* (Kluwer Academic/Plenum Publishers, New York, 1999).

## X Dynamical (e,2e) studies of tetrahydropyran and 1,4-dioxane

J. D. Builth-Williams,[1] G. B. da Silva,[1,2] L. Chiari,[1] D. B. Jones,[1] Hari Chaluvadi,[3] D. H. Madison,[3] and M. J. Brunger*[1,4,]

[1]School of Chemical and Physical Sciences, Flinders University, GPO Box 2100, Adelaide, South Australia 5001, Australia.

[2]Universidade Federal de Mato Grosso, Barra do Garças, MT 78600-000, Brazil.

[3]Department of Physics, Missouri University of Science and Technology, Rolla, Missouri 65409, USA.

[4]Institute of Mathematical Sciences, University of Malaya, 50603 Kuala Lumpur, Malaysia.

### Abstract

We present experimental and theoretical results for the electron-impact ionization of the highest occupied molecular orbitals of tetrahydropyran and 1,4-dioxane. Using an (e,2e) technique in asymmetric coplanar kinematics, angular distributions of the slow ejected electron, with an energy of 20 eV, are measured when incident electrons at 250 eV ionize the target and scatter through an angle of either -10° or -15°. The data are compared with calculations performed at the molecular 3-body distorted wave level. Fair agreement between the theoretical model and the experimental measurements was observed. The similar structures for these targets provide key insights for assessing the limitations of the theoretical calculations. This study in turn facilitates an improved understanding of the dynamics in the ionization process.

## Introduction

The interaction between low-energy charged particles with molecules of biological significance has attracted great interest in the last decade. In some medical procedures, such as radiotherapy and medical imaging, living tissue is routinely exposed to ionizing radiation. Here, a single high-energy ionizing particle can induce a cascade of ionization events that can produce up to $3\times10^4$ low-energy secondary electrons.[1] These low energy electrons may then cause cell damage or death by initiating mutagenic, genotoxic or DNA lesions.[2] In this respect, low-energy electrons are probably the most important species in radiation chemistry.[3] In order to predict the effects of exposing living tissue to ionizing radiation, many groups have developed Monte Carlo track structure codes[4-11] that simulate the charged-particle paths. However, the majority of these track simulations have been formulated assuming that the biological medium consists entirely of water. This practice probably reflects the lack of available data for complex biomolecules that can be included in the Monte Carlo codes. Here the absence of robust molecular scattering data sets reflects the inherent difficulty in performing experimental measurements and computationally demanding theoretical calculations for studying complex biomolecules.

In this context, there have been recent systematic investigations to study the dynamics of the ionization processes for molecules that can approximate the building blocks of a biological system. These have included water,[12] DNA bases and their sub-structures (pyrimidine,[13] thymine[14]) and analogues to the DNA backbone (tetrahydrofuran[15,16] and tetrahydrofuryl alcohol[16,17]). To utilize these measurements in Monte Carlo simulations, complete cross section sets over a wide range of projectile energies and kinematical conditions are required. It has become apparent that the long

experimental run times required for obtaining triple differential cross sections limits the capability of experiments to measure complete cross section sets over the large range of incident electron energies and the kinematical conditions that are required for Monte Carlo based simulation codes. This generates an urgent demand for developing theoretical models that can reliably and efficiently generate such complete cross section sets. It is therefore important that experimental measurements provide a strong foundation for assessing the importance of chemical composition and structure on the electron scattering behavior, so that theoretical computations can be benchmarked, and their limitations established, over a range of kinematical conditions.

We have previously investigated electron-impact ionization of the structurally similar cyclic ethers tetrahydrofuran (THF),[15] tetrahydropyran (THP),[15] and 1,4-dioxane,[15] with kinematical conditions that investigated the Bethe surface well-below the bound Bethe Ridge.[15] Here we expand that work with additional experimental measurements and calculations for the ionization of the highest occupied molecular orbitals (HOMOs) of both THP (15a′ orbital) and 1,4-dioxane ($8a_g$ orbital). For both targets the HOMO is dominated by the out-of plane Oxygen (2p) contribution. The similar, yet different, structures of these targets provide opportunities to gain insights into the importance of structure in the dynamics of ionization. By combining these measurements with our earlier data[15] we can map the Bethe surface for these species below the bound Bethe ridge. The investigation of ionization dynamics for kinematical conditions that map the Bethe surface, below the bound Bethe ridge, are essential for understanding the dynamics of the electron-impact ionization process. Here the experimental results are compared to theoretical calculations obtained within a molecular

3-body distorted wave (M3DW) framework. Through the comparison of theory and experimental data over structurally similar targets it is becoming feasible to fully assess the limitations of theoretical models, and identify how they may be improved.

## Experimental Method

We have used an (e,2e) coincidence technique under asymmetric coplanar kinematical conditions, in order to obtain triple differential cross sections for electron-impact ionization of THP and 1,4-dioxane. The full details of the method employed can be found elsewhere.[15,18,19] Briefly, a highly collimated beam of electrons with well-defined energy $E_0$ and momentum $p_0$, is incident on a beam of the target molecule, *M*. When the target is ionized, the fast (scattered) and slow (ejected) electrons are detected. Here a time-coincidence method is used to ensure that the two detected electrons originated from the same ionization event. The kinematically complete reaction can be described by:

$$K = p_0 - p_a \qquad (1)$$

where $M^+$ is the residual ion produced in the ionization process. The energies and momenta for the scattered and ejected electrons are given by $(E_a, p_a)$ and $(E_b, p_b)$ respectively. $\varepsilon_i$ is the energy required to ionize the *i*-th molecular orbital. The conservation of energy during the ionization process requires:

$$E_0 = \varepsilon_i + E_a + E_b \qquad (2)$$

Likewise, to conserve linear momentum during the ionization process, the residual ion recoils with momentum:

$$q = p_0 - (p_a + p_b) \qquad (3)$$

In the present asymmetric kinematics, the incident electron and slow electron energies are fixed at $E_0$ = 250 eV and $E_b$ = 20 eV, respectively. Angular distributions of the slow ejected electron ($\theta_b$) are measured while the direction of the fast electron is fixed at polar angles of either $\theta_a$ =-10° or -15°. Note that all angles are referenced to the incident electron beam direction. The angle through which the incident electron is deflected also defines the momentum transferred to the target:

$$K = p_0 - p_a . \qquad (4)$$

The ionization potentials of the HOMO's of THP (15a′ orbital) and 1,4-dioxane ($8a_g$ orbital) are 9.46 and 9.37 eV,[20] respectively. When the scattered electron is detected at $\theta_a$ =-10° or -15° the magnitudes of the momentum transfer are 0.77 and 1.12 a.u., respectively. For an ejected electron with $E_b$ = 20 eV ($|p_b|$ = 1.21 a.u.), these momentum values lie below and approximate the bound Bethe-Ridge condition of $K = |p_b|$. These measurements can be combined with earlier measurements at $\theta_a$ =-5° ($|K|$ = 0.45 a.u.) to map out the ionization behavior below the bound Bethe-Ridge. Under these conditions the magnitude of the momentum transfer and the ejected electron's momentum are comparable to the momentum of the valence electrons bound to the target.

When the ejected electron leaves the collision in a direction close to that of the momentum transfer (+***K***), the recoil momentum is minimized, and the collisions are said to be binary. Similarly, when the electron is ejected in a direction nearly anti-parallel to that of the momentum transfer (-***K***), the target recoil momentum must be at its maximum to conserve momentum. In this angular region, collisions are said to be recoil in nature.

**Theoretical Method**

Within the molecular 3-body distorted wave (M3DW) framework, the electron-impact ionization scattering amplitude can be described by:

$$T_{dir} = \left\langle \chi_a^-(\vec{k}_a, \mathbf{r}_1)\chi_b^-(\vec{k}_b, \mathbf{r}_2)C_{scat-eject}(r_{12}^{ave}) \,|\, V - U_0 \,|\, \phi_{DY}^{OA}(\mathbf{r}_2)\chi_0^+(\vec{k}_0, \mathbf{r}_1) \right\rangle \qquad (5)$$

Here the initial state is described as the product of an incident distorted wave $\chi_0^+(\vec{k}_0, \mathbf{r}_1)$ and the orientation averaged Dyson orbital $\phi_{DY}^{OA}(\mathbf{r}_2)$. Within a frozen orbital approximation, the Dyson orbital is described by the ionized Kohn-Sham orbital of the target ground state. In this work, the molecular wave functions were calculated using density functional theory (DFT) along with the standard hybrid B3LYP[21] functional using the ADF 2007 (Amsterdam Density Functional) program[22] with the TZ2P (triple-zeta with two polarization functions) Slater type basis set. The final state was described by distorted waves $\chi_a^-(\vec{k}_a, \mathbf{r}_1)$ and $\chi_b^-(\vec{k}_b, \mathbf{r}_2)$ for the fast and slow outgoing electrons, and the Ward-Macek[23] Coulomb distortion factor, $C_{scat-eject}(r_{12}^{ave})$. The initial interaction between the incident electron and the neutral molecule is described by the potential $V$, while $U_0$ is a spherically symmetric distorting potential which is used to calculate the incident initial-state distorted wave, $\chi_0^+(\vec{k}_0, \mathbf{r}_1)$. Here the distorted waves are calculated using a distorting potential that combines the exchange potential of Furness and McCarthy (corrected for sign errors),[24] the correlation potential of Perdew and Zunger[25] (see also Padial and Norcross[26]) and a spherically symmetric target potential that combines the target electron charge density (obtained by summing $2\left|\phi_j(\mathbf{r})\right|^2$ over all occupied orbitals) and spheres that describe the different charged nuclei within the center-of-mass frame.

The parameters describing the distorting potential of THP and 1,4-dioxane are the same as those employed previously.[15] The final state distorted waves are obtained in the same way except that the potential $U_0$ is modified to account for the change in the final state charge density.

The triple differential cross section for electron-impact ionization can be obtained through:

$$\frac{d\sigma}{d\Omega_a d\Omega_b dE_b} = \frac{1}{(2\pi)^5}\frac{k_a k_b}{k_0}\left(|T_{dir}|^2 + |T_{exc}|^2 + |T_{dir} - T_{exc}|^2\right) \qquad (6)$$

Here $T_{dir}$ and $T_{exc}$ are the direct and exchange scattering amplitudes, respectively. Both amplitudes are calculated using equation (5) with and without the interchange of the electrons in the final state. The full description of this theoretical method can be obtained elsewhere.[16,27-29]

## Results

In Figures 1 and 2, the experimental TDCS for electron-impact ionization of the highest occupied molecular orbital (HOMO) of THP (15a′ orbital) and 1,4-dioxane ($8a_g$ orbital), respectively, are presented when the scattered electron is detected at (a) $\theta_a$ = -5°,[15] (b) $\theta_a$ = -10° , and $\theta_a$ = -15°. Note that a small error that affected the binary recoil ratio was found in our previous experimental analysis.[15] The corrected experimental data for $\theta_a$ = -5° is presented here. Also shown in these figures are the theoretical TDCSs obtained within the M3DW method, to compare with the experimental measurements. Here the experimental data has been normalized to the M3DW calculation in order to obtain the best visual fit in the binary region. We begin by first comparing the experimental data to the theoretical calculations for each molecule independently. This is then followed by a discussion about how the respective structures of the molecules may

influence the observed scattering dynamics and how these results may improve our understanding of the ionization process.

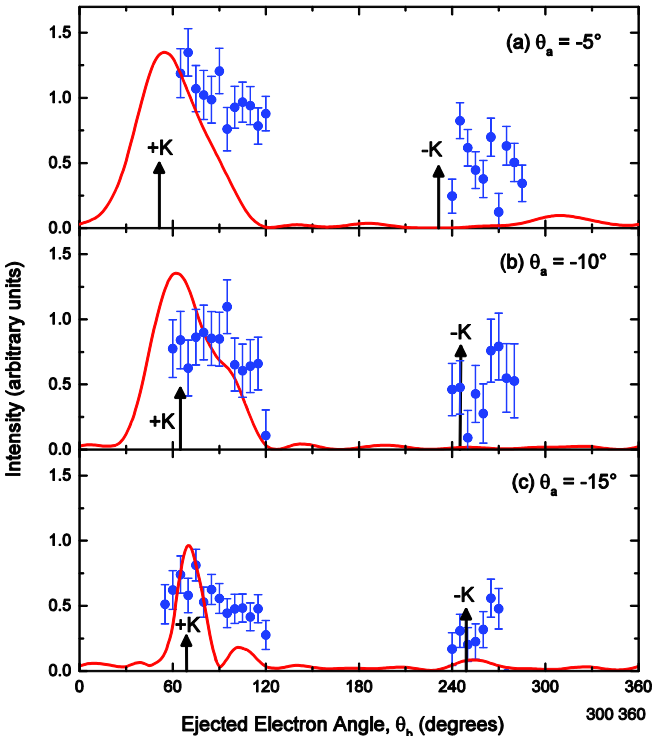


Figure. 1. TDCS for electron impact ionization of the HOMO of THP (15a′) with $E_0$=250eV, $E_b$=20eV and transferred momentum (a) K = 0.45 a.u. ($\theta_a$ = -5°), (b) K = 0.77 a.u. ($\theta_a$ = -10°) and (c) K = 1.12 a.u. ($\theta_a$ = -15°). The M3DW calculation results (——) are compared to the experimental data (●). The directions parallel (+K) and anti-parallel (-K) to the transferred momentum are represented by the arrows.

**A.Tetrahydropyran (THP)**

For the measurements at $\theta_a$ = -10°, the intensity observed in the binary region is quite broad, having significant intensity over the measured angular range of the experiment. This observation is consistent with the wide binary peak calculated within the M3DW model. The M3DW calculation predicts a large peak centered close to the momentum transfer direction that has a significant shoulder close to $\theta_b$ ~ 90°. While this peak structure is not observed in the experimental data for $\theta_a$ = -10°, the experiment

exhibits the shoulder structure predicted by the theory. In the recoil region for $\theta_a$ = -10°, the experimental data certainly suggests that a peak may exist in the angular region of $\theta_b$ ~ 270°. While the M3DW does predict a number of small peaks at different angular positions, the intensity of these features is significantly below that which is observed experimentally.

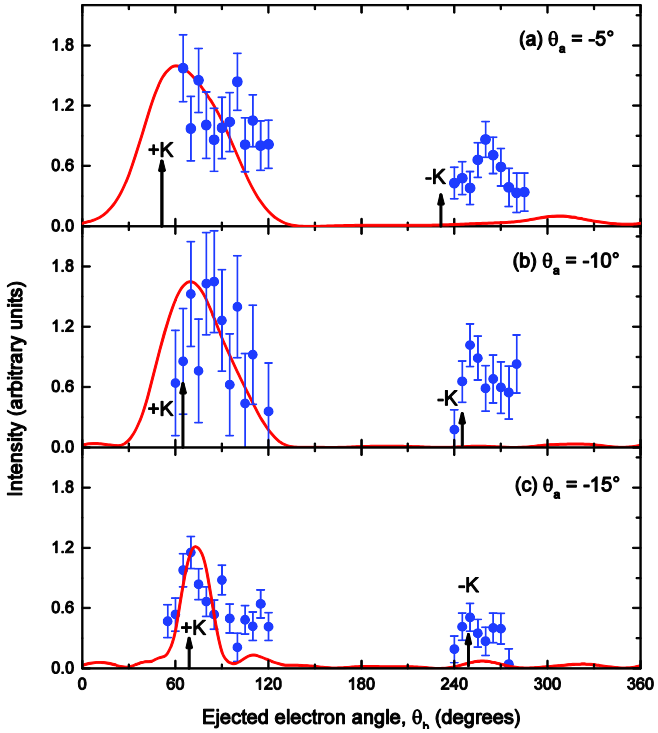


Figure. 2. TDCS for electron impact ionization of the HOMO of 1,4-dioxane ($8a_g$) with $E_0$=250eV, $E_b$=20eV and momentum transfer values of (a) K = 0.45 a.u. ($\theta_a$ = -5°), (b) K = 0.77 a.u. ($\theta_a$ = -10°) and (c) K = 1.12 a.u. ($\theta_a$ = -15°). Experimentally measured data (●) and M3DW calculation results (——) are plotted. The directions parallel (+K) and anti-parallel (-K) to the transferred momentum are represented by the arrows.

For THP at a scattering angle of $\theta_a$ = -15°, the experimental data in the binary region suggests two experimental features. Here there is a peak observed in the direction of the momentum transfer that has a substantial shoulder in the $\theta_b$ ~ 90-120° angular range. The M3DW calculation also predicts the peak and shoulder in the binary region.

However, the calculation does underestimate the intensity of the shoulder. In the recoil region, the experimental data again suggests the presence of a peak that has been shifted away from the direction anti-parallel to the momentum transfer. However, the finite angular range of our experimental measurements, limited by the physical constraints of the detectors, limits the full assessment of the shape of this feature. Note that the M3DW does predict a relatively substantial peak, compared to that at $\theta_a$ = -10°, in the recoil region. This feature is, however, centered in the direction anti-parallel to the momentum transfer. The intensity of this feature is also below that observed experimentally.

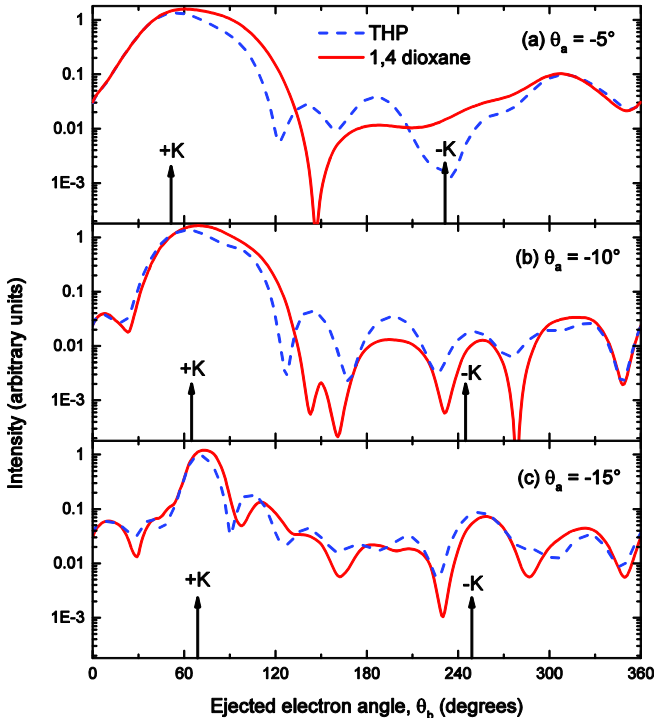


Figure. 3. Comparison of the M3DW TDCS for the 15a′ HOMO of THP (— —) and the $8a_g$ HOMO of 1,4-dioxane (——), calculated for $E_0$=250eV, $E_b$=20eV and momentum transfer values of (a) K = 0.45 a.u. ($\theta_a$ = -5°) , (b) K = 0.77 a.u. ($\theta_a$ = -10°) and (c) K = 1.12 a.u. ($\theta_a$ = -15°).

**B. 1,4-Dioxane**

The experimental data for 1,4-dioxane at $\theta_a$ = -10° displays a broad peak in the binary region. This peak has been shifted away from the momentum transfer direction, and has a maximum at $\theta_b$ ~ 80°. The M3DW calculation also predicts a single broad peak in the binary region under this kinematical condition. Both the experimental data and the M3DW calculations display asymmetry in the peak profile, which has a significant tail in the 90-120° angular range. While the M3DW predicts the correct shape for this binary feature, it appears to overestimate the width observed experimentally. Also, the M3DW underestimates the shift of this peak away from the momentum transfer direction.

At $\theta_a$ = -15°, the experimental data for 1,4-dioxane contains two spectral features in the binary region; it has a strong peak located along the momentum transfer direction, and a shoulder in the $\theta_b$ ~ 90-120° angular range. For $\theta_a$ = -15°, the M3DW calculation does a good job at reproducing the shape of the TDCS in the binary region, although again in this case, the M3DW calculation fails to predict the substantial intensity observed experimentally for the shoulder. In the recoil region, the M3DW predicts a peak close to the direction anti-parallel to the momentum transfer. This peak position is consistent with that of the experimental data observed in this recoil region. However, the intensity of this recoil peak predicted by the M3DW calculation still significantly underestimates the magnitude of the experimental data.

**C. Discussion**

Owing to the structural similarities between THP and 1,4 dioxane, it is interesting to establish how these structures influence the cross sections. In this way we hope to provide a foundation for understanding the importance of structure in the dynamics of the

ionization process. To assist in this discussion, the M3DW calculations for THP and 1,4-dioxane are compared in Fig. 3.

From Fig. 3, it is apparent that the TDCS for both THP and 1,4-dioxane have a number of similar features in the calculated cross sections at the M3DW level. Here the peak positions of the binary and recoil features are in good accord across the two different targets. In the cross sections for all scattering angles there are a number of peaks and troughs at the intermediate angles between the binary and recoil features. The positioning of these features, and their relative shifts as the kinematical conditions change, reveal that these features are related to the similar structures of the targets. Specifically, the presence of these minima appears to reflect an interference-like effect. It is interesting to note that minima in 1,4 dioxane are more prominent than those observed in THP. Here the higher symmetry of 1,4-dioxane places all of the nuclear charge on 4-nuclear spheres, that may make nuclear interference effects much more prominent. For THP, the reduced molecular symmetry leads to the distribution of the nuclear potentials across 12 nuclear spheres. This distribution of charge across the larger number of scattering centers smears out the interference effect in THP. Similar behavior has been previously observed in (e,2e) TDCS that were attributed to Young-type interference effects.[30] Further, three body distorted waves calculations for small atoms (3DW) and molecules (M3DW) have also provided evidence to support the deep minima observed in (e,2e) cross sections measured in an out-of-plane symmetric geometry.[31] In order to fully assess the importance of the present observations, we must first consider the limitations of the M3DW calculation for predicting cross sections.

We begin by discussing the behavior in the binary region. Comparing the calculated TDCS to the experimental data, it becomes apparent that the M3DW calculation works better, in terms of reproducing the shape of the experimental cross section, for 1,4-dioxane than THP. The clues for this may lie in the momentum profiles presented in Fig. 5 of our previous paper.[15] The momentum profiles for THP and 1,4-dioxane can be separated into two distinct components. First, we have the p-character from the O(2p) contribution which gives rise to the momentum profile peak at q ~ 1.2 a.u. Secondly, we have the s-character arising from the coupling of the O(2p) with the σ-bonding carbon frame. This s-character gives rise to the maximum in the momentum profile at q = 0 a.u. The momentum profiles for THP and 1,4-dioxane reflect the enhanced interaction that the two O(2p) electrons create with the carbon frame in the HOMO of 1,4-dioxane. The nature of these interactions has significant ramifications in the M3DW calculation. Here the highly symmetric s-orbital character is maintained through the orientation averaging, but the phase of the p-orbital is problematic and may lead to this contribution being cancelled out. The enhanced s-character in 1,4-dioxane may explain the better agreement observed for this target than that seen for THP.

The present results display similar characteristics to those observed in Ar $(3p)^{-1}$ experiments[32] performed under asymmetrical kinematics with $E_0$ = 195 eV, $E_b$ = 20 eV, and $\theta_a$ = -5°, -10° and -15° that nearly match those presented here. In that study the shape of the measured data was well reproduced by hybrid distorted wave plus R-matrix calculations (DWB2-RM) that are available for atomic targets. The DWB2-RM calculations use a multi-configuration expansion of the initial and final target states, but do not directly include post collision interaction (PCI) effects. The results from that study

are interesting for two reasons. First, it suggests that the target description may hold the key to accurately reproducing the shape of the binary feature in the present measurements. The experimental data in the binary region for argon are quite asymmetric, being skewed with the maximum intensity at the larger scattering angles. This behavior is somewhat reproduced in argon by the DWB2-RM method, that provides a seemingly adequate description of the collision through the use of distorted waves for the incident and fast outgoing electron, and a coupling of a slow electron with an accurate target description. The key interaction to improve cross section calculations for molecules might therefore be an improved description of the coupling of the slow ejected electron to the target, and how it may change the target structure, that is neglected in the present study. Second, despite the aforementioned good shape agreement, under the more forward scattering condition of $\theta_a$ = -5° or -10° the DWB2-RM calculations underestimated the shift of these experimental binary features from the momentum transfer direction to larger scattering angles. This is also apparent in our present measurements for THP and 1,4-dioxane, where the experimentally measured binary peak is substantially shifted away from the momentum transfer direction. The shift in the TDCS away from the momentum transfer direction is classically described as a PCI effect, which is not directly included in the DWB2-RM calculation. As such, the inclusion of PCI may still play an important role under these scattering conditions. This is in contrast to previous calculations on molecules[17] that were performed both with and without PCI effects, and displayed minimal difference. The quality of the slow-ejected electrons coupling with the target description may therefore influence the ability to fully assess any PCI effect.

As both THP and 1,4-dioxane have O(2p) orbital contributions, the substantial experimental intensity seen in the 90°-120° angular regions, underestimated theoretically, may have similar origins to the skewed asymmetrical behavior observed in the binary peak of Ar $(3p)^{-1}$. In this respect, the ionization of orbitals with non-zero orbital angular momentum is known to be problematic in computing orientation averaged cross sections. The observed similarities between the experimental measurements of ionization dynamics with complex targets and those of atoms are encouraging, in particular, for trying to relate well-established atomic physics phenomena to molecular targets.

For both THP and 1,4 dioxane, the experimental measurements for scattering angles of $\theta_a$ = -10°, and -15° all exhibit substantial intensity in the recoil region. Here the observed intensities are comparable to that observed for other large molecules under very similar kinematical conditions, such as THFA.[17] Here we note that the M3DW calculations fail to reproduce the experimental intensity observed in the recoil region under all kinematical conditions.

To try and address these issues, work has begun on performing distorted wave calculations that perform a "proper" average over all molecular orientations studied in the experiment. The first calculations have been performed for $CH_4$ and the properly averaged results are in much better agreement with experiment.[33] It is hoped that, through such an averaging approach, the discrepancies observed between the theoretical calculations and experimental results can be resolved at least in part. However, the full averaging approach is computationally demanding, and cannot be performed with available local computing resources. We performed the $CH_4$ calculation using our

Extreme Science and Engineering Discovery Environment (XSEDE) allocation for this year and we will submit a proposal to examine other molecules next year.

The present study identifies a clear path forward for how some of the limitations encountered in dynamical (e,2e) investigations of molecular targets can be understood, through performing systematic evaluations of the approximations employed for atomic targets. This is an important prerequisite for developing reliable scattering models for electron-impact ionization of molecules. It is also essential for ascertaining if current predictions of interference effects, as displayed by the deep theoretical minima, are real. Further, dynamical (e,2e) experiments for molecular targets, that can achieve higher statistical precision over larger angular ranges, in the hope of observing these deep minima, are also desirable.

## Conclusions

We have presented experimental measurements and theoretical calculations for triple differential cross sections of the electron impact ionization of the HOMO's of THP and 1,4-dioxane under asymmetrical kinematical conditions. The data for all electron scattering angles exhibit relatively large recoil peaks, which were underestimated by the M3DW calculations. The binary peaks calculated at the M3DW level resemble those observed experimentally at all scattering angles. Earlier measurements for Ar $(3p)^{-1}$, under similar experimental conditions, give results which suggest that the target description in the calculation may be inadequate in this kinematic regime. Specifically, this result may reflect the inadequate description of p-like orbital contributions in the spherically-averaged Dyson orbital. In spite of these short comings, the M3DW suggests that interference phenomena relating to the structure of the target may be reflected in the TDCS. The suggestion of interference effects in the theoretical cross sections thus

provides significant opportunities to glean more insights into the dynamics of ionization from complex targets. Finally, work has begun at calculating cross sections within the 3-distorted wave framework that perform a proper average over all molecular orientations studied in the experiment and first results are encouraging.

## Acknowledgements

This research was supported by the Australian Research Council (ARC) Centre of Excellence for Antimatter-Matter Studies and by the US National Science Foundation under Grant. No. PHY-1068237 (HC and DHM). GBS thanks CAPES (Proc. No. BEX 17756/12-0) and Flinders University for financial assistance during his stay in Australia. DBJ gratefully acknowledges support provided through an ARC Discovery Early Career Researcher Award.

## References

1.L. Sanche, in *Radiation Induced Molecular Phenomena in Nucleic Acids*, edited by M. Shukla and J. Leszczynski (Springer Netherlands, 2008), Vol. 5, pp. 531.

2.B. Boudaiffa, P. Cloutier, D. Hunting, M. A. Huels and L. Sanche, Science **287**, 1658 (2000).

3.S. M. Pimblott and J. A. LaVerne, Radiat. Phys. Chem. **76**, 1244 (2007).

4.A. G. Sanz, M. C. Fuss, A. Munoz, F. Blanco, P. Limao-Vieira, M. J. Brunger, S. J. Buckman and G. Garcia, Int. J. Radiat. Biol. **88**, 71 (2012).

5.Z. L. Petrović, S. Marjanović, S. Dujko, A. Banković, G. Malović, S. Buckman, G. Garcia, R. White and M. Brunger, Appl. Radiat. Isotopes **83, Part B**, 148 (2014).

6.Z. Francis, S. Incerti, R. Capra, B. Mascialino, G. Montarou, V. Stepan and C. Villagrasa, Appl. Radiat. Isotopes **69**, 220 (2011).

7.I. Plante and F. A. Cucinotta, New J. Phys. **10**, 125020 (2008).

8.S. Agostinelli, *et al.*, Nuclear Instruments and Methods in Physics Research Section A: Accelerators, Spectrometers, Detectors and Associated Equipment **506**, 250 (2003).

9.J. Allison, *et al.*, IEEE Transactions on Nuclear Science **53**, 270 (2006).

10.F. Salvat, J. M. Fernandez-Varea and J. Sempau, *PENELOPE2011, A Code System for Monte-Carlo Simulation of Electron and Photon Transport*. (OECD - Nuclear Energy Agency, 2011).

11.C. Champion, C. Le Loirec and B. Stosic, Int. J. Radiat. Biol. **88**, 54 (2012).

12.D. S. Milne-Brownlie, S. J. Cavanagh, B. Lohmann, C. Champion, P. A. Hervieux and J. Hanssen, Phys. Rev. A **69**, 032701 (2004).

13.J. Builth-Williams, S. M. Bellm, D. B. Jones, H. Chaluvadi, D. Madison, C. G. Ning, B. Lohmann and M. J. Brunger, J. Chem. Phys. **136**, 024304 (2012).

14.S. M. Bellm, C. J. Colyer, B. Lohmann and C. Champion, Phys. Rev. A **85**, 022710 (2012).

15.J. D. Builth-Williams, *et al.*, J. Chem. Phys. **139**, 034306 (2013).

16.D. B. Jones, *et al.*, Chem. Phys. Lett. **572**, 32 (2013).

17.S. M. Bellm, *et al.*, J. Chem. Phys. **136**, 244301 (2012).

18.S. J. Cavanagh and B. Lohmann, J. Phys. B: At. Mol. Opt. Phys. **32**, L261 (1999).

19.C. J. Colyer, S. M. Bellm, B. Lohmann, G. F. Hanne, O. Al-Hagan, D. H. Madison and C. G. Ning, J. Chem. Phys. **133**, 124302 (2010).

20.M. Yamauchi, H. Yamakado and K. Ohno, J. Phys. Chem. A **101**, 6184 (1997).

21.C. Lee, W. Yang and R. G. Parr, Phys. Rev. B **37**, 785 (1988).

22.C. Fonseca Guerra, J. G. Snijders, G. te Velde and E. J. Baerends, Theor. Chem. Acc. **99**, 391 (1998).

23.S. J. Ward and J. H. Macek, Phys. Rev. A **49**, 1049 (1994).

24.J. B. Furness and I. E. McCarthy, J. Phys. B: Atom. Molec. Phys. **6**, 2280 (1973).

25.J. P. Perdew and A. Zunger, Phys. Rev. B **23**, 5048 (1981).

26.N. T. Padial and D. W. Norcross, Phys. Rev. A **29**, 1742 (1984).

27.J. F. Gao, D. H. Madison and J. L. Peacher, J. Chem. Phys. **123**, 204314 (2005).

28.J. F. Gao, J. L. Peacher and D. H. Madison, J. Chem. Phys. **123**, 204302 (2005).

29.J. F. Gao, D. H. Madison and J. L. Peacher, J. Phys. B: At. Mol. Opt. Phys. **39**, 1275 (2006).

30.D. S. Milne-Brownlie, M. Foster, J. Gao, B. Lohmann and D. H. Madison, Phys. Rev. Lett. **96**, 233201 (2006).

31.J. Colgan, O. Al-Hagan, D. H. Madison, A. J. Murray and M. S. Pindzola, J. Phys. B: At. Mol. Opt. Phys. **42**, 171001 (2009).

32.X. Ren, A. Senftleben, T. Pflüger, A. Dorn, K. Bartschat and J. Ullrich, Phys. Rev. A **83**, 052714 (2011).

33.H. Chaluvadi, C. G. Ning and D. H. Madison, Phys. Rev. A **89**, 062712 (2014).

# XI Theoretical Triple Differential Cross Sections of Methane Molecule by Proper Averaged Method

Hari Chaluvadi[1], C. G. Ning[2] and Don Madison[1]

[1]Missouri University of Science and Technology, Rolla, USA

[2]*Department of Physics and State Key Laboratory of Low-Dimensional Quantum Physics, Tsinghua University, Beijing 100084, China*

## Abstract

For the last few years, our group has calculated cross section for electron impact ionization of molecules using the Molecular 3 body distorted wave (M3DW) approximation coupled with the Orientation Averaged Molecular orbital (OAMO) approximation. This approximation was very successful for calculating ionization cross sections for hydrogen molecules and to a lesser extent nitrogen molecules. Recently we used the approximation to calculate single ionization cross sections for the $1t_2$ state of methane ($CH_4$) and we found major discrepancies with the experimental data. Here we investigate the validity of the OAMO approximation by calculating cross sections that have been properly averaged over all molecular orientations. These new calculations with proper averages are in much better agreement with experiment than the OAMO calculations.

## Introduction

In fundamental physics, one of the most important unsolved problems is the few body problem where we have to deal with more than two particles. Since we cannot solve the Schrodinger equation analytically for more than two particles, we have to use approximations for the theoretical models whose validity can only be checked by

comparing with the experiments. One of the ways to study the few body problem is through electron impact ionization of atoms or molecules.

The study of electron impact single ionization of atoms has provided valuable information about fundamental collisions for decades. More recently, molecules are starting to receive significant attention, at least partially due to the fact that there are potentially significant applications. For example, studies of the electron-impact ionization of biomolecules provide important information on the role of electrons in causing damage to DNA in biological systems. It is now well established that low energy secondary electrons produced by high energy primary radiation are responsible for much of the damage to DNA in living tissues [1,2]. The most detailed information about ionizing collisions between an electron and molecule is obtained from the triple differential cross sections (TDCS) in which the energy and momentum of all three final state particles are determined. The molecular 3 body distorted wave (M3DW) approximation has been one of the most successful theories for calculating TDCS for molecules.

Until very recently, the experimentally measured TDCS for electron-impact ionization of molecules did not determine the orientation of the molecule so theory needed to average over all possible orientations to compare with experimental data. When we started performing M3DW calculations for molecules, we only had access to single processor computers and it was estimated that one calculation performing a proper average over orientations would take 1-2 years, depending on the size of the molecule. Since this was obviously not a practical possibility, we introduced the Orientation Averaged Molecular Orbital approximation (OAMO) for the M3DW [3]. In the OAMO approximation, instead of averaging over orientation-dependent cross sections, the

orientation dependent molecular orbitals are averaged to obtain a spherically symmetric molecular orbital to use in the cross section calculation. This average is performed once per molecule independent of the kinematics of the collision. Using this approximation, we found very good agreement with experimental data for ionization of the $H_2$ molecule [4–7] and reasonable agreement with the data for ionization of $N_2$ [8]. We extended the OAMO approach to compare with experimental data for ionization of the methane molecule (the simplest hydrocarbon). We examined ionization of the $1t_2$ and $2a_1$ states of methane, which have *p*-like and *s*-like characteristics respectively. While the OAMO results were in relatively good agreement with experimental data for the low energy symmetric scattering plane [9], there were some significant discrepancies with data for the asymmetric scattering plane calculations [10]. For the perpendicular plane, Al-Hagan et al. [11] predicted that if a molecule has a nucleus at the center of mass (CM), the cross sections in the perpendicular plane should exhibit a three peak structure. Since methane has a nucleus at the CM, a three peak structure was expected. However, the experimental data exhibited a two peak structure [10,12].

To better understand the methane results, we examined the iso-electronic targets ($CH_4$, $NH_3$ and Ne) [9,10,12,13] . The $CH_4$ molecule $1t_2$ state and $NH_3$ molecule $3a_1$ and $le_1$ states all have p-like characteristics while the $CH_4$ molecule $1a_1$ state and the $NH_3$ molecule $2a_1$ state have s-like characteristics. However, both the p-like and s-like states in $CH_4$ and $NH_3$ exhibited similar trends for the theoretical cross sections. This result may be caused by the orientation average approximation since, in the OAMO calculations, we are integrating wavefunction over orientations, which may change p-type structure into a spherical shape.

Xu et al. [10] compared experiment with the M3DW for electron-impact ionization of methane. They looked at asymmetric scattering both in the scattering plane and the perpendicular plane. They found that the agreement between the theory and experiment was not good, particularly in the perpendicular plane. While agreement with experiment was a little better in the scattering plane, it was still far from good. With increasing projectile scattering angle, the relative size of the experimental recoil peak became larger while the theoretical intensity of the recoil peak decreased. The fact that the recoil peak is weaker than experiment suggests that nuclear scattering is underestimated in the theoretical model. Toth et al., [14] and Senftleben et al., [15] suggested that one way to increase the strength of the nuclear scattering is to move the nuclei closer to the CM. We did observe a better agreement with experiment in the recoil region by decreasing the radius of the hydrogen nuclei which suggests that the OAMO approximation is underestimating the strength of the nuclear scattering.

In this paper, we report results of a M3DW calculation for which a proper average over molecular orientations is performed. Our proper average calculations are in much better agreement with the experimental data for $CH_4$ than the OAMO results. We have been using the Ward - Macek (WM) approximation. [16] for the final-state interaction between the outgoing electrons (post-collision-interaction – PCI) since it gave better agreement with experimental data for the $H_2$ molecule than the exact columbic interaction [16]. We tested the two methods for including PCI for the proper average calculations, and we found that the results obtained using the exact Coulomb interaction were in better agreement with experiment than those obtained using the WM approximation.

## Theory

The molecular 3-body distorted wave (M3DW) approximation has been presented in previous publications [3] - [17] so only a brief outline of the theory will be presented. The triple differential cross section (TDCS) for the M3DW is given by:

$$\frac{d\sigma}{d\Omega_a d\Omega_b dE_b} = \frac{1}{(2\pi)^5}\frac{k_a k_b}{k_i}\left(|T_{dir}|^2 + |T_{exc}|^2 + |T_{dir} - T_{exc}|^2\right) \quad (1)$$

where $\vec{k}_i$, $\vec{k}_a$, and $\vec{k}_b$ are the wave vectors for the initial, scattered and ejected electrons, $T_{dir}$ is the direct scattering amplitude, and $T_{exc}$ is the exchange amplitude. The direct scattering amplitude is given by:

$$T_{dir} = \left\langle \chi_a^-(\vec{k}_a, \mathbf{r}_1)\, \chi_b^-(\vec{k}_b, \mathbf{r}_2)\, C_{\text{scat-eject}}(r_{12})\, |V - U_i|\, \phi_{DY}(\mathbf{R}, \mathbf{r}_2)\, \chi_i^+(\vec{k}_i, \mathbf{r}_1) \right\rangle \quad (2)$$

Where $r_1$ and $r_2$ are the coordinates of the incident and the bound electrons, $\chi_i$, $\chi_a$, and $\chi_b$ are the distorted waves for the incident, scattered, and ejected electrons respectively, $\phi_{DY}(\mathbf{R}, \mathbf{r}_2)$ is the initial bound-state Dyson molecular orbital, and **R** is the orientation of the molecule. In the OAMO approximation, $\phi_{DY}(\mathbf{R}, \mathbf{r}_2)$ is replaced with $\phi_{DY}^{OA}(r_2)$ which is the molecular orbital averaged over all orientations **R**. In M3DW-OAMO calculations, we average all orientations for the molecular orbital once independent of the kinematics of the collision and then we find TDCS with a single calculation of the T-matrix. In the proper average calculations, we find the TDCS for each orientation and then we average over all orientations. The molecular wave functions were calculated using density functional theory (DFT) along with the standard hybrid B3LYP [18] functional by means of the ADF 2007 (Amsterdam Density Functional)

program [19] with the TZ2P (triple-zeta with two polarization functions) Slater type basis sets.

The factor $C_{\text{scat-eject}}(r_{12})$ is the final state Coulomb interaction between the two outgoing electrons (post-collision-interaction – PCI). We have been using the Ward-Macek (WM) average Coulomb-distortion factor between the two final state electrons [16] since it gave good agreement with experiment for ionization of $H_2$ (using the OAMO approximation). In this work, we compare the results obtained using the WM approximation with results obtained using the exact Coulomb interaction.

The remaining undefined symbols used in the T-matrix are V which is the initial state interaction potential between the incident electron and the neutral molecule, and $U_i$ which is a spherically symmetric initial-state distorting potential which is used to calculate the initial-state distorted wave for the incident electron $\chi_i^+(\vec{k}_i, \mathbf{r}_1)$.

Details about the calculation of initial and final state distorted waves can be found in Madison and Al-Hagan [20]. For the exchange amplitude, particles 1 and 2 are interchanged in the final state wavefunction in eq. (2) [12].

## Results and Discussion

### A. Accuracy of proper average calculations

Since we have found good agreement between experiment and the M3DW for ionization of $H_2$ using the OAMO approximation, the first question that we wanted to address concerns the accuracy of the OAMO approximation for $H_2$. Figure 1 contains a comparison between $H_2$ results calculated using the OAMO approximation and with proper averages for scattering into the perpendicular plane with both final state electrons having the same energy and a relatively low incident electron energy of 54 eV which is in

the energy range of several recent experiments. As can be seen from the figure, the difference between the two calculations is smaller than typical experimental errors. We have tried other cases with similar kinematics and found analogous results so we conclude that the OAMO approximation is valid for $H_2$ at least for these kinematics. Of course, this is to be expected since we have shown the validity of the OAMO approximation for $H_2$ previously using an analytic approximation for the ground state wavefunction (13). Consequently, we conclude that the good agreement we have achieved for $H_2$ using the OAMO approximation is not fortuitous. We were also pleasantly surprised to find that we could get converged averages for $H_2$ using only 25 different orientations.

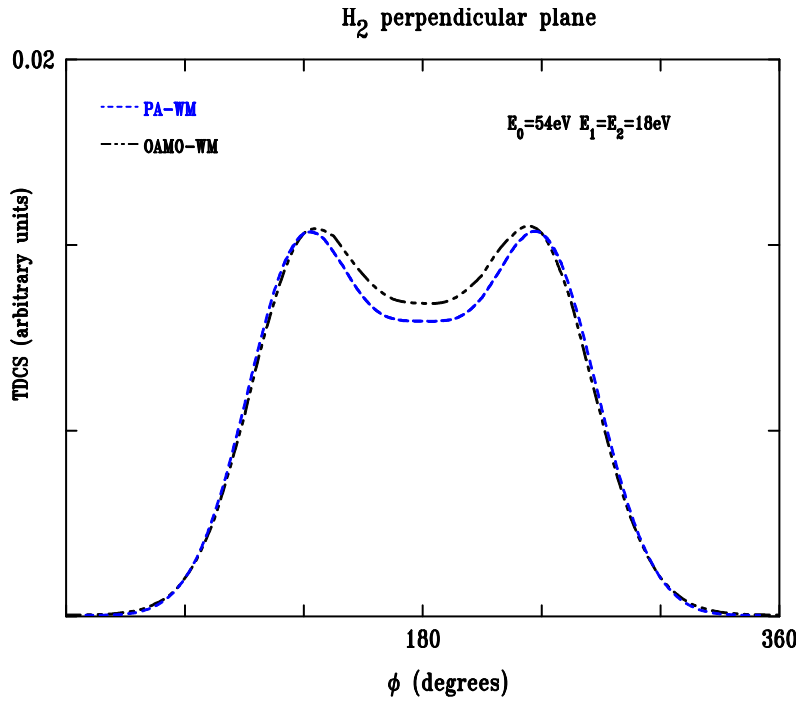


Figure 1: Triple Differential Cross Sections as a function of ejected electron angle for 54 eV electron impact ionization of $H_2$ in the perpendicular plane. Both scattered and ejected electrons have an energy of 18 eV. The solid - dotted curves are M3DW – OAMO calculations and the broken curves are PA calculations for the M3DW.

**B. Proper average calculations of methane**

Next we compared theoretical OAMO and Proper Average (PA) cross sections for electron-impact ionization of the $1t_2$ state of methane with experimental data for 54 eV incident electron energy.

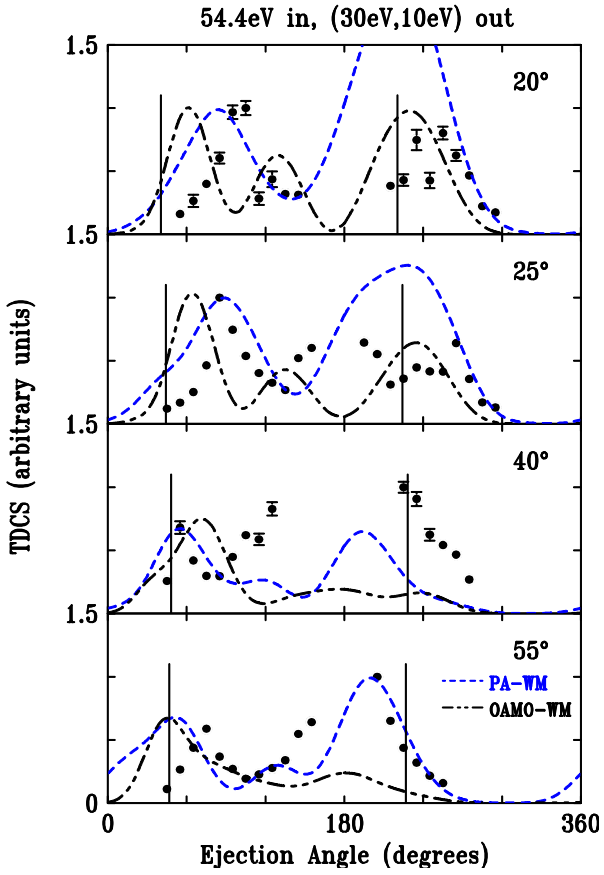


Figure 2 TCDS for 54.4 eV electron impact ionization of the $1t_2$ state of methane in the scattering plane. The horizontal axis is the ejected (slower final state) electron detection angle. The energy of the scattered electron (faster final state electron) is 30 eV and the energy of the ejected electron is 10 eV. Results are presented for projectile scattering angles ranging between $20^0$ (top) to $55^0$ (bottom). The solid vertical line in the small angular range corresponds to the classical momentum transfer direction. The solid vertical line for large angles corresponds to the classical momentum transfer direction plus $180^0$. Circles are the experimental data of Xu *et* al. [10] (reference), solid - dotted lines are M3DW-OAMO calculations and broken lines are M3DW PA calculations. The WM approximation for PCI was used for both theoretical curves.

The Ionization energy of the 1t2 state is 14 eV, so the rest of the energy (40 eV) is shared by the scattered and ejected electrons. We examined different sets of energy for the scattered and ejected electrons and for different fixed scattering angles for the fast electrons from 15° to 55°. The experimental data had been measured by Alexander Dorn's group at Heidelberg, Germany for both coplanar and perpendicular plane geometry.

**C. Coplanar geometry**

If the ejected electrons are detected in the scattering plane (plane determined by the incident and faster final state electron wave vectors), the process is called coplanar geometry. In Fig.2, experimental and theoretical results are presented for the case where the scattered and ejected electron energies have energies of 30 eV and 10 eV respectively. Cross sections are presented for four different projectile (faster final state electron) scattering angles ranging between 20° to 55°. For each figure, the experimental data are normalized to the unity for the largest cross section and the theoretical results are normalized to the best visual fit to the data. All of the theoretical results were obtained using the WM approximation for PCI.

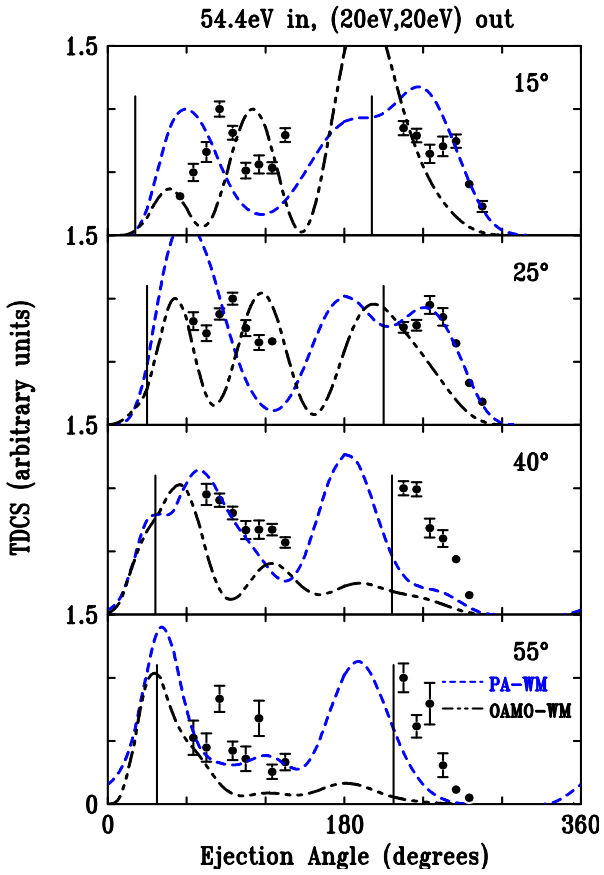


Figure 3: Same as Fig. 2 except that both final state electrons have an energy of 20 eV

Conventionally, the angular distributions are divided into two regions. These are the angular region between 0° and180°, which is known as the binary region, and the region between 180° and 360° which is called the recoil region [21]. Typically, the angular distributions have one peak in the binary region located near the momentum transfer direction (left vertical line in the figure) and this peak is attributed to a binary collision between the projectile and target electrons. In the recoil region, there is normally also one peak (generally much smaller than the binary peak) and this peak is normally located near the momentum transfer direction plus $180^0$ (right vertical line in the figure). This peak is attributed to a double collision mechanism where the first

collision is the binary collision ejecting the electron in the momentum transfer direction. However, as the electron leaves the target, there is a second collision with the attractive nuclei which backscatters the electron by $180^0$. From Fig. 2, it is seen that the recoil peak is larger than the binary peak for the larger projectile scattering angles and that the peak location for both the binary and recoil peaks are significantly shifted from the vertical lines. The OAMO calculations have a split in a binary peak for projectile scattering angles of 20° and 25° which is not uncommon for atomic p-states. However, the experimental data does not appear to have a split binary peak.

Our PA calculations exhibited better agreement with the experimental data than the OAMO results. For the binary region, the PA did not predict a split binary peak in accordance with experiment and the binary peak locations were also closer to the data. For the recoil peak, the experimental data shows the relative intensity of recoil peak to increase with increasing projectile scattering angle. Whereas the OAMO predicted that the intensity will decrease, our PA calculations predicted recoil peaks in better accord with the experimental data.

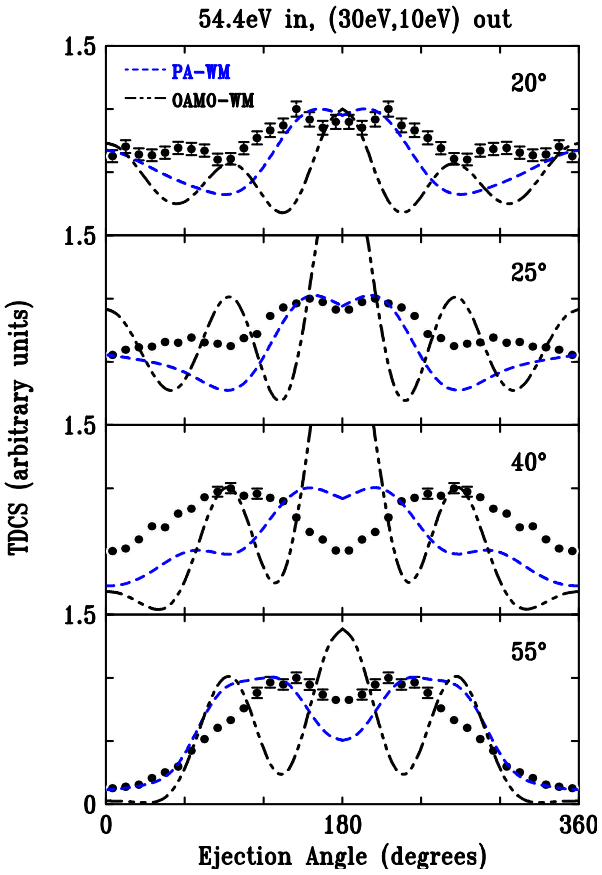


Figure 4 Same as Fig. 2 except for the perpendicular plane.

Figure 3 contains results similar to Fig. 2 except that the scattered and ejected electron energies are both 20 eV. OAMO calculations again predict a broad split in the binary peak region for the three smallest projectile scattering angles and relative recoil peak intensities much smaller than experiment for the two largest projectile scattering angles. The PA calculations are again in much better agreement with experimental data in general, and in particular, the relative magnitudes of the binary and recoil are much better than the OAMO results.

**D. Perpendicular geometry**

As mentioned in the introduction, Al-Hagan *et al.* [7] predicted that one should expect three peaks (two elastic scattering and one nuclear scattering) for electron-impact ionization of molecules that have a nucleus at the CM which is the case for methane. The published OAMO calculations exhibited a three peak structure for the perpendicular plane for both symmetric and asymmetric energy sharing [10] [12]. Figure 4 contains a comparison between experiment and theory in the perpendicular plane for the asymmetric energy sharing case. As before, the experimental data is normalized to unity and the theoretical calculations are normalized for a best visual fit to the experimental data. Instead of having a maximum at $180^0$ as predicted by the OAMO approximation, the experimental data has a local minimum and the PA calculations also have a $180^0$ minimum in accordance with experiment. Overall, the PA calculations are in reasonably good qualitative agreement with the experimental data. The most significant disagreement between experiment and theory occurs at a projectile scattering angle of 40° where the $180^0$ experimental dip is smaller than the theoretical and $55^0$ where the theoretical dip is smaller.

Figure 5 presents the same comparison as Fig. 4, except that the two final state electrons both have the same energy of 20 eV. For this case, the OAMO results only have a single peak at $180^0$ in accordance with experiment for the smallest projectile scattering angle of $15^0$. For the three larger projectile scattering angles, the OAMO results have the expected three peaks. The experiment, on the other hand, exhibits a (small) $180^0$ peak for all projectile scattering angles with a single peak for the two smaller angles and three peaks for the two larger projectile scattering angles. The PA calculations are in qualitative agreement with experiment for all four projectile scattering angles with the

biggest disagreement with experiment occurring for projectile scattering angles of $15^0$ (small and large ejection angles) and $40^0$ ($180^0$ peak too large).

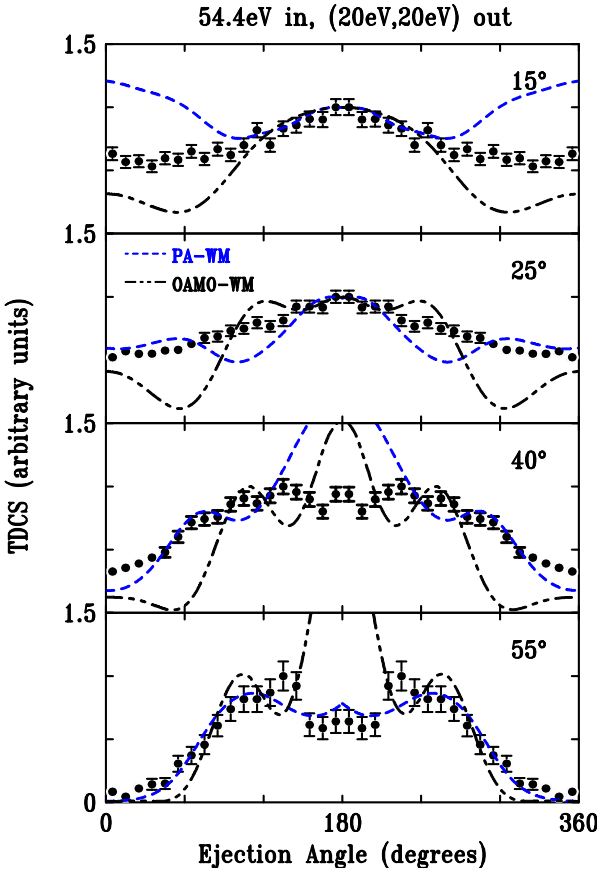


Figure 5 Same as Fig. 3 except for the perpendicular plane.

**E. Postcollision interaction**

In the final channel, there is a Columbic interaction between the two outgoing electrons (PCI). In DWBA calculations, this interaction can be either approximated by the WM approximation [16] or the Columb interaction can be treated exactly. The WM approximation (or a variant) has been very popular since it can be used in a distorted-wave calculation with essentially no additional work. To use the exact interaction is much more difficult [19]. However, since we do everything numerically, there is no time savings for us to use the WM approximation. However, we have been using it since we

found that, for ionization of $H_2$ (and using the OAMO approximation), the WM approximation consistently gave better agreement with experiment than using the exact full Coulomb interaction [16]. This always seemed a bit odd to us so we decided to test it again for our PA calculations.

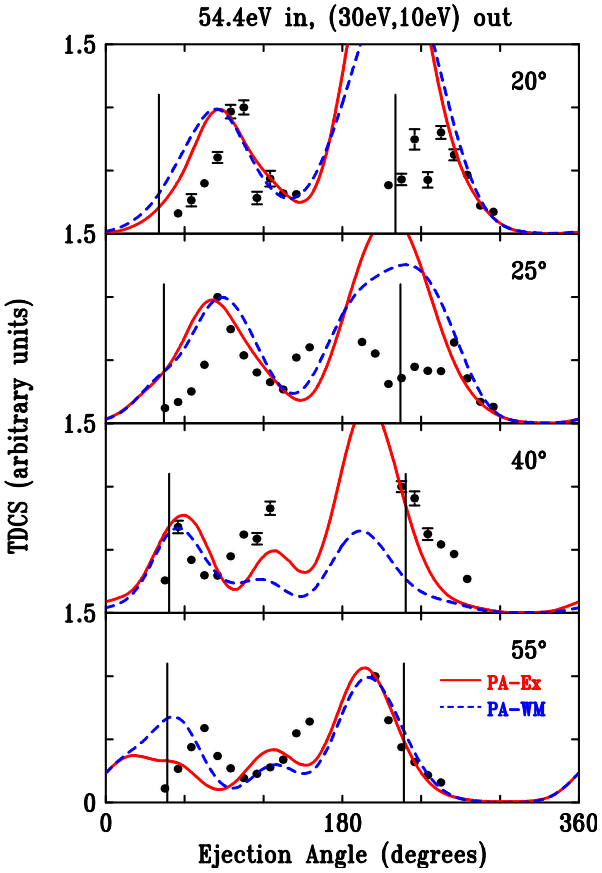


Figure 6 Same as Fig. 2 except that both theoretical calculations are M3DW with PAs over orientations with different treatments of PCI. For the broken curve, the WM approximation is used for PCI and for the solid curve the full exact Coulomb interaction is used for PCI

Figure 6 contains a comparison of M3DW results properly averaged over orientations and with PCI treated either using the WM approximation or using the proper Columbic interaction for coplanar asymmetric scattering (same as Fig. 2). From the figure, it is seen that the two different treatments of PCI give similar results except for a

projectile scattering angle of $40^0$ where there was a big change in the recoil region with the exact PCI treatment giving results in much better agreement with experimental data. For the other four projectile scattering angles, it is difficult to claim that one is better than the other. Figure 7 contains the same comparison except for equal energy final state electrons. In this case, there is not much difference for all projectile scattering angles and it is difficult to claim that one is better than the other.

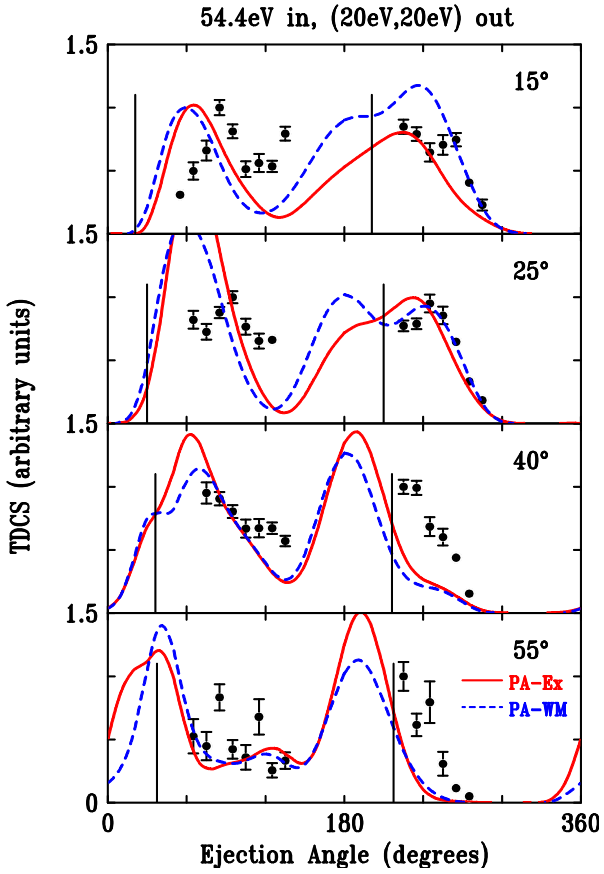


Figure 7 Same as Fig. 6 except that both final state electrons have an energy of 20 eV

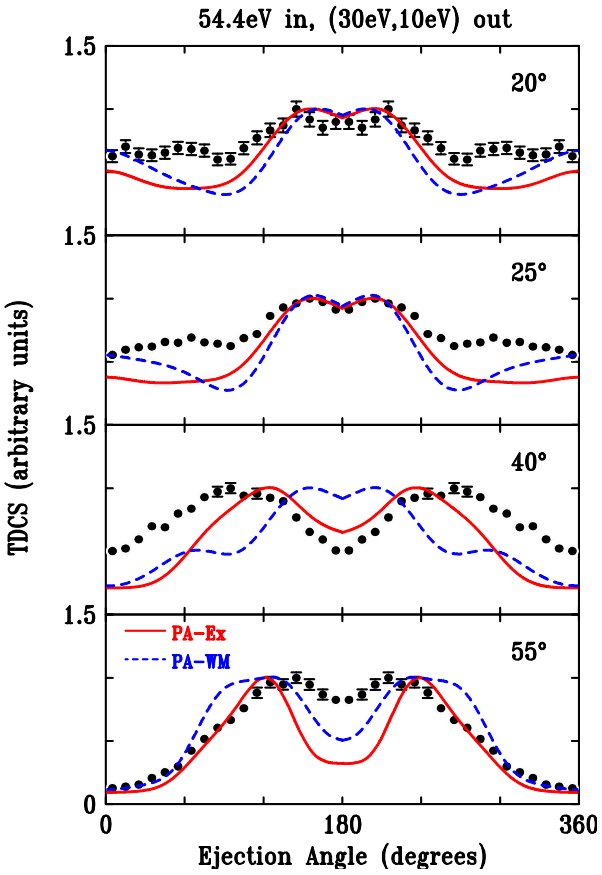


Figure 8 Same as Fig. 6 except for the perpendicular plane.

Figures 8 and 9 contain M3DW results properly averaged over orientations and with PCI treated either using the WM approximation or using the proper Columbic interaction for perpendicular plane scattering (same as Figs. 4 and 5). For the perpendicular plane, the full exact treatment of exchange clearly results in much better agreement with experiment. The most dramatic case is for a scattering angle of $40^0$ and equal energy electrons where the peak at $180^0$ become a shallow minimum in agreement with experiment. The worst agreement with experiment was found for unequal electron energies and the largest projectile scattering angle of $55^0$ where the $180^0$ minimum was significantly deeper than the experimental one. However, overall the agreement between

experiment and PA exact PCI M3DW results was very good for all the perpendicular plane measurements.

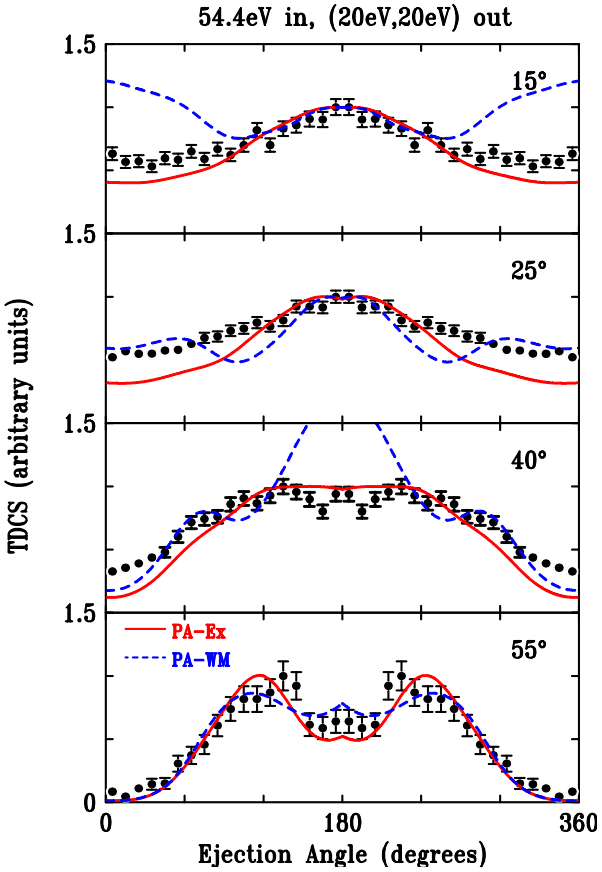


Figure 9 Same as Fig. 7 except for the perpendicular plane.

## Conclusions

We have presented PA M3DW calculation for (e, 2e) ionization of molecules. We had previously shown that the OAMO approximation should be valid for $H_2$ by using analytic wavefunctions for the ground state (13) and we verified that the OAMO and properly averaged results were the same to within experimental error for 54 eV incident electrons and equal energy final state electrons which is the energy range of many of the recent experiments. We then calculated the TDCS for (e,2e) ionization of the $1t_2$ molecular state of methane. A comparison was made between the experimental data,

OAMO calculations and PA calculations for coplanar and perpendicular plane scattering. The PA calculations were in much better agreement with experimental data than the OAMO calculations. For coplanar scattering, the PA calculations did a better job of predicting the number and location of binary peaks and they were also in much better agreement with experiment for the recoil peak. However, the most dramatic improvement occurred for the perpendicular plane where the OAMO approximation normally predicted three peaks with one peak at $180^0$ electron ejection angle while experiment predicted a minimum for most cases. The PA calculations, on the other hand, properly predicted the number of peaks for all cases except one and qualitatively predicted the shape of the experimental data.

We also tested the treatment of PCI (post collision interaction). We had previously found for $H_2$ using the OAMO approximation, that the Ward-Macek (WM) [16] yielded better agreement with experiment that the full exact treatment of PCI. We performed M3DW PA calculations treating PCI either with the WM approximation or with the full exact Coulomb interaction. For coplanar scattering, there was not much difference between exact PCI and WM except for one case where the exact treatment clearly predicted a better recoil peak. For the perpendicular plane, on the other hand, the exact treatment yielded better agreement with experiment for all cases (some more dramatic than others) and the exact treatment results are in fairly good agreement with all the perpendicular plane measurements (better than the coplanar).

## Acknowledgements

H.C. and D.M. acknowledge support of the US National Science Foundation under Grant No. PHY-1068237 and XSEDE resources [22] provided by the Texas Advanced Computing Center (Grant No. TG-MCA07S029). XSEDE systems are hosted

by Indiana University, LONI, NCAR, NCSA, NICS, ORNL, PSC, Purdue University, SDSC, TACC, and UC/ANL. C.G.N. would like to acknowledge the support of the National Natural Science Foundation of China under Contract No. 10704046.

## References

[1] B. Boudaïffa, Science (80-. ). **287**, 1658 (2000).

[2] F. Martin, P. Burrow, Z. Cai, P. Cloutier, D. Hunting, and L. Sanche, Phys. Rev. Lett. **93**, 068101 (2004).

[3] J. Gao, J. L. Peacher, and D. H. Madison, J. Chem. Phys. **123**, 204302 (2005).

[4] J. Gao, D. H. Madison, and J. L. Peacher, J. Phys. B At. Mol. Opt. Phys. **39**, 1275 (2006).

[5] J. Gao, D. H. Madison, J. L. Peacher, A. J. Murray, and M. J. Hussey, J. Chem. Phys. **124**, 194306 (2006).

[6] D. Milne-Brownlie, M. Foster, J. Gao, B. Lohmann, and D. Madison, Phys. Rev. Lett. **96**, 233201 (2006).

[7] Z. N. Ozer, H. Chaluvadi, M. Ulu, M. Dogan, B. Aktas, and D. Madison, Phys. Rev. A **87**, 042704 (2013).

[8] A. J. Murray, M. J. Hussey, J. Gao, and D. H. Madison, J. Phys. B At. Mol. Opt. Phys. **39**, 3945 (2006).

[9] K. L. Nixon, A. J. Murray, H. Chaluvadi, C. Ning, and D. H. Madison, J. Chem. Phys. **134**, 174304 (2011).

[10] S. Xu, H. Chaluvadi, X. Ren, T. Pflüger, a Senftleben, C. G. Ning, S. Yan, P. Zhang, J. Yang, X. Ma, J. Ullrich, D. H. Madison, and a Dorn, J. Chem. Phys. **137**, 024301 (2012).

[11] O. Al-Hagan, C. Kaiser, D. Madison, and A. J. Murray, Nat. Phys. **5**, 59 (2008).

[12] K. L. Nixon, A. J. Murray, H. Chaluvadi, S. Amami, D. H. Madison, and C. Ning, J. Chem. Phys. **136**, 094302 (2012).

[13] K. L. Nixon, A. J. Murray, H. Chaluvadi, C. Ning, J. Colgan, and D. H. Madison, J. Chem. Phys. **138**, 174304 (2013).

[14] I. Tóth and L. Nagy, J. Phys. B At. Mol. Opt. Phys. **43**, 135204 (2010).

[15] a Senftleben, T. Pflüger, X. Ren, B. Najjari, a Dorn, and J. Ullrich, J. Phys. B At. Mol. Opt. Phys. **45**, 021001 (2012).

[16] H. Macek, **49**, 1049 (1994).

[17] J. Gao, D. Madison, and J. Peacher, Phys. Rev. A **72**, 032721 (2005).

[18] C. Lee, C. Hill, and N. Carolina, **37**, (1988).

[19] C. F. Guerra, J. G. Snijders, G. Velde, and E. J. Baerends, 391 (1998).

[20] D. H. Madison and O. Al-Hagan, J. At. Mol. Opt. Phys. **2010**, 1 (2010).

[21] J. D. Builth-Williams, S. M. Bellm, D. B. Jones, H. Chaluvadi, D. H. Madison, C. G. Ning, B. Lohmann, and M. J. Brunger, J. Chem. Phys. **136**, 024304 (2012).

[22] C. Catlett et al., in HPC and Grids in Action, edited by Luco Grandinetti (IOS Press, Amsterdam, 2007).

# XII Observation of Two-Center Interference Effects for Electron Impact Ionization of $N_2$

Hari Chaluvadi[1], Zehra Nur Ozer[2], Mevlut Dogan[2], Chuangang Ning[3], James Colgan[4], and Don Madison[1]

[1]Department of Physics, Missouri University of Science and Technology, Rolla, Missouri, USA

[2]Department of Physics, e-COL Laboratory, Afyon Kocatepe University, 03200, Afyonkarahisar, Turkey

[3]Department of Physics, and State Key Laboratory of Low-Dimensional Quantum Physics, Tsinghua University, Beijing 100084, China

[4]Theoretical Division, Los Alamos National Laboratory, Los Alamos, New Mexico, USA

## Abstract

In 1966, Cohen and Fano [*Physical Review 150*, 30 (1966)] suggested that one should be able to observe the equivalent of Young's double slit interference if the double slits were replaced by a diatomic molecule. This suggestion inspired many experimental and theoretical studies searching for double slit interference effects both for photon and particle ionization of diatomic molecules. These effects turned out to be so small for particle ionization that this work proceeded slowly and evidence for interference effects were only found by looking at cross section ratios. Most of the early particle work concentrated on double differential cross sections for heavy particle scattering and the first evidence for two-center interference for electron-impact triple differential scattering (TDCS) did not appear until 2006 for ionization of $H_2$. Subsequent work has now firmly

established that two-center interference effects can be seen in the TDCS for electron-impact ionization of $H_2$. However, in spite of several experimental and theoretical studies, similar effects have not been found for electron-impact ionization of $N_2$. Here we report the first evidence for two-center interference for electron-impact ionization of $N_2$.

## Introduction

The concept of wave-particle duality is considered a milestone in the development of quantum mechanics. The observation of interference fringes from coherent light passing through two closely spaced slits became the basis for the modern wave theory of light. These early studies for photons helped establish the foundations of interference phenomena as a fundamental signature for quantum ideas and subsequent interference experiments for particle impact were carried out using several particles including electrons, neutrons and heavy species such as bare carbon ions and Kr ions [1,2,3].

The idea of interference in collisions of diatomic molecules with photons was first discussed by Cohen and Fano [4] in 1966. Based upon the wave-particle duality, one would expect that effects similar to those seen for photons should also be seen for particle impact. Most of the early particle work concentrated on double differential cross sections (DDCS) and the first experimental evidence for double-slit interference effects in single ionization of molecules by ion impact was presented by Stolterfoht et al. [3] in 2001. In 2002, Stia et al. [5,6] suggested that Cohen-Fano interference effects should also be expected for electron impact ionization of $H_2$. The first evidence for electron-$H_2$ interference was reported by Milne-Brownlie *et al.* [7] in 2007 by looking at the relative sizes of the binary and recoil peaks in the coplanar Triple Differential Cross Section

(TDCS) for electron-impact ionization of $H_2$. This observation was subsequently confirmed for different kinematics by Casagrande *et al.* [8].

In the Cohen-Fano model, the incident projectile is a photon. Consequently, the only two-center interference physics contained in the model for the ejected electron is emission from two different scattering centers (i.e. the two slits in the Young's experiment). However, for incident electrons, there are (at least) three different possible two-center interference effects: (i) incident electron being diffracted by two scattering centers; (*ii*) scattered electron being emitted from two centers; and (*iii*) ejected electron wave being emitted from two centers. Madison and coworkers [9,10] examined the three different types of possible two-center interference effects for electron-impact ionization of $H_2$ using the molecular three-body distorted wave (M3DW) approximation. Since the model of Stia et al. [5] is based upon the Cohen-Fano approach, the only two-center interference effects in this model is also the ejected electron being emitted from two nuclei. The M3DW calculations for $H_2$ [9,10], on the other hand, contain all three possible two-center interference effects and model calculations indicated that the most important contribution to two-center interference is coming from the diffraction of the incident projectile from two scattering centers.

As mentioned above, looking at the ratio of binary to recoil peaks provides indirect evidence for two-center interference effects at the molecular level. A different approach for finding Young's two-center interference effects for $H_2$ was recently reported by our group. Cohen-Fano noted that the best way to look for double-slit interference effects was to look at the ratio of the molecular $H_2$ cross section to the atomic H cross section. The logic is that this ratio, called the interference factor (I-factor), should

contain only the two-center effects since the single center effects should cancel. Due to the difficulty of measuring atomic H cross sections, we looked at the ratio of molecular $H_2$ to He cross sections both experimentally and theoretically and we found a rich structure in both the experiment and theory. This structure was interpreted as a direct observation of two-center interference effects and very nice agreement between experiment and theory was found [9,10]. The Cohen-Fano I-factor [4] ( $I^{CF}$ ) (same as the Stia *et al*. [5] I-factor) was only in very rough qualitative agreement with experiment and $I^{CF}$ did not predict any of the detailed structure which indicates that the full two-center interference effects are much more complicated that just the double-slit component.

If two-center interference effects are present for $H_2$, then one would expect that they should also be seen for $N_2$. However, in spite of several searches, no conclusive evidence for two-center interference effects have been found for $N_2$ (11-16). In a theoretical study of low incident-energy electron-impact ionization of the $N_2$ ($3\sigma_g$) molecular state, Gao et al. [11] predicted strong Young's double slit type interference effects for highly asymmetric scattering for coplanar $180^0$ (back scattering). Murray *et al.* [12,13] performed experiments on the $3\sigma_g$ and $3\sigma_u^*$ states of $N_2$ in a coplanar asymmetric geometry and the predicted interference peak was outside the experimentally accessible angular range. Several other studies of TDCS for electron-impact ionization of $N_2$ have been performed [14,15,16] and none of them found any evidence for two-center interference for $N_2$.

In this paper, we report a study looking for evidence of two-center interference in (e,2e) ionization of $N_2$ by looking at the I-factor which, in this case, is the ratio of the molecular $N_2$ cross sections divided by the atomic nitrogen N cross

sections. Similar to the $H_2$ study, we do not have experimental data for ionization of atomic N. In this case, we use theoretical N cross sections calculated in the M3DW as the denominator for both experiment and theory (as has been routinely done for heavy particle scattering [2,3]). In this paper, TDCS measurements and ratios are presented for ionization of the $3\sigma_g$ valance molecular orbital of $N_2$ in the intermediate-energy range and very strong interference effects are found. A preliminary report of this work was recently published in a Conference Series [17].

**Experiment**

This study has been conducted in a conventional (e,2e) spectrometer (see in figure 1.a) which has been well documented in previous works [17,18] and so will only be briefly described here. The spectrometers in electron collision laboratory (e-COL) have been used to measure TDCSs for electron impact ionization of He, Ar and $H_2$ [9,10,19-22]. A vacuum pressure of $\approx 8.10^{-8}$ mbar is achieved. The magnetic field in the collision region is reduced to about 3 mG by using μ-metal shielding as well as the Helmholtz coils that eliminate the Earth's magnetic field. The electron gun consists of a tungsten filament, and 7 element electrostatic lenses including electrostatic deflectors allowing the beam to be focused onto the 2 mm diameter interaction region. The incident electron beam energy can be varied from 40-350 eV. Typical electron currents are around 1 to 3 μA and the electron current remains stable over a long time. It is essential for the (e,2e) technique to obtain accurate knowledge of the energies of the incident, scattered and ejected electrons. Scattered and ejected electrons are determined by two hemispherical electrostatic analyzers. Each analyzer consists of a five element input electrostatic lens system and a Channeltron (CEM). The (e,2e) technique has an advantage for identifying single ionization events for which the outgoing electrons are originated from the same

ionization event. Using standard coincidence timing techniques, the arrival times of the electrons detected in each analyzer were used to determine if the electrons originated from the same ionization event. Coincidence electronics are shown in figure 1.b.

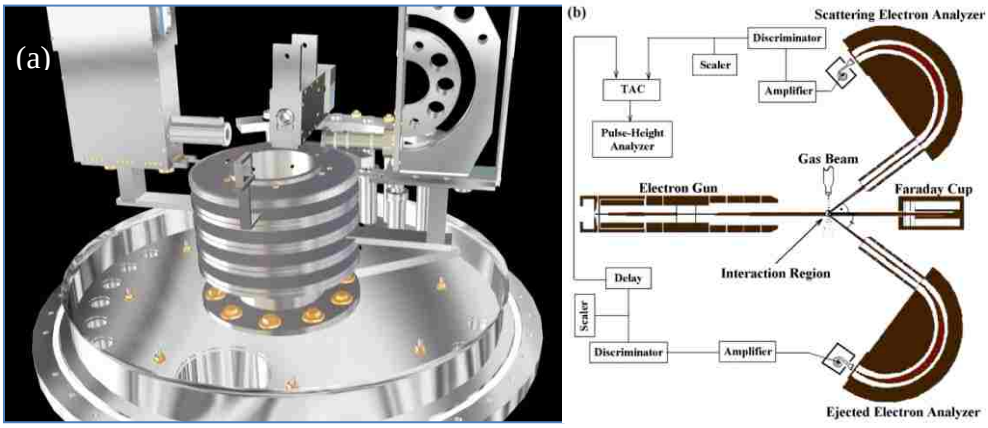


Figure 1(a) Sketch of electron spectrometer. The main components are: electron gun, two electron analyzers and a Faraday cup and (b) coincidence electronics used to accumulate the coincidence timing spectrum at each set of kinematics.

The results for ionization from $3\sigma_g$ orbital of $N_2$ presented in this paper were collected in a coplanar asymmetric geometry, where the scattered and ejected electrons are detected on the same plane.

The incident electron current was around 3μA. In this study the obtained binding energy resolution was ≈1.4 eV (FWHM) for an incident electron energy $E_0$ = 250 eV, with the scattered electron being detected in coincidence with an ejected electron with $E_b$ = 50 eV.

## Theory

We have used the molecular 3-body distorted wave (M3DW) approximation to calculate the TDCS for $N_2$ and the atomic 3-body distorted wave (3DW) approximation to calculate the TDCS for N. The theory for these calculations has been presented elsewhere [11,24,25] so we will not repeat the equations here. However, we should note

that we have used the orientation-averaged molecular orbital (OAMO) approximation [23] which was shown to give very good agreement with experimental TDCS data for $H_2$. For the N calculation, we have used Hartree-Fock bound state wavefunctions and for $N_2$, we have used wavefunctions calculated using density functional theory. Finally, we have used the exact final state electron-electron interaction (normally called post-collision-interaction or PCI).

## Results and Discussion

In previous papers, we compared experimental and theoretical interference factors (I-factors) for electron-Impact ionization of the $H_2$ molecule [9,10]. We found that the I-factor exhibited a very complicated structure and, overall, there was very good agreement between theoretical cross sections and experimental data. The observed theoretical and experimental two-center interference factor exhibited significantly more structured than the double-slit Cohen-Fano interference factor ( $I^{CF}$ ). We found that interference is more sensitive to the projectile scattering angle than the ejected electron energy and we found that projectile diffraction from two scattering centers is more important than the ejected electron being emitted from the two different centers [9].

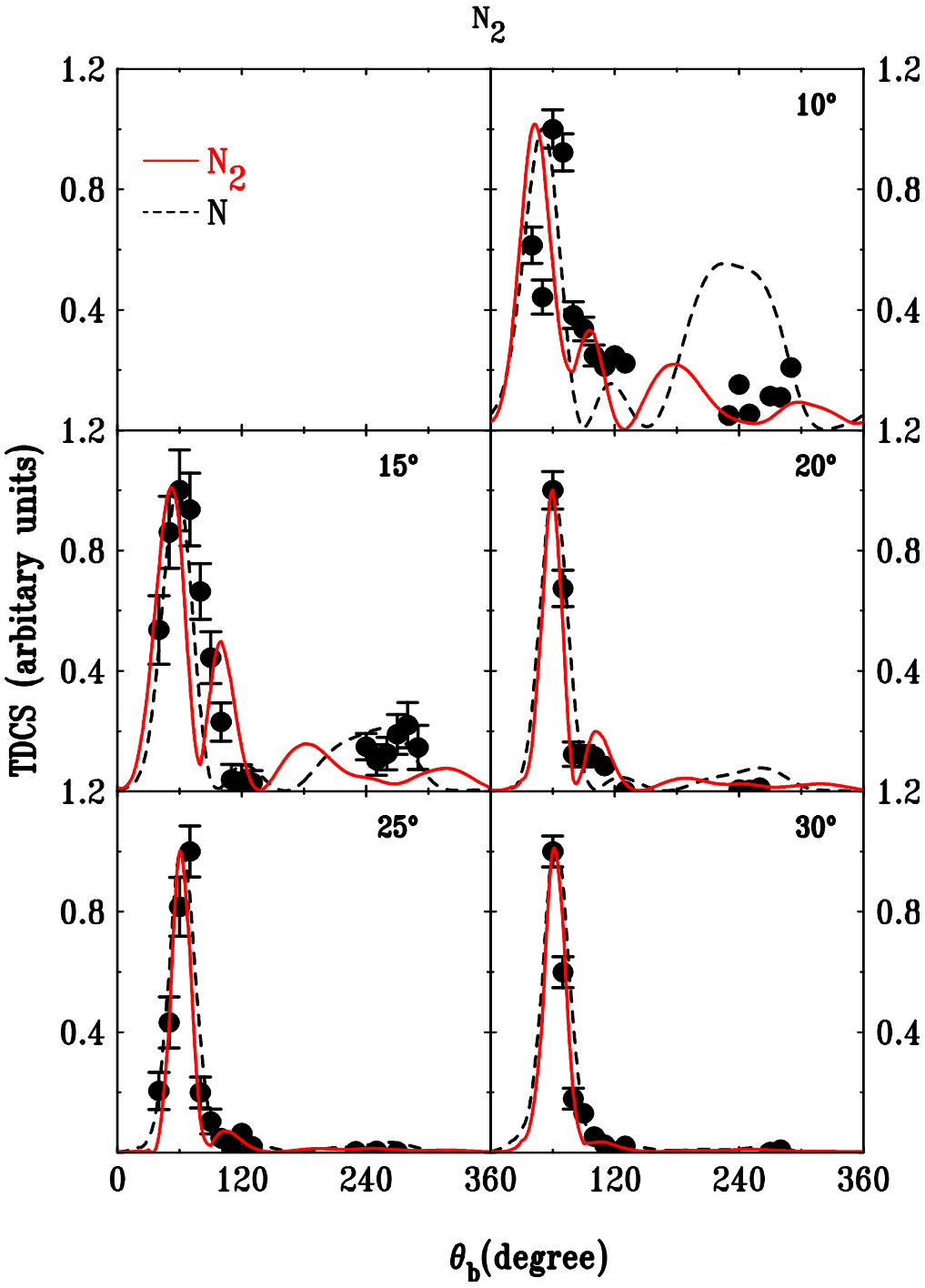


Figure. 2. TDCS for 250 eV electron impact ionization of the 3σg valance state of $N_2$ and atomic N as a function of the ejected electron angle $\theta_b$. The projectile scattering angle is noted in each sub-figure from 10° to 30° in steps of 5°. Solid circles – $N_2$ experimental data, solid (red) curve – M3DW calculations for the N2 molecule and dashed (black) curve – 3DW calculations for the Nitrogen atom.

Theoretical calculations for $N_2$ consistently predict a shoulder in the binary region around 100°, with the intensity of the shoulder decreasing with increasing projectile scattering angle from 15°. Although this shoulder is not seen in the experimental data, there is a small suggestion for the possibility of a shoulder at 10° and also perhaps at 25°. Overall, the theoretical calculations for $N_2$ are in reasonably good agreement with the experimental data.

For the low-angle peak, both the M3DW results and experiment predict the peak at the same angle and they are in an excellent agreement. Theory predicts two more peaks - one around the 150° and one in the $330^0 – 360^0$ range, both of which are inaccessible to experiment although there is a suggestion for the high-angle peak at large projectile scattering angles.

The Cohen-Fano I-factor $I^{CF}$ predicts a broad peak for small ejected-electron angles with the maximum occurring at significantly smaller angles than was found in either the present experiment or theory. For the larger ejection angles, $I^{CF}$ predicts a very broad small peak which is also not found in either the experiment or theory. For the $H_2$ molecule, we found a qualitative agreement between our results and $I^{CF}$. However, for the $N_2$ molecule, there is little similarity between $I^{CF}$ and the present results which indicates that the three different possible two-center effects yield a much more complicated interference pattern that the single double-slit possibility.

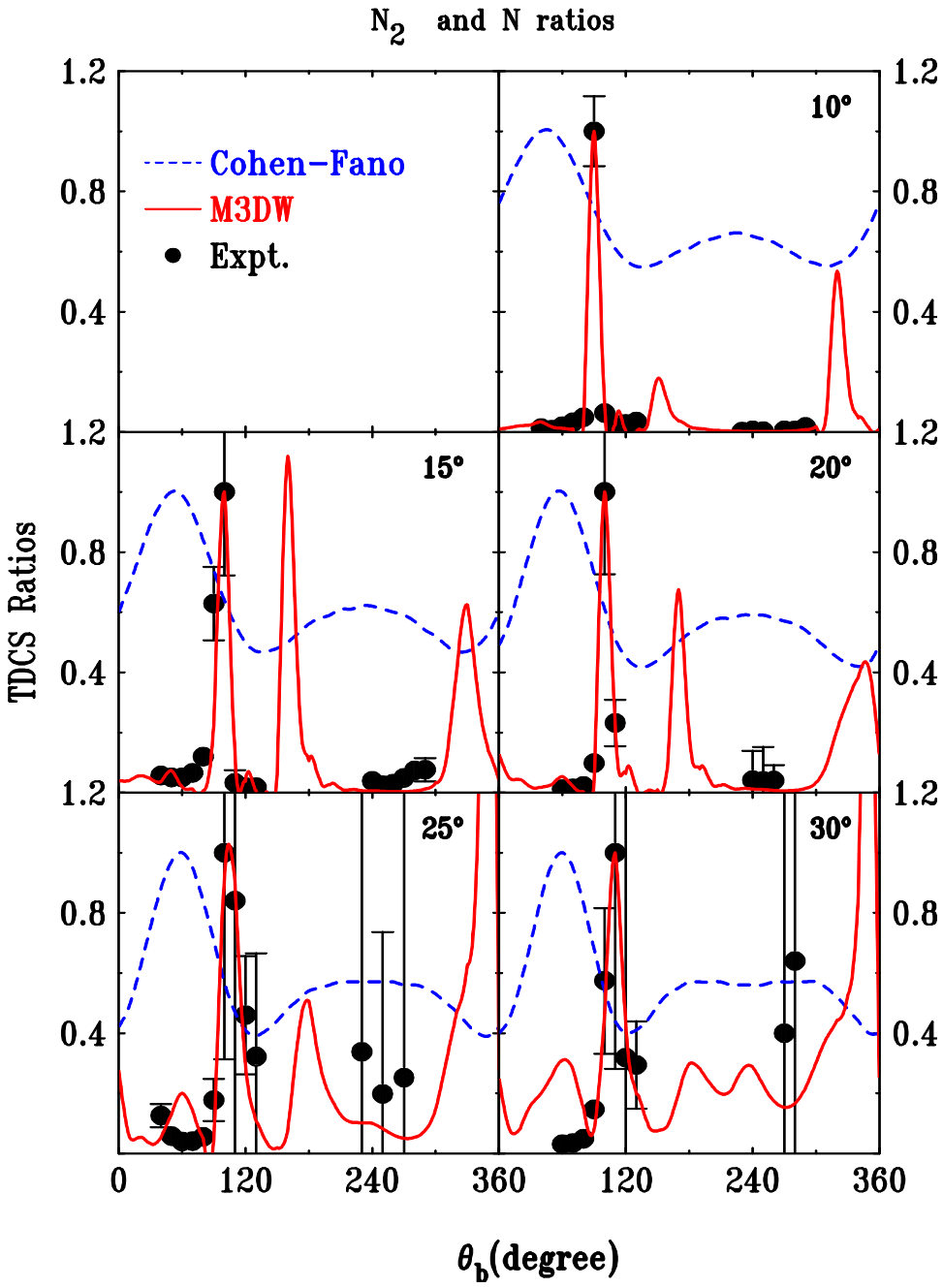


Figure. 3. Interference factor for 250 eV electron impact ionization of the $N_2$ molecule as a function of the ejected electron angle $\theta_b$. The projectile scattering angle is noted in each sub-figure from 10° to 30° in steps of 5°. Solid circles – Experimental data, solid (red) curve – M3DW, and dashed (blue) cuve - $I^{CF}$.

Gao *et al.*, [11] found evidence for a strong interference effect for $N_2$ in the scattering plane for electron emission at $180^0$. Andrew Murray's group looked for

interference effects for $N_2$ [13] and they did find any. In this work, there is also a theoretical suggestion for interference effects near $180^0$ (which is not experimentally accessible). On the other hand, the excellent agreement between experiment and theory found for the main peak around $100^0$ represents the first direct evidence for two-center interference effects in electron-impact ionization of $N_2$. One might think that the theoretical peak results from the (probably) unphysical shoulder on the binary peak. However, we checked and this is not the case. There is no obvious shoulder in the experimental data and it has a peak at exactly the same angle as the theory. This peak is more strongly influenced by the shape of the atomic N cross sections than the molecular $N_2$ cross sections. The weakness of this approach is that the same atomic cross sections are used for both experiment and theory and it would be much better to have experimental cross sections as we did for $H_2$. Nevertheless, we think that the good agreement between experiment and theory is significant and represents the first evidence for interference effects for $N_2$.

## Conclusions

We compared experimental and theoretical (e,2e) cross sections and I-factors for 250 eV electron-impact ionization of the $N_2$ molecule in the scattering plane. We found reasonably good agreement between the theoretical M3DW TDCS results and experiment. However, comparing experiment and theory for the TDCS does not provide a very good method for identifying two-center interference effects since it is not clear how these effects are manifested in the cross sections. In 1966, Cohen-Fano [4] noted that a better test is to take ratios of the TDCS for the molecule divided by the TDCS for the corresponding atom (the I-factor). The logic was that dividing by the atomic cross sections would remove single center effects and leave only two-center effects.

Evidence for two-center interference effects have now been demonstrated for electron-$H_2$ scattering [7-10]. Although there were several experimental attempts to find two-center interference effects for $N_2$, no experimental evidence has been found in prior work. In this work, we compared the theoretical and experimental I-factors for $N_2$ and found a strong peak within the angular range of the binary peak and the theoretical and experimental results were in excellent agreement with each other. This observation represents the first evidence for two-center interference effects to be seen for $N_2$. The I-factor represents a better test for interference than looking directly at the TDCS since it is not clear how interference effects will be manifested directly in the cross sections. Previous works for $N_2$ did not look at the I-factor and this is the reason they did not see any evidence for two-center interference.

## Acknowledgements

H.C. and D.M. acknowledge the support of the U.S. National Science Foundation under Grant No. PHY-1068237, XSEDE resources provided [26] by the Texas Advanced Computing Center (Grant No. TG-MCA07S029) and partial computational work was performed with Institutional Computing resources made available through Los Alamos National Laboratory. C.G.N. would like to acknowledge the support of the National Natural Science Foundation of China under Contract No. 11174175. The experimental part of this work was supported by the Scientific and Technological Research Council of Turkey (TUBITAK) through Grant No. 109T738 and by BAPK through Grant No. 12.FENED.05.

## References


[1] Misra, D., Kelkar, A., Kadhane, U., Kumar, A., Tribedi, L. C., & Fainstein, P. D. (2006). Influence of Young-type interference on the forward-backward asymmetry in electron emission from H 2 in collisions with 80-MeV bare C ions. *Physical Review A*, *74*(6), 060701.

[2] Misra, D., Kelkar, A., Kadhane, U., Kumar, A., Singh, Y. P., Tribedi, L. C., & Fainstein, P. D. (2007). Angular distribution of low-energy electron emission in collisions of 6-MeV/u bare carbon ions with molecular hydrogen: Two-center mechanism and interference effect. *Physical Review A*, *75*(5), 052712.

[3] Stolterfoht, N., Sulik, B., Hoffmann, V., Skogvall, B., Chesnel, J. Y., Rangama, J., Rivarola, R. D. (2001). Evidence for Interference Effects in Electron Emission from H 2 Colliding with 60 MeV/u Kr 3 4+ Ions. *Physical Review Letters*, *87*(2), 023201.

[4] Cohen, H. D., Fano, U. (1966). Interference in the photo-ionization of molecules. *Physical Review*, *150*(1), 30.

[5] Stia, C. R., Fojón, O. A., Weck, P. F., Hanssen, J., Joulakian, B., Rivarola, R. D. (2002). Molecular three-continuum approximation for ionization of $H_2$ by electron impact. *Physical Review A*, *66*(5), 052709.

[6] Stia, C. R., Fojón, O. A., Weck, P. F., Hanssen, J., Rivarola, R. D. (2003). Interference effects in single ionization of molecular hydrogen by electron impact. *Journal of Physics B: Atomic, Molecular and Optical Physics*, *36*(17), L257.

[7] Milne-Brownlie, D. S., Foster, M., Gao, J., Lohmann, B., Madison, D. H. (2006). Young-Type Interference in (e, 2 e) Ionization of H 2. *Physical review letters*, *96*(23), 233201.

[8] Casagrande, E. S., Naja, A., Mezdari, F., Lahmam-Bennani, A., Bolognesi, P., Joulakian, B., Bray, I. (2008). (e, 2e) ionization of helium and the hydrogen molecule: signature of two-centre interference effects. *Journal of Physics B: Atomic, Molecular and Optical Physics*, *41*(2), 025204.

[9] Ozer, Z. N., Chaluvadi, H., Ulu, M., Dogan, M., Aktas, B., Madison, D. (2013). Young's double-slit interference for quantum particles. *Physical Review A*, *87*(4), 042704.

[10] Ozer, Z. N., Chaluvadi, H., Ulu, M., Dogan, M., Aktas, B., & Madison, D. (2014, April). Young Double Slit Interference Effects at Quantum Level. In *Journal of Physics: Conference Series* (Vol. 488, No. 1, p. 012059). IOP Publishing.

[11] Gao, J., Madison, D. H., Peacher, J. L. (2005). Interference effects for low-energy electron-impact ionization of nitrogen molecules. *Physical Review A*, *72*(3), 032721.

[12] Murray, A. J., Hussey, M. J., Kaiser, C., Gao, J., Madison, D. H. (2007). Electron impact ionization of molecules at low to intermediate energies—a search for Young's double slit type interferences. *Journal of Electron Spectroscopy and Related Phenomena*, *161*(1), 11-16.

[13] Murray, A. J., Hussey, M. J., Gao, J., Madison, D. H. (2006). states of N2—comparison between experiment and theoretical predictions of the effects of exchange, polarization and interference. *J. Phys. B: At. Mol. Opt. Phys*, *39*, 3945-3956.

[14] Hargreaves, L. R., Colyer, C., Stevenson, M. A., Lohmann, B., Al-Hagan, O., Madison, D. H., Ning, C. G. (2009). (e, 2 e) study of two-center interference effects in the ionization of N 2. *Physical Review A*, *80*(6), 062704.

[15] Naja, A., Staicu-Casagrande, E. M., Lahmam-Bennani, A., Nekkab, M., Mezdari, F., Joulakian, B., Madison, D. H. (2007). Triply differential (e, 2e) cross sections for ionization of the nitrogen molecule at large energy transfer. *Journal of Physics B: Atomic, Molecular and Optical Physics*, *40*(18), 3775.

[16] Lahmam-Bennani, A., Casagrande, E. S., Naja, A. (2009). Experimental investigation of the triple differential cross section for electron impact ionization of N2 and CO2 molecules at intermediate impact energy and large ion recoil momentum. *Journal of Physics B: Atomic, Molecular and Optical Physics*, *42*(23), 235205.

[17] Zehra Nur Ozer, Hari Chaluvadi, Don Madison and Mevlut Dogan, Interference effects for intermediate energy electron-impact ionization of $H_2$ and $N_2$ molecules, Journal of Physics: Conference Series **601**, 012003 (6pp) (April 2015).

[17] Dogan, M., Ulu, M., Sise, O. (2007). Design, simulation and construction of an electron–electron coincidence spectrometer. *Journal of Electron Spectroscopy and Related Phenomena*, *161*(1), 58-62.

[18] Dogan, M., Ulu, M., Ozer, Z. N., Yavuz, M., Bozkurt, G. (2013). Double Differential Cross-Sections for Electron Impact Ionization of Atoms and Molecules. *Journal of Spectroscopy*, *2013*.

[19] Sise, O., Dogan, M., Okur, I., Crowe, A. (2011). Electron-impact excitation of the (2p 2) 1 D and (2 s 2 p) 1 P o autoionizing states of helium. *Physical Review A*, *84*(2), 022705.

[20] Ozer, Z. N., Sahlaoui, M., Bouamoud, M., & Dogan, M. (2013). Theoretical and Experimental Studies on the Electron Impact Ionization of Helium at Intermediate Energies. *Chinese Journal of Physics*, *51*(6), 1330-1335.

[21] Ulu, M., Ozer, Z. N., Yavuz, M., Zatsarinny, O., Bartschat, K., Dogan, M., Crowe, A. (2013). Experimental and theoretical investigation of (e, 2e) ionization of Ar (3p) in asymmetric kinematics at 200 eV. *Journal of Physics B: Atomic, Molecular and Optical Physics*, *46*(11), 115204.

[22] Amami, S., Ulu, M., Ozer, Z. N., Yavuz, M., Kazgoz, S., Dogan, M., Madison, D. (2014). Theoretical and experimental investigation of (e,2e) ionization of argon 3p in asymmetric kinematics at intermediate energy. *Physical Review A, 90*(1), 012704.

[23] D.H. Madison and O. Al-Hagan, Journal of Atomic, Molecular, and Optical Physics 2010, 367180, (2010).

[24] J. Gao, D.H. Madison, and J.L. Peacher, J. Chem. Phys. 123 204314 (2005).

[25] J. Gao, D.H. Madison, and J.L. Peacher, J. Chem. Phys. 123 204302 (2005).

[26] C. Catlett et al., in HPC and Grids in Action, edited by Luco Grandinetti (IOS Press, Amsterdam,2007).

**SECTION**

# 2 CONCLUSIONS

For the simplest molecule $H_2$, our theoretical M3DW-OAMO calculations showed an excellent agreement with the experimental data. We observed a two-centre interference pattern for the $H_2$ molecule. We found the theoretical and experimental interference factor (I-factor) has significantly more structure than the Cohen-Fano I-factor ($I^{CF}$) and it is more sensitive to the angle scan than energy scan. We examined the three possible different types of double-slit interference effects: (i) incident electron being diffracted by two scattering centers; (ii) scattered electron being emitted from two centers; and (iii) ejected electron wave being emitted from two centers, and found that the $1^{st}$ case contributed the most to the interference. We observed the same double-slit interference pattern for the $N_2$ molecule.

We compared the experimental data and M3DW-OAMO calculations for electron-impact ionization of the $CH_4$ molecule for different geometries. For the coplanar symmetric geometry, we examined ionization of both the $1t_2$ and $2a_1$ molecular orbitals. Since the $2a_1$ molecular orbital is almost spherical in nature and does not have parity inversion, we expected that the OAMO approximation should be valid for this state. Surprisingly, better agreement was found for the $1t_2$ than the $2a_1$ orbital.

For the perpendicular plane geometry, it had been predicted that, if a molecule has a nucleus at the center of mass (c.m.), the cross sections should exhibit a three-peak

structure. Since methane has a nucleus at the c.m., a three-peak structure was expected. But, the experimental data showed only a two-peak structure.

For the coplanar geometry, the agreement between experiment and theory was better for smaller scattering angles. As the scattering angle increases, the experimental relative size of the recoil peak increased, whereas the theoretical recoil peak decreased in magnitude. This suggests that nuclear scattering is underestimated in the theoretical model. We moved the H nuclei closer to the c.m., and we found an increase in the recoil peak intensity as expected.

The $CH_4$ molecule $1t_2$ state and the $NH_3$ molecule $3a_1$ and $1e_1$ states all have *p*-like characteristics, whereas the $CH_4$ molecule $1a_1$ state and the $NH_3$ molecule $2a_1$ state have *s*-like characteristics. However, both the *p*-like and *s*-like states in $CH_4$ and $NH_3$ exhibited similar trends for the theoretical cross sections. This result may be caused by the OAMO approximation, which changes *p*-type structure into a spherical shape.

Studies of the electron-impact ionization of biomolecules provide important information on the role of electrons in causing damage to DNA in biological systems. It is now well established that low energy secondary electrons produced by high energy primary radiation are responsible for much of the damage to DNA in living tissue.

We studied several DNA base molecules like Pyrimidine, THF, THFA, THP and 1,4-dioxane. When we compared our OAMO calculations with experimental data, we found a better agreement with the binary peak than the recoil peak. We observed increasing discrepancy in the recoil region while decreasing the scattering angle.

We proposed Proper Average (PA) calculations. We verified that the OAMO and PA results for the $H_2$ molecule, were the same to within experimental error.

The PA results for $CH_4$ showed much better agreement with experimental data than the OAMO. For the coplanar scattering, the PA calculations did a better job of predicting the number of lobes and location of the binary peak as well as intensity of the recoil peak. For the perpendicular plane, the OAMO approximation predicted three peaks with one peak at 180° electron ejection angle, whereas experiment predicted a minimum at 180° for most cases. The PA calculations, properly predicted the number of peaks for all cases except one and yielded reasonably good agreement with the shape and magnitude of the experimental data.

# BIBLIOGRAPHY

[1] B. H. Bransden and C. J. Joachain. (2003) Physics of Atoms and Molecules. Pearson,

[2] C. F. Guerra, J. G. Snijders, G. te Velde, and E. J. Baerends, Theor. Chem. Acc. 99, 391 (1998).

# VITA

Hari Hara Kumar Chaluvadi was born and grew up in Eluru, India. He received his Master of Science degree in Physics from Andhra University, India in 2007. He joined the Department of Physics in Missouri University of Science and Technology, Rolla, USA in 2009. Here, he worked as a Graduate Teaching Assistant and Graduate Research Assistant from Fall 2010 till Spring 2015. He was awarded a Ph.D. degree in Physics in August 2015 by Missouri University of Science and Technology for his work on "Accuracy of Theory for Calculating Electron Impact Ionization of Molecules". His research was conducted under the guidance of Dr. Don Madison.

He was awarded the second place winner of the 19th and the 21st Annual Laird D. Schearer Research Prize competition in November 2012 and December 2014. He was awarded for the 1st prize (2013) and two times 2nd prize (2014 & 2015) for the annual research poster presentation in Graduate research showcase at Missouri University of Science and Technology.

He served as the Physics Department representative for the Council of Graduate students from Spring 2010 till Spring 2014, and received the 2013 and 2014 Council of Graduate Students Best Representative Award for the valuable services. He organized the Physics Graduate Student Seminars in Spring 2015.

Hari has published 12 peer-reviewed articles. He has presented his research work in several national and international conferences. He was invited speaker at the International Conference on Many Particle Spectroscopy of Atoms, Molecules, Clusters and Surfaces in 2012 and the 66th Annual Gaseous Electronics Conference in 2013.